

NO-A182 668

DETERMINATION AND REDUCTION OF UNWANTED ELECTROMAGNETIC

1/3

WAVE REFLECTIONS I (U) AIR FORCE INST OF TECH

WRIGHT-PATTERSON AFB OH SCHOOL OF ENGI

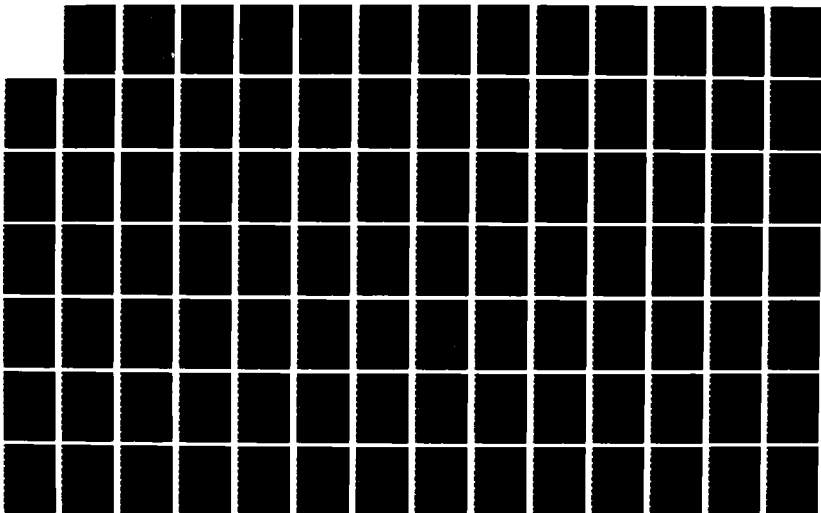
K A BRUNER

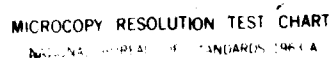
UNCLASSIFIED

MAR 87 AFIT/GE/ENG/87M-8

F/G 28/3

NL





AD-A182 668



DETERMINATION AND REDUCTION OF
UNWANTED ELECTROMAGNETIC WAVE REFLECTIONS
IN AN EMP SIMULATOR

DTIC
ELECTE
JUL 24 1987
S D E

DEPARTMENT OF THE AIR FORCE
AIR UNIVERSITY
AIR FORCE INSTITUTE OF TECHNOLOGY

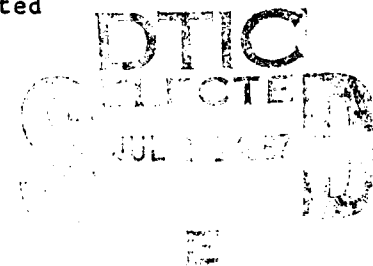
Wright-Patterson Air Force Base, Ohio

This document has been approved
for public release and sale; its
distribution is unlimited.

87 7 22 080

DETERMINATION AND REDUCTION OF
UNWANTED ELECTROMAGNETIC WAVE REFLECTIONS
IN AN EMP SIMULATOR

Approved for public release; distribution unlimited



DETERMINATION AND REDUCTION OF UNWANTED
ELECTROMAGNETIC WAVE REFLECTIONS IN AN EMP SIMULATOR

THESIS

Presented to the Faculty of the School of Engineering
of the Air Force Institute of Technology
Air University

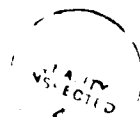
In Partial Fulfillment of the
Requirements for the Degree of
Master of Science in Electrical Engineering

Kenneth A. Bruner, B.E.E.E
Captain, USAF

March 1987

Accession For	
NTIS GRA&I	<input checked="checked" type="checkbox"/>
DTIC TAB	<input type="checkbox"/>
Unannounced	<input type="checkbox"/>
Justification	
By _____	
Distribution/	
Availability Codes	
Dist	Avail and/or Special
A-1	

Approved for public release; distribution unlimited



Preface

The purpose of this thesis was to determine and reduce unwanted wave reflections within an EMP illuminator located at Kirtland AFB. This illuminator is used to test the linear hardening devices placed on aircraft as a protection against EMP. The wave reflections occur by the interaction between a highly conductive planar surface and the aircraft under test. The method chosen to reduce these reflections was to place an absorber material in key locations within the simulator. This document presents an analysis of the electric field within the simulator at 5 discrete frequencies with and without a test object, and an evaluation of the characteristics of the absorber material.

This project was an analytical and mathematical analysis of the characteristics of the illuminator and the material. No experimentation with the illuminator or the material was accomplished. The characteristics of the simulator, were analyzed using a method of moments program called GEMACS. This program was also useful in determining the field characteristics of the simulator when a simple test object was placed within the working volume. The absorber material was analyzed by modelling the material as a two-port network, and determining the reflection and transmission coefficients of the material. A further definition of the field characteristics within the illuminator and testing of the absorber need to be accomplished to validate the results of this project.

Several people aided me while I was working on this project. First I would like to thank my thesis advisor Capt Randy Jost for his patience and aid in all aspects of this project, Maj Ed Kolesar for his

assistance as a reader, Capt Frank Tomko for his expertise in utilizing the GEMACS code, 2LT John Joseph for his help in determining different methods of analyzing the absorber material, and my wife Tammy for her help and support throughout all aspects of this project.

Kenneth A. Bruner

Table of Contents

	<u>page</u>
Preface	iii
List of Figures	vii
List of Tables	xiv
Abstract	xv
I. Introduction	1
1.1 Foreword	1
1.2 Background	1
1.3 Problem	2
1.4 Scope	2
1.5 Statement of Goals	4
1.6 Assumptions	4
1.7 General Approach	5
1.8 Sequence of Presentation	7
II. Analysis of Absorber Material	8
2.1 Introduction	8
2.2 Background	9
2.3 Material Choice	11
2.4 Description of Emerson and Cuming ECCOSORB NZ-31.	12
2.5 EM Wave Reactions	14
2.6 Applicability to Problem	23
III. Hardness Surveillance Illuminator	27
3.1 General	27
3.2 Description of HSI	27
3.3 Theory of Operation	31
3.4 Quasi-Static Analysis	33
3.5 The Harvard EMP and Rhombic Simulators	37
3.6 Method of Moments Results	40
IV. Illuminator Environment	60
4.1 General	60
4.2 Surface Interactions	60
4.3 Wire Model of the Test Object	65

Table of Contents (cont.)

	<u>page</u>
V. Material Use Within the HSI	86
5.1 General	86
5.2 Absorber Characteristics on a Concrete Surface. .	87
5.3 Methods of Reducing Incident Waves Beneath the Test Object	89
5.4 Suggested Use of the Absorber within the HSI. . .	92
VI. Summary, Conclusions, and Recommendations	94
6.1 Conclusions	94
6.2 Recommendations for Further Study	97
6.3 Summary	98
Appendix A. GEMACS	100
Appendix B. Additional Electric Field Plots for the HSI. .	111
Appendix C. Additional Electric Field Plots Beneath the Test Object.	142
Bibliography	179
Vita	182

List of Figures

	<u>page</u>
1-1 Hardness Surveillance Illuminator.	3
2-1 Wave Interaction on Absorber	16
2-2 Equivalent Two-Port Network for Material In TEM Field.	17
3-1 HSI in Common and Differential Mode	29
3-2 Differential and Common Mode Excitations	30
3-3 Image Theory Approximation and Wave Propagation in HSI	32
3-4 Illustration of Equation 3-1	35
3-5 Illustration of Equation 3-2	36
3-6 HES and RS Simulators.	39
3-7 Orientation of Axes for GEMACS model	46
3-8 Common Mode Electric Field Magnitude and Phase For 6 MHz in Longitudinal Direction at $X=0$ m, $Z=4$ m. . . .	50
3-9 Common Mode Electric Field Magnitude and Phase For 8 MHz in Longitudinal Direction at $X=0$ m, $Z=4$ m. . . .	51
3-10 Common Mode Electric Field Magnitude and Phase For 10.71 MHz in Longitudinal Direction at $X=0$ m, $Z=4$ m. .	52
3-11 Common Mode Electric Field Magnitude and Phase For 12 MHz in Longitudinal Direction at $X=0$ m, $Z=4$ m. . . .	53
3-12 Common Mode Electric Field Magnitude and Phase For 30 MHz in Longitudinal Direction at $X=0$ m, $Z=4$ m. . . .	54
3-13 Differential Mode Electric Field Magnitude and Phase For 6 MHz in Longitudinal Direction at $X=0$ m, $Z=4$ m. .	55
3-14 Differential Mode Electric Field Magnitude and Phase For 8 MHz in Longitudinal Direction at $X=0$ m, $Z=4$ m. .	56
3-15 Differential Mode Electric Field Magnitude and Phase For 10.71 MHz in Longitudinal Direction at $X=0$ m, $Z=4$ m	57
3-16 Differential Mode Electric Field Magnitude and Phase For 12 MHz in Longitudinal Direction at $X=0$ m, $Z=4$ m .	58

List of Figures (cont.)

	<u>page</u>
3-17 Differential Mode Electric Field Magnitude and Phase For 30 MHz in Longitudinal Direction at X=0 m, Z=4 m .	59
4-1 Ground Plane Regions for the HSL	61
4-2 EC-135 Diagram	67
4-3 Wire Model Approximation For Test Object	68
4-4 Current Distribution on Wire Model Radiated by Vertically Polarized Plane Wave at 6 MHz.	70
4-5 Current Distribution on Wire Model Radiated by Horizontally Polarized Plane Wave at 6 MHz.	71
4-6 Current Distribution on Wire Model Radiated by Vertically Polarized Plane Wave at 8 MHz.	72
4-7 Current Distribution on Wire Model Radiated by Horizontally Polarized Plane Wave at 8 MHz.	73
4-8 Current Distribution on Wire Model Radiated by Vertically Polarized Plane Wave at 10.71 MHz.	74
4-9 Current Distribution on Wire Model Radiated by Horizontally Polarized Plane Wave at 10.71 MHz.	75
4-10 Current Distribution on Wire Model Radiated by Vertically Polarized Plane Wave at 12 MHz.	76
4-11 Current Distribution on Wire Model Radiated by Horizontally Polarized Plane Wave at 12 MHz.	77
4-12 Electric Field Magnitude at 3 Meters Below the Test Object for 30 MHz With No Ground Plane (Vertical Polarization).	79
4-13 Electric Field Magnitude at 3 Meters Below the Test Object for 30 MHz With No Ground Plane (Horizontal Polarization).	80
4-14 Electric Field Magnitude at 3 Meters Below the Test Object for 30 MHz With Concrete Ground Plane (Vertical Polarization).	81
4-15 Electric Field Magnitude at 3 Meters Below the Test Object for 30 MHz With Concrete Ground Plane (Horizontal Polarization).	82

List of Figures (cont.)

	<u>page</u>
4-16 Power Ratio at 3 Meters Below the Test Object for Vertical Polarization.	84
4-17 Power Ratio at 3 Meters Below the Test Object for Horizontal Polarization.	85
5-1 Suggested Use of Absorber Material Within the HSI. . .	93
A-1. Geometry of Wire Segment of Length 1	106
B-1 Common Mode Electric Field Magnitude and Phase For 6 MHz in Longitudinal Direction at X=15 m, Z=4 m . . .	112
B-2 Common Mode Electric Field Magnitude and Phase For 6 MHz in Longitudinal Direction at X=15 m, Z=8 m . . .	113
B-3 Common Mode Electric Field Magnitude For 6 MHz in Vertical and Horizontal Direction.	114
B-4 Common Mode Electric Field Magnitude and Phase For 8 MHz in Longitudinal Direction at X=15 m, Z=4 m . . .	115
B-5 Common Mode Electric Field Magnitude and Phase For 8 MHz in Longitudinal Direction at X=15 m, Z=8 m . . .	116
B-6 Common Mode Electric Field Magnitude For 8 MHz in Vertical and Horizontal Direction.	117
B-7 Common Mode Electric Field Magnitude and Phase For 10.71 MHz in Longitudinal Direction at X=15 m, Z=4 m .	118
B-8 Common Mode Electric Field Magnitude and Phase For 10.71 MHz in Longitudinal Direction at X=15 m, Z=8 m .	119
B-9 Common Mode Electric Field Magnitude For 10.71 MHz in Vertical and Horizontal Direction.	120
B-10 Common Mode Electric Field Magnitude and Phase For 12 MHz in Longitudinal Direction at X=15 m, Z=4 m . .	121
B-11 Common Mode Electric Field Magnitude and Phase For 12 MHz in Longitudinal Direction at X=15 m, Z=8 m . .	122
B-12 Common Mode Electric Field Magnitude For 12 MHz in Vertical and Horizontal Direction	123
B-13 Common Mode Electric Field Magnitude and Phase For 30 MHz in Longitudinal Direction at X=15 m, Z=4 m . .	124

List of Figures (cont.)

	<u>page</u>
B-14 Common Mode Electric Field Magnitude and Phase For 30 MHz in Longitudinal Direction at X=15 m, Z=8 m . .	125
B-15 Common Mode Electric Field Magnitude For 30 MHz in Vertical and Horizontal Direction	126
B-16 Differential Mode Electric Field Magnitude and Phase For 6 MHz in Longitudinal Direction at X=15 m, Z=4 m. . .	127
B-17 Differential Mode Electric Field Magnitude and Phase For 6 MHz in Longitudinal Direction at X=15 m, Z=8 m. . .	128
B-18 Differential Mode Electric Field Magnitude For 6 MHz in Vertical and Horizontal Direction	129
B-19 Differential Mode Electric Field Magnitude and Phase For 8 MHz in Longitudinal Direction at X=15 m, Z=4 m. . .	130
B-20 Differential Mode Electric Field Magnitude and Phase For 8 MHz in Longitudinal Direction at X=15 m, Z=8 m. . .	131
B-21 Differential Mode Electric Field Magnitude For 8 MHz in Vertical and Horizontal Direction	132
B-22 Differential Mode Electric Field Magnitude and Phase For 10.71 MHz in Longitudinal Direction at X=15 m, Z=4 m.	133
B-23 Differential Mode Electric Field Magnitude and Phase For 10.71 MHz in Longitudinal Direction at X=15 m, Z=8 m.	134
B-24 Differential Mode Electric Field Magnitude For 10.71 MHz in Vertical and Horizontal Direction.	135
B-25 Differential Mode Electric Field Magnitude and Phase For 12 MHz in Longitudinal Direction at X=15 m, Z=4 m . .	136
B-26 Differential Mode Electric Field Magnitude and Phase For 12 MHz in Longitudinal Direction at X=15 m, Z=8 m . .	137
B-27 Differential Mode Electric Field Magnitude For 12 MHz in Vertical and Horizontal Direction	138
B-28 Differential Mode Electric Field Magnitude and Phase For 30 MHz in Longitudinal Direction at X=15 m, Z=4 m . .	139
B-29 Differential Mode Electric Field Magnitude and Phase For 30 MHz in Longitudinal Direction at X=15 m, Z=8 m . .	140

List of Figures (cont.)

	<u>page</u>
B-30 Differential Mode Electric Field Magnitude For 30 MHz in Vertical and Horizontal Direction	140
C-1 Electric Field Magnitude at 3 Meters Below Test Object Horizontal Incident Field at 6 MHz with No Ground Plane	143
C-2 Electric Field Magnitude at 3 Meters Below Test Object Horizontal Incident Field at 6 MHz with No Ground Plane	144
C-3 Electric Field Magnitude at 3 Meters Below Test Object Horizontal Incident Field at 6 MHz with No Ground Plane	145
C-4 Electric Field Magnitude at 3 Meters Below Test Object Horizontal Incident Field at 6 MHz with Concrete Ground Plane	146
C-5 Electric Field Magnitude at 3 Meters Below Test Object Horizontal Incident Field at 6 MHz with Concrete Ground Plane	147
C-6 Electric Field Magnitude at 3 Meters Below Test Object Horizontal Incident Field at 6 MHz with Concrete Ground Plane	148
C-7 Power Ratio Graphs at 3 Meters Below Test Object For Horizontal Polarization at 6 MHz.	149
C-8 Power Ratio Graphs at 3 Meters Below Test Object For Horizontal Polarization at 6 MHz.	150
C-9 Power Ratio Graphs at 3 Meters Below Test Object For Horizontal Polarization at 6 MHz.	151
C-10 Electric Field Magnitude at 3 Meters Below Test Object Vertical Incident Field at 6 MHz with No Ground Plane	152
C-11 Electric Field Magnitude at 3 Meters Below Test Object Vertical Incident Field at 6 MHz with No Ground Plane	153
C-12 Electric Field Magnitude at 3 Meters Below Test Object Vertical Incident Field at 6 MHz with No Ground Plane	154
C-13 Electric Field Magnitude at 3 Meters Below Test Object Vertical Incident Field at 6 MHz with Concrete Ground Plane	155

List of Figures (cont.)

	<u>page</u>
C-14 Electric Field Magnitude at 3 Meters Below Test Object Vertical Incident Field at 6 MHz with Concrete Ground Plane	156
C-15 Electric Field Magnitude at 3 Meters Below Test Object Vertical Incident Field at 6 MHz with Concrete Ground Plane	157
C-16 Power Ratio Graphs at 3 Meters Below Test Object For Vertical Polarization at 6 MHz.	158
C-17 Power Ratio Graphs at 3 Meters Below Test Object For Vertical Polarization at 6 MHz.	159
C-18 Power Ratio Graphs at 3 Meters Below Test Object For Vertical Polarization at 6 MHz.	160
C-19 Electric Field Magnitude at 3 Meters Below Test Object Horizontal Incident Field at 12 MHz with No Ground Plane	161
C-20 Electric Field Magnitude at 3 Meters Below Test Object Horizontal Incident Field at 12 MHz with No Ground Plane	162
C-21 Electric Field Magnitude at 3 Meters Below Test Object Horizontal Incident Field at 12 MHz with No Ground Plane	163
C-22 Electric Field Magnitude at 3 Meters Below Test Object Horizontal Incident Field at 12 MHz with Concrete Ground Plane	164
C-23 Electric Field Magnitude at 3 Meters Below Test Object Horizontal Incident Field at 12 MHz with Concrete Ground Plane	165
C-24 Electric Field Magnitude at 3 Meters Below Test Object Horizontal Incident Field at 12 MHz with Concrete Ground Plane	166
C-25 Power Ratio Graphs at 3 Meters Below Test Object For Horizontal Polarization at 12 MHz	167
C-26 Power Ratio Graphs at 3 Meters Below Test Object For Horizontal Polarization at 12 MHz	168
C-27 Power Ratio Graphs at 3 Meters Below Test Object For Horizontal Polarization at 12 MHz	169
C-28 Electric Field Magnitude at 3 Meters Below Test Object Vertical Incident Field at 12 MHz with No Ground Plane	170

List of Figures (cont.)

	<u>page</u>
C-29 Electric Field Magnitude at 3 Meters Below Test Object Vertical Incident Field at 12 MHz with No Ground Plane	171
C-30 Electric Field Magnitude at 3 Meters Below Test Object Vertical Incident Field at 12 MHz with No Ground Plane	172
C-31 Electric Field Magnitude at 3 Meters Below Test Object Vertical Incident Field at 12 MHz with Concrete Ground Plane	173
C-32 Electric Field Magnitude at 3 Meters Below Test Object Vertical Incident Field at 12 MHz with Concrete Ground Plane	174
C-33 Electric Field Magnitude at 3 Meters Below Test Object Vertical Incident Field at 12 MHz with Concrete Ground Plane	175
C-34 Power Ratio Graphs at 3 Meters Below Test Object For Vertical Polarization at 12 MHz	176
C-35 Power Ratio Graphs at 3 Meters Below Test Object For Vertical Polarization at 12 MHz	177
C-36 Power Ratio Graphs at 3 Meters Below Test Object For Vertical Polarization at 12 MHz	178

List of Tables

Table	<u>page</u>
2-1 Physical Specifications of ECCOSORB NZ-31	12
2-2 Electrical Specifications of ECCOSORB NZ-31	14
2-3 Reflection and Transmission Losses for a Slab of Unbacked and Metal Backed ECCOSORB NZ-31 at 30 MHz . .	24
2-4 Reflection and Transmission Losses for a Slab of Unbacked and Metal Backed ECCOSORB NZ-31 at 50 MHz . .	25
2-5 Reflection and Transmission Losses for a Slab of Unbacked and Metal Backed ECCOSORB NZ-31 at 250 MHz. .	26
4-1 Dielectric Constants and Conductivities for Concrete .	64
4-2 Reflection Coefficient Magnitudes for Concrete	64
4-3 Reflection Coefficient Magnitudes for Soil	65
5-1 Reflection Loss for ECCOSORB NZ-31 Located on a Concrete Surface	88

Abstract

This investigation determined the electromagnetic (EM) wave characteristics of an electromagnetic pulse (EMP) simulator from 6 MHz to 30 MHz, and determined a method of reducing unwanted wave reflections within the simulator. The electromagnetic fields produced by the EMP simulator were determined by using a method of moments routine for both a perfectly conducting ground plane and a concrete ground plane. Comparisons of the method of moments results with theoretical results were accomplished.

The electromagnetic wave absorber ECCOSORB NZ-31 was evaluated for use within the EMP simulator. The absorber was analyzed using two-port network theory. Data for the absorption characteristics of the material when used with various surface are provided.

An analysis of the scattering characteristics of a wire model used within the EMP simulator was accomplished using a method of moments approach. Determination of the electromagnetic wave reflections on the wire was assessed.

A determination of the optimal placement of the absorber material within the EMP simulator is made. A combination of techniques to further reduce wave reflections is suggested.

I. Introduction

1.1. Foreword

The effects of electromagnetic pulses (EMP) caused by the detonation of a nuclear device in the upper atmosphere of the earth have been studied in depth for several decades. During this time, methods of determining the effects of EMP on aircraft have been developed. These techniques involve both analysis and simulation of the EMP signal itself. Since it is neither practical nor feasible to detonate a nuclear device in order to provide an EMP signal, methods of simulating EMP have been devised. Such techniques generally require a test object, such as an aircraft, to be exposed to a high power impulse signal so the effects of the burst on avionics, flight controls, and other on-board systems can be measured. Once the vulnerabilities of an aircraft have been determined, corrections are made. Such testing is often difficult and expensive. New simulators are being designed that allow testing of individual on-board components, as well as the entire system. These simulators are less costly to operate than a full EMP simulator, and can give valid results. This thesis effort is involved with the analysis and operation of one of these EMP simulators called the Hardness Surveillance Illuminator (HSI) located at Kirtland AFB, NM.

1.2. Background

The HSI is a low power system that tests an aircraft's EMP linear protection devices in order to determine the amount of protection an aircraft has against EMP. It is designed to provide either a horizontally or a vertically polarized electric field with a continuous frequency to a test object located within the HSI. The frequency range

of the HSI is 100 kilohertz (KHz) to 100 megahertz (MHz) (9:1). This frequency range contains a significant portion of the frequencies created by an EMP burst. The HSI consists of two wires stretched above a nonhomogeneous surface (see Figure 1-1). The surface is comprised of three distinct regions. Region 1 is a conducting ground plane, region 2 is a hardened concrete surface, and region 3 is soil. Because of this configuration, the exact field distributions of the HSI are unknown, and it is believed that the interaction of the test object with the concrete pad will cause unacceptable field distortions (9:24,25).

1.3. Problem

The problem of this thesis is to determine and reduce unwanted EM wave distortions and diffractions within the HSI by introducing absorbing material in key locations.

1.4. Scope

This thesis effort is a mathematical analysis of the HSI, its environment, and the placement of an absorber material within that environment. It addresses the electric field uniformity within the HSI, diffractions due to discontinuities within the structure, and methods of reducing field diffractions by the placement of absorber material within the environment. This thesis was accomplished in three phases. Phase 1 addressed the field distribution within the HSI structure without a test object, phase 2 addressed the diffraction and scattering of the incident waves on the planar ground surface and the test object, and phase 3 addressed the placement of the absorber within the HSI. As previously mentioned, the frequency range of the HSI spans from 100 KHz to 100 MHz. This study was concerned with

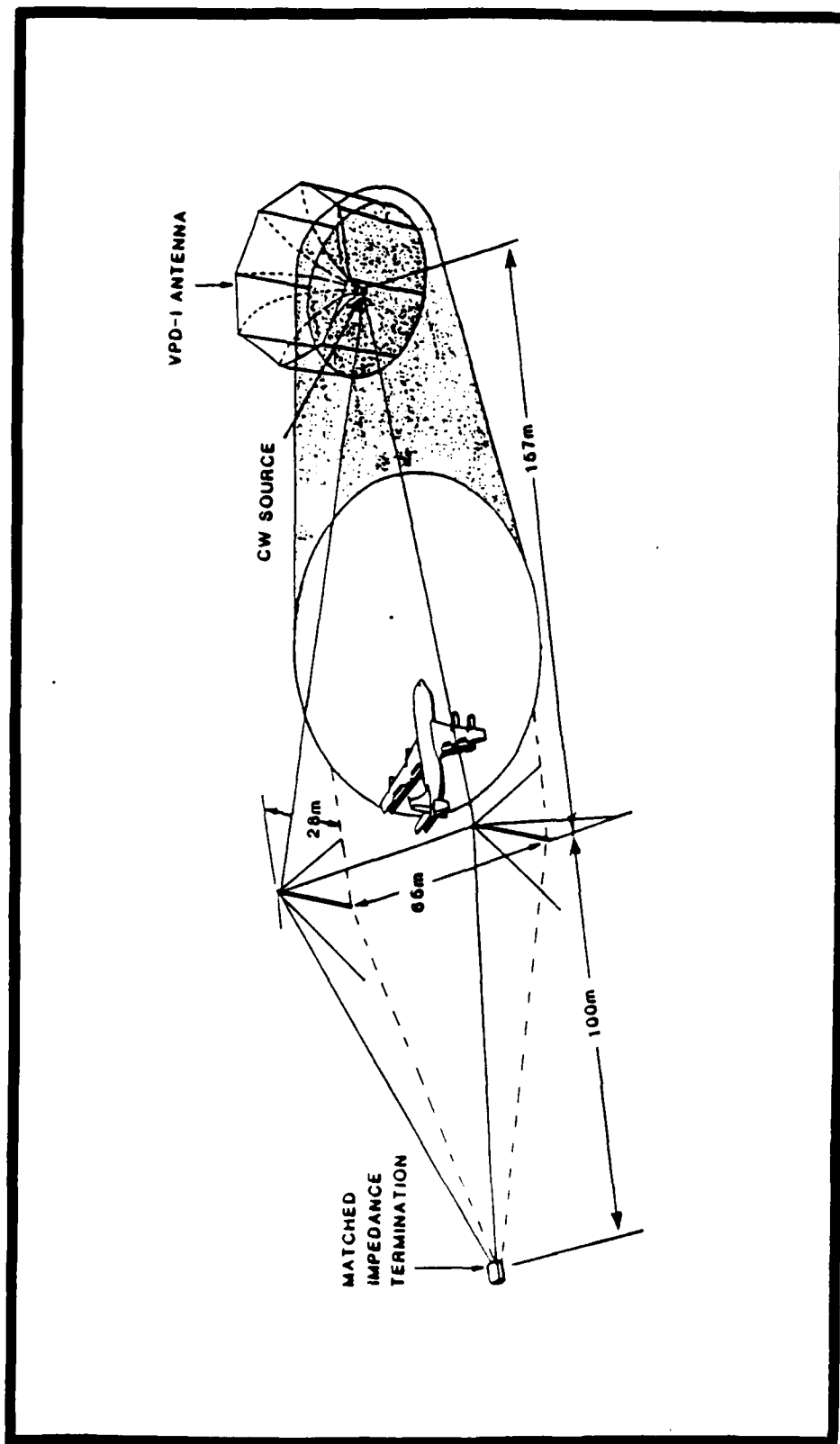


Figure 1-1. Hardness Surveillance Illuminator (6:8)

frequencies from 25 MHz to 500 MHz, due to the lower frequency limit of the absorber material that was analyzed. In addition, the frequency ranges of different stages of the thesis varied due to limitations of some of the tools used for analysis. Other means of extending the frequency range to cover 25 MHz to 500 MHz by interpolation are done where applicable. All information regarding the absorber material is theoretical, since no testing of the material was accomplished.

1.5. Statement of Goals

The overall goal of this project was to reduce undesired electric field scattering, and thus better approximate a free space environment within the HSI. Several subgoals were accomplished during this project: first, the analysis of the electric fields within the HSI for different frequencies and determination of whether the fields behaved as predicted by other efforts was performed; second, the effects of a nonhomogenous ground plane within the HSI, were determined; third, the changes in the test object surface current due to the presence of a ground plane were assessed; and fourth, the determination of whether an absorber material could be placed within the HSI and reduce reflections and diffractions was made. Each of these goals are addressed throughout this document.

1.6. Assumptions

Several assumptions were made during this project that simplified the analysis. First, it was assumed that the absorber could be analyzed as a homogeneous dielectric material with magnetic properties. The parameters provided by the manufacturer of the material, were determined using this assumption, and therefore it was necessary to make the same assumption in order to utilize the parameters provided. Although the

material will likely not have a constant homogeneity for all samples of the material, it was necessary to make this assumption in order to perform the material calculations. Testing of the material will need to be accomplished in order to assess the effects of nonhomogeneity on the reflection and transmission properties of the material. Second, it was assumed that the absorber and test object could be analyzed with an incident planar, transverse electromagnetic (TEM) wave. Chapter 3 discusses the validity of this assumption. Third, it was assumed that the EM wave within the HSI was propagating along the length of the HSI. The validity of this assumption is discussed in Chapter 3. Fourth, it was assumed that a wire model of the test object would provide a sufficiently accurate model of the test object. This is discussed further in Chapter 4. Finally, it was assumed that any diffraction due to the interface between the ground plane regions was negligible since the discontinuities are small with respect to the wavelength, and the electrical properties of the regions are similar.

1.7. General Approach

As discussed above, this thesis effort was broken down into three phases. Each of these phases were conducted separately and then integrated into the overall product so that a continuous flow could be achieved. Phase 1 was accomplished by researching the literature for information regarding rhombic EMP simulators utilizing the same basic structure. This resulted in the determination that the structure of the HSI is relatively unique and that no detailed analysis of the structure in its current state had been accomplished. This required that the interior field patterns of the HSI be analyzed. One method of

performing this analysis is by a method of moments (MOM) routine. A MOM routine is a numerical method of solving the wave equation for thin wires. More detail regarding the MOM routine will be provided in later chapters. The general electromagnetic model for the analysis of complex systems (GEMACS) program developed by the BDM Corporation was utilized for this phase. This program permitted the analysis of the structure to be accomplished for different ground planes so that the effect of the surface could be better understood. The MOM solution of the HSI was then compared to theoretical and experimental analysis of similar EMP simulators. For completeness, this analysis included comparison with the quasi-static model and the Harvard EMP simulator. Phase 2 involved the reflections and diffractions of the incident fields on the surface of the HSI. The analysis of the planar surfaces was accomplished by using the method of images and determining the reflection coefficients of each region. The initial analysis of the HSI indicated that the electric fields could be approximated by a planar wave. The analysis of the test object was accomplished with the use of GEMACS. A wire model of an EC-135 sized aircraft was analyzed. This model was assumed to be adequate for low frequency calculations since the wavelengths investigated were bigger than the discontinuities on an aircraft. This model was utilized to determine the effects of the ground plane on the current distribution of the model and the field patterns beneath the model. The model was simple enough to allow it to simulate other aircraft of this relative size. Phase 3 was the analysis of the chosen wave absorber material. Although the material was not tested, calculated data were provided by the manufacturer for the necessary analysis. In addition, an analysis of the placement of the absorber

within the HSI was accomplished.

1.8. Sequence of Presentation

This document is presented in the order of research of each item. Chapter 2 contains the analysis of the material chosen. It contains material regarding the attenuation, and the reflection and transmission coefficients. Chapters 3 and 4 contain the analysis of the HSI and its environment. More specifically, Chapter 3 contains the analysis of the fields produced by the HSI with a concrete ground plane. Comparison of the method of moments calculations with both experimental and theoretical analysis of the Harvard EMP simulator, and the quasi-static model are also presented. Chapter 4 contains the analysis of the nonhomogeneous planar surface. In addition, it contains the analysis of the wire model used with and without a concrete ground plane. Chapter 5 ties Chapters 2, 3, and 4 together by discussing how and where the material could be placed within the HSI for optimal effectiveness. Chapter 6 contains the final summary, conclusions and recommendations. The appendices contain other supporting information useful for understanding the project and its completion.

II. Analysis of Absorber Material

2.1. Introduction

The original goal of this thesis was to determine whether a method of providing a free space environment within the HSI could be accomplished by introducing an electromagnetic (EM) wave absorbing material into the HSI. For this to be accomplished, the material must have an intrinsic impedance (Z) equal to that of free space (Z_0), a bandwidth equal to or greater than that of the HSI, and at least 3 dBw absorption across the frequency band of interest. Such a material does not exist. To start with, no wave absorbers made of a single material have a bandwidth covering the entire frequency range of the HSI. In fact, most materials do not absorb energy in the lower frequency ranges of the HSI at all. Secondly, no materials have an intrinsic impedance equal to free space (377 ohms) over the entire frequency range of the HSI. Thirdly, the absorption characteristics of materials are also frequency dependent, which causes unequal absorption across the bandwidth of the material. Because of these problems, the original goals could not be met. Therefore, the goals were altered so that the study could be accomplished by using an absorber that covers part of the frequency range of the HSI. The characteristics of candidate materials were reviewed in order to determine the best material suited for the study. Important analysis factors included the lower frequency limit, overall bandwidth, reflection and transmission characteristics, and availability of material. Further characteristics will be addressed throughout this chapter.

2.2. Background

2.2.1. General. Absorber materials can be grouped into four different categories: materials that have complex magnetic permeabilities and electric permittivities essentially equal, materials that are resonant over a range of frequencies, broad-band absorbers which have varying impedances along their length, and surface current absorbers which reduce surface currents at discontinuities along a surface (14). Each of these absorber types have their advantages; however, only the first three have any applicability to this thesis effort.

2.2.2. Free Space Absorbers. The first absorber type is one that has its complex permeability and permittivity essentially equal. These materials are found in the ferrite family and can be thought of as having properties of a magnetic dielectric. These materials are generally thin compared to a wavelength and can be used at frequencies of 30 MHz and higher. By having equal complex permittivities and permeabilities, the impedance of the material is the same as free space. This property ensures that the incident wave is minimally reflected. Such materials can often provide reflection reductions of 10 to 25 dBw with a thickness of a quarter of an inch (12). Another advantage of ferrites is its weather durability.

2.2.3. Resonant Absorbers. The second type of absorber is the resonant absorber. Resonant absorbers reduce reflections by using the width of the material to cancel the front face reflections with the reflections from the rear. This is accomplished by having a thickness equal to a quarter of a wavelength. These absorbers are resonant at only one

frequency, and therefore, have narrow bandwidths. These absorbers generally have low frequency cutoffs well above the upper limit of the HSI. Some resonant absorbers have lower frequency limits of around 120 MHz (14).

2.2.4. Broad-Band Absorbers. The third absorber type is the broad-band absorber. Broad-band absorbers use material thickness and a varying impedance to reduce reflectivity. These are designed with low leading edge impedances so that reflection at the front surface is minimized. As the material depth increases, the impedance and the loss factor also increases. The reflection of the wave off the back face of the material is reduced sufficiently so that it may be negligible. This type of absorber is also generally used for frequencies higher than the upper limit of the HSI. One type of broad band absorber has been used at frequencies down to 26 MHz. This type is the geometrically shaped absorber. It has either a conical or a pyramidal shape. The shape of this absorber causes the incident wave to experience a smoothly changing ratio of medium to adjacent air. This in effect is similar to a non-shaped absorber having a smoothly changing medium throughout the structure. When the shape is pyramidal, interface reflections are negligible (14). Such absorbers can have reflection losses of -60 dB. The major drawback to this type absorber is its thickness. For the absorption of a wave at 26 MHz, it is necessary for the thickness to be on the order of 4.5 m (14). This thickness is larger than the distance between the bottom of the test object and the ground plane. Therefore, this material could not be used beneath the test object. In addition, the absorber characteristics are reduced as the angle of incidence on

the absorber approaches grazing incidence, so that placement of this absorber on the ground plane prior to the test object would result in few losses. For these reasons, it was felt that this absorber would not be suitable for use within the HSI.

2.2.5. Multiple Material Absorbers. One other possible method of reducing reflections within the HSI is by the use of a multiple material absorber. Such an absorber is similar in concept to the shaped absorber, and may be able to expand the frequency range of absorption below 30 MHz. This type of absorber was not analyzed during this project because it was desired that a methodology be determined for analyzing materials, and use of a simple absorber material could be used to determine generalized procedures. A multiple material absorber can be analyzed using the techniques developed in this chapter if the electrical characteristics of the materials are known. For the purposes of this project, it appears that the use of a ferrite material for analysis is the best candidate since the electrical characteristics of the material are provided.

2.3. Material Choice

The focus of the material research was centered around ferrite materials. These were the only compounds that would provide a low reflectivity at a size and frequency range that were acceptable. It was desired that the material be obtainable at a reasonable price and that it be readily available. Ferrite absorbers are produced by several manufacturers such as TDK Corporation, Coretronics, and Emerson and Cuming. Not all of the ferrites produced have absorber characteristics in the frequency ranges useful for this project. Some of the ferrite

compounds do absorb energy within part of the bandwidth of the HSI. One absorber that is typical for low frequency ferrites is the Emerson and Cuming ECCOSORB NZ-31. This absorber has a frequency range of 25 MHz to 3.0 GHz. The lower frequency range of this absorber is the best value that was readily available with a single material absorber.

2.4. Description of Emerson and Cuming ECCOSORB NZ-31

Eccosorb NZ-31 is a sintered ferrite based material. The actual composition of the material was not released by Emerson and Cuming since that information is proprietary; however, it is essentially a powdered iron sintered into a hardened ceramic. The general specifications of the material are given in Table 2-1 (14).

TABLE 2-1

Physical Specifications of Eccosorb NZ-31

Frequency Range (MHz)	25 - 3,000
Physical Form	flat tile
Nominal Length and Width (cm)	6.0 x 6.0
Nominal Thickness (cm)	0.64
Nominal Weight (Lbs/sq. ft.)	6.7
Service Temperature (F°)	-65 - 500
Power Handling (Watts/cm ²)	3.1

Although the ECCOSORB NZ-31 material was not tested during this effort, calculated values for complex relative permeability and relative permittivity were provided by Emerson and Cuming. From the information provided, it was easy to calculate additional parameters of interest

such as the material's impedance (Z) and the reflection and transmission coefficients. The electrical characteristics of a material are defined by the complex permittivity (ϵ^*) and complex permeability (μ^*). These parameters are defined by the following equations (20:4-5):

$$\epsilon^* = \epsilon' - j \epsilon'' \quad \text{Farads/m} \quad (2-1)$$

$$\mu^* = \mu' - j \mu'' \quad \text{Henries/m} \quad (2-2).$$

The values of ϵ' and μ' define the electric and magnetic dispersion characteristics of the material, and ϵ'' and μ'' define the electric and magnetic absorption characteristics of the material (20:253). A dissipation factor or loss tangent for the electric and magnetic properties can be determined as; $\tan \delta_d = \epsilon'' / \epsilon'$, and $\tan \delta_m = \mu'' / \mu'$. In addition, the conductivity of the material is defined as $\sigma = \omega \epsilon''$ mhos/m (20:4-5), where ω is the radian frequency of the incident wave. It is often useful to normalize the permittivity and permeability by the free space permittivity (ϵ_0) or permeability (μ_0) to obtain relative values. The value of ϵ_0 is 8.85×10^{-12} Farads/m and the value of μ_0 is 1.25×10^{-6} Henries/m (20:273). The relative permittivity and permeability are denoted by the following equations (14):

$$K^* = \epsilon^* / \epsilon_0 = K' + jK'' = \epsilon' / \epsilon_0 + j \epsilon'' / \epsilon_0 \quad (2-3)$$

$$K_m^* = \mu^* / \mu_0 = K_m' + jK_m'' = \mu' / \mu_0 + j \mu'' / \mu_0 \quad (2-4)$$

The relative permittivity and permeability values provided by the manufacturer are given in Table 2-2.

TABLE 2-2

Electrical Specifications of ECCOSORB NZ-31

Frequency	K_m'	K_m''	K'	K''
30 MHz	25	60	11	0.2
50 MHz	19	53	11	0.2
250 MHz	1.0	27	11	0.2

The intrinsic impedance of the material is dependent on the values of K^* , K_m^* , the angle of incidence of the wave, and the polarization of the wave. For a linear plane wave, two impedance values must be specified; one normal to the plane of incidence and one parallel to the plane of incidence. The equations for both polarizations with arbitrary incidence normalized by the free space impedance are (5:88)

$$Z_n = \frac{K_m^* \cos(\theta_i)}{(K_m^* K^* - \sin^2 \theta_i)^{1/2}} \quad (2-5)$$

$$Z_p = \frac{(K_m^* K^* - \sin^2 \theta_i)^{1/2}}{K^* \cos(\theta_i)} \quad (2-6)$$

where Z_n and Z_p are symbols denoting impedance of a normally incident component (Z_n) and a tangentially incident component (Z_p). The values of Z above will be used to calculate the reflection and transmission coefficients of the material.

2.5. EM Wave Reactions

Since ECCOSORB NZ-31 has a high permeability, it can be considered a magnetic dielectric. As seen previously, it is possible to

characterize the material with the four parameters; K' , K'' , K'_m , and K''_m . In attempting to analyze the effectiveness of the material, it is necessary to calculate the reflection coefficient and the transmission coefficient. It is assumed that the wave incident on the material is a transverse EM (TEM) wave. Since the HSI generates a predominate TEM mode, this is a valid assumption. The field characteristics will be addressed in Chapter 3. The derived equations are valid for any wave transmission system for which only a forward and backward travelling wave exists (5:80). Before determining the overall reflection and transmission coefficients, it is necessary to define the reflection due to the interface of a discontinuity. This value denoted as R^* , is defined using the values in equations 2-5 and 2-6. As mentioned earlier, the incident wave can be divided into two components, one tangential to the plane of incidence, and one normal to the plane of incidence. This is illustrated in Figure 2-1. It was, therefore, necessary to define the reflection coefficients for both normal and tangential components. The interface reflection coefficient is given as (5:91)

$$R^* = (Z_2 - Z_1) / (Z_2 + Z_1). \quad (2-7)$$

The values of Z_1 and Z_2 are the intrinsic impedances of the interface materials (such as air and the absorber) and are dependent on the polarization of the wave. Using this information it is possible to analyze the wave interactions of the material by using two-port circuit theory, modified to suit the problem (5:77). As developed in Collin (5), it is possible to determine the reflection and transmission coefficients due to a discontinuity, by solving a system of equations. As illustrated in Figure 2-2, the reflected and transmitted waves can be

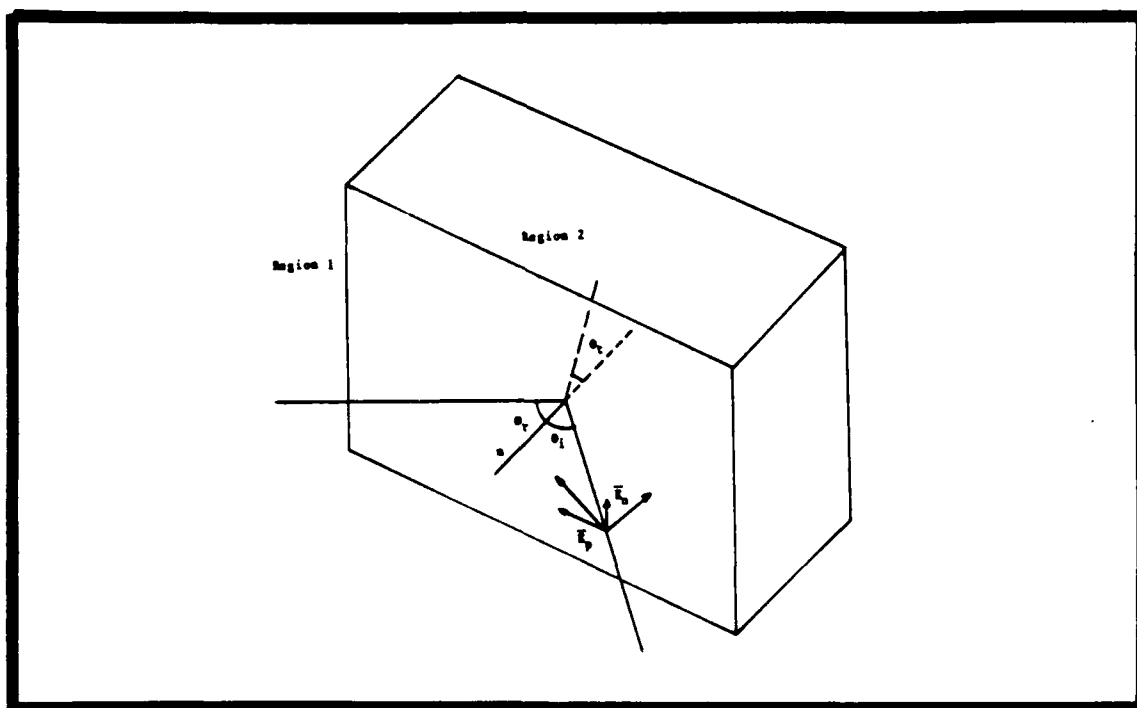


Figure 2-1

Wave Interaction on Absorber

written as (5:79):

$$\begin{aligned} b_1 &= R_1 c_1 + T_{21} b_2 \\ c_2 &= c_1 T_{12} + b_2 R_2 \end{aligned} \quad (2-8)$$

or in terms of region 1 parameters,

$$\begin{aligned} b_1 &= (T_{21} - R_1 R_2 / T_{12}) b_2 + R_1 / T_{12} c_2 \\ c_1 &= c_2 / T_{12} - R_2 b_2 / T_{12} \end{aligned} \quad (2-9)$$

where c_1 is the incident wave, b_1 is the reverse wave in region 1, c_2 is the forward wave in region 2, and b_2 is the reverse wave in region 2.

Region 1 and region 2 are semi-infinite on either side of the discontinuity. The values of R_1 and R_2 are the reflection coefficients

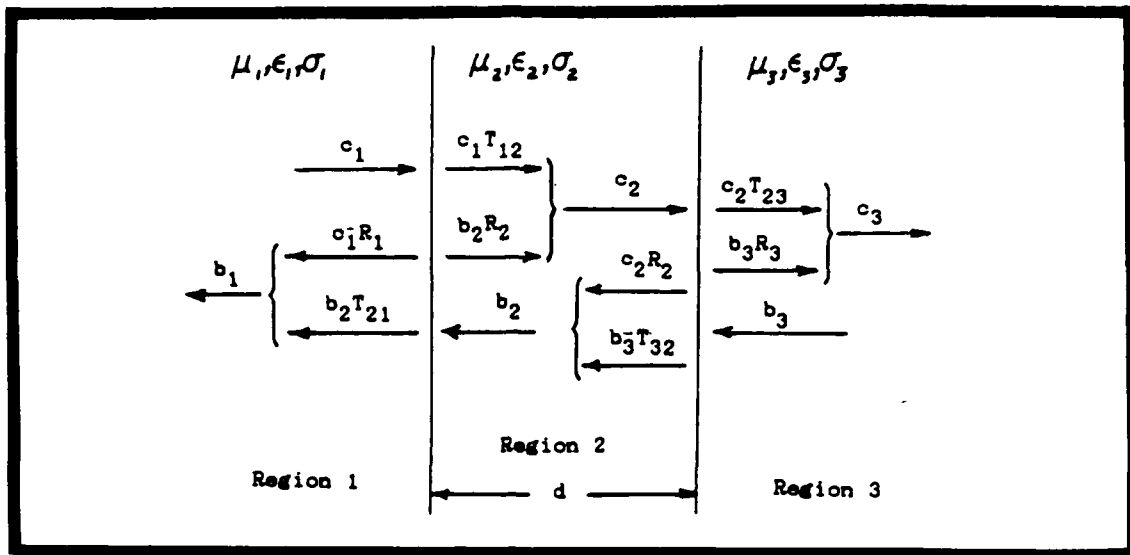


Figure 2-2

Equivalent Two-Port Network for Material in a TEM Field

from the discontinuity into the specified region. T_{21} is the transmission coefficient from region 2 into region 1, while T_{12} is the transmission coefficient from region 1 into region 2. Equation 2-9 can be written in a matrix form as (5:79),

$$\begin{bmatrix} c_1 \\ b_1 \end{bmatrix} = \frac{1}{T_{12}} \begin{bmatrix} 1 & -R_2 \\ R_1 & T_{12}T_{21} - R_1R_2 \end{bmatrix} \begin{bmatrix} c_2 \\ b_2 \end{bmatrix} \quad (2-10)$$

The reflection and transmission coefficients can be determined by simple linear algebra, so that (5:80)

$$\begin{aligned} R_1 &= b_1/c_1 \quad | b_2=0 \\ R_2 &= c_2/b_2 \quad | c_1=0 \\ T_{12} &= c_2/c_1 \quad | b_2=0 \\ T_{21} &= b_1/b_2 \quad | c_1=0 \end{aligned} \quad (2-11)$$

For a planar discontinuity, the matrix elements reduce to (5:82)

$$A_{11} = 1/T_{12}$$

$$A_{12} = -R_2/T_{12} = R_1/T_{12}$$

$$A_{21} = R_1/T_{12}$$

$$A_{22} = (T_{12}T_{21} - R_1R_2)/T_{12} = 1/T_{12}$$

since $R_1 = -R_2$, $1 + R_1 = T_{12}$, and $1 + R_2 = T_{21}$. With these reductions, equation 2-10 can be rewritten as

$$\begin{bmatrix} c_1 \\ b_1 \end{bmatrix} = \frac{1}{T_{12}} \begin{bmatrix} 1 & R_1 \\ R_1 & 1 \end{bmatrix} \begin{bmatrix} c_2 \\ b_2 \end{bmatrix} \quad (2-12)$$

To further analyze this problem, an electrical length must be specified. This is obtained by considering forward and reverse propagating waves, $c_1 \exp(jkz_1)$ and $b_1 \exp(-jkz_1)$ respectively. The parameter k , can be obtained from $k = \omega(\mu\epsilon)^{1/2} = 2\pi/\lambda$, and z_1 is an arbitrary distance from the discontinuity. Let $c_2 = c_1 \exp(-jkz_1)$ and $b_1 = b_2 \exp(jkz_1)$. Solving these two equations for c_1 and b_2 , results in $c_1 = c_2 \exp(-jkz_1)$ and $b_1 = b_2 \exp(-jkz_1)$. By defining the electrical length, L , as kz_1 , the following matrix is obtained (5:83):

$$\begin{bmatrix} c_1 \\ b_1 \end{bmatrix} = \begin{bmatrix} \exp(jL) & 0 \\ 0 & \exp(-jL) \end{bmatrix} \begin{bmatrix} c_2 \\ b_2 \end{bmatrix} \quad (2-13)$$

It is now possible to determine the waves effects on a finite length material by combining equations 2-11 and 2-12 (5:83). The resulting equation is

$$\begin{bmatrix} c_1 \\ b_1 \end{bmatrix} = \frac{1}{T_1} \begin{bmatrix} 1 & R_1 \\ R_1 & 1 \end{bmatrix} \begin{bmatrix} \exp(jL_1) & 0 \\ 0 & \exp(-jL_1) \end{bmatrix} \begin{bmatrix} c_2 \\ b_2 \end{bmatrix} \quad (2-14)$$

$$= \frac{1}{T_1} \begin{bmatrix} \exp(jL_1) & R_1 \exp(-jL_1) \\ R_1 \exp(jL_1) & \exp(-jL_1) \end{bmatrix} \begin{bmatrix} c_2 \\ b_2 \end{bmatrix}$$

The amplitudes c_2 and b_2 can also be used as solutions to a system of equations with independent variables c_3 and b_3 , as shown in Figure 2-2. The interface matrix for this case is similar to equation 2-14, but with the values of R_1 and L_1 changed to R_2 and L_2 for the second interface. By continually doing this, it is obvious that an interface matrix for n -sections can be defined as the product of the individual matrix equations. That is (5:84),

$$\begin{bmatrix} c_1 \\ b_1 \end{bmatrix} = \frac{1}{T_i} \begin{bmatrix} \exp(jL_i) & R_i \exp(-jL_i) \\ R_i \exp(jL_i) & \exp(-jL_i) \end{bmatrix} \begin{bmatrix} c_{n+1} \\ b_{n+1} \end{bmatrix} \quad (2-15)$$

where R_i is the discontinuity reflection coefficient for the i^{th} section, and L_i is the electrical length of each section. The above information can be used to solve for the reflection and transmission coefficients for a slab of absorber material. For the purposes of this analysis, only a two-section matrix will be used since it is desired to determine only the transmission and reflection coefficients due to the absorber. If a multiple material absorber were to be analyzed, more sections would be required. For the purposes of the single material analysis, the thickness of region 3 will be considered infinite. By making this assumption, it is possible to neglect fields due to interface reflections in region 3. The electrical thickness of the

material can be determined for all angles of incidence from 0 to 90 degrees, by modifying the length equation provided earlier. The electrical thickness of the material can then be written as (5:89)

$$D = 2 \pi d / \lambda \cos(\theta_t) \quad (2-16)$$

where d is the physical thickness of the material, λ is the free space wavelength, and θ_t is the angle of the transmission into the material. Using Snell's Law which states (20:50),

$$\sin(\theta_i) / \sin(\theta_t) = (K^* K_m^*)^{1/2}$$

it is possible to rewrite equation 2-16 as

$$D = 2 \pi d / \lambda (K^* K_m^* - \sin^2 \theta_i)^{1/2}.$$

With the above information, the matrix equations that are to be used for the absorber problem are

$$\begin{bmatrix} c_1 \\ b_1 \end{bmatrix} = \frac{1}{T_1 T_2} \begin{bmatrix} \exp(jD) & R_1 \exp(-jD) \\ R_1 \exp(jD) & \exp(-jD) \end{bmatrix} \begin{bmatrix} 1 & R_2 \\ R_2 & 1 \end{bmatrix} \begin{bmatrix} c_3 \\ b_3 \end{bmatrix} \quad (2-17)$$

$$= \frac{1}{T_1 T_2} \begin{bmatrix} \exp(jD) + R_1 R_2 \exp(-jD) & R_2 \exp(jD) + R_1 \exp(-jD) \\ R_1 \exp(jD) + R_2 \exp(-jD) & R_1 R_2 \exp(jD) + \exp(-jD) \end{bmatrix} \begin{bmatrix} c_3 \\ b_3 \end{bmatrix} \quad (2-18)$$

where $T_1 = 1 + R_1$ and $T_2 = 1 + R_2$. To determine the transmission and reflection coefficients, the value of b_3 is set to zero. This models the material having an incident wave from only one direction. Since the absorber will likely be used to cover a surface, this approximation is valid. Two configurations of this matrix will be calculated for this chapter. The first configuration will be the use of the material in

free space, where Z_2 is equal to the free space impedance, Z_0 , and $R_2 = -R_1$ (20:59). The second configuration will be for a metal backed plate. For the second configuration, the impedance (Z_m) of the metal is defined as $Z_m = (\omega \mu_0 / 2 \sigma)^{1/2} (1+j)$ (5:95). As the conductivity of the metal approaches infinity, Z_m approaches zero. Thus R_2 approaches -1, and T_2 approaches zero. These two configurations will provide a baseline for comparison of the absorber with other surfaces. Using the above conditions for both the configurations, equation 2-17 can be written as

Case 1:

$$\begin{bmatrix} c_1 \\ b_1 \end{bmatrix} = \frac{1}{1-R_1^2} \begin{bmatrix} \exp(jD) - R_1^2 \exp(-jD) & -R_1 [\exp(jD) - \exp(-jD)] \\ R_1 [\exp(jD) - \exp(-jD)] & -R_1^2 \exp(jD) + \exp(-jD) \end{bmatrix} \begin{bmatrix} c_3 \\ 0 \end{bmatrix} \quad (2-19)$$

Case 2:

$$\begin{bmatrix} c_1 \\ b_1 \end{bmatrix} = \frac{1}{T_1 T_2} \begin{bmatrix} \exp(jD) - R_1 \exp(-jD) & R_1 [\exp(-jD) - \exp(jD)] \\ R_1 \exp(jD) - \exp(-jD) & \exp(-jD) - R_1 \exp(jD) \end{bmatrix} \begin{bmatrix} c_3 \\ 0 \end{bmatrix} \quad (2-20)$$

which approaches infinity as σ approaches infinity.

The transmission and reflection coefficients can now be determined from equations 2-19 and 2-20 by applying equation 2-11.

Case 1:

$$\begin{aligned} b_1 &= \frac{R_1 [\exp(jD) - \exp(-jD)]}{1-R_1^2} c_3 \\ c_1 &= \frac{\exp(jD) - R_1^2 \exp(-jD)}{1-R_1^2} c_3 \\ R_{fs} = b_1/c_1 &= \frac{R_1 [\exp(jD) - \exp(-jD)]}{\exp(jD) - R_1^2 \exp(-jD)} \end{aligned} \quad (2-21)$$

$$T_{fs} = c_3/c_1 = \frac{1-R_1^2}{\exp(jD) - R_1^2 \exp(-jD)} \quad (2-22)$$

Case 2:

$$b_1 = \frac{1}{T_1 T_2} [R_1 \exp(jD) - \exp(-jD)] c_3$$

$$c_1 = \frac{1}{T_1 T_2} [\exp(jD) - R_1 \exp(-jD)] c_3$$

$$R_{sc} = \frac{b_1}{c_1} = \frac{R_1 \exp(jD) - \exp(-jD)}{\exp(jD) - R_1 \exp(-jD)} \quad (2-23)$$

The subscripts on the reflection and transmission coefficients denote the configuration of Free Space (fs) or Short Circuit (sc). For the metal backed absorber, the values of c_3 and T_2 are approximately zero. Although b_1 and c_1 are indeterminate as T_2 approaches zero, the quotient, R_{sc} , is defined since c_3 and T_2 are constants that never become zero. Thus c_3/c_3 and T_2/T_2 will have the value of 1.0 as c_3 and T_2 approach zero. The equations for the reflection and transmission coefficients listed above can be verified from both Von Hippel (20:58-59), and the Emerson and Cuming Product Catalog (14). The power magnitudes of the reflection and transmission losses for an unbacked and metal backed slab of material in free space are provided in Tables 2-3 through 2-5. From these values the effectiveness of the absorber may be assessed. The values for Tables 2-3 through 2-5 were obtained by using a basic material thickness of 0.64 cm. The other values provided are for thicknesses of multiples of 0.64 cm. The total loss indicated

in the tables are calculated by taking the sum of the squares of the reflection and transmission coefficients, and then converting to a dBw scale.

2.6. Applicability to Problem

Tables 2-3 through 2-5 illustrate several interesting concepts regarding this material. To start with, it should be noted that for both polarizations, as the thickness of the slab increases, the overall loss for a slab in free space increases. This is due mostly to the increase of the transmission loss through the slab. For a metal backed slab, the values are not as clear cut. The maximum loss of the metal backed slab is dependent on the thickness of the slab. In addition, the thickness that produces the maximum loss is dependent on the frequency. Since this material can only be used in multiples of 0.64 cm, the thickness that produces the greatest losses for the three frequencies analyzed are: 2.56 cm for 30 MHz, 1.28 cm for 50 cm, and 0.64 cm for 250 MHz. This information will be useful when evaluating the absorber when used with a conducting surface. As illustrated in the tables, a loss of 13 to 23 dBw is possible when used with a metal plate. The tables show that the total losses for the absorber in free space are low, with values not exceeding 7 dBw at any frequency. This indicates that the material is well suited to reduce reflections from metal planar surfaces, but are poor absorbers when used in a free space environment.

Table 2-3

Reflection and Transmission Losses for a Slab of
Unbacked and Metal Backed ECCOSORB NZ-31 at 30 MHz

Thickness = 0.64 cm								
Normal Component					Parallel Component			
Angle (Deg)	Unbacked			Metal	Unbacked			Metal
	R (dBw)	T (dBw)	Total (dBw)	R (dBw)	R (dBw)	T (dBw)	Total (dBw)	R (dBw)
0	-19.2	-.996	-.930	-4.24	-19.2	-.996	-.930	-4.24
15	-19.5	-.964	-.903	-4.10	-18.9	-1.03	-.958	-4.40
30	-20.4	-.869	-.821	-3.67	-18.0	-1.14	-1.05	-4.92
45	-22.1	-.717	-.686	-2.99	-16.3	-1.38	-1.24	-6.05
60	-24.6	-.519	-.502	-2.11	-13.7	-1.90	-1.62	-8.66
75	-22.4	-.305	-.279	-1.09	-9.37	-3.39	-2.42	-14.1
85	-12.5	-.395	-.133	-.367	-4.28	-7.79	-2.68	-5.43
Thickness = 1.28 cm								
Normal Component					Parallel Component.			
Angle (Deg)	Unbacked			Metal	Unbacked			Metal
	R (dBw)	T (dBw)	Total (dBw)	R (dBw)	R (dBw)	T (dBw)	Total (dBw)	R (dBw)
0	-14.1	-1.89	-1.64	-8.76	-14.1	-1.89	-1.64	-8.76
15	-14.3	-1.83	-1.60	-8.45	-13.8	-1.95	-1.68	-9.08
30	-15.2	-1.66	-1.47	-7.54	-13.0	-2.15	-1.81	-10.2
45	-16.8	-1.38	-1.26	-6.11	-11.5	-2.58	-2.06	-12.3
60	-19.1	-1.02	-.949	-4.28	-9.28	-3.48	-2.46	-14.3
75	-16.8	-.652	-.548	-2.20	-5.85	-5.87	-2.85	-8.18
85	-7.29	-1.22	-.263	-.740	-2.38	-11.9	-1.92	-2.69
Thickness = 2.56 cm								
Normal Component					Parallel Component			
Angle (Deg)	Unbacked			Metal	Unbacked			Metal
	R (dBw)	T (dBw)	Total (dBw)	R (dBw)	R (dBw)	T (dBw)	Total (dBw)	R (dBw)
0	-9.66	-3.44	-2.51	-15.3	-9.66	-3.44	-2.51	-15.3
15	-9.89	-3.34	-2.48	-15.4	-9.43	-3.54	-2.55	-15.1
30	-10.6	-3.05	-2.36	-15.2	-8.74	-3.88	-2.65	-14.0
45	-12.1	-2.58	-2.12	-13.2	-7.55	-4.57	-2.80	-11.6
60	-14.1	-1.96	-1.71	-9.18	-5.81	-5.96	-2.87	-7.99
75	-11.7	-1.47	-1.07	-4.60	-3.39	-9.36	-2.41	-4.02
85	-3.58	-3.46	-.512	-1.53	-1.26	-16.7	-1.14	-1.34

Table 2-4

Reflection and Transmission Losses for a Slab of
Unbacked and Metal Backed ECCOSORB NZ-31 at 50 MHz

Thickness = 0.64 cm								
Normal Component					Parallel Component			
Angle (Deg)	Unbacked			Metal R (dBw)	Unbacked			Metal R (dBw)
	R (dBw)	T (dBw)	Total (dBw)		R (dBw)	T (dBw)	Total (dBw)	
0	-16.4	-1.43	-1.29	-6.38	-16.4	-1.43	-1.29	-6.38
15	-16.6	-1.38	-1.26	-6.15	-16.1	-1.47	-1.33	-6.61
30	-17.5	-1.25	-1.15	-5.49	-15.2	-1.63	-1.45	-7.42
45	-19.1	-1.04	-0.972	-4.45	-13.7	-1.96	-1.68	-9.22
60	-21.0	-0.762	-0.722	-3.13	-11.3	-2.67	-2.11	-13.2
75	-18.0	-0.487	-0.411	-1.61	-7.42	-4.62	-2.79	-12.0
85	-8.50	-0.898	-0.203	-0.542	-3.19	-9.88	-2.35	-3.82
Thickness = 1.28 cm								
Normal Component					Parallel Component			
Angle (Deg)	Unbacked			Metal R (dBw)	Unbacked			Metal R (dBw)
	R (dBw)	T (dBw)	Total (dBw)		R (dBw)	T (dBw)	Total (dBw)	
0	-11.6	-2.66	-2.14	-13.8	-11.6	-2.66	-2.14	-13.8
15	-11.9	-2.58	-2.10	-13.3	-11.4	-2.74	-2.18	-14.2
30	-12.6	-2.35	-1.96	-11.8	-10.6	-3.00	-2.31	-15.5
45	-14.1	-1.98	-1.72	-9.46	-9.33	-3.56	-2.54	-15.9
60	-15.8	-1.49	-1.34	-6.51	-7.35	-4.71	-2.83	-11.7
75	-12.6	-1.10	-0.808	-3.30	-4.45	-7.64	-2.75	-5.75
85	-4.28	-2.67	-0.391	-1.10	-14.4	-1.73	-1.50	-1.90
Thickness = 2.56 cm								
Normal Component					Parallel Component			
Angle (Deg)	Unbacked			Metal R (dBw)	Unbacked			Metal R (dBw)
	R (dBw)	T (dBw)	Total (dBw)		R (dBw)	T (dBw)	Total (dBw)	
0	-7.79	-4.69	-2.96	-12.4	-7.79	-4.69	-2.96	-12.4
15	-7.99	-4.58	-2.95	-12.9	-7.59	-4.82	-2.98	-11.9
30	-8.65	-4.22	-2.88	-14.9	-6.99	-5.22	-3.01	-10.4
45	-9.87	-3.65	-2.72	-19.2	-5.95	-6.06	-3.00	-8.20
60	-11.4	-2.93	-2.35	-16.1	-4.48	-7.72	-2.79	-5.62
75	-8.33	-2.66	-1.62	-7.23	-2.52	-11.6	-2.01	-2.85
85	-2.13	-6.39	-0.748	-2.33	-9.13	-19.5	-0.853	-9.52

Table 2-5

Reflection and Transmission Losses for a Slab of
Unbacked and Metal Backed ECCOSORB NZ-31 at 250 MHz

Thickness = 0.64 cm								
Normal Component					Parallel Component			
Angle (Deg)	Unbacked			Metal R (dBw)	Unbacked			Metal R (dBw)
	R (dBw)	T (dBw)	Total (dBw)		R (dBw)	T (dBw)	Total (dBw)	
0	-9.84	-3.46	-2.56	-23.8	-9.84	-3.46	-2.56	-23.8
15	-9.98	-3.38	-2.52	-22.0	-9.70	-3.54	-2.60	-25.8
30	-10.4	-3.15	-2.39	-17.8	-9.20	-3.82	-2.72	-27.5
45	-10.7	-2.80	-2.15	-12.9	-8.21	-4.42	-2.90	-18.0
60	-9.96	-2.46	-1.75	-8.38	-6.54	-5.67	-3.07	-10.8
75	-5.85	-2.94	-1.15	-4.11	-3.96	-8.81	-2.73	-5.12
85	-1.38	-7.88	-5.05	-1.36	-1.54	-15.8	-1.38	-1.68
Thickness = 1.28 cm								
Normal Component					Parallel Component			
Angle (Deg)	Unbacked			Metal R (dBw)	Unbacked			Metal R (dBw)
	R (dBw)	T (dBw)	Total (dBw)		R (dBw)	T (dBw)	Total (dBw)	
0	-6.88	-6.57	-3.71	-10.5	-6.88	-6.57	-3.71	-10.5
15	-7.01	-6.48	-3.72	-10.8	-6.75	-6.67	-3.70	-10.1
30	-7.35	-6.21	-3.73	-12.1	-6.32	-7.02	-3.65	-9.01
45	-7.71	-5.86	-3.67	-14.1	-5.49	-7.78	-3.48	-7.29
60	-7.14	-5.71	-3.36	-13.4	-4.17	-9.39	-3.03	-5.09
75	-4.05	-7.22	-2.34	-6.95	-2.34	-13.3	-2.01	-2.61
85	-1.15	-13.7	-9.19	-2.29	-8.42	-21.2	-8.03	-8.75
Thickness = 2.56 cm								
Normal Component					Parallel Component			
Angle (Deg)	Unbacked			Metal R (dBw)	Unbacked			Metal R (dBw)
	R (dBw)	T (dBw)	Total (dBw)		R (dBw)	T (dBw)	Total (dBw)	
0	-6.50	-13.3	-5.67	-6.42	-6.50	-13.3	-5.67	-6.42
15	-6.64	-13.2	-5.77	-6.77	-6.35	-13.3	-5.56	-6.27
30	-7.06	-13.0	-6.07	-7.02	-5.87	-13.6	-5.20	-5.78
45	-7.56	-12.8	-6.42	-7.65	-4.98	-14.3	-4.50	-4.89
60	-7.27	-12.9	-6.23	-7.69	-4.58	-14.7	-4.18	-4.50
75	-4.58	-14.8	-4.19	-5.11	-1.91	-19.9	-1.84	-1.89
85	-1.61	-21.3	-1.56	-1.83	-6.42	-28.1	-6.35	-6.41

III. Hardness Surveillance Illuminator

3.1. General

This chapter describes the theory, operation, and MOM results for the HSI, providing the necessary background needed in determining the field characteristics of the HSI. An understanding of the field characteristics is important when determining a methodology for reducing unwanted wave reflections and diffractions within the HSI. The analysis presented in this chapter describes the HSI with a homogeneous planar surface. The MOM routine was performed for a concrete surface described in Chapter 4. The MOM routine used for analysis was resident in the GEMACS program from the BDM Corporation. This program solved the currents along the wires, and then performed a numerical integration of the wave equation to obtain the electrical field components at several points within the working volume of the HSI from 6 MHz to 30 MHz. Attempts to extend the frequency range beyond 30 MHz proved futile with the GEMACS program. A complete discussion regarding this problem is provided within this Chapter. Based upon calculated results, it was possible to draw conclusions regarding the operation of the HSI at intermediate and high frequencies.

3.2. Description of the HSI

The HSI is essentially two wires stretched above a planar surface forming a rhombic-like structure (see Figure 3-1). The structure can be broken down into two sections: the input section and the termination section. The input section has the CW source at the vertex of the two wires while the termination section has a matched load at the vertex. The planar surface is divided into three regions. Region 1 is a

conducting ground plane, region 2 is a concrete pad, and region 3 is soil. The planar surface is divided in this way as an attempt to reduce reflections between the test object and the surface (21:27). It will be shown later that the concrete surface has characteristics similar to the conductive ground plane, so that ground plane reflections are still a problem. The overall dimensions of the HSI can be seen in Figure 3-1; however, it is important to note that the input section of the HSI is longer than the termination section. This is important for two reasons. First, the termination section is shortened in order to reduce reflections from the termination section into the working volume. Second, the input section is long in order to provide a wave that more closely resembles a plane wave. The wires are supported by a dielectric cable supported by two wooden poles. The separation of the wires can be varied to provide two modes of operation: common mode and differential mode. When the wires are driven in phase (common mode), the wire separation is 32 m (see Figure 3-1). When the wires are driven anti-phase (differential mode), the wire separation is 65 m (see Figure 3-1). When driven in common mode, it will be shown that the predominant polarization of the wave is vertical. When driven in differential mode, the overall polarization is more difficult to determine; however, it will be shown that the polarization of the field is predominantly horizontal near the center of the working volume and vertical further out. The conceptual excitations produced by both modes are illustrated in Figure 3-2. The test object is placed in a working volume approximately 40 m x 45 m x 15 m. This volume is located in the input section of the HSI and extends toward the source. It is desired that the generated wave be approximately planar throughout the working

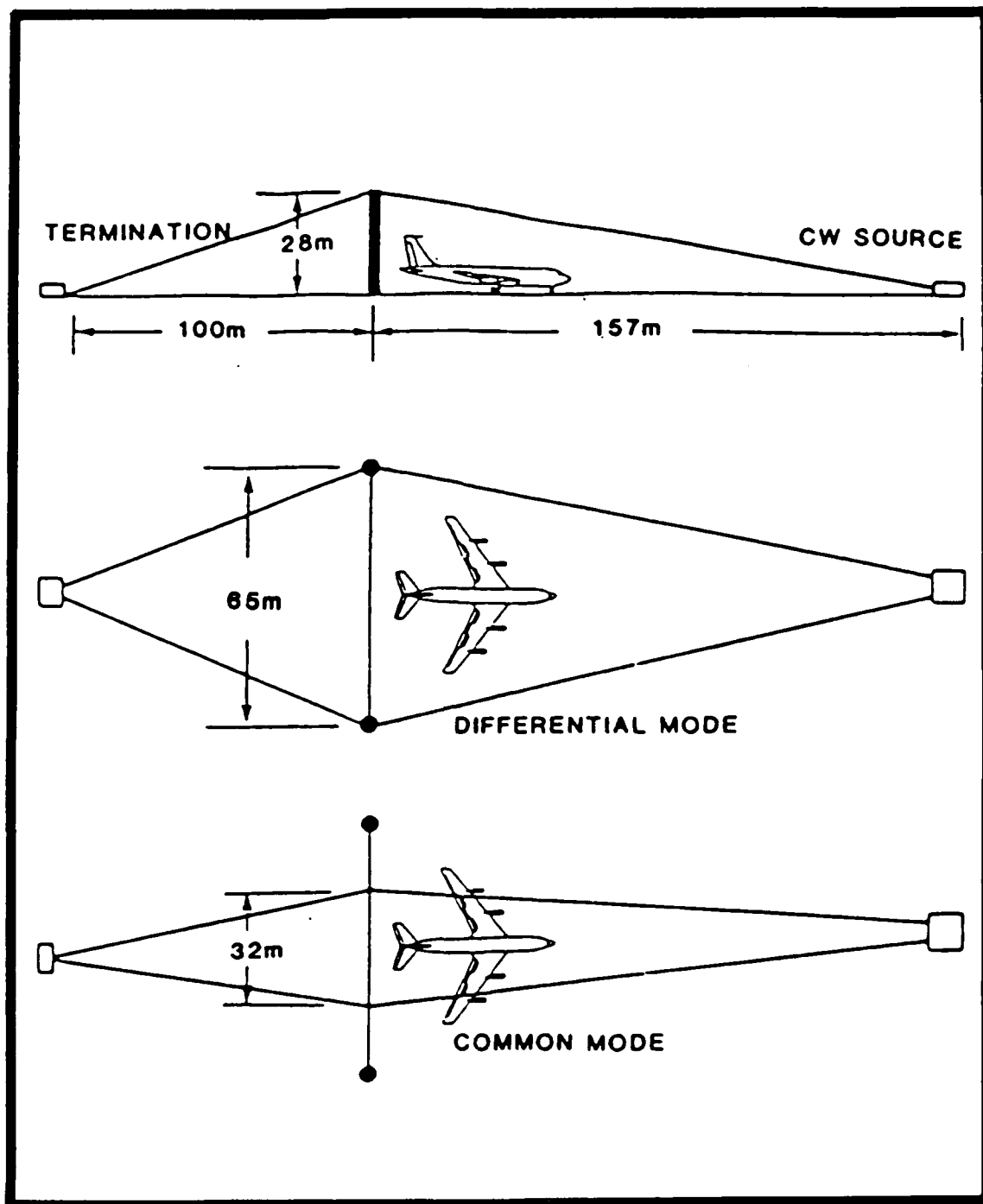


Figure 3-1

HSI in Common and Differential Mode (9:17)

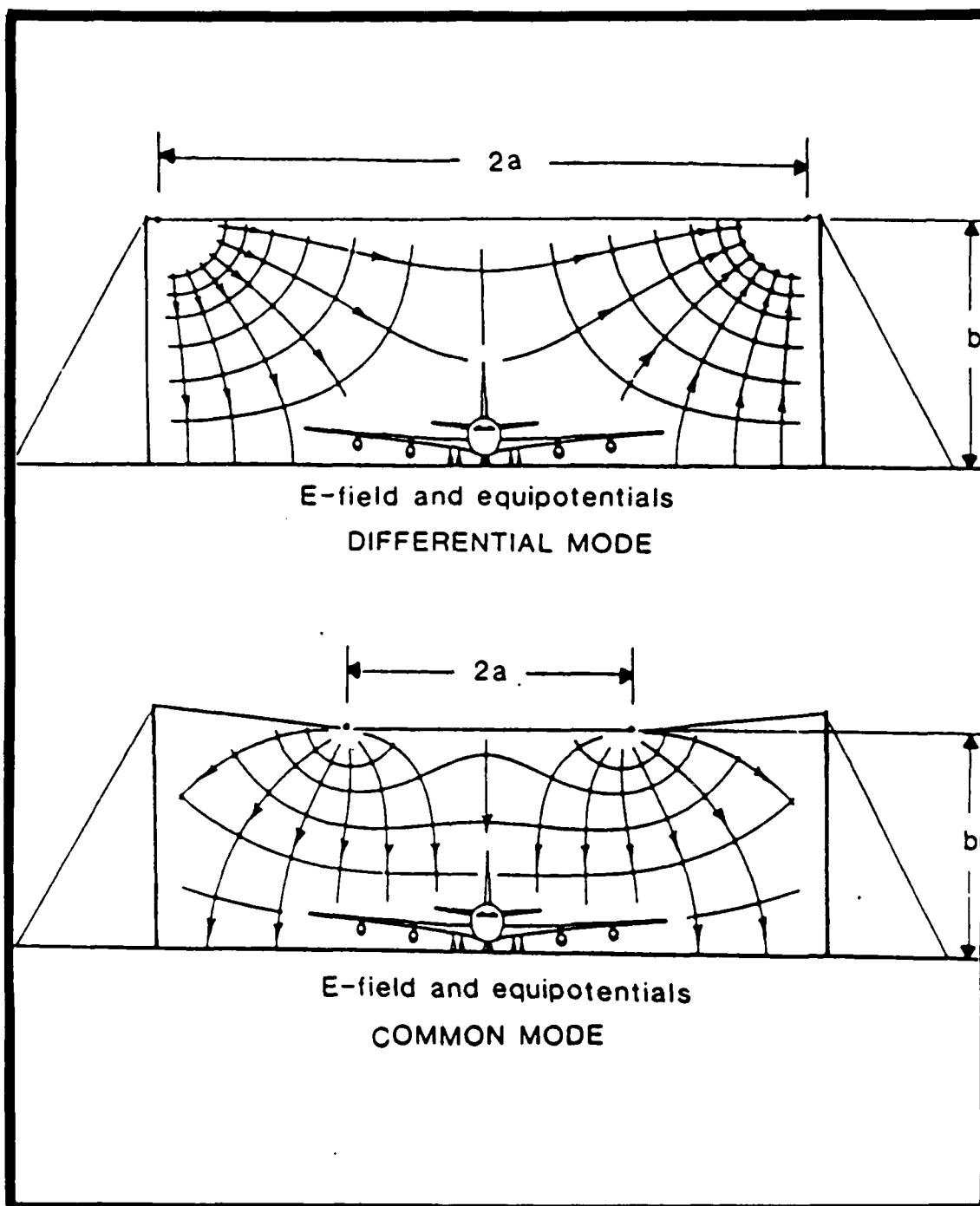


Figure 3-2

Differential and Common Mode Excitations (9:9).

volume.

3.3. Theory of Operation

The design of the HSI is conceptually easy to analyze. Its configuration suggests that it can be analyzed as a conical transmission line. A conical transmission line is defined as, "... two or more separate conductors (assumed perfect conductors) which can be generated (geometrically) by lines which all pass through one point (the apex)" (2:2). The two sections of the HSI satisfy this definition. It is possible to use the theory of images to define the structure to be analyzed. Simply stated, the theory of images allows analysis to be performed on structures located above an infinite plane conductor by replacing the conducting plane with properly placed virtual sources to account for reflections from the conducting plane. Using this theory, it is possible to consider the structure as a four wire conical transmission line (see figure 3-3). A conical transmission line, produces a spherical transverse electromagnetic (TEM) wave, with its origin at the apex of the wires (2:4). If the input section is long, then the wave is approximately planar throughout the working volume. The direction of propagation of the spherical wave is in the positive 'y' direction as shown in figure 3-3. For the HSI problem, the ground plane is not an infinite perfect conductor. However, the concrete pad that comprises most of the ground plane throughout the working volume can be considered a good conductor. The general criteria for determining whether a material is a good conductor is to show that $\sigma / \omega \epsilon \gg 1$, where σ is the conductivity of the material, ω is the radian frequency, and ϵ is the permittivity of the material (6:399).

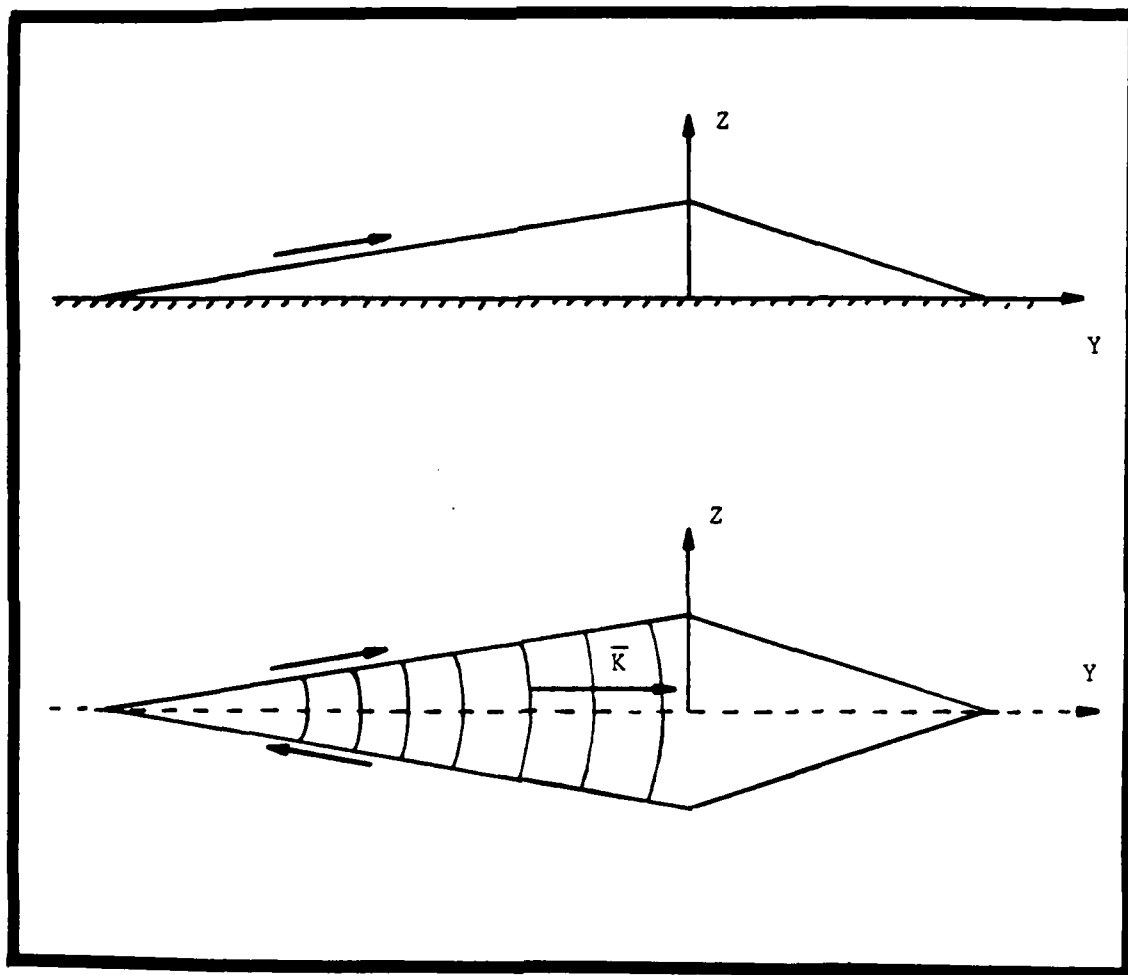


Figure 3-3

Image Theory Approximation and Wave Propagation in HSI.

These values are calculated in Chapter 4. As an example, consider a frequency of 30 MHz. The value of $\sigma / \omega \epsilon = 31.1$, which is $\gg 1$; therefore, concrete can be considered a good conductor at 30 MHz. Similar calculations verify that concrete is a good conductor at the other frequencies used in this study. To reduce reflections from the termination section of the structure, the structure is terminated in a matched load. The TEM mode is the only mode supported by the HSI when operating at wavelengths longer than the height of the structure (16:354). When the wavelengths become approximately the same or shorter than the height of the HSI, transverse magnetic (TM) and transverse electric (TE) modes are also supported (11:265). The above discussion is an analysis of the HSI using basic transmission line theory. It gives a general understanding of the fields to be expected within the working volume. In addition to the above general theory, two other methods for defining the electromagnetic field environment within the working volume were used. The first method is a quasi-static approximation of the structure, and the second method to be discussed is a complete theoretical and experimental evaluation of a pair of scale models of a rhombic simulator.

3.4. Quasi-Static Analysis (9,21)

An analysis of the electromagnetic fields within the working volume was accomplished by approximating the structure of the HSI as a pair of parallel wires above an infinite, perfectly conducting ground plane. This approximation is possible since the HSI has a long input section, and the fields within the working volume were sufficiently planar (21:5). By making this approximation, the analysis of the HSI could be

simplified to a two-dimensional, quasi-static, TEM approximation. The cross-sectional electromagnetic fields for this approximation can be determined by making a conformal transformation and using image theory. An example of these fields is illustrated in Figure 3-2. The magnitudes for the predominant field components generated by this approximation are (21:5):

Common Mode

$$E_z = \frac{q}{2\pi\epsilon_0} \left[\frac{z-b}{(x-a)^2 + (z-b)^2} + \frac{z-b}{(x+a)^2 + (z-b)^2} - \frac{z+b}{(x-a)^2 + (z+b)^2} - \frac{z+b}{(x+a)^2 + (z+b)^2} \right] \quad (3-1)$$

Differential Mode

$$E_x = \frac{q}{2\pi\epsilon_0} \left[\frac{x+a}{(x+a)^2 + (z-b)^2} - \frac{x-a}{(x-a)^2 + (z-b)^2} - \frac{x+a}{(x+a)^2 + (z+b)^2} + \frac{x-a}{(x-a)^2 + (z+b)^2} \right] \quad (3-2)$$

where q is the charge per unit length, ϵ_0 is the free space permittivity, 'a' is the half width separation of the wires, and 'b' is the height of the wires. The variables 'x' and 'z' refer to the horizontal and vertical measurements, respectively. For investigation purposes, the values 'a' and 'b', were given as the values that would provide the best planar fields within the working volume. These values are: $a = 16$ m, $b = 28$ m for the common mode; and $a = 32.5$ m, $b = 28$ m for the differential mode. The electric field magnitudes calculated by equations 3-1 and 3-2 are illustrated in Figures 3-4 and 3-5. The value

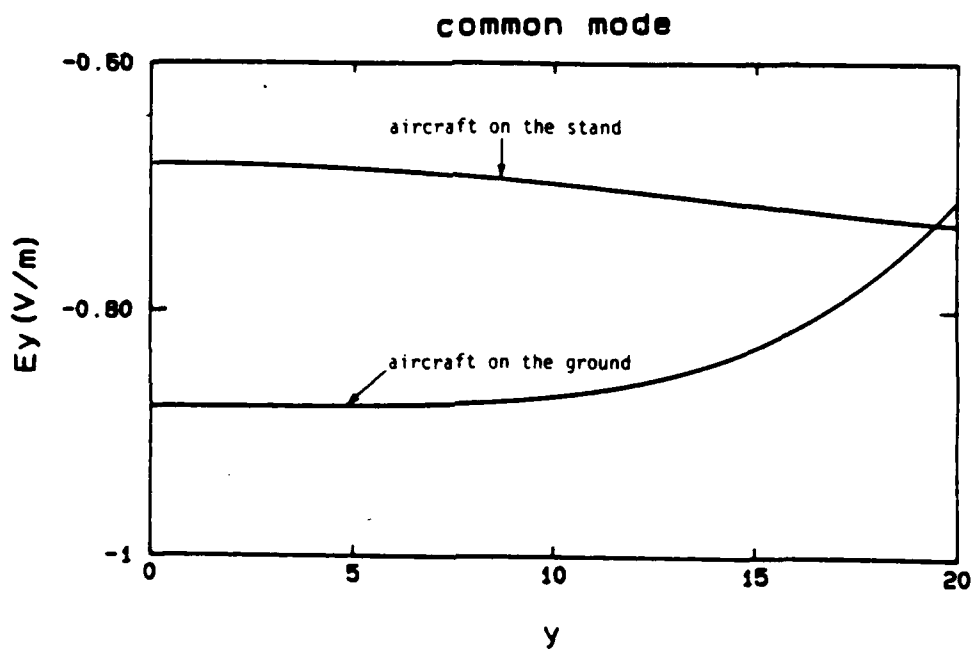
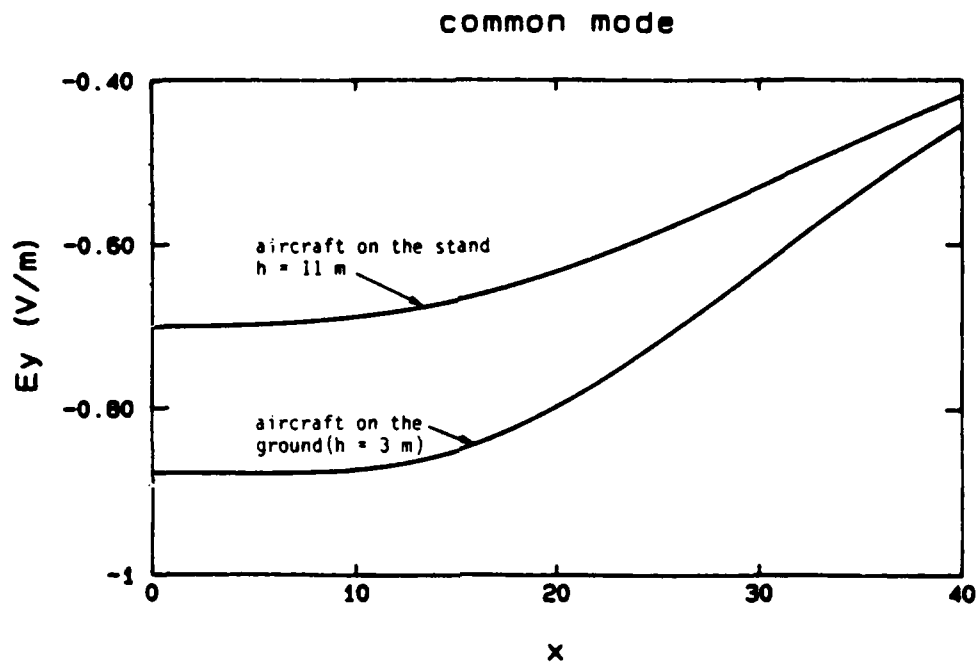


Figure 3-4

Illustration of Equation 3-1 (9:67,68).

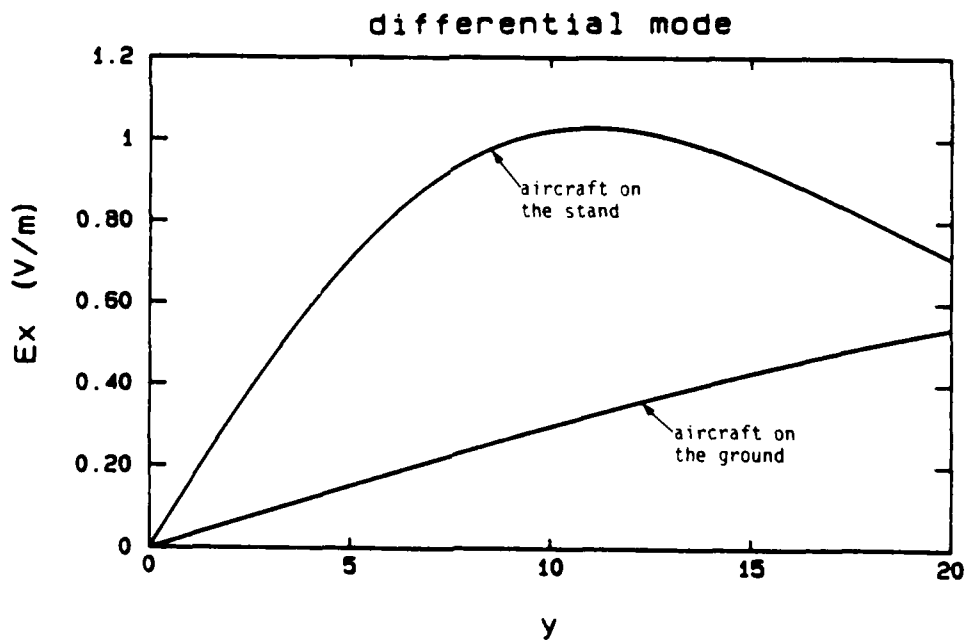
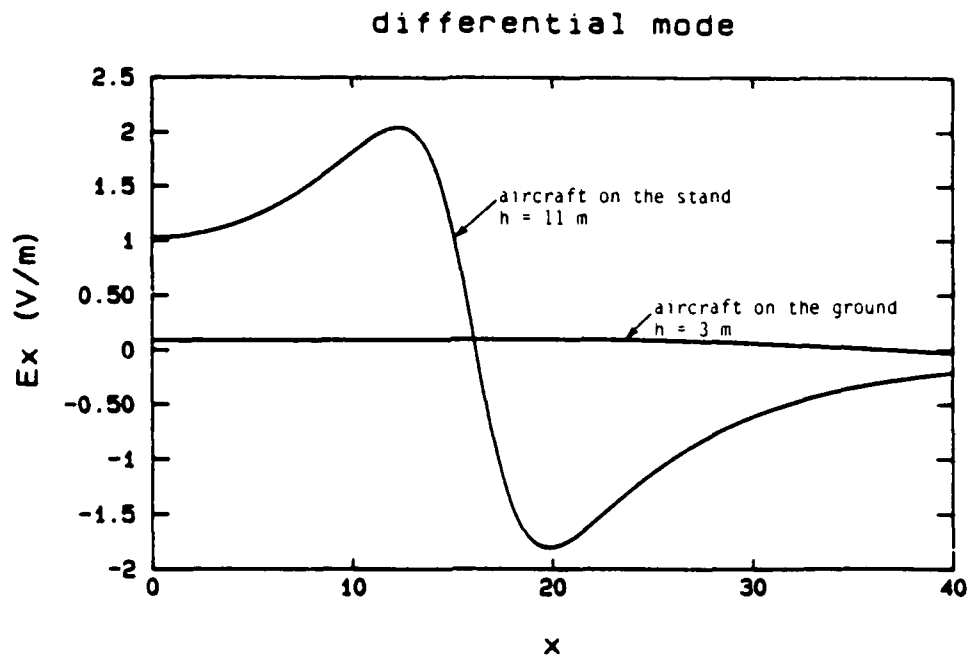


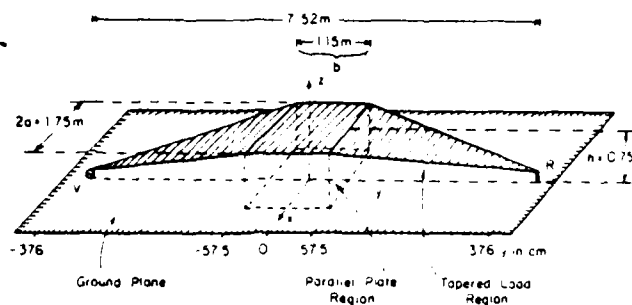
Figure 3-5

Illustration of Equation 3-2 (9:69,70).

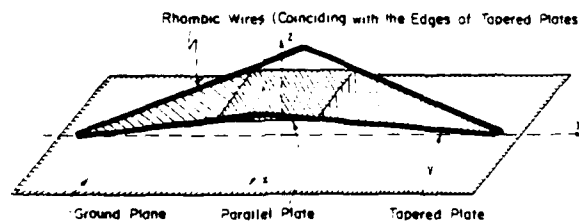
of E_x near the ground plane is near zero for the differential mode. This is due to the solution of the boundary conditions at the air-ground interface, which states that the tangential component of the field across an interface is continuous. Since the ground plane was assumed to be perfectly conducting, the tangential field within the conductor must be zero, and therefore, the incident tangential field must be zero at the interface (6:361). It is expected that the value of E_x would be higher if the ground plane were a material other than a perfectly conducting ground plane.

3.5. The Harvard EMP and Rhombic Simulators

The Harvard EMP (HES) and rhombic (RS) simulators are two scale model simulators used at Harvard for EMP simulation and experimentation. The HES is a parallel plate simulator with a triangular input and output section, with a parallel plate section between the the input and the output (see Figure 3-6a). It has been used to calculate the frequency response of the electric fields within such a simulator. The RS is a system based on the HES that uses four straight brass tubes supported by styrofoam columns. The tubes coincide with the edges of the plates of the HES (see Figure 3-6b.) (16:349). There is no parallel plate section in the RS. Neither of these models have dimensions that are the same as the HSI; however, the models are able to determine the general electromagnetic field characteristics of similar EMP test beds. All of the measurements and theoretical analysis of these simulators have been accomplished using the common mode only. Therefore, only common mode values obtained with the MOM routine will be compared to the RS and HES models. The structures for both the HES and the RS are symmetric with



A. HES Structure (11:264)



B. RS Structure (16:349)

Figure 3-6

HES and RS Simulators.

the wire lengths being equal around the structure. It is important to note that the working volumes of the HES and the RS are centralized with respect to the longitudinal axis. Therefore, the analysis performed on the working volumes for $y > 0$ does not have direct applicability to the HSI problem. The analysis and experimentation were accomplished at

three frequencies, corresponding to a low, intermediate, and high frequency range of the structure. The limits for the frequency ranges are determined by the wavelength and the physical size of the structure. The low frequency range is defined for wavelengths that are much longer than the maximum height of the simulator, the intermediate frequency range is defined for wavelengths approximately equal to the height of the simulator, and the high frequency range is defined for wavelengths much shorter than the maximum height of the simulator. The values used for this analysis were, $h/\lambda = 0.325$, $h/\lambda = 1.3$, and $h/\lambda = 2.6$. For the RS, this corresponds to $\lambda = 300$ cm, $\lambda = 75$ cm, and $\lambda = 37.5$ cm (16:351). Theory and experimentation with both the HES and the RS show that for the low frequency range, the structure produces a TEM mode with very low standing wave ratios (SWR) when loaded with a characteristic impedance at the termination section. The electric field is essentially vertically polarized with constant amplitude. For intermediate frequencies, both TEM modes and TM modes are supported within the HES and the RS. The HES has a high SWR of approximately 5 for the TEM mode, and a SWR of 25 for the TM mode (16:355). This is essentially characterized by a notch within the working volume of the structures. The SWR for the RS in the intermediate frequency range is generally low (about 1.8); however, calculations show that a deep notch is present in the 70-130 cm range along the main axis of the simulator (16:355). This notch causes SWR readings to be significantly worse than 1.8. This notch is located in the terminal section of the illuminator. Since the working volume of the HSI is located strictly in the input section of the structure, this should not be a problem for the HSI. The longitudinal component (E_y) is significant in both the HES and the RS

and is caused by the TM mode (11:265). For the upper frequency range, the SWR is again reduced. The SWR is on the order of 1.36 for the HES and 2 for the RS. The load plays little part in the formation of the wave (16:355). Instead, a significant amount of the power is radiated into space prior to reaching the load. There is, again a significant longitudinal field component caused by the TM mode (11:265). To summarize, the HES and RS showed that the common mode electric field is generally vertically polarized. For low frequencies, a TEM mode is supported, and low SWR measurements obtained. For intermediate and high frequencies, TEM, TE, and TM modes are supported. The TM modes cause a longitudinal field component to be produced. The SWR for the intermediate frequency is high in the HES, and relatively low in the RS.

3.6. Method of Moments Results

The two efforts previously mentioned provided useful insight to the problem of determining the EM field behavior within the HSI. However, both methods had deficiencies that needed to be resolved. For the first effort, general field approximations were determined by making key approximations were determined. The first approximation made was that the structure could be viewed as a parallel wire configuration. The second approximation that was made was that only a TEM wave was supported by the HSI. For the second effort, the ratios of the dimensions for the models were different than for the HSI. Also, only the common mode was analyzed. For both efforts, the only planar surface that was analyzed was a perfectly conducting ground plane. Although both efforts were useful in determining the field characteristics of the HSI, it was felt that additional modelling of the HSI was necessary to

more accurately describe the electromagnetic fields within the working volume. The method chosen to accomplish the modelling was to perform a MOM analysis on the structure itself. The MOM code is a low frequency code that adapts itself to several applications.

3.6.1. Description of MOM. The MOM calculations were performed by the GEMACS code written by the BDM Corporation. A MOM code is a method of solving the current distribution on a finite diameter wire by subdividing the wire into small segments. By segmenting the wire into small regions it is relatively easy to solve either Pocklington's integral equation or Hallen's integral equation which are (1:304-307):

Hallen's Integral Equation.

$$\int_{-L/2}^{L/2} I(z') \exp(-jkR)/(4\pi R) dz' = -j/Z [A_1 \cos(kz) + B_1 \sin(k|z|)] \quad (3-3)$$

where A_1 is a constant determined by the boundary conditions and B_1 is a constant equal to $V_i/2$, k is the propagation constant, and Z is the intrinsic impedance of the material.

Pocklington's Integral Equation.

$$\begin{aligned} \int_{-L/2}^{L/2} I(z') [(\partial^2 / \partial z^2 + k^2) \exp(-jkR)/(4\pi R)] dz' &= j\omega\epsilon E_z^s(z) \\ &= -j\omega\epsilon E_z^i(z) \end{aligned} \quad (3-4)$$

where $R = [(x-x')^2 + (y-y')^2 + (z-z')^2]^{1/2}$, $E_z^s(z)$ is the scattered electric field, and $E_z^i(z)$ is the incident electric field.

Pocklington's equation can be presented in many other forms. The solution of the moment method requires that the integral equations be expanded in terms of an unknown and a basis function. Common basis

functions include a piecewise constant, where the function is constant over the range of interest and zero elsewhere; piecewise linear, where the function is triangular over the domain of interest; piecewise sinusoid, and truncated cosine (1:308-310). Other basis functions may also be used. In order to solve for the current, an interaction matrix must be established and solved. The size of the matrix is dependent on the number of segments into which the wire is subdivided. It is important that the segments be small with respect to the wavelength in order to produce an accurate result. For wire structures, a segment size of $.1\lambda$ has produced adequate results (7:56). Once the current on the wires is found, the electric field can be determined from the wave equation. Two computer programs were evaluated that performed the MOM routine; Mini-NEC and GEMACS. Mini-NEC is a program written in the Basic language for use on microcomputers. It was determined that this program was inadequate for this project, due to its inability to perform near-field calculations, and its inability to calculate electric fields due to a planar surface other than a perfectly conducting ground plane. For this project, it was necessary to obtain this information.

3.6.2. General Description of GEMACS. GEMACS solves the current distribution by using Pocklington's equation. It uses as its basis functions: pulse, sine, and cosine in the form (7:30)

$$I_i/\lambda = A_i + B_i \cos(2\pi t) + C_i \sin(2\pi t)$$

where A_i , B_i , and C_i are constants given in terms of the segment midpoint currents I_{j-1} , I_{j+1} , ..., I_{j+m} (7:31). This program was able to calculate the near-zone electric fields of the HSI given the structure

of the HSI, the source, the load, and the conductivity of the planar surface. The field distributions were calculated for 150 discrete points within the working volume of the HSI for the frequencies of 6, 8, 10.71, and 30 MHz. By obtaining this information it was possible to determine the field characteristics produced by the HSI, especially around the resonance frequency of the HSI. The resonance frequency of the HSI is 10.71 MHz. Several limitations of the GEMACS program became evident during this project. The biggest problem with this code and any other MOM code used for analyzing the HSI is the size and number of the segments needed to describe the structure. It is suggested in the GEMACS operating manual that a segment size equal to $.1\lambda$ will be sufficient to describe a segment. Due to the size of the HSI, this criteria requires that hundreds of segments be used to analyze the structure. The GEMACS code has a theoretical upper limit on the number of segments that can be used, defined by the quantity $5500/6$ or 916 segments (4). By using a $.1\lambda$ segment size as the standard, it was necessary to use 909 segments to model the HSI operating in differential mode at 50 MHz. The GEMACS code was not able to analyze the the 50 MHz model, however. When it was run, the resulting error indicated that the number of segments being used was higher than could be analyzed. Two methods of reducing the number of segments that the GEMACS program must analyze were attempted. Each method was initially tested at 6 MHz, to determine the effects of the method on the program. The frequency of 6 MHz was used since the GEMACS analysis of that frequency was relatively fast (3-4 minutes) when compared to the higher frequencies tested (4-28 hours). The first method was to increase the size of the segment to 0.14λ . Initial results at 6 MHz, indicated that this segment size

could be used successfully. Further analysis at 30 MHz indicated that errors greater than 20 percent occurred, when normalized and compared to the standard. It was felt that these errors were excessive, and therefore, this method was disregarded. One run at 50 MHz using this method produced electric field data. Although this run was considered to be erroneous, it was determined that a segment size of 0.84 m, resulting in a total of 642 segments, could be analyzed. This is important since it indicates that a frequency range of approximately 36 MHz could be analyzed when using the standard technique. An attempt to raise the frequency range to 40 MHz using the standard was unsuccessful for the same reasons as the 50 MHz runs. This indicated that an upper value for the total number of segments is between 642 and 718. Although the information obtained for the runs indicated that a frequency of approximately 36 MHz could be analyzed, it was felt that the inclusion of this frequency in this report would not significantly enhance the findings of this project. The second method used an imbedded code in the GEMACS program called the Banded Matrix Iteration (BMI) technique. The BMI is generally used when the problem is large in order to save computation time. This method reduces the number of unknowns that need to be solved by partitioning the interaction matrix into upper, lower, and central or, banded sections. The BMI technique then solves only the banded section (7:5). When using the BMI, the convergence measure, and the maximum number of iterations needed to reach convergence must be specified. Three measures can be specified in the GEMACS code: the Boundary Condition Relative Error (BCRE), the Iterative Relative Error (IRE), and the Predicted Relative Error (PRE) (7:14). The BCRE measures how well the solution matches the boundary conditions of the structure.

This method is not suggested since it can have large errors near resonance (7:14). The IRE is a measure of the relative change between successive approximations to a solution. The iterative process may be ended early for slowly converging problems (7:15). The PRE is an exponential fit to the two previous methods, and has been shown to be a close approximation of the actual relative error after only four iterations (7:15). The PRE is the method suggested for most problems, and was used in this project. A convergence value of 1 percent was suggested for near-field problems (7:15). The BMI was tested at 6 MHz to determine its effectiveness, and to determine the necessary parameters of convergence and the banded section size. It was found during this testing that the solution of this method was exact when using a banded section of 75 out of 111 total segments. This resulted in a ratio of approximately 68 percent. Using this ratio at 50 MHz resulted in a banded section of 619 segments; well within the segment limits noted above. Unfortunately, this method also failed at 50 MHz. This was due to a failure of the BMI technique to converge on a value. An increase in the maximum number of iterations required for convergence to 30, yielded similar results. All runs at 50 MHz required from 20 to 28 CPU hours on the computer.

3.6.3. Description of GEMACS Implementation.

The HSI is a simple structure for GEMACS to solve. Since the MOM routine is configured for wire inputs, all that was necessary to provide as a geometry was the overall dimensions of the HSI, the wire segmentation data, the source positions and types, the load, and the type of ground plane desired. The GEMACS model was configured in the

same fashion as the RS model with the axes located as shown in Figure 3-7. It was not possible to exactly implement the structure as desired. The real HSI utilizes a "T" network for the loading. Since GEMACS only allows one value for the load, a single lumped load was placed between the last two segments in the termination section and the ground. For the common mode, a value of 215 ohms was used, and a value of 700 ohms was used for the differential mode. These impedance values were obtained from the sponsor (19), and then tested at 6 MHz to ensure that these values minimized the SWR. The sources used to drive the structure were two delta-gap voltage sources at either the same potential for common mode or opposite potentials for differential mode. The homogeneous planar surface was a concrete surface with a conductivity and dielectric constant determined in Chapter 4. The intent of using GEMACS was to determine the patterns of the fields within the HSI in order to verify or refute the theoretical values. The values of the

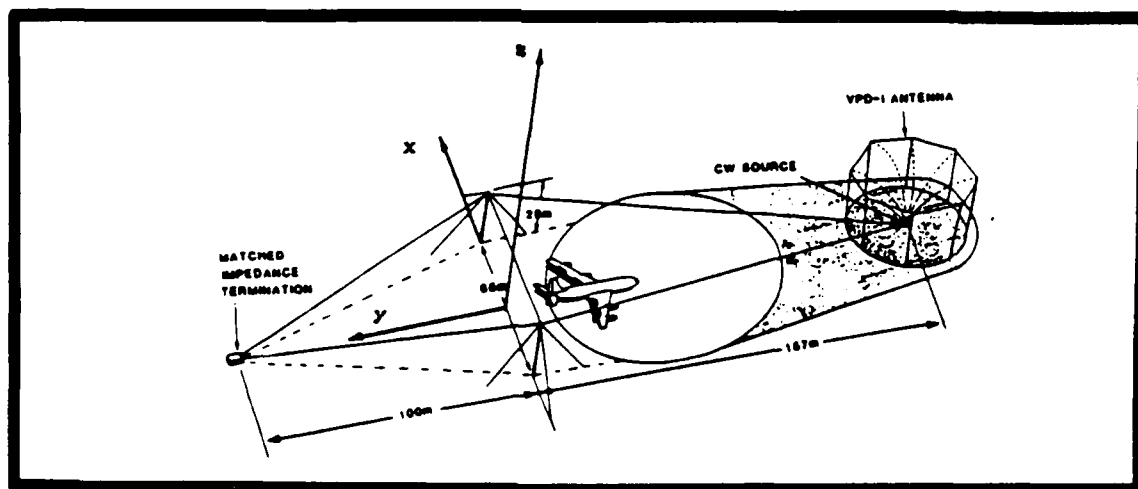


Figure 3-7

Orientation of Axes for GEMACS Model (6:8)

voltage levels were not considered exact, since an arbitrary value of 1000 volts was used as the input voltage. The field values should be accurate given this input voltage.

3.6.4. Results. The results for the MOM calculations at $X=0$ m, and $Z=4$ m are provided in Figures 3-8 through 3-17. These are plotted as the magnitude and phase of the electric field with the longitudinal axis of the HSI as the dependent variable. The range of interest for the dependent variable is 0 to 50 m. Other figures are provided in Appendix B that further illustrate the electric fields at other values of X and Z , and illustrate the horizontal and vertical characteristics of the electric fields. Data were calculated for $X=0$ to 20 m considering the symmetry of the structure. For the common mode, the values will be the same from $X=0$ to -20 m as from $X=0$ to 20 m. In the differential mode, the magnitudes are the same for both sides, however, the phases differ by 180° for E_y and E_z . The phase is the same for E_x .

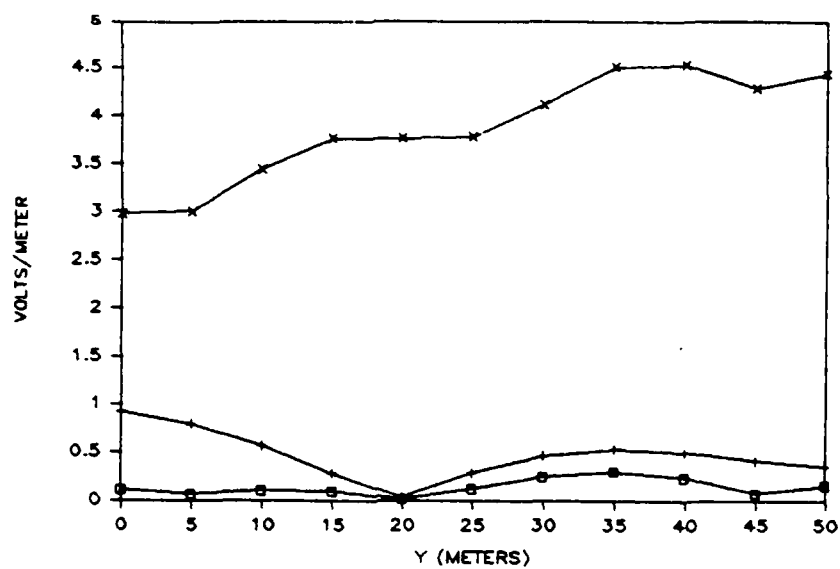
3.6.4.1. Common Mode. Figures 3-8 through 3-12 illustrate the electric fields calculated for common mode with a concrete ground plane. From these figures, it is readily shown that the predominant field is the E_z field. This supports the theory and the experimental data previously discussed in Section 3-4. The SWR at the lower frequency ranges are relatively low, with values ranging from about 1.2 to about 2.0. There is no apparent notch in the intermediate frequency range as was discussed previously. The phase terms remain linear throughout the working volume. For 30 MHz, the SWR becomes considerably higher. Here the SWR ranges from about 1.7 to nearly 5.0, as the x and y parameters are varied. The phase is again linear over the range. This phenomenon

will need further study in order to determine the cause of these high SWR's. It is also apparent, that there is a non-zero longitudinal component. This component increases as the operating frequency increases. This is expected since the TM modes are emphasized as the wavelengths become shorter. The linearity of the fields illustrated in the Figures verify that a TEM mode is supported by the HSI throughout the working volume. In addition, the overall consistency of the electric field throughout the working volume indicates that the field is sufficiently planar.

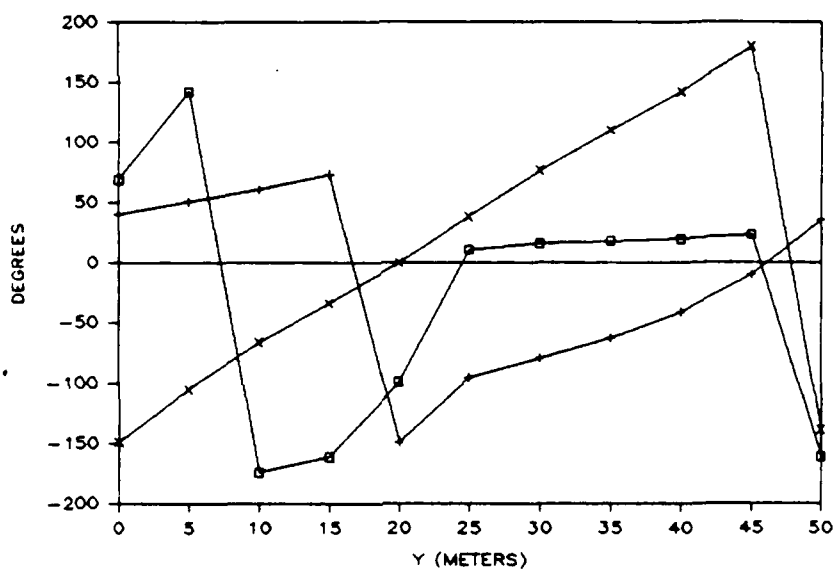
3.6.4.2 Differential Mode. Figures 3-13 through 3-17 illustrate the electric fields calculated for differential mode with a concrete ground plane. The differential mode has completely different characteristics than the common mode. These are also apparent from the figures. For this mode, there is a strong horizontally directed component at $x=0$ through about $x = 10$ m. As x increases, the field becomes vertically polarized (see Appendix B). As illustrated in Figures B-18a, B-21a, B-24a, and B-27a, the predominance of the horizontal and vertical components change between $x = 5$ m and $x = 10$ m. This substantiates the theoretical field distribution as shown in Figure 3-2. The SWR for the differential mode is substantially worse than for the common mode. Typical values for SWR are from 3.0 to 6.5. This mode obviously creates higher order standing waves than the common mode does. The SWR is considerably lower for 30 MHz than it is for the other frequencies. Once again, there is a strong longitudinal component of the electric field. Since the longitudinal component of the field is higher for the differential mode than for the common mode, it is apparent that the the

TM field is stronger in the differential mode than in common mode. The TEM field is also supported by the differential mode.

3.6.4 Summary. The results of the MOM calculations for the HSI with a concrete ground plane substantiate the results obtained with the quasi-static approximation, and the RS and HES theory and experimentation. The common mode produces a predominantly vertically polarized, near planar, TEM wave throughout the working volume. The differential mode produces a strong horizontally polarized, near planar, TEM wave near the center of the HSI. The wave becomes more vertically polarized as the distance away from the center of the HSI increases.



A. Magnitude

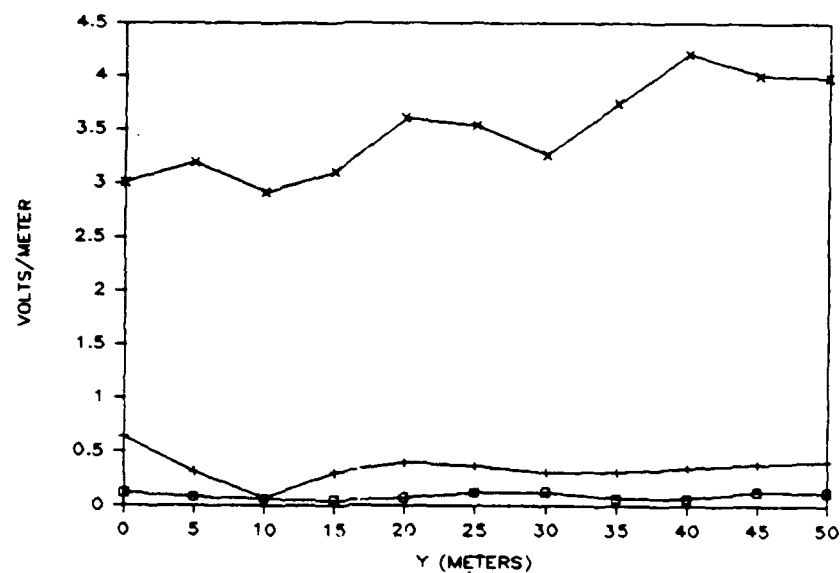


B. Phase

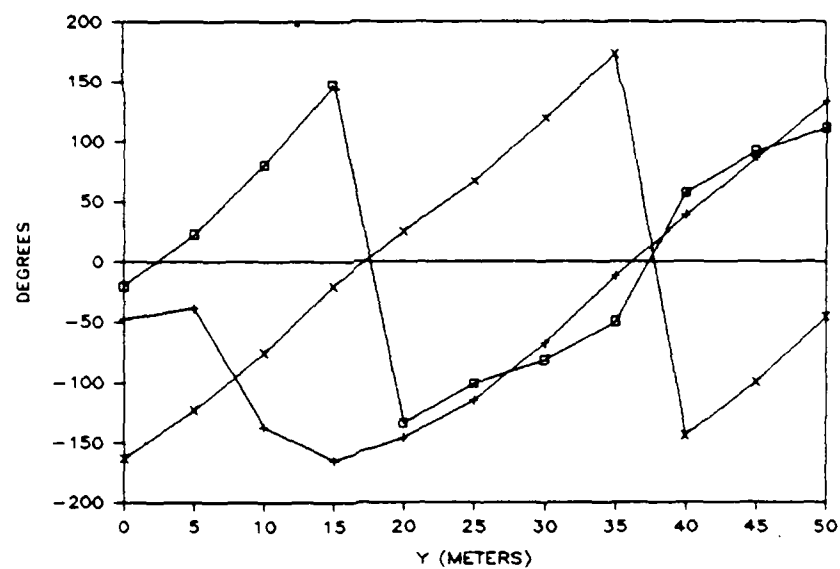
□ E_x + E_y x E_z

Figure 3-8

Common Mode Electric Field Magnitude and Phase For 6 MHz in Longitudinal Direction at $X=0$ m, $Z=4$ m.



A. Magnitude

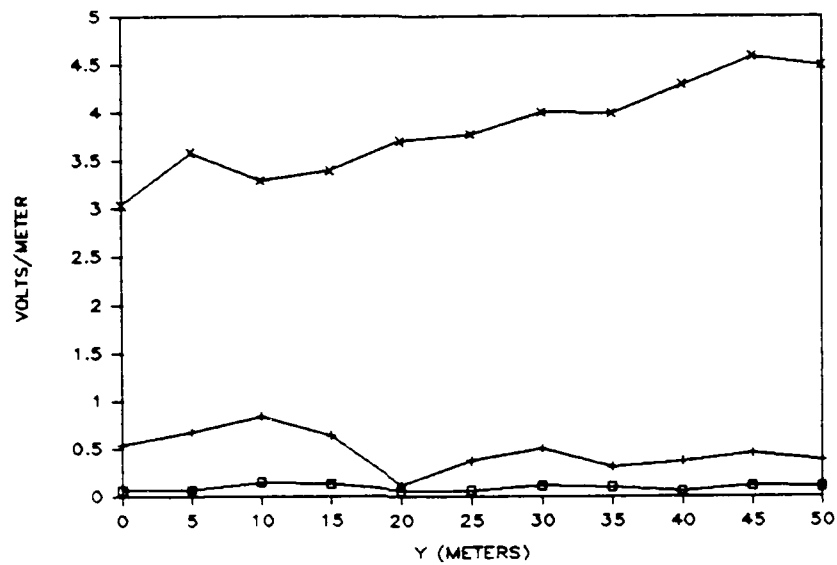


B. Phase

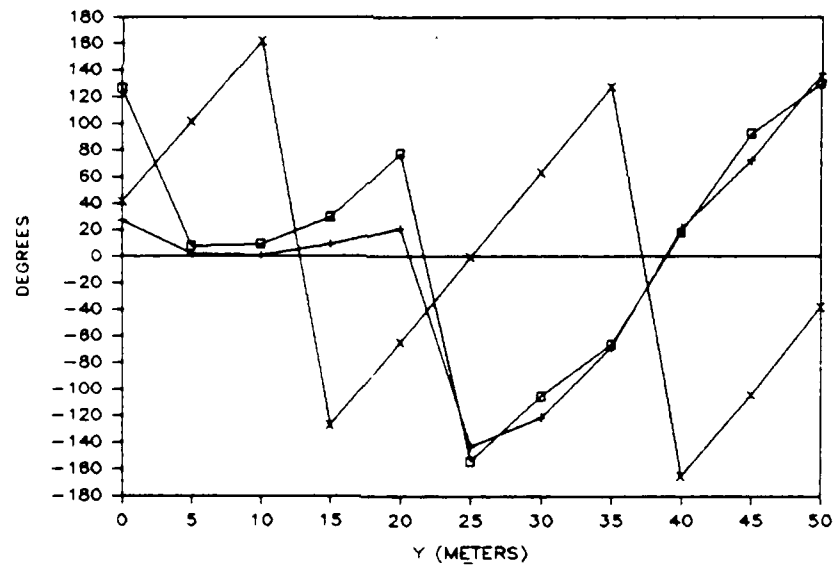
□ E_x + E_y x E_z

Figure 3-9

Common Mode Electric Field Magnitude and Phase For 8 MHz in Longitudinal Direction at X=0 m, Z=4 m.



A. Magnitude

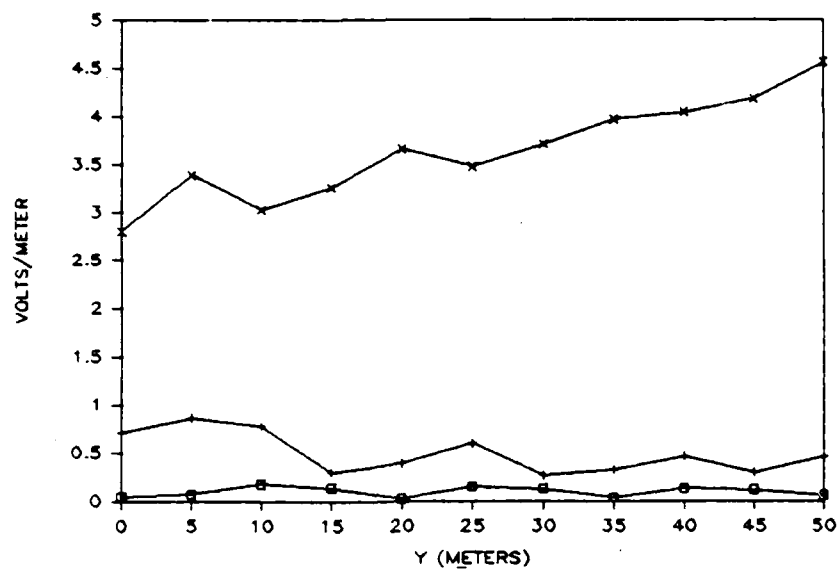


B. Phase

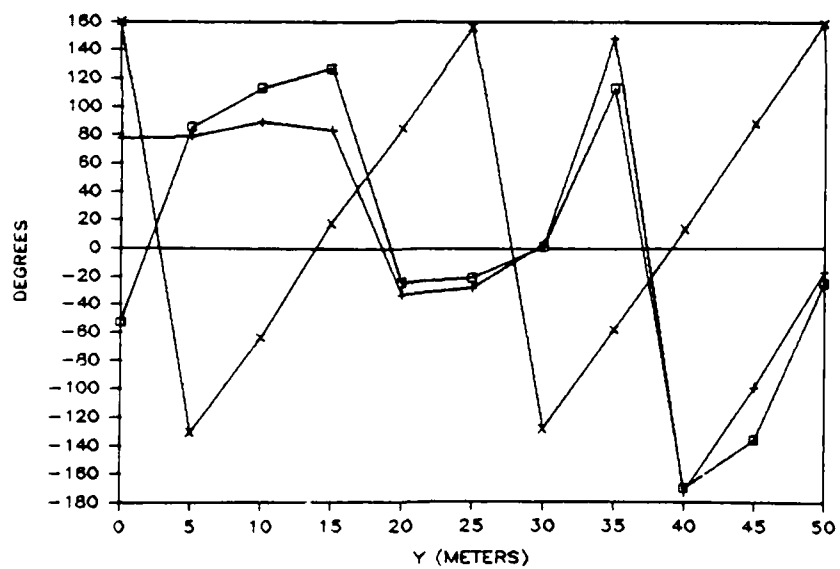
□ E_x + E_y × E_z

Figure 3-10

Common Mode Electric Field Magnitude and Phase For 10.71 MHz in Longitudinal Direction at $X=0$ m, $Z=4$ m.



A. Magnitude

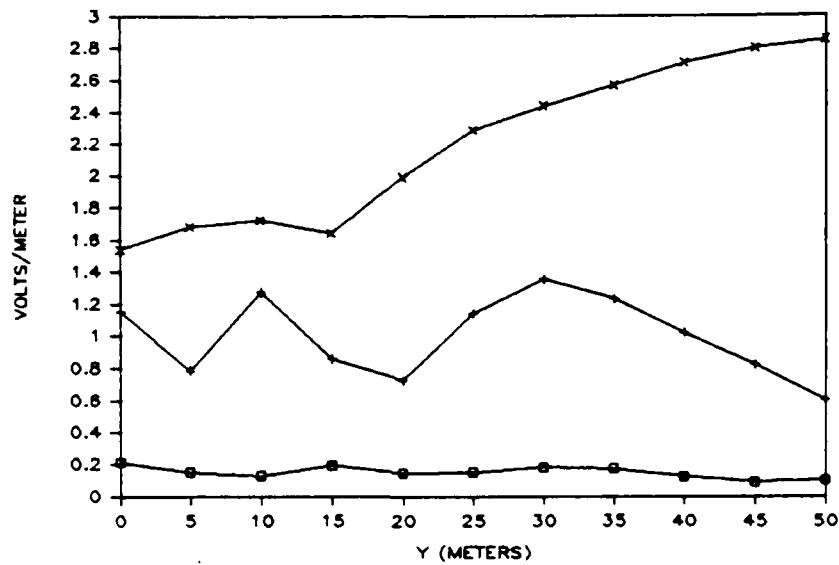


B. Phase

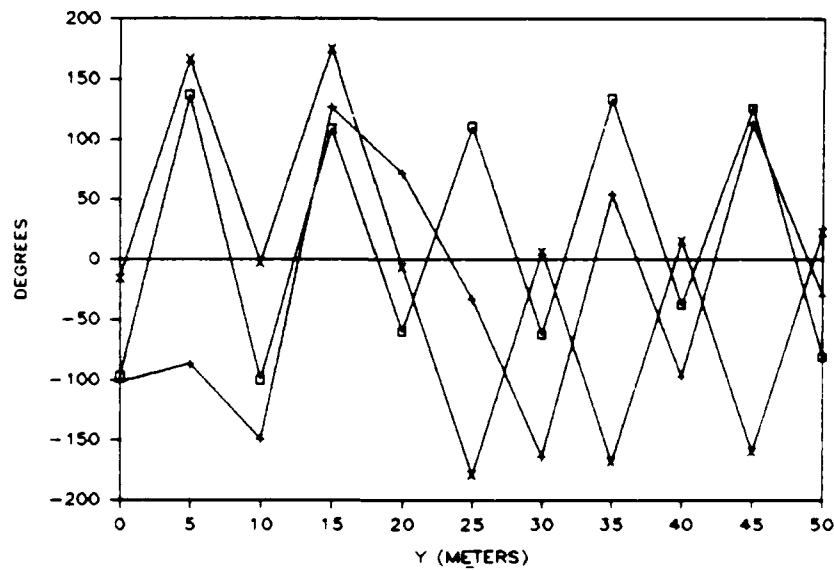
$\square E_x$ $+ E_y$ $\times E_z$

Figure 3-11

Common Mode Electric Field Magnitude and Phase For 12 MHz in Longitudinal Direction at $X=0$ m, $Z=4$ m.



A. Magnitude

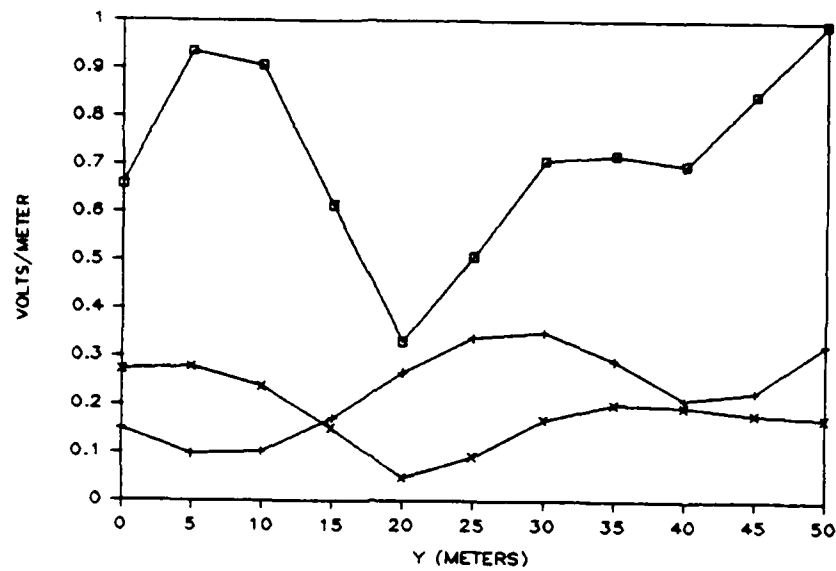


B. Phase

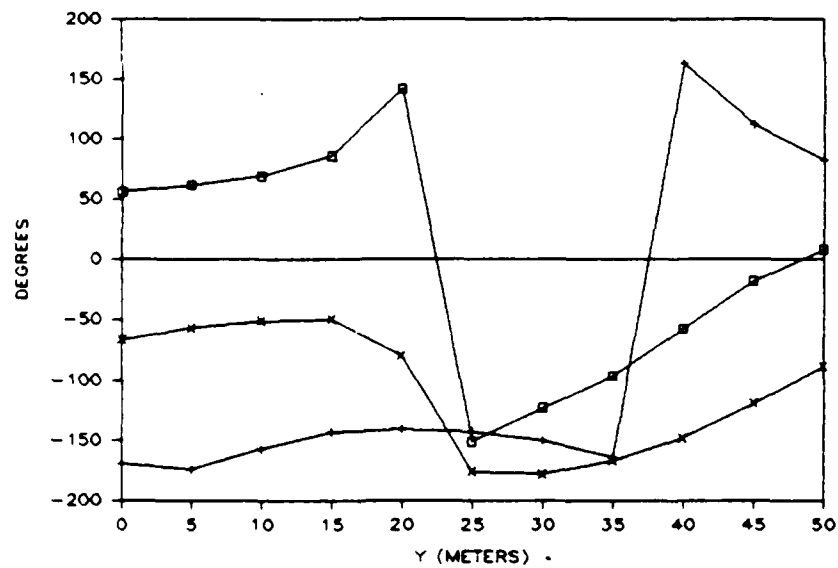
\square E_x \times E_y \circ E_z

Figure 3-12

Common Mode Electric Field Magnitude and Phase For 30 MHz in Longitudinal Direction at $X=0$ m, $Z=4$ m.



A. Magnitude

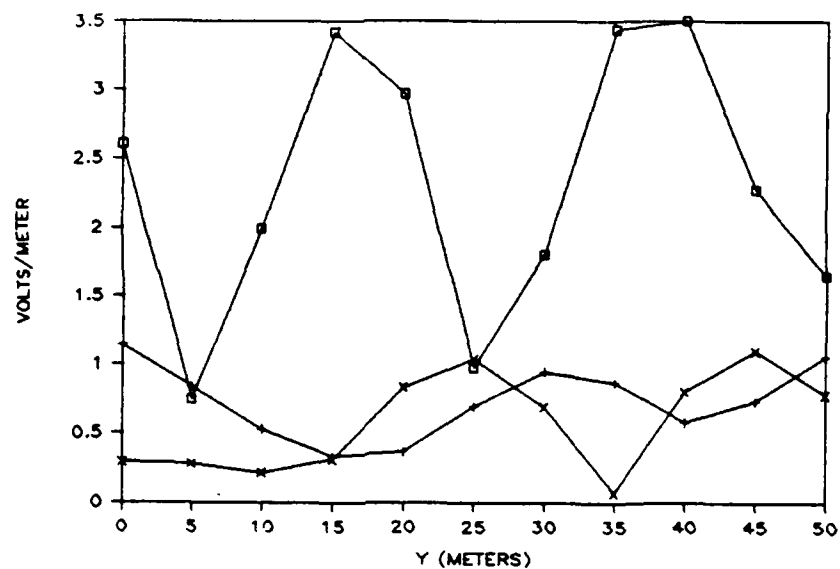


B. Phase

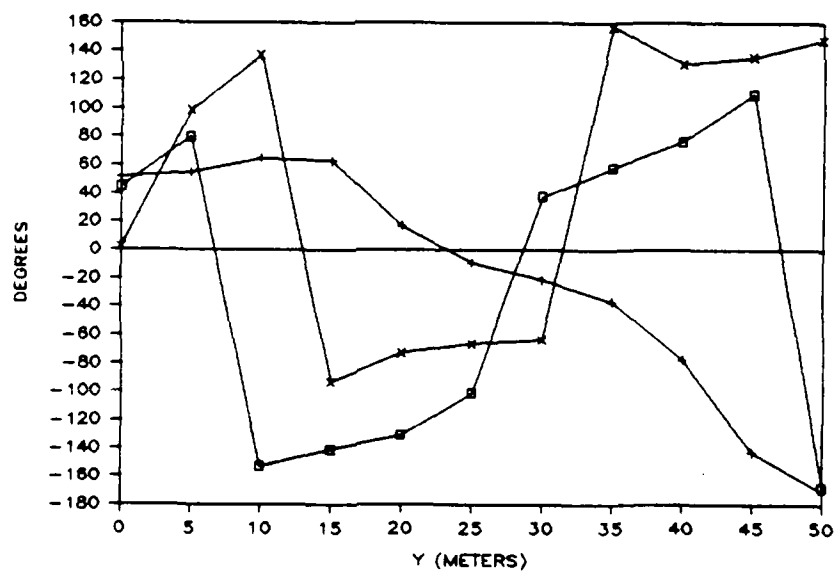
$\square E_x$ $+ E_y$ $\times E_z$

Figure 3-13

Differential Mode Electric Field Magnitude and Phase For
6 MHz in Longitudinal Direction at $X=0$ m, $Z=4$ m.



A. Magnitude

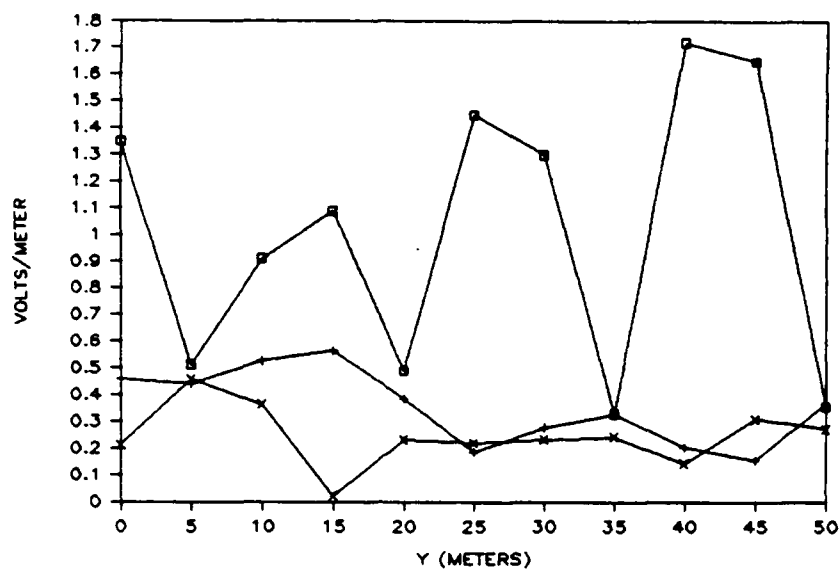


B. Phase

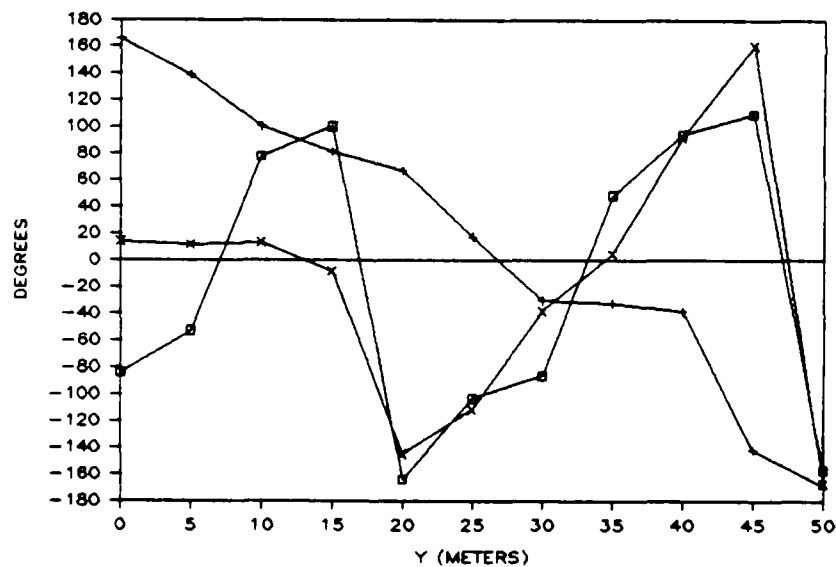
□ E_x + E_y × E_z

Figure 3-14

Differential Mode Electric Field Magnitude and Phase For
8 MHz in Longitudinal Direction at $X=0$ m, $Z=4$ m.



A. Magnitude

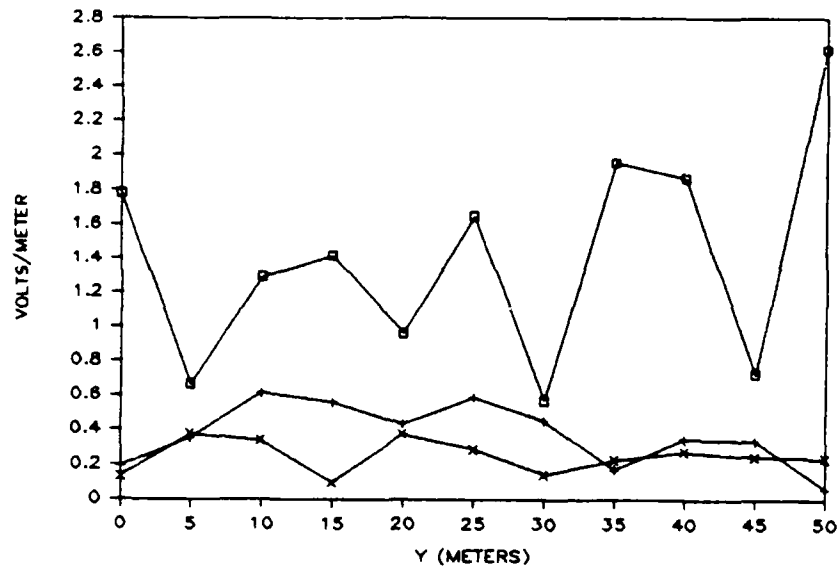


B. Phase

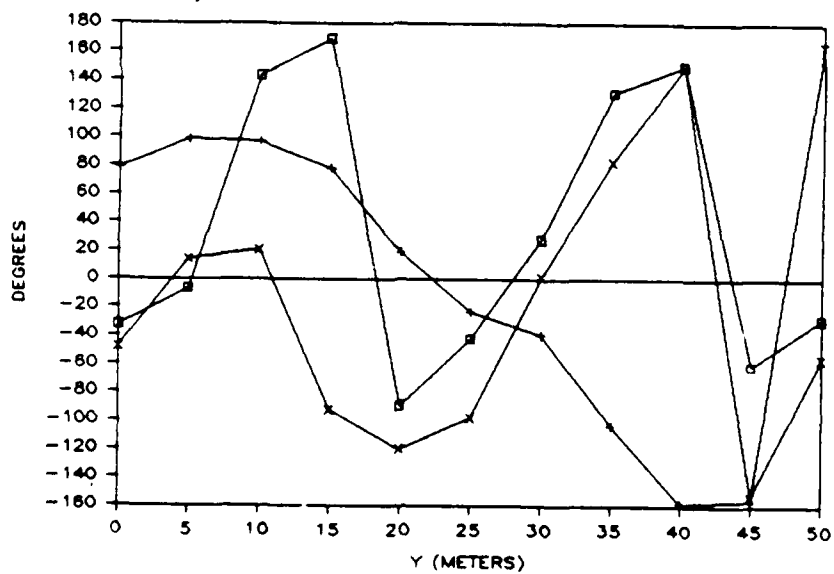
$\square E_x$ $+ E_y$ $\times E_z$

Figure 3-15

Differential Mode Electric Field Magnitude and Phase For
10.71 MHz in Longitudinal Direction at $X=0$ m, $Z=4$ m.



A. Magnitude

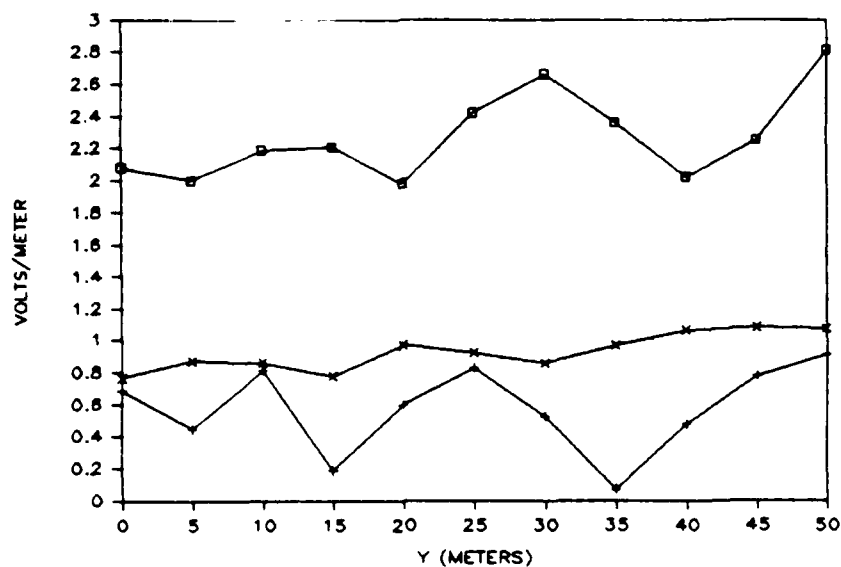


B. Phase

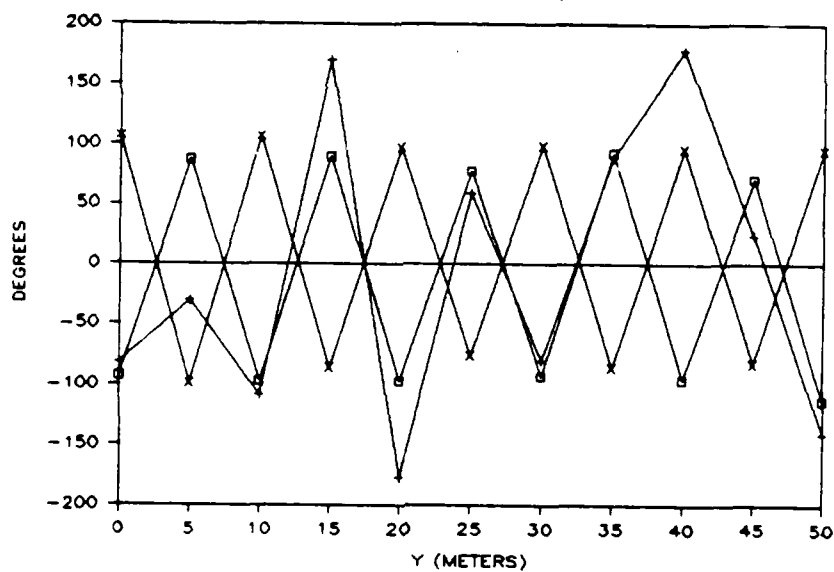
\square E_x $+$ E_y \cdot E_z

Figure 3-16

Differential Mode Electric Field Magnitude and Phase For
12 MHz in Longitudinal Direction at $X=0$ m, $Z=4$ m.



A. Magnitude



B. Phase

$\square E_x$ $+ E_y$ $\times E_z$

Figure 3-17

Differential Mode Electric Field Magnitude and Phase For
30 MHz in Longitudinal Direction at $X=0$ m, $Z=4$ m.

IV. Illuminator Environment

4.1. General

The analysis of the HSI was accomplished with a homogeneous planar surface in Chapter 3. As previously discussed, the HSI does not have a homogeneous planar surface, but has three distinct regions shown in Figure 4-1. These regions are a conducting ground plane, a circular concrete pad, and soil. This chapter analyzes the planar surface by determining the reflection and transmission coefficients from each surface. By obtaining this information, it is possible to determine the effects of the planar surface within the structure. In addition to the surface calculations, MOM solutions to the scattering of EM waves from an EC-135 sized test object are provided.

4.2. Surface Interactions

The effects of the surface on the field distributions can be analyzed by the method of images for all frequencies. Even though the entire surface is not a perfectly conducting ground plane, the method of images is still valid when the different surface regions are taken into account. However, the magnitude of the reflected wave will be reduced according to the reflection coefficient of the surface. How the regions affect the direction of propagation is unknown; however, since the concrete pad is considered a good conductor at the frequencies listed in this report, then no significant change in the direction of propagation should be apparent. An assessment of the scattering due to the regional interfaces is estimated.

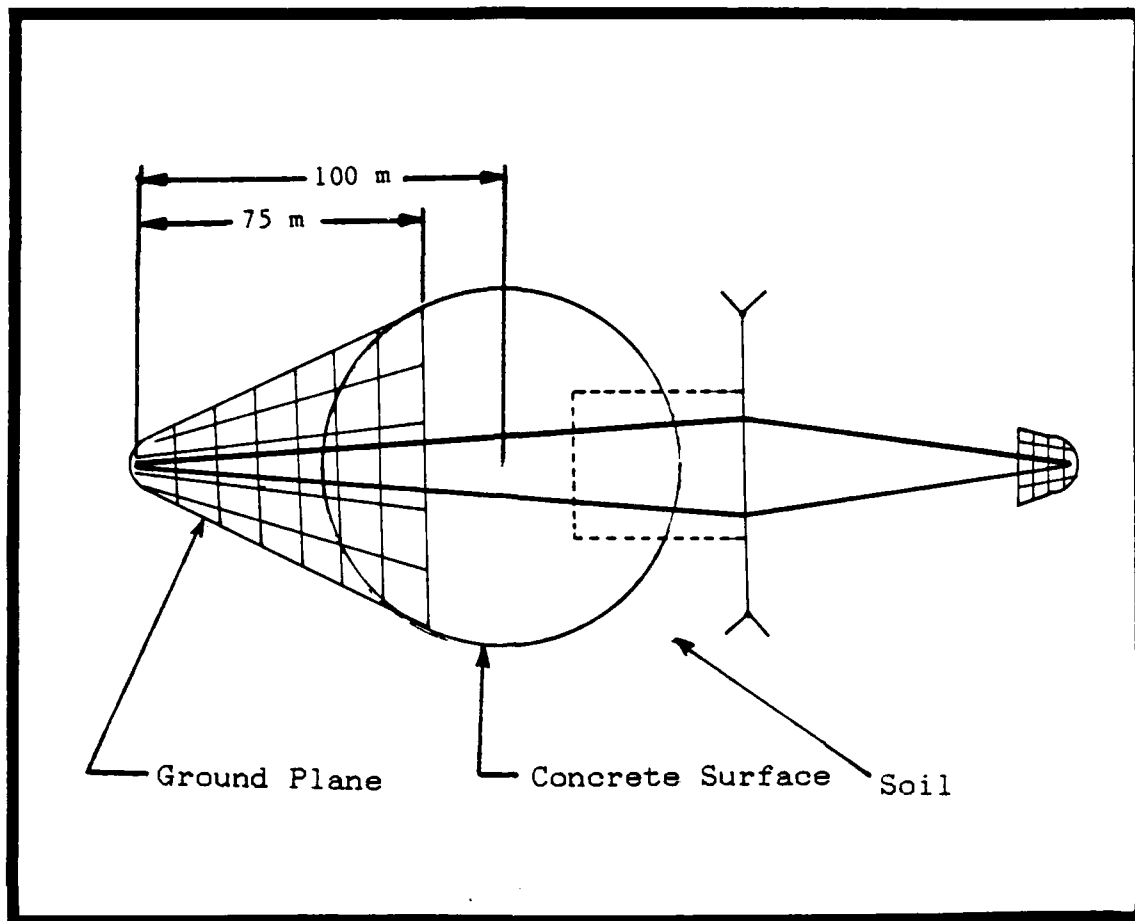


Figure 4-1

Ground Plane Regions for the HSI

4.2.1 Region 1: Ground Plane

The conducting ground plane of the HSI extends from the vertex of the wires in the input section to 75 m. The ground plane is an existing structure used with the VPD-I simulator. It is essentially a wire mesh configured as shown in Figure 4-1. Since the mesh size is less than the wavelengths used in the HSI, it is considered to be a good conductor. For simplicity in analysis it will be assumed that the ground plane could be considered a perfect conductor. This simplifying

assumption is reasonable since any losses associated with a conductor can be considered negligible. Given this assumption, it was possible to approximate the magnitude of the reflection coefficients for normal and parallel polarization (R_n) as 1 (3:338,341) for all angles of incidence.

4.2.2. Region 2: Concrete Surface

The concrete surface is a circular pad with its center located 100 m from the vertex of the input section. As seen in Figure 4-1, the pad terminates prior to the wire bends. It was mentioned previously that the concrete surface exhibits properties similar to a good conductor. To prove this, it was necessary to obtain both the relative permittivity and the conductivity of concrete. Both of these quantities are given by the following two equations (18)

$$\sigma = 10 \exp(-8.5000018 + 3.33333419 f' - 0.60000013 f'^2 + 0.03666667 f'^3) \text{ mhos/m} \quad (4-1)$$

$$\epsilon_r = 10 \exp(10.54500178 - 3.36083418 f' + 0.42500013 f'^2 - 0.01916667 f'^3) \quad (4-2)$$

where $f' = \log_{10}(\text{freq})$. Although it was not specifically mentioned in the reference, it appears as if these equations were obtained by empirical methods. The solution of these equations leads to Table 4-1. As shown in Table 4-1, the concrete pad is can be considered a good conductor since $\sigma/\omega\epsilon \gg 1$. Using the values of conductivity and relative permittivity, it was possible to obtain the reflection coefficients in a manner similar to the method used in Chapter 2. The calculations for the concrete surface were performed using a thickness

of 0.5 m. As the thickness increased the electrical properties of the surface approached the properties of a perfect conductor. The construction of the concrete surface is unknown; however, if steel reinforcements were used, the conductivity of the pad would increase and the pad would more closely approximate a perfect conductor. Testing of the ground plane should be able to reveal the electrical properties. Using soil with a constant dielectric constant and conductivity as the material beneath the concrete, the reflection coefficient magnitudes in Table 4-2 are provided. It should be noted that the reflection coefficient is almost unity, for most angles. As shown in the table, the reflection coefficient for a parallel polarized wave was reduced as the angle was increased. Although not shown, the reflection coefficient was unity at grazing incidence.

4.2.3. Region 3: Soil

The parameters for soil were relatively simple to evaluate. Its relative permittivity and conductivity was constant over the frequency range of interest. By assuming that the soil was sandy and dry, the relative permittivity could be approximated as 2.8, and its conductivity as 10^{-5} mhos/m (6:508-509). Using the same techniques generated in Chapter 2, it was easy to determine the reflection coefficients shown in Table 4-3.

4.2.4. Regional Interfaces.

It was difficult to determine exact edge diffractions of the interfaces without a computer code that permitted an interface of two different materials. In addition, due to the physical configuration of the HSI, it was assumed that the diffraction due to the regional interface could be considered negligible

Table 4-1

Dielectric Constants and Conductivities of Concrete

FREQ (MHz)	Relative Permittivity	Conductivity (mhos/m)	$\sigma/\omega\epsilon$ (mho s/farad)
6	37.50814	1.282510	102.4851
8	36.41361	1.326857	81.91194
10.71 (resonance)	35.60856	1.366952	65.53617
12	34.97515	1.403922	60.15600
20	33.29367	1.531614	41.36515
30	32.03035	1.664517	31.15173
50	30.49113	1.885438	22.24055
100	28.43403	2.322359	14.68817
250	25.66170	3.310085	9.278775

Table 4-2

Reflection Coefficient Magnitudes for Concrete

Angle	Frequency					
	30 MHz		50 MHz		250 MHz	
	Parallel	Normal	Parallel	Normal	Parallel	Normal
0	0.956	0.956	0.946	0.946	0.908	0.908
15	0.954	0.957	0.944	0.948	0.905	0.911
30	0.949	0.961	0.938	0.953	0.895	0.920
45	0.938	0.968	0.925	0.962	0.873	0.934
60	0.913	0.981	0.895	0.973	0.826	0.953
75	0.840	0.988	0.808	0.986	0.694	0.975
85	0.607	0.996	0.552	0.995	0.409	0.992

Table 4-3
Reflection Coefficient Magnitudes for Soil

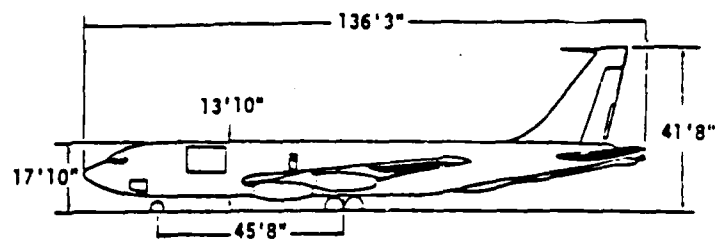
Angle	Frequency					
	30 MHz		50 MHz		250 MHz	
	Parallel	Normal	Parallel	Normal	Parallel	Normal
0	0.252	0.252	0.252	0.252	0.254	0.252
15	0.241	0.262	0.241	0.262	0.242	0.262
30	0.206	0.297	0.206	0.297	0.202	0.297
45	0.133	0.365	0.133	0.364	0.126	0.364
60	0.011	0.482	0.011	0.482	0.016	0.482
75	0.307	0.681	0.307	0.681	0.308	0.681
85	0.693	0.878	0.693	0.878	0.693	0.878

compared to the reflected waves. This assumption was valid since both regions 1 and 2 are considered to be good conductors, and the interface between region 2 and 3 was behind the test object. For these reasons, the interface diffractions were ignored, and only the reflections from the surfaces were determined.

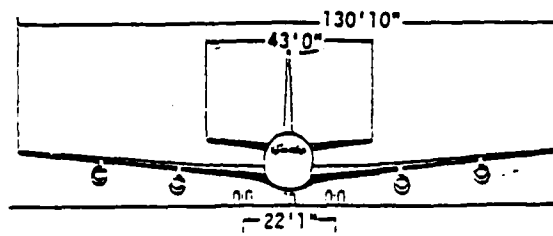
4.3. Wire Model of the Test Object

The test object used to characterize the reflections between the test object and the ground plane was an EC-135 sized aircraft (see Figure 4-2). For the purposes of this project, the aircraft was modelled as four wires with finite thicknesses as shown in Figure 4-3. Wire models have been used extensively in EMP modelling (13). These models are valid for long wavelengths since the scattering of

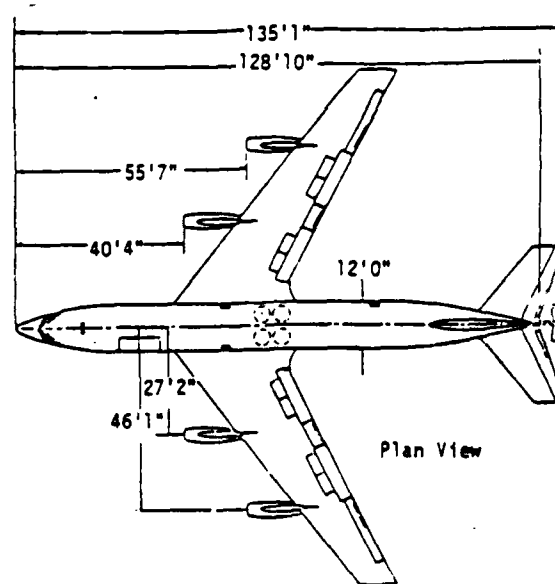
discontinuities on the test object are negligible at wavelengths longer than the dimensions of the test object. By using this model the planar surfaces could be replaced with wires. The equivalent radius for the wire replacing the planar surfaces was obtained by using the equation $a_e = 0.25 \times W$, where W is the width of the wing (1:338). By assuming the width was approximately 7 m, the equivalent wire radius was 1.75 m. This technique was not used for the 30 MHz calculations. The GEMACS operating manual suggests the use of wire diameters of $.025\lambda$. For this reason, the wire diameters for the 30 MHz model were 0.25 m thick. The wire models are more accurate for the wavelengths that are longer than the dimensions of the model. For these wavelengths, the scattering from the discontinuities on the model are in the Rayleigh region where the scattering cross-section is proportional to λ^{-4} . As the wavelength decreases to where it has a length less than or equal to the size of the discontinuity, the scattering from the discontinuity becomes more predominant and a more accurate model must be utilized. To accurately describe the test object, it would have been better to use wire segments for the outline of the test object at low frequencies, and a Geometrical Theory of Diffraction (GTD) model at high frequencies. Attempts to obtain a GTD model using GEMACS resulted in a floating point divide error in the code. No further attempts were made to resolve this error. Testing with simplified objects such as planes, and cylinders, resulted in similar errors. Discussions with Dr. Edgar Coffey formerly of BDM Corporation, indicated that the code being used was indeed configured correctly (4). This error indicated that it was not possible to obtain electric field data between the test object and the surface using a GTD configuration. Since it was desired that a qualitative analysis of the



Side View



Front View



Plan View

Figure 4-2

EC-135 Diagram. (15:2)

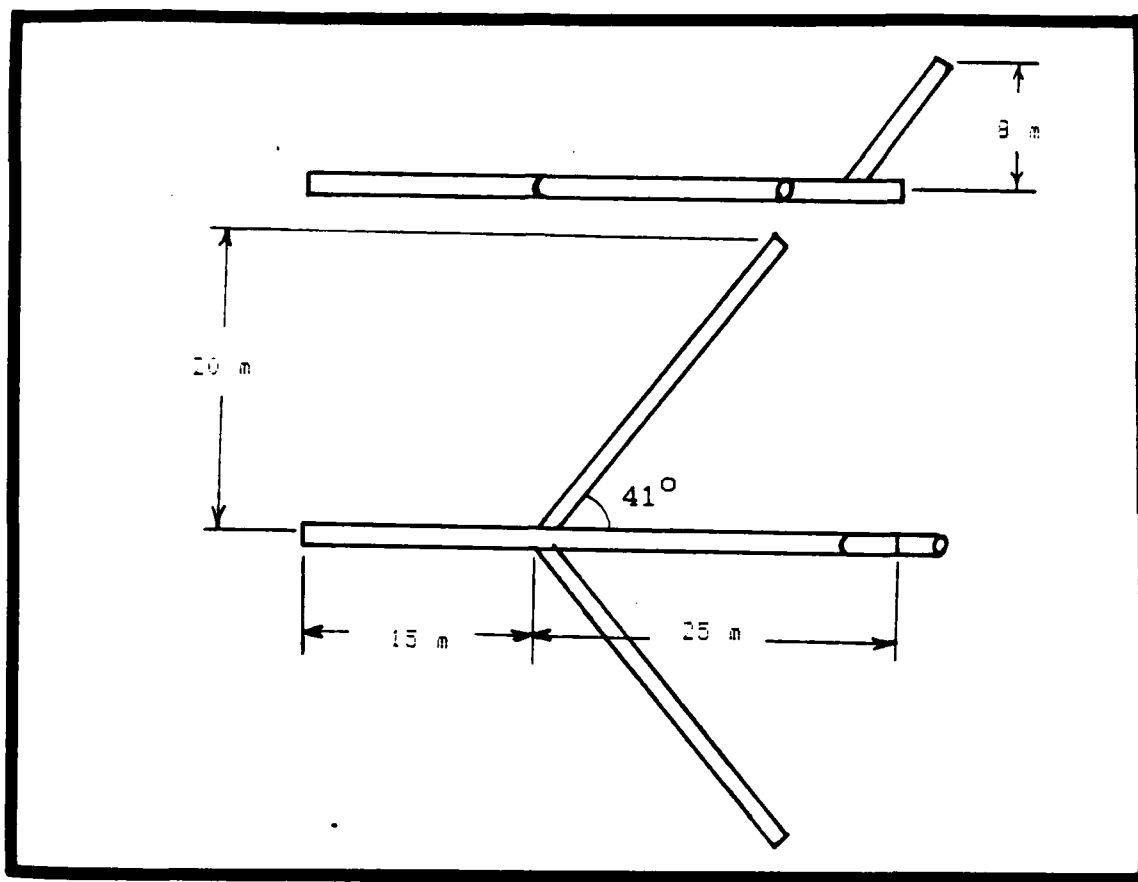
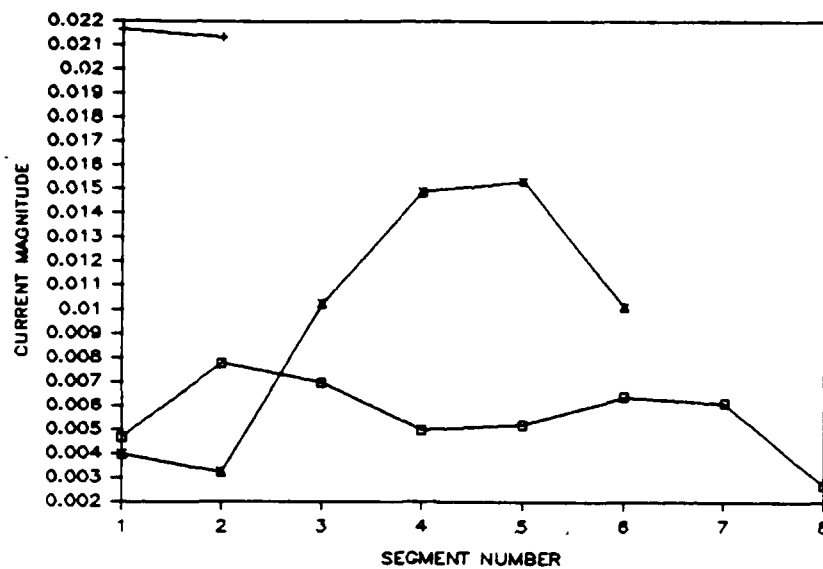


Figure 4-3

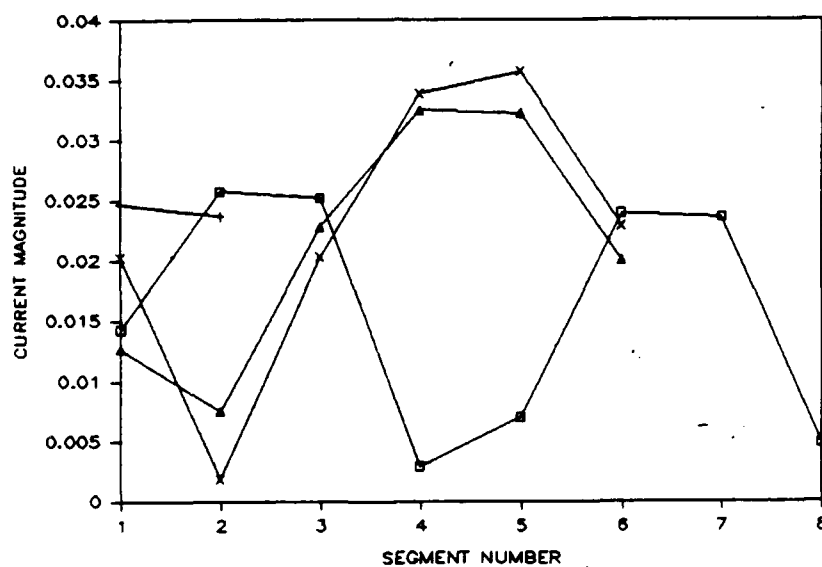
Wire Model Approximation For Test Object

electric fields between the test object and the surface be obtained, it was felt that the simple wire model would provide adequate results. Since the diameter of the wires were, in general, considered "thick", it was possible to solve the currents on the wires and the fields by a MOM technique. Once again, the GEMACS program was used. By using the program, the currents on the wires for both a wire model in free space and with a concrete ground plane were solved. By comparing the results, it was possible to determine the effects of a concrete surface on the current distribution recorded on a test object. The calculated current

data are provided in Figures 4-4 through 4-11. The current distribution on the wires at 30 MHz was not obtained since it was felt that the wire model did not adequately describe the test object at that frequency. Figures 4-4 through 4-11 display the currents on each segment of the test object as defined by the MOM routine. This data was taken with an angle of incidence of 85 degrees measured with respect to the surface normal, and along the length of the fuselage. The preliminary data showed that the current distribution was approximately the same when the angle of incidence was increased to 90 degrees. As shown in the figures, the current is sinusoidal along the wires for all configurations. It should also be noted that the expected symmetry of the current along the wings is disturbed when the effects of a concrete ground plane are considered. The effects of the ground plane on the model current were determined by finding the difference between the current on the model with and without a concrete ground plane. In general, it can be seen by comparing the graphs in each figure that the ground plane has a smaller effect on the vertical stabilizer than on the other surfaces. This was expected. The ground plane generally increases the magnitudes of the currents on the test object. The overall shapes of the curves are similar; however, the differences in the minimums and maximums are more emphasized with the ground plane. In addition, the figures indicate that the current densities become less affected by the ground plane at the higher frequencies. The electric field was determined from these wire currents by GEMACS. The field data were collected at 3.0 m below the test object. Once again, it was possible to determine the effects of the ground plane on the electric field by comparing the results of the electric field calculations



A. No Ground Plane

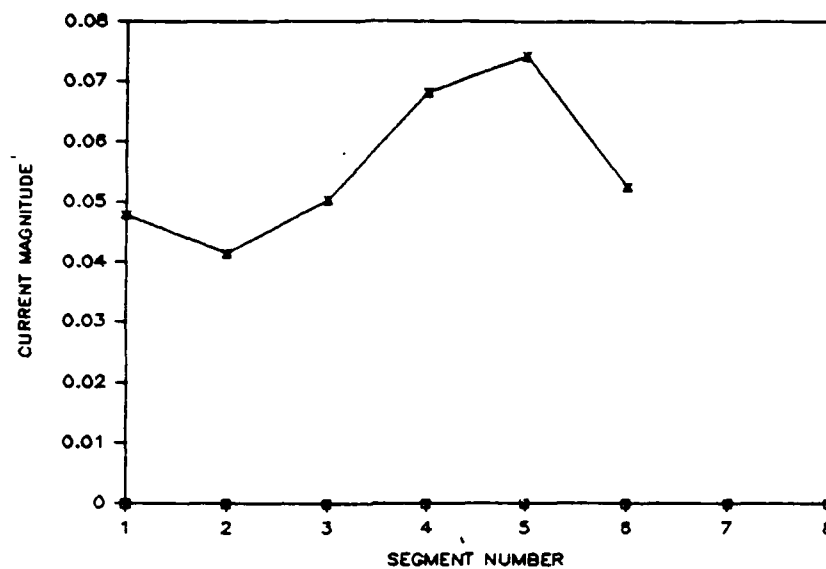


B. Concrete Ground Plane

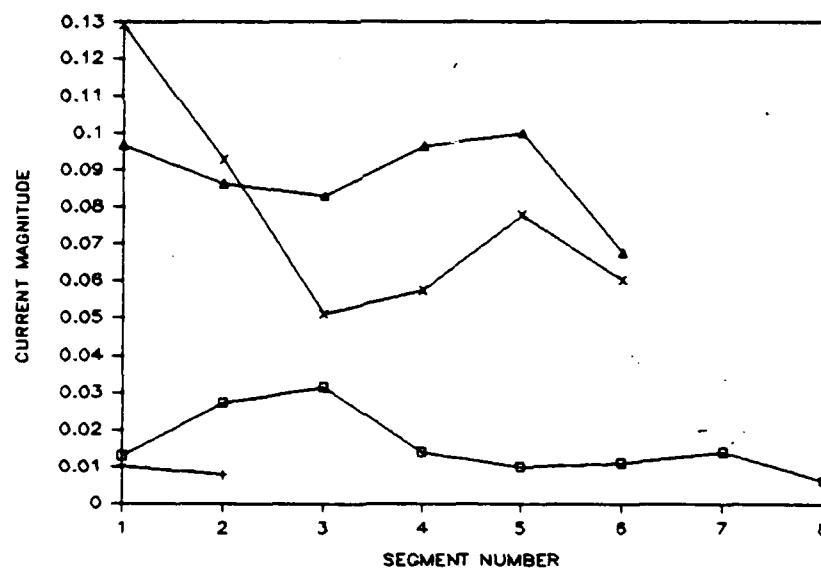
□ Fuselage + Vertical Stabilizer
 x Left Wing Δ Right Wing

Figure 4-4

Current Distribution on Wire Model Radiated by
 Vertically Polarized Plane Wave at 6 MHz.



A. No Ground Plane

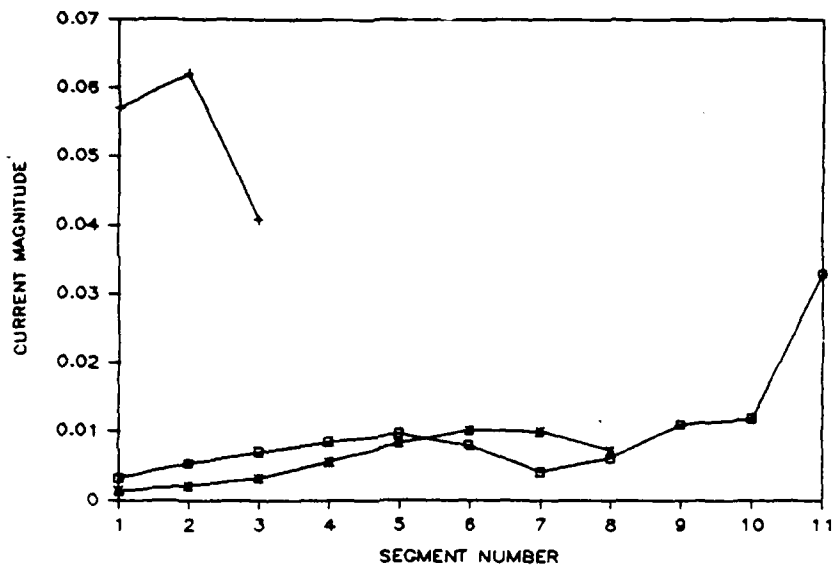


B. Concrete Ground Plane

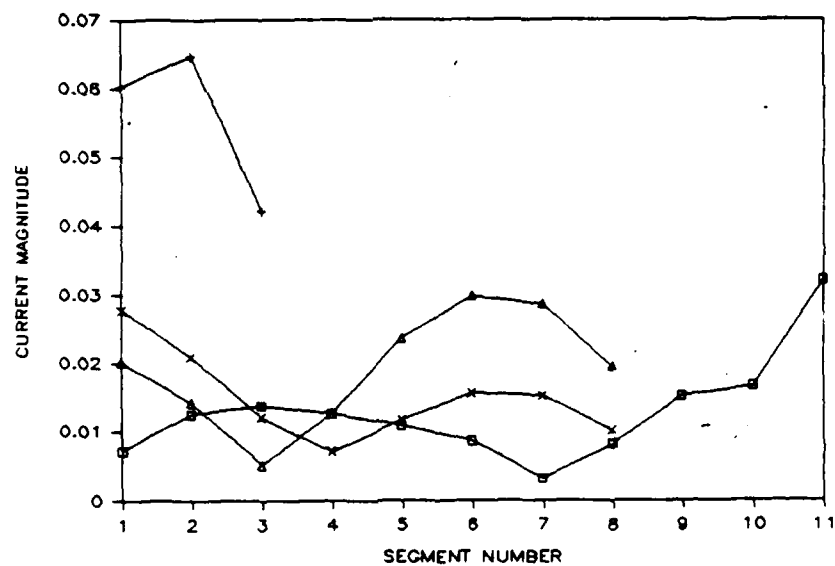
□ Fuselage + Vertical Stabilizer
 × Left Wing △ Right Wing

Figure 4-5

Current Distribution on Wire Model Radiated by Horizontally Polarized Plane Wave at 6 MHz.



A. No Ground Plane

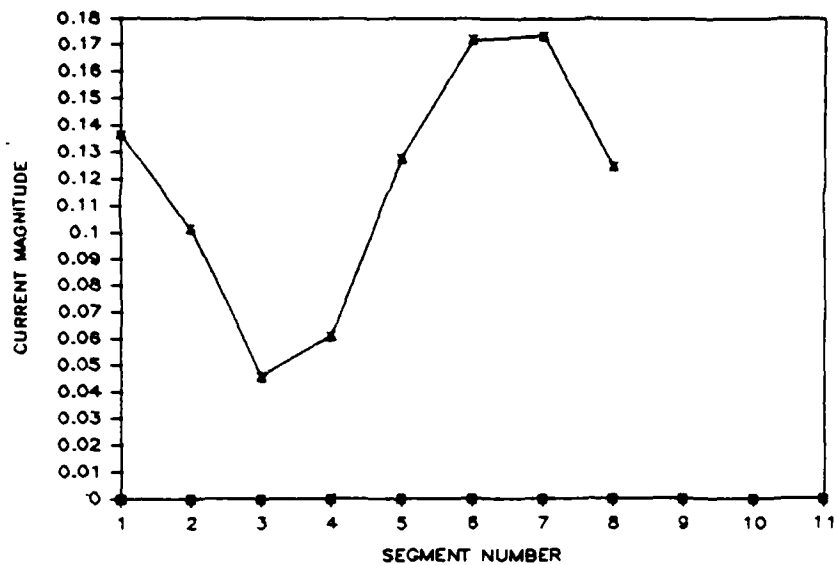


B. Concrete Ground Plane

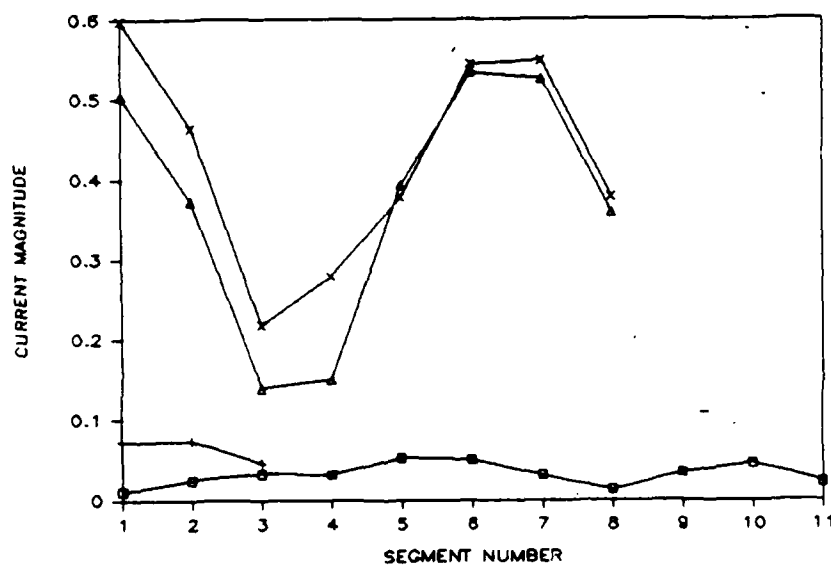
□ Fuselage ◇ Vertical Stabilizer
 × Left Wing △ Right Wing

Figure 4-6

Current Distribution on Wire Model Radiated by
 Vertically Polarized Plane Wave at 8 MHz.



A. No Ground Plane

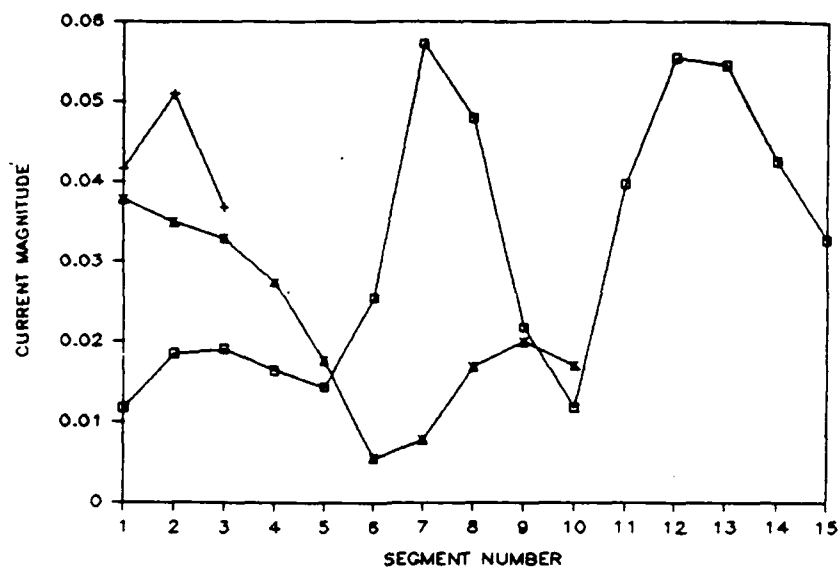


B. Concrete Ground Plane

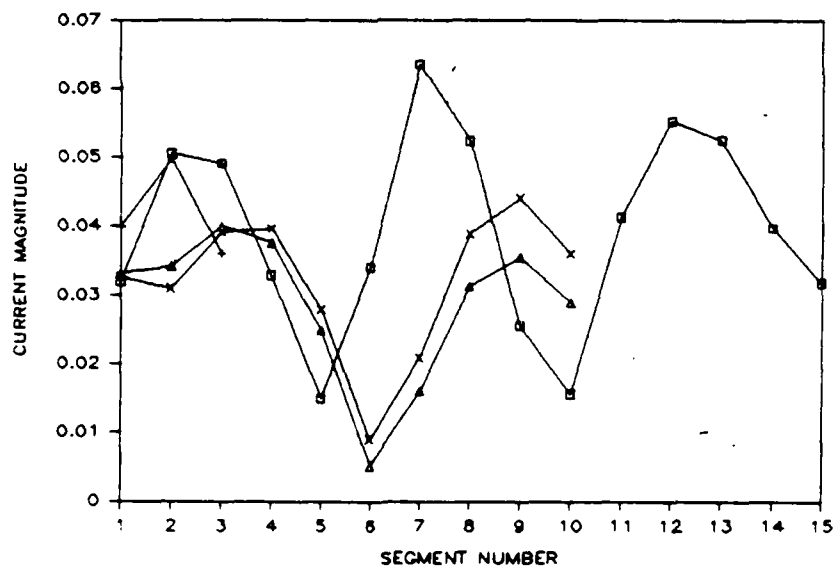
□ Fuselage + Vertical Stabilizer
 ✓ Left Wing △ Right Wing

Figure 4-7

Current Distribution on Wire Model Radiated by
 Horizontally Polarized Plane Wave at 8 MHz.



A. No Ground Plane

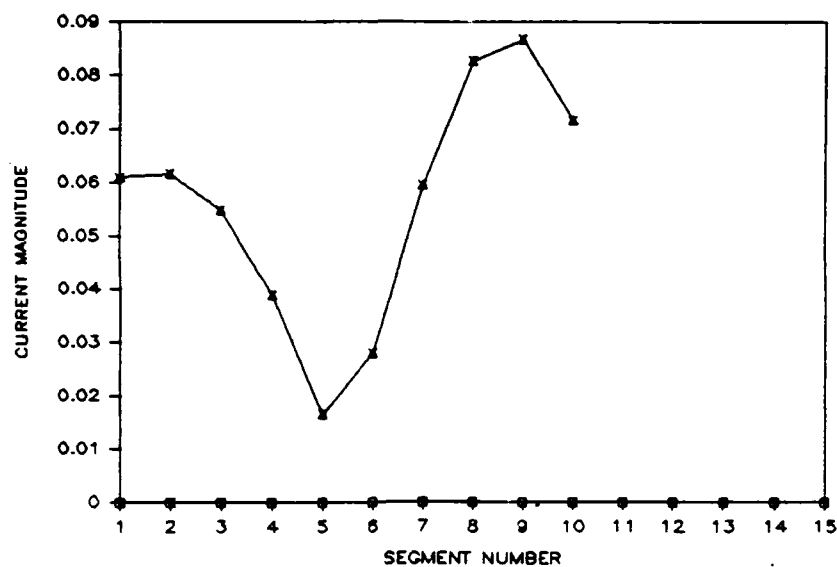


B. Concrete Ground Plane

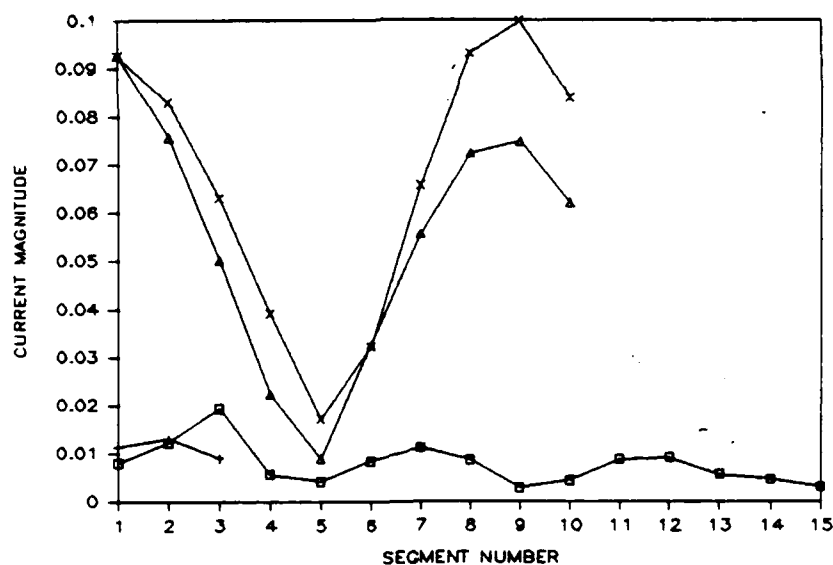
□ Fuselage + Vertical Stabilizer
 ◇ Left Wing △ Right Wing

Figure 4-8

Current Distribution on Wire Model Radiated by Vertically Polarized Plane Wave at 10.71 MHz.



A. No Ground Plane

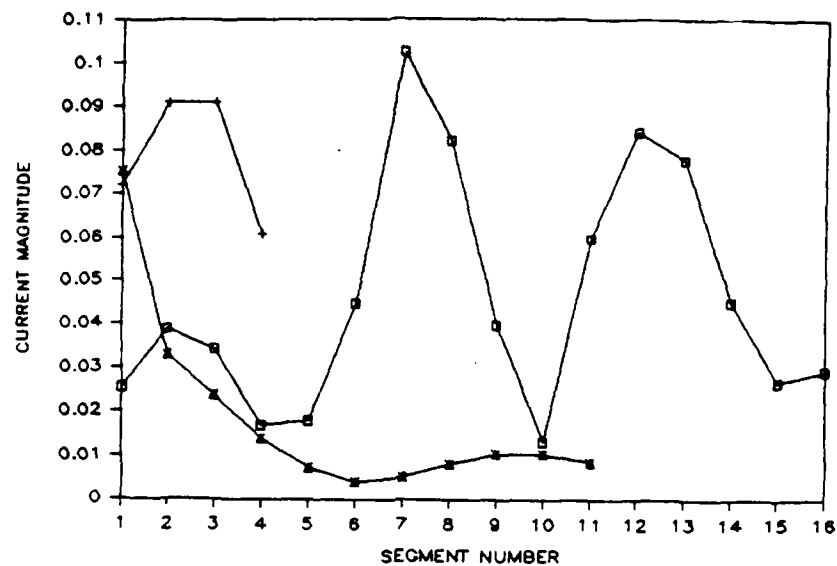


B. Concrete Ground Plane

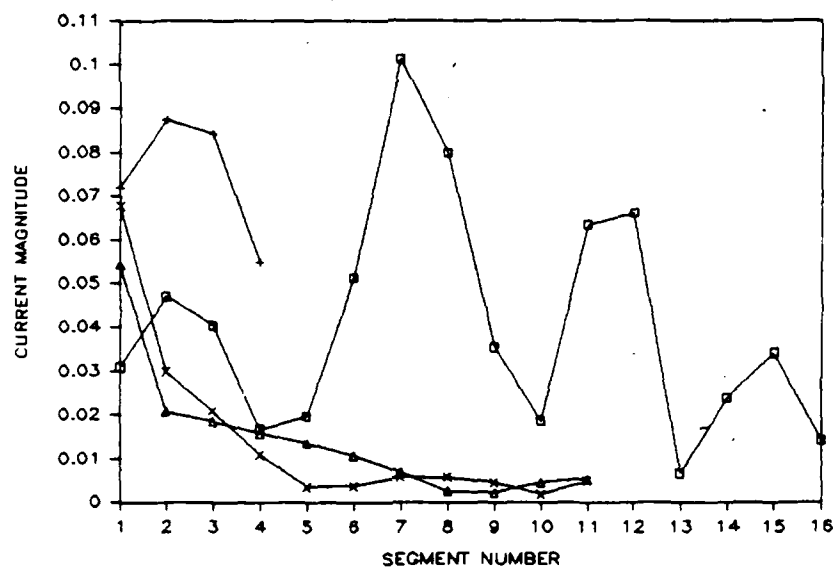
□ Fuselage + Vertical Stabilizer
 ○ Left Wing △ Right Wing

Figure 4-9

Current Distribution on Wire Model Radiated by Horizontally Polarized Plane Wave at 10.71 MHz.



A. No Ground Plane

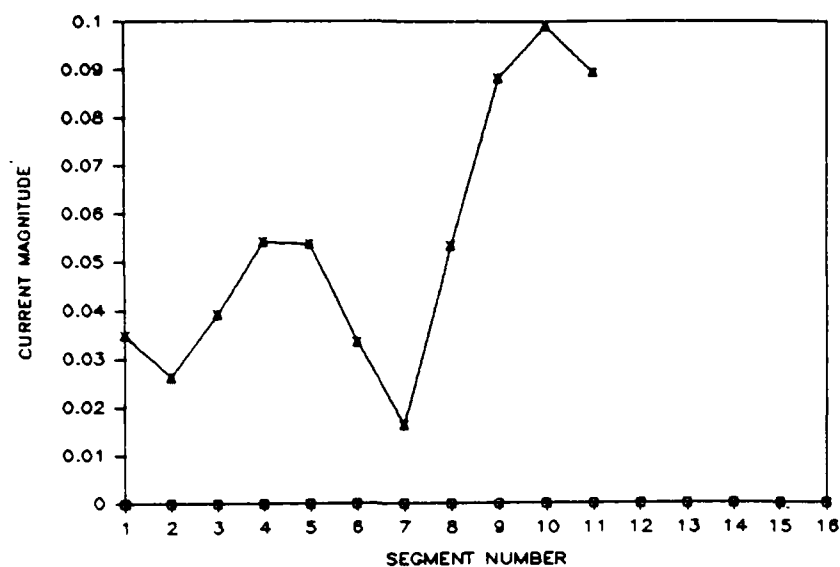


B. Concrete Ground Plane

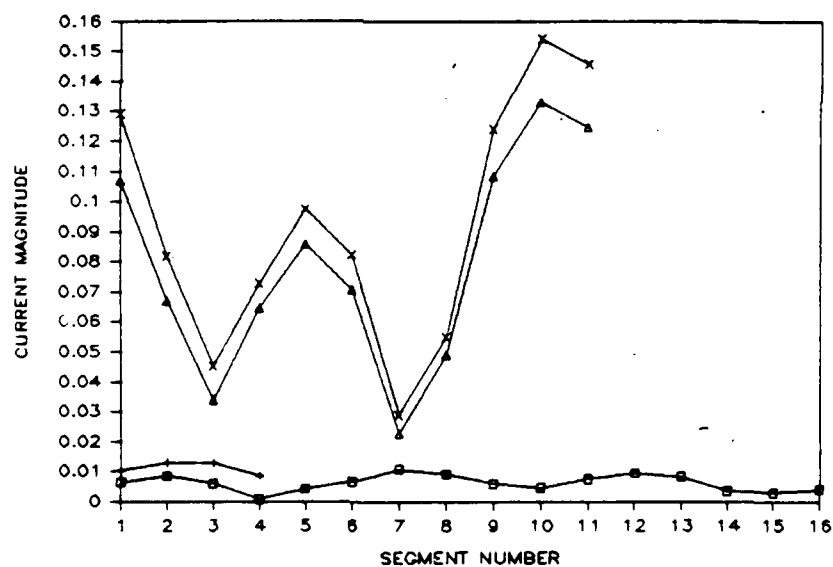
□ Fuselage + Vertical Stabilizer
 • Left Wing △ Right Wing

Figure 4-10

Current Distribution on Wire Model Radiated by
 Vertically Polarized Plane Wave at 12 MHz.



A. No Ground Plane



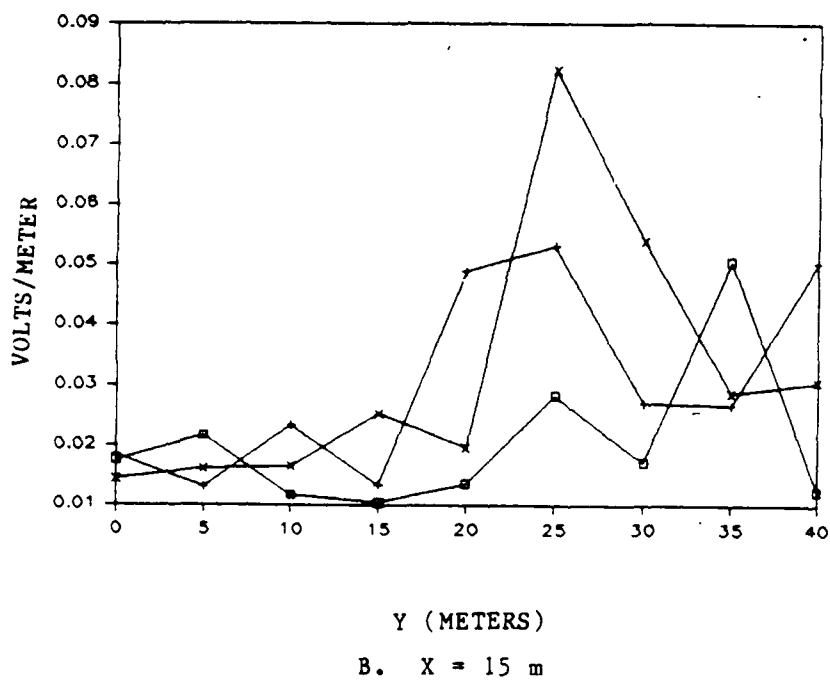
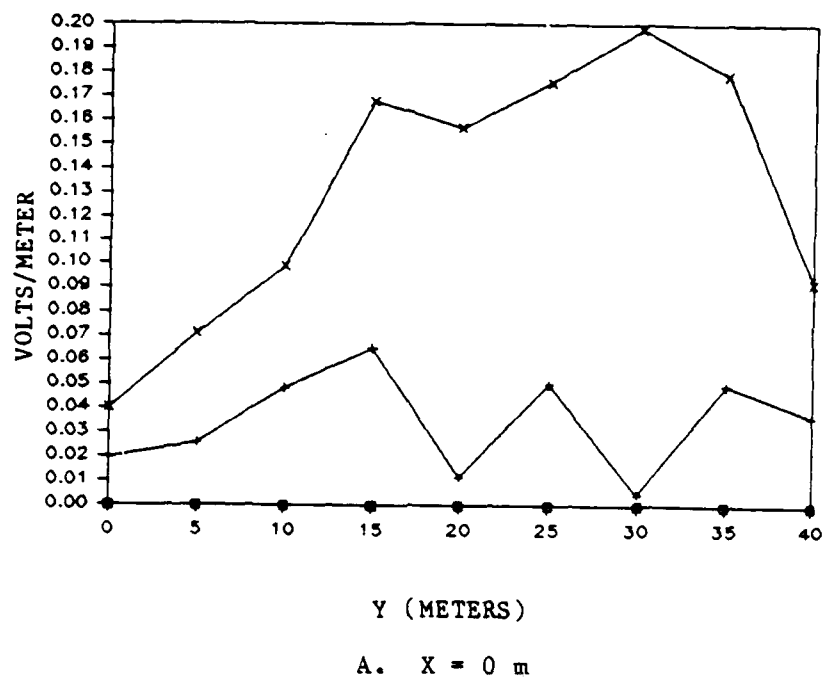
B. Concrete Ground Plane

□ Fuselage + Vertical Stabilizer
 ✓ Left Wing △ Right Wing

Figure 4-11

Current Distribution on Wire Model Radiated by Horizontally Polarized Plane Wave at 12 MHz.

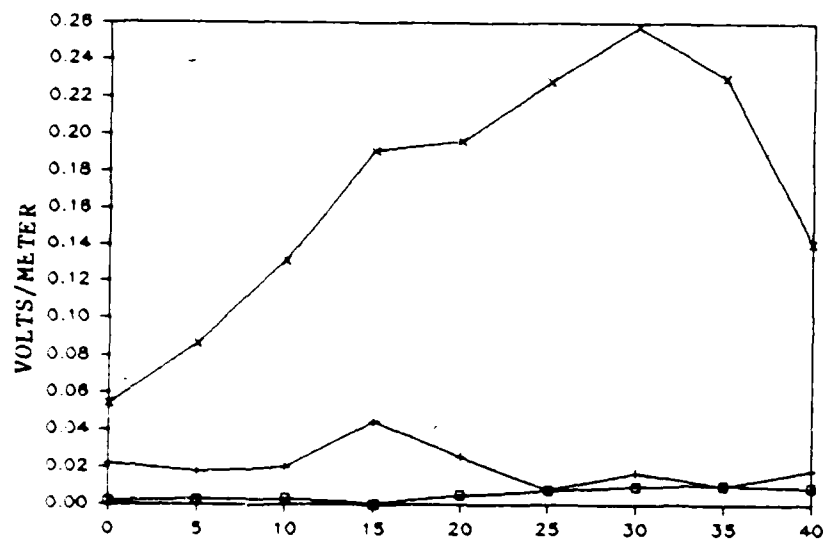
between the surface of the ground plane and the target. The electric field data included in this report are at frequencies of 6.0 MHz, 12.0 MHz, and 30 MHz. Although each frequency has field components that are not the same as the others, the general conclusions about the field data are the same. The plots for the field data taken at 30 MHz are provided for horizontal values of 0 and 15 m in Figures 4-12 through 4-15. The other data is provided in Appendix C. In general, these plots showed that the vertical component of the wave is emphasized along the structure of the wing. This feature is apparent for both the data taken with the concrete ground plane, and without the concrete ground plane. Another feature that should be emphasized, is that the horizontal and longitudinal components are larger for the fields calculated without the ground plane. Although it is not readily apparent in the plots given in Figures 4-12 through 4-15, the horizontal component remains high then falls off gradually beyond the wing, for 30 MHz plots without a plane. This also seems true for the concrete ground plane data; however, the horizontal components fall off at a more rapid rate. The field between the fuselage and the ground plane is considerably different than the fields near the wings. For horizontal polarization, the vertical component of the field is emphasized at low frequencies, while the horizontal component is emphasized at high frequencies. This is a direct consequence of the ground plane since the field without a ground plane has only a horizontal component. For vertical polarization, the vertical component of the field is emphasized. In addition, a resonance occurs for frequencies close to 6 MHz and 12 MHz. This property may occur at the other frequencies used in the test; however, it cannot be determined due to the resolution of the data. It was possible to



$\square = E_x$ $+$ E_y $\times = E_z$

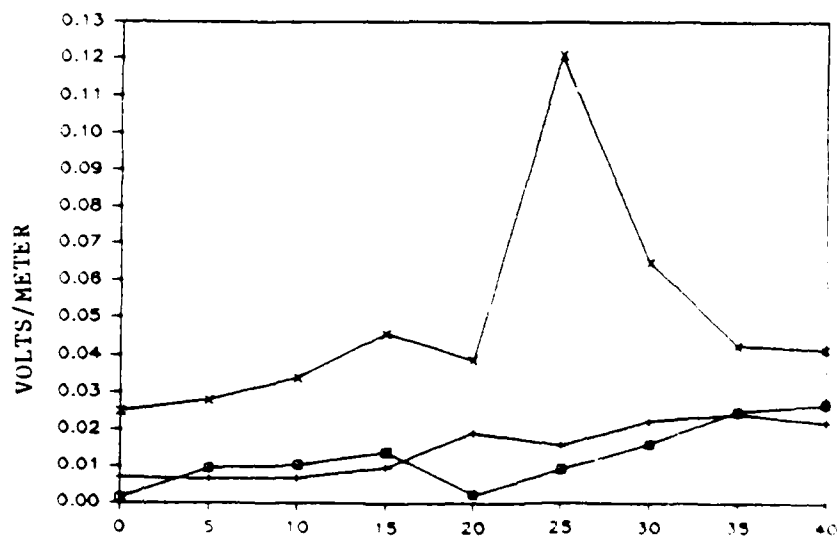
Figure 4-12

Electric Field Magnitude at 3 Meters Below the Test Object
for 30 MHz With No Ground Plane (Vertical Polarization)



Y (METERS)

A. $X = 0$ m.



Y (METERS)

B. $X = 10$ m.

E_x (Volts/Meter)

Figure 1

Electric Field Magnitude vs Y (Meters) for $MHz = 100$ and 1000

AD-A182 668

DETERMINATION AND REDUCTION OF UNWANTED ELECTROMAGNETIC

2/3

WAVE REFLECTIONS I (U) AIR FORCE INST OF TECH

WRIGHT-PATTERSON AFB OH SCHOOL OF ENGI

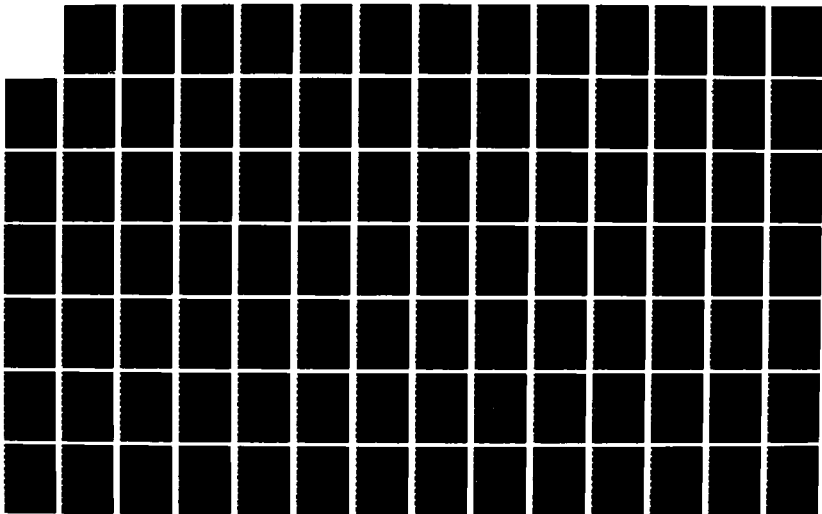
K A BRUNER

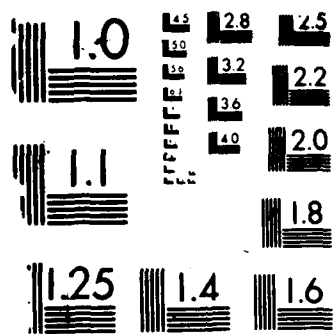
UNCLASSIFIED

MAR 87 AFIT/GE/ENG/87M-8

F/G 20/3

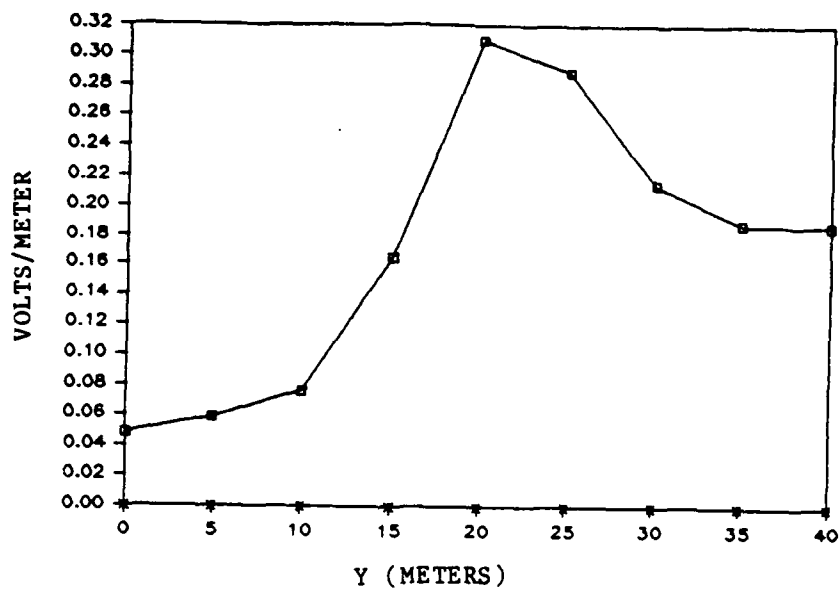
NL



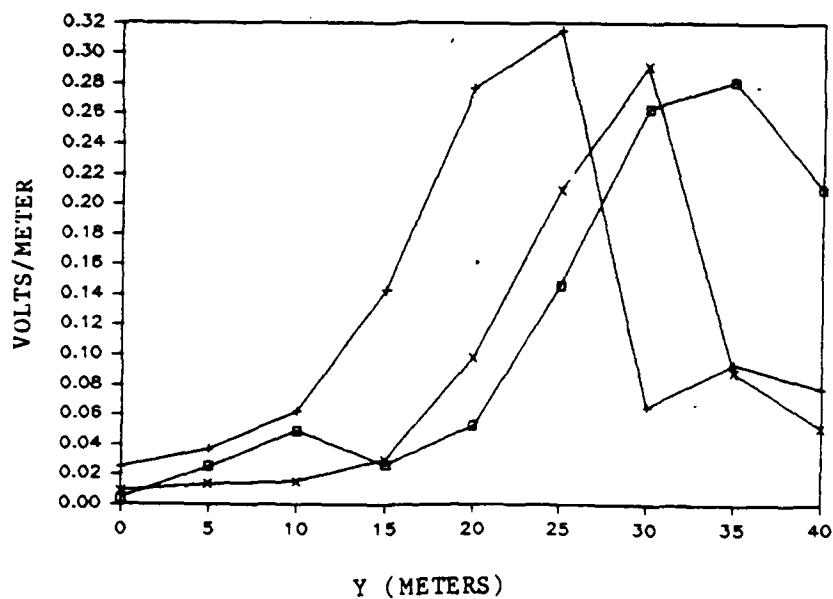


MICROCOPY RESOLUTION TEST CHART

ANSI AND ISO STANDARDS



A. $X = 0$ m.

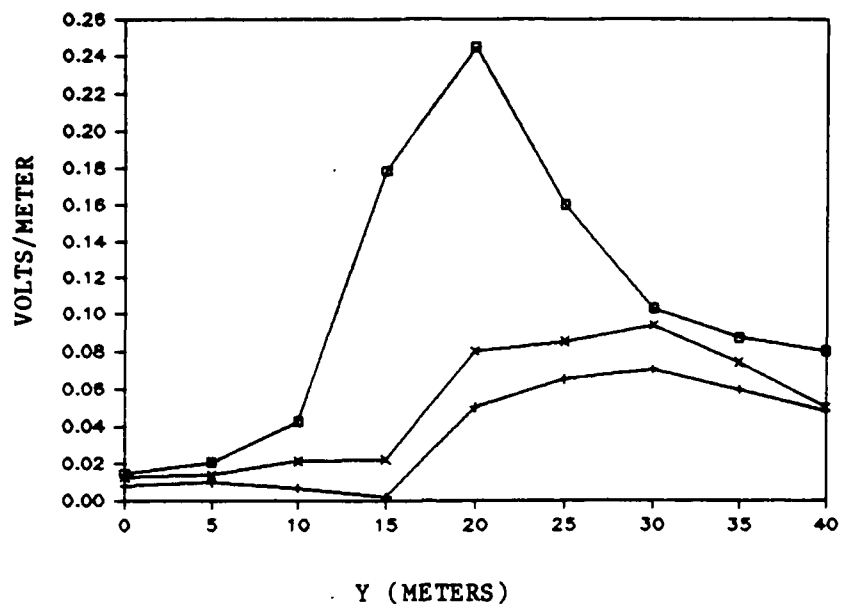


B. $X = 15$ m.

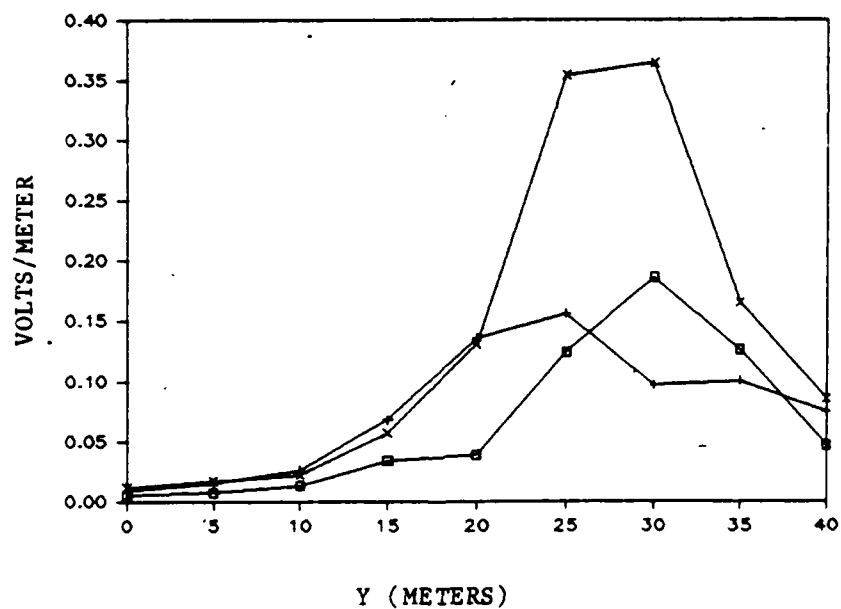
$\square E_x$ $\circ E_y$ $\times E_z$

Figure 4-14

Electric Field Magnitude at 3 Meters Below the Test Object
at 30 MHz With No Ground Plane. (Horizontal Polarization)



A. $X = 0$ m.



B. $X = 15$ m.

$\square E_x$ $+ E_y$ $\cdot E_z$

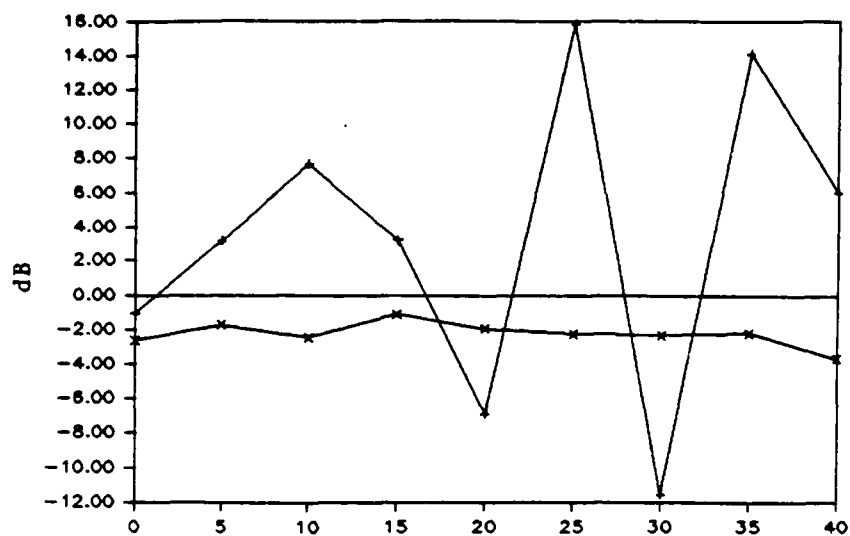
Figure 4-15

Electric Field Magnitude at 3 Meters Below the Test Object
for 30 MHz With Concrete Ground Plane. (Horizontal Polarization)

calculate the power differences between the fields with and without a ground plane. This calculation was accomplished with the general equation

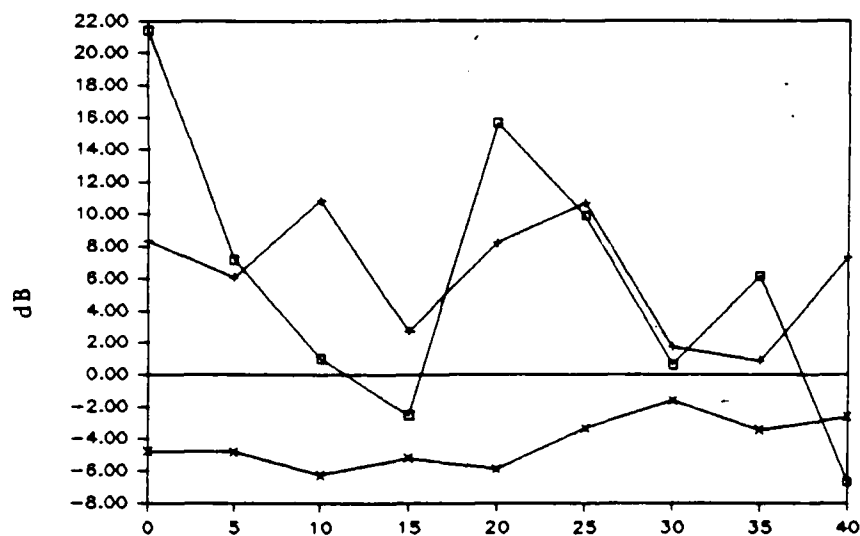
$$\text{Power ratio} = 20 \log_{10} (E_{np}/E_{cc}), \quad (4-3)$$

where E_{np} is the electric field component for the calculations without a ground plane, and E_{cc} is the electric field component for the calculations with a ground plane. From these figures, it was easy to see that the vertical component of the electric field was emphasized by the use of a ground plane. Plots of these values for 30 MHz are provided in Figures 4-16 and 4-17. Additional values are provided in Appendix C. It was noted that for 30 MHz, the ratios for the vertical component were relatively linear, with small ratios. This indicates that the ground plane adds linearly to the incident field. As mentioned previously, the horizontal component of the fields is generally greater when no ground plane is used. No definite patterns could be determined for the longitudinal components. Although no definitive information regarding the effects of the concrete ground planes could be determined, the data did show where the greatest discrepancies between the electric fields obtained with and without a ground plane occurred. This information can be utilized in determining the optimum placement of the absorber material within the HSI. This is discussed further in Chapter 5.



Y (METERS)

A. X = 0 m.



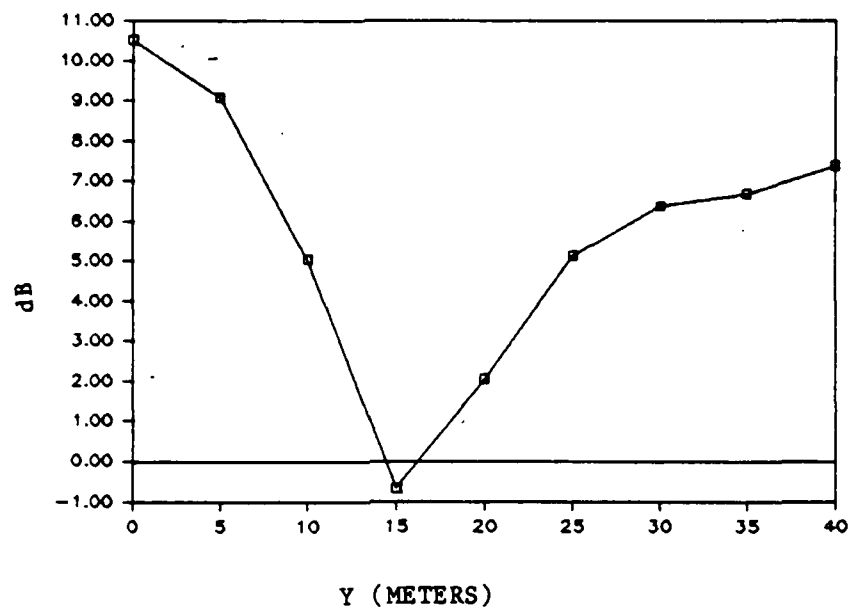
Y (METERS)

B. X = 15 m.

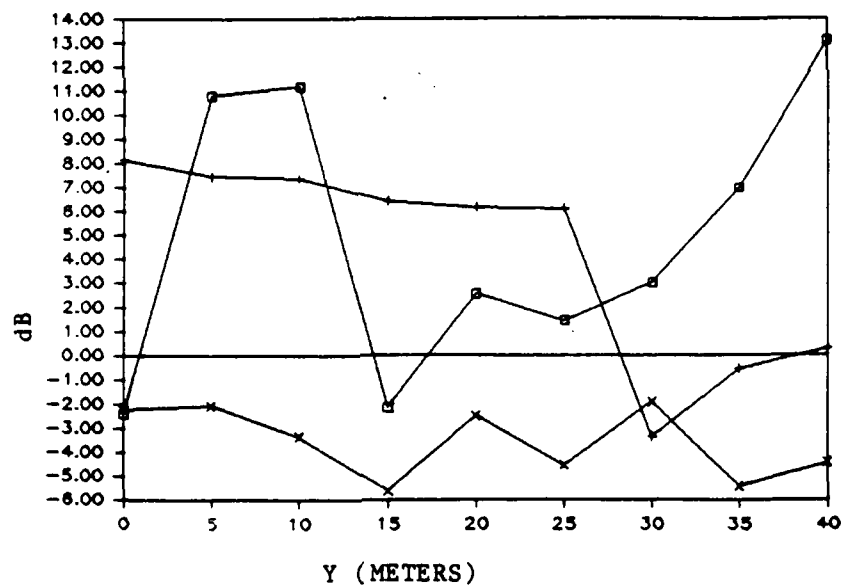
$\square E_x$ $+ E_y$ $\circ E_z$

Figure 4-16

Power Ratio at 3 Meters Below the Test Object
For Vertical Polarization



A. $X = 0$ m.



B. $X = 15$ m.

$$\square E_x + E_y \quad \cdot E_z$$

Figure 4-17

Power Ratio at 3 Meters Below the Test Object
For Horizontal Polarization

V. Material Use Within the HSI

5.1. General

The previous chapters discussed in detail the characteristics of the absorber material, the HSI, the reflection characteristics of the ground plane, and the interaction of the concrete ground plane with the test object. The purpose of this chapter is to combine the individual analysis performed in the previous chapters, and determine a method of placing the absorber within the HSI to reduce the ground plane reflections. Testing of the proposed absorber placement was not accomplished. Therefore, only generalized procedures for the placement of the absorber can be provided. Two techniques of utilizing the wave absorber material were investigated. The first technique was the placement of the wave absorber on the concrete ground plane beneath the test object to absorb energy reflected and radiated by the test object, while the second technique was the use of the wave absorber and a metal plate to stop the incident EM energy from going between the test object and the ground plane. Both of these solutions can reduce the reflected energy significantly and can also be used in combination. From the analysis performed in Chapter 3, the direction of propagation of the incident EM wave can be considered tangential to the concrete ground plane. This approximation is used when attempting to determine the optimum placement of the absorber material within the HSI. Both of the techniques outlined above are more thoroughly discussed in upcoming sections. A final determination of the deployment within the HSI of the best method for reducing the ground effects is also included.

5.2. Absorber Characteristics on a Concrete Surface

In order to determine the effectiveness of the absorber material, it was necessary to determine the characteristics of the absorber when placed on the concrete pad. This was accomplished using the same techniques as those described in Chapter 2. The concrete ground plane can be generally considered a good conductor. Proof of this statement is found in previous chapters. It was possible to compare the overall reflection loss of the absorber on a conductive ground plane with that of the absorber on the concrete pad. The values for the absorber on a concrete pad are provided in Table 5-1. Comparing the values of Table 5-1 with the values in Tables 2-3 through 2-5, it was apparent that the reflection loss was greater for the absorber on the concrete pad than for the absorber on the metal sheet. This was attributed to the transmission of energy into the concrete surface. It should be noted that the maximum loss created from the absorber/concrete interface is thickness and frequency dependent just as the absorber/metal interface loss characteristics are thickness and frequency dependent. Although the analysis performed in Chapter 2 was accomplished for a TEM wave incident upon the absorber, the analysis is still valid for the wave characteristics displayed between the test object and the ground plane. With the absorption characteristics of the absorber on the concrete surface known, it was necessary to study the figures of Chapter 4 in order to determine the best placement of the material. It was apparent that the vertical component of the field was increased by the ground plane. The effects of the ground plane on the other field components were not as obvious. Using the vertical component as a baseline, the absorber must be placed beneath the

Table 5-1

Reflection Loss for ECCOSORB NZ-31
Located on a Concrete Surface

Frequency = 30 MHz						
Angle (Degrees)	0.64 cm		1.28 cm		2.56 cm	
	Normal (dBw)	Parallel (dBw)	Normal (dBw)	Parallel (dBw)	Normal (dBw)	Parallel (dBw)
0	-4.64	-4.64	-9.14	-9.14	-14.9	-14.9
15	-4.48	-4.81	-8.83	-9.47	-15.1	-14.6
30	-4.01	-5.37	-7.89	-10.5	-15.1	-13.5
45	-3.27	-6.60	-6.41	-12.6	-13.4	-11.1
60	-2.31	-9.34	-4.49	-13.6	-9.44	-7.70
75	-1.19	-12.9	-2.31	-7.62	-4.73	-3.89
85	-.402	-4.76	-.776	-2.52	-1.57	-1.30
Frequency = 50 MHz						
Angle (Degrees)	0.64 cm		1.28 cm		2.56 cm	
	Normal (dBw)	Parallel (dBw)	Normal (dBw)	Parallel (dBw)	Normal (dBw)	Parallel (dBw)
0	-6.88	-6.88	-14.1	-14.1	-11.9	-11.9
15	-6.63	-7.13	-13.7	-14.1	-12.5	-11.4
30	-5.92	-7.99	-12.3	-15.5	-14.4	-10.0
45	-4.81	-9.87	-9.86	-15.1	-18.6	-7.95
60	-3.38	-13.6	-6.80	-11.0	-16.6	-5.46
75	-1.74	-10.5	-3.44	-5.43	-7.44	-2.77
85	-.585	-3.43	-1.15	-1.80	-2.40	-.926
Frequency = 250 MHz						
Angle (Degrees)	0.64 cm		1.28 cm		2.56 cm	
	Normal (dBw)	Parallel (dBw)	Normal (dBw)	Parallel (dBw)	Normal (dBw)	Parallel (dBw)
0	-30.3	-30.3	-10.1	-10.1	-6.37	-6.37
15	-27.1	-32.9	-10.5	-9.73	-6.52	-6.22
30	-20.4	-25.1	-11.6	-8.69	-6.96	-5.74
45	-14.3	-16.3	-13.7	-7.03	-7.58	-4.86
60	-9.05	-10.0	-13.6	-4.92	-7.61	-3.56
75	-4.40	-4.81	-7.15	-2.52	-5.06	-1.88
85	-1.45	-1.58	-2.35	-.847	-1.82	-.638

fuselage and the wings to reduce the reflected energy. Since the exact field distribution between the test object and the ground plane is unknown, the thickness of the absorber must be determined experimentally. If it can be assumed that the field reflected and diffracted from the test object is normal or close to normal to the ground plane, then it is possible to determine a thickness for use. The optimum thickness would then be dependent on the frequency as discussed in Chapter 2. As an example of this problem consider a 30 MHz incident wave incident on a test object. Assuming that the incident field and the ground reflected field can be neglected, then the only field is due to the radiation of the target. Assume that the direction of propagation of the field beneath the wings is normally incident on the concrete pad for simplicity. From the data provided in Table 5-1, the optimum thickness would be approximately 2.56 cm, or four times the thickness of the standard slab. This would provide a power loss of -14.9 dB. For the general case, the EM field will be a combination of reflections from the ground plane and the test object. For this reason, a primary direction of propagation will not be apparent. Therefore, it is advised to use the thickness that provides the best overall loss across the range of incident angles.

5.3. Methods of Reducing Incident Waves Beneath the Test Object

The previous section discussed the placement of the absorber material beneath the test object to reduce the effects of the ground plane directly beneath the test object. It was also important to reduce the fields reflected off of the ground plane prior to the test object. Two methods were investigated for reducing the ground plane reflections.

The first was to place the material on the concrete pad in front of the test object, while the second was to place sections of material perpendicular to the ground plane. The first method could not provide sufficient loss for a wave near grazing incidence. In addition, to reduce the maximum amount of power, it would be necessary to use enormous quantities of material slabs. With these problems in mind, this technique was dismissed as too costly. The second method could be used at a fraction of the cost of the first method. This method was broken down into two configurations. The first configuration was the use of the absorber material alone, and the second configuration was the use of the absorber backed by a metal plate or short circuit configuration.

5.3.1. Absorber in Free Space. The absorber characteristics when used in free space were discussed in Chapter 2. To summarize the results listed in Tables 2-3 through 2-5, the transmission losses increase as the thickness of the material increases, transmission losses are generally low for normal angles of incidence for frequencies less than 250 MHz, and losses increase with frequency. For this configuration, it was desired to maximize the transmission loss while minimizing the reflection. By using Tables 2-3 through 2-5 it is possible to determine the best thickness for the angle of incidence. The transmission loss increases as the the thickness of the material increases. Therefore, there is no limit to the loss that can be obtained by using this technique. However, the limiting factor is the thickness of the material. To provide a baseline, a thickness of no more than 2.56 cm will be considered. With an upper limit of the

thickness established, the losses are approximately -3.4 dB for 30 MHz and -4.5 dB for 50 MHz. The losses for 250 MHz are approximately 3 times greater than those at 30 and 50 MHz; however, since this frequency is above the capabilities of the HSI, it will not be used for evaluation. In order for the absorber to be used, it must be mounted on a plate of some type. One suggested plate is a thin wooden structure. Wood is, in general, a low loss, low reflection material, and if the thickness is kept small, there will be no significant contribution to the overall losses of the absorber.

5.3.2. Short Circuit Configuration. The short circuit configuration is the absorber backed by a metal plate. The use of this configuration is to completely block the incident and ground reflected waves from interacting on the volume beneath the test object. The absorber reduces the power of the wave reflected off of the metal plate in order to keep the field integrity of the HSI from being disturbed. To block the incident energy from interacting on the ground plane beneath the test object, it is necessary for the plate/absorber combination to extend from the ground plane to the bottom of the test object. Any diffractions due to the edges of the plates are considered negligible since the edges are small with respect to the wavelength. The reflection losses of this configuration are provided in Table 2-3 through 2-5. As previously mentioned, the short circuit configuration is frequency dependent. Therefore, the maximum loss that is expected for the configuration is determined by frequency. For 30 MHz, the thickness of the absorber on the metal plate is approximately 2.56 cm for an overall loss of -15.3 dB at normal incidence. For 50 MHz, the

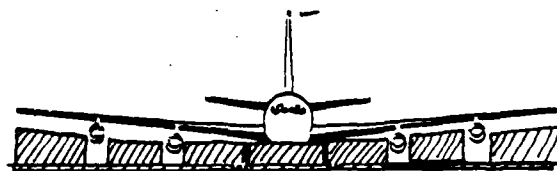
thickness of the absorber on the metal plate would be 1.92 cm for an overall loss of -16.4 dB at normal incidence. The reflection losses would not vary greatly for the assumed directions of propagation. It is necessary to attach the absorber material to both sides of the metal plate, so that reflections from the test object are not reflected back by the metal plate. The energy losses will be the same as those discussed for an absorber on a metal plate.

5.4. Suggested Use Within the HSI

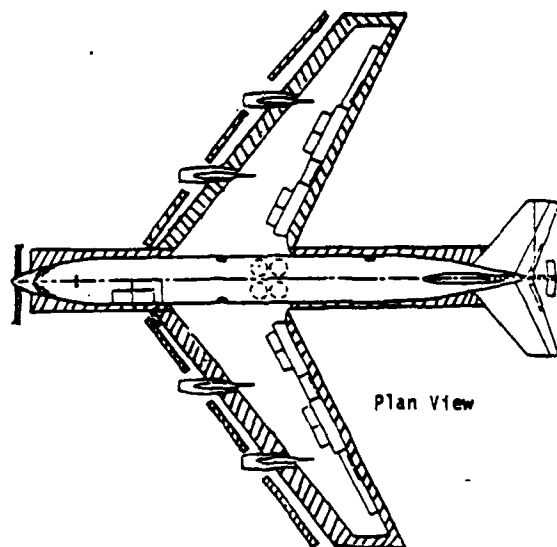
The method of deployment of the absorber within the HSI is suggested in the above sections. The methods that seem to have the best chance to succeed in reducing the EM wave are a combination of the techniques previously described. The combination consists of the absorber placed beneath the fuselage and wings to reduce the reflections on the ground plane caused by the surface currents on the test object, and a short circuit configuration located in front of the test object to stop the incident and reflected waves from entering the volume beneath the test object. The thicknesses of the material used for the combination range from 0.64 cm to 2.56 cm. Although, the only thicknesses listed are for 30, 50, and 250 MHz, the material thicknesses for other frequencies can be determined by interpolating between the listed frequencies. A physical interpretation of the placement of the absorber within the HSI is shown in Figure 5-1.



Side View



Front View



Plan View

Figure 5-1

Suggested Use of Absorber Material Within the HSI (15:2)

VI. Conclusions, Recommendations, and Summary

6.1 Conclusions

This thesis was designed to determine a method for reducing EM waves within an EMP simulator. The thesis was accomplished in three phases: phase 1 addressed the field distribution caused by the HSI, phase 2 addressed the diffraction and scattering of the incident waves on the surface plane and test object, and phase 3 addressed the absorber material and its placement within the HSI.

6.1.1. Phase 1: Field Distributions in the HSI

The purpose of phase 1 was to determine the field distribution caused by the HSI structure. Theory suggested that the field within the HSI was a planar TEM wave throughout the working volume located in the central region of the HSI. Computer modelling of the HSI revealed that the fields within the working volume could be considered sufficiently planar and exhibited either mostly vertical polarization for the common mode excitation, or a strong horizontal component for the differential mode excitation throughout the central section of the working volume. A transverse component of the electric field occurred at all frequencies under consideration. This component was caused by the TM mode supported by the HSI at intermediate and high frequencies. The SWRs for the common mode are reasonably low, with values generally no larger than 2.0, but the SWRs for the differential mode are large with values from 3.0 to 6.0. The differences in the two modes are obvious from the figures in Chapter 3.

6.1.2. Phase 2: Wave Interaction with the Test Object

The test object was modelled as a wire figure as illustrated in Chapter 4. Sample points were taken within the working volume at 3 m below the test object, and at a distance of 0 and 15 m from the central axis with and without a concrete ground plane. It was shown that for both vertical and horizontal polarization the vertical component was emphasized along the wings. The field along the fuselage was dependent on the polarization and the frequency. For vertical polarization, the vertical component is emphasized along the fuselage. For horizontal polarization, the vertical component of the field was emphasized for the lower frequencies while the horizontal field was emphasized for the higher frequency. This may have been due to the wavelengths of the lower frequencies being close to the length of the test object. The field along the fuselage resembled a standing wave at 6 and 12 MHz. The other frequencies may also have exhibited this characteristic, but there were not enough data points to obtain the necessary resolution. The current along the wires of the test object was sinusoidal in nature. The currents on the test object were symmetric about the central axis of the fuselage when no ground plane was used. This was expected. However, when a concrete ground plane was added, the current along one wing was greater than the current along the other wing. This phenomenon is probably due to nonlinear characteristics of the concrete ground plane.

6.1.3. Phase 3: Absorber Material and Placement Within the HSI

The goal of this project was to develop a methodology for reducing the reflections and diffractions within the HSI caused by the ground plane. The method used for this project was to introduce an EM wave absorber into the HSI. The absorber chosen as a representative material was the ECCOSORB NZ-31 produced by Emerson and Cuming. ECCOSORB NZ-31 is a sintered ferrite described by the values K' , K'' , K'_m , and K''_m given in Table 2-2. This material absorbs EM energy from 25 MHz to 3 GHz. The amount of energy that is absorbed is dependent on the thickness of the material. This is an important consideration when a good conductor is placed behind the material and reflection measurements are taken. The absorber is generally effective in the range of interest for thicknesses from 0.64 cm to 2.56 cm. The material characteristics, when used with a good conductor, were used when determining the optimal placement of the material within the HSI. Due to the characteristics of the structure and the test object, it was decided that two methods of using the absorber would provide the desired results. The first method was to place the absorber beneath the test object on the ground plane. Power losses of 15 dB are possible with this configuration. The second method was to place the material on metal plates, and place the plates in front of the test object to stop the incoming waves from interacting in the space between the test object and the ground plane. The absorber should be placed on both sides of the metal plates to reduce reflections caused by the test object, and to eliminate the incident wave from interacting on the volume beneath the test object. The material can reduce the reflected power by approximately 13 to 15 dB, depending on frequency and material thickness. Since this method stops the incident

and reflected waves from interacting in the space beneath the test object, the only fields beneath the test object are those caused by the currents on the test object itself. The absorber material on the ground plane should reduce these fields sufficiently to approximate a free space condition.

6.2. Recommendations for Further Study

6.2.1. Project 1: Absorber Testing The wave absorber ECCOSORB NZ-31 was not tested during this effort. Its evaluation was based on calculated data. It is necessary to test the absorber in order to verify its permittivity, permeability, and absorption characteristics. Examination of the calculated data suggests that useful absorption using metal backed plates and the concrete ground plane is possible for a frequency range beyond that suggested by the manufacturer.

6.2.2 Project 2: Development of a High Frequency Test Object Model.

The wire model approximation of the test object was a very simple model used to determine rough estimates of the fields between the test object and the ground plane. This model was only valid for low frequency approximations. An attempt to obtain a high frequency model by using a geometrical theory of diffraction (GTD) configuration failed. The same program used to determine the MOM currents could also provide a GTD configuration; however, this routine could not determine the electric field patterns between the test object and the concrete ground plane. It is necessary to determine an accurate high frequency model of the test object in order to validate the results obtained in this project.

6.2.3 Project 3: Development and Testing of an HSI Scale Model

Simulator. This thesis was a mathematical evaluation of EM fields within the HSI and the absorption characteristics of an absorber material. In order to validate the results included in this document, it is necessary to obtain experimental data on the HSI or a scale model simulator. The construction of scale model simulator could be performed at AFIT and experimental results obtained. The frequency range of the HSI would have to be scaled accordingly. It would also be useful to test the absorber material within the model's environment. Since the absorber material is frequency dependent, it would be necessary to reduce the thickness of the material in order to model the absorption characteristics accurately.

6.2.4 Project 4: Analysis and Testing of Multiple Material Absorber.

As discussed in Chapter 2, a layered material absorber may have use in reducing EM wave reflections. This project would require that a group of materials be analyzed separately and then analyzed in a layered configuration. Testing of this configuration would also be necessary to obtain experimental data.

6.3. Summary

This study presented an overview of a methodology that can be used to place an absorber material within an EMP simulator to reduce the effects of a conducting ground plane on the current distributions of the test object. This study is significant in several respects. First, the analysis of the simulator extends the knowledge base regarding EMP simulators of this type to include the effects of a nonperfectly conducting ground plane on the electric field distributions within the

working volume. In addition, the MOM analysis of the EMP simulator is the first such analysis of the HSI configuration. Although the MOM calculations are a mathematical solution of the EM fields, it has been shown that MOM results are valid when compared to experimental data. Second, the MOM analysis did not indicate the "notch" in the fields as predicted by the Harvard Simulators. Third, this project determined that it was possible to place a test object near a ground plane and still obtain a free space environment by placing an absorber material in key locations within the HSI. Fourth, the ground plane effects on the test object were determined using a planar, TEM wave at angles tangent to the ground plane. This also extends the knowledge base regarding the effects of a ground plane on the test object. This project is only a starting point for other projects that need to be accomplished in this field. By determining the field characteristics of the HSI, it is possible to build on this information and help provide a better EMP simulator.

Appendix A. GEMACS

A.1. General

The General Electromagnetic Model for the Analysis of Complex Systems (GEMACS) is a computer code developed by the BDM Corporation and is used to evaluate the current distributions and electric field components of complex electromagnetic (EM) geometries. It solves a system of equations for the currents on a set of wires and patches, then solves the electric field equation to determine the fields. The wires used are thin wire approximations where the radius of the wire is much less than the wavelength. This approximation allows the azimuthal current flow around the target to be neglected, the longitudinal current to be independent of azimuth, and the surface integration to be replaced with a line integral (7:26). Thin wire approximations have been used successfully in radiation and scattering problems.

A.2. Integral Equation Formulation

The equations solved by the GEMACS routine are related to the general electric field equations. Approximations to reduce the equations into one-dimensional integral equations are used. The integral equations are used for wire calculations by GEMACS. The electric field equation due to a volume current ($\bar{J}(\bar{r}_0)$) can be written as (7:23)

$$\bar{E}(\bar{r}_0) = \iiint_V j\omega\mu_0 \bar{J}(\bar{r}_0) \cdot \underline{G}(\bar{r}, \bar{r}_0) dV \quad (A-1)$$

where \bar{r}_0 is the observation point and \bar{r} is the source point. The value for $\underline{G}(\bar{r}, \bar{r}_0)$ can be found from the following equation (5:58)

$$\underline{G}(\bar{r}, \bar{r}_0) = \underline{I} \frac{1}{4\pi} g(\bar{r}, \bar{r}_0)$$

where

$$\underline{I} = a_x a_x + a_y a_y + a_z a_z$$

$$g(\bar{r}, \bar{r}_0) = \frac{\exp(-jk |\bar{r} - \bar{r}_0|)}{|\bar{r} - \bar{r}_0|}$$

$$k = \omega(\mu_0 \epsilon_0)^{1/2}$$

Since the wire models used were perfectly conducting, thin wire models, it was possible to use the boundary conditions and equation A-1 to reduce the electric field integral equation to (7:25)

$$-\mathbf{s}_0 \cdot \bar{\mathbf{E}}^i(\bar{r}_0) = \left(\frac{-j\omega\mu_0}{4\pi} \right) \int_L \left[\mathbf{s} \cdot \mathbf{s}_0 - \frac{1}{k^2} \frac{\partial^2}{\partial s \partial s_0} \right] I_s(s) g(\bar{r}, \bar{r}_0) ds \quad (\text{A-2})$$

where \mathbf{s} is the unit tangent vector at \bar{r} pointing in the direction of the current, \mathbf{s}_0 is the unit tangent at the observation point, and $I_s(s)$ is the surface current on the wire. Therefore, the electric field equation is reduced to a one-dimensional integral which can be solved by numerical techniques. This equation is a form of Pocklington's equation (7:24-26).

A.3. Method of Moments Calculations (1:304-315)

The numerical solution of the above integral equation is known as the method of moments (MOM). Mathematically, equation A-2 is in the form of (1:307)

$$F(g) = h \quad (\text{A-3})$$

where F is a known operator, h is a known excitation function, and g is a

response function (1:307). It is desired that the value of g be determined given F and h . The MOM expands the response function in terms of a linear combination of N terms. This can be written as (1:307)

$$g = \sum g_n c_n \quad (A-4)$$

where c_n is a unknown constant and g_n is known basis function. Given this information, equation A-3 can be rewritten as

$$h = \sum c_n F(g_n). \quad (A-5)$$

In order to solve A-4, it is necessary to obtain N linearly independent equations. This can be accomplished by evaluating A-4 at N different points by applying the boundary conditions at these points. This method is referred to as collocation and is the method used by GEMACS (7:29).

It is necessary to define an inner product $\langle w, g \rangle$ (where w is a weighting function) that satisfies the following laws (1:311)

$$\begin{aligned} \langle w, g \rangle &= \langle g, w \rangle \\ \langle af + bg, w \rangle &= a \langle f, w \rangle + b \langle g, w \rangle \\ \langle g^*, g \rangle &> 0 \quad \text{if } g \neq 0 \\ \langle g^*, g \rangle &= 0 \quad \text{if } g = 0. \end{aligned}$$

With the inner product defined, A-4 can be rewritten as (1:311)

$$c_n \langle w_m, F(g_n) \rangle = \langle w_m, h \rangle \quad m=1, 2, \dots, N. \quad (A-6)$$

This can be rewritten in matrix form as

$$[F_{mn}][c_n] = [h_m] \quad (A-7)$$

where

and

$$[F_{mn}] = \langle w_m, F(g_n) \rangle$$

$$[h_m] = \langle w_m, h \rangle.$$

If an inversion of $[F_{mn}]$ exists, it is possible to solve for c_n and then determine the function g by solving equation A-4. It is important to determine the correct basis functions and weighting functions. The weighting functions used in GEMACS are a set of Dirac delta functions of the form (1:313)

$$w_m = \delta(p - p_m) = \delta(p - p_1), \delta(p - p_2), \dots$$

where p is a position with respect a reference, and p_m is a point where the boundary conditions are being applied. Use of this weighting function yields (1:313)

$$c_n F(g_n) |_{p=p_m} = h |_{p=p_m} \quad m=1,2,\dots,N$$

The use of delta functions can be seen as a relaxation of the boundary conditions so that they are enforced only at discrete points (B1:312,313). GEMACS employs constant, sine, and cosine terms for the basis function so that the current function can be written as

$$\begin{aligned} I(s) &= U_j(s) [A_j + B_j \sin k(s-s_j) + C_j \cos k(s-s_j)] \\ &= U_j(s) I_j(s). \end{aligned}$$

where A_j , B_j , and C_j are unknown constants. From this equation, the currents along various segments can be solved.

A.4. Magnetic Field Integral Equation

GEMACS uses the the magnetic field integral equation to model electromagnetic (EM) response to large smooth surfaces. It was used to determine the response of the ground plane within the HSI. The general magnetic field integral equation is given by (7:37)

$$\begin{aligned} \bar{H}(\bar{r}_o) = & T\bar{H}^i(\bar{r}_o) + T/(4\pi) \int_V [-j\omega\bar{K}\epsilon + \bar{J} \times \bar{\nabla}'\phi + m/\bar{\nabla}'\phi] dv \\ & + T/4\pi \iint [j\omega\epsilon (\bar{n}' \times \bar{E}) + (\bar{n}' \times \bar{H}) \times \bar{\nabla}'\phi \\ & + (\bar{n}' \cdot \bar{H}) \bar{\nabla}'\phi] dA' \end{aligned} \quad (A-8)$$

where

\bar{H} = Magnetic Field

\bar{H}^i = Incident Magnetic Field

$T = \begin{cases} 1 & \text{Observation Point not on surface} \\ 2 & \text{Observation Point on Surface} \end{cases}$

\bar{K} = Magnetic Current Density

\bar{J} = Electric Current Density

m = Magnetic Charge Density

\bar{E} = Electric Field

\bar{r}_o = Observation Point

\bar{r} = Source Point

\bar{n}' = Outward Normal from Surface

$\phi = \exp(-jk|\bar{r}_o - \bar{r}|)/(|\bar{r}_o - \bar{r}|)$

In the source free region, there are no magnetic or electric current densities or magnetic charge densities. Therefore, the first integral

conveniently equals 0. The scattered magnetic field ($\bar{H}^s(\bar{r}_0)$), can be determined from the second integral, where $T=1$ or $T=2$. In a source free region, equation A-8 reduces to (7:38)

$$\bar{H}(\bar{r}_0) = T\bar{H}^i(\bar{r}_0) + T/(4\pi) \iint_s [j\omega\epsilon(\mathbf{n}' \times \bar{E})\phi + (\mathbf{n}' \times \bar{H}) \times \nabla'\phi + (\mathbf{n}' \cdot \bar{H})\nabla'\phi] dA' \quad (A-9)$$

Since $\bar{H}(\bar{r}_0) = \bar{H}^i(\bar{r}_0) + \bar{H}^s(\bar{r}_0)$, then the scattered magnetic field away from the scatterer is (7:38)

$$\bar{H}^s(\bar{r}_0) = 1/(4\pi) \iint_s [j\omega\epsilon(\mathbf{n}' \times \bar{E})\phi + (\mathbf{n}' \times \bar{H}) \times \nabla'\phi + (\mathbf{n}' \cdot \bar{H})\nabla'\phi] dA'$$
 where $T=1$. For the observation point on the scatterer, $\mathbf{n} \times \bar{E} = 0$, since the tangential field equals zero, and $\mathbf{n} \times \bar{H} = \mathbf{m} = 0$, since the magnetic charge is zero. Therefore, the magnetic field on the scatterer can be written (7:39)

$$\bar{H}(\bar{r}_0) = 2\bar{H}^i(\bar{r}_0) + 2/(4\pi) \iint_s [(\mathbf{n}' \times \bar{H}) \times \nabla'\phi] dA'$$

Taking the cross product with the surface normal yields

$$\mathbf{n}' \times \bar{H}(\bar{r}_0) = 2\mathbf{n}' \times \bar{H}^i(\bar{r}_0) + 1/(2\pi) \mathbf{n}' \times \iint_s (\mathbf{n}' \times \bar{H}) \times \nabla'\phi dA'.$$

Letting the surface current density, $\bar{J}_s = \mathbf{n}' \times \bar{H}$, the following magnetic integral equation is obtained (7:39)

$$-\mathbf{n}' \times \bar{H}^i(\bar{r}_0) = -1/2 \bar{J}_s + 1/(4\pi) \mathbf{n}' \times \iint_s \bar{J}_s \times \nabla'\phi dA' \quad (A-10)$$

Therefore, it is possible to obtain the surface current density from the incident magnetic field.

A.5. Computation of the Electric Field (7:55-58)

For this project, all of the electric field measurements are taken in the near field. The field due to the current on a wire segment is obtained by performing the vector sum of all three current distributions of sine, cosine, and constant on the wire segment. Consider a wire segment as illustrated in Figure A-1. The electric field due to the wire segments can be written in the following closed form for a sine, and cosine distribution as (7:56)

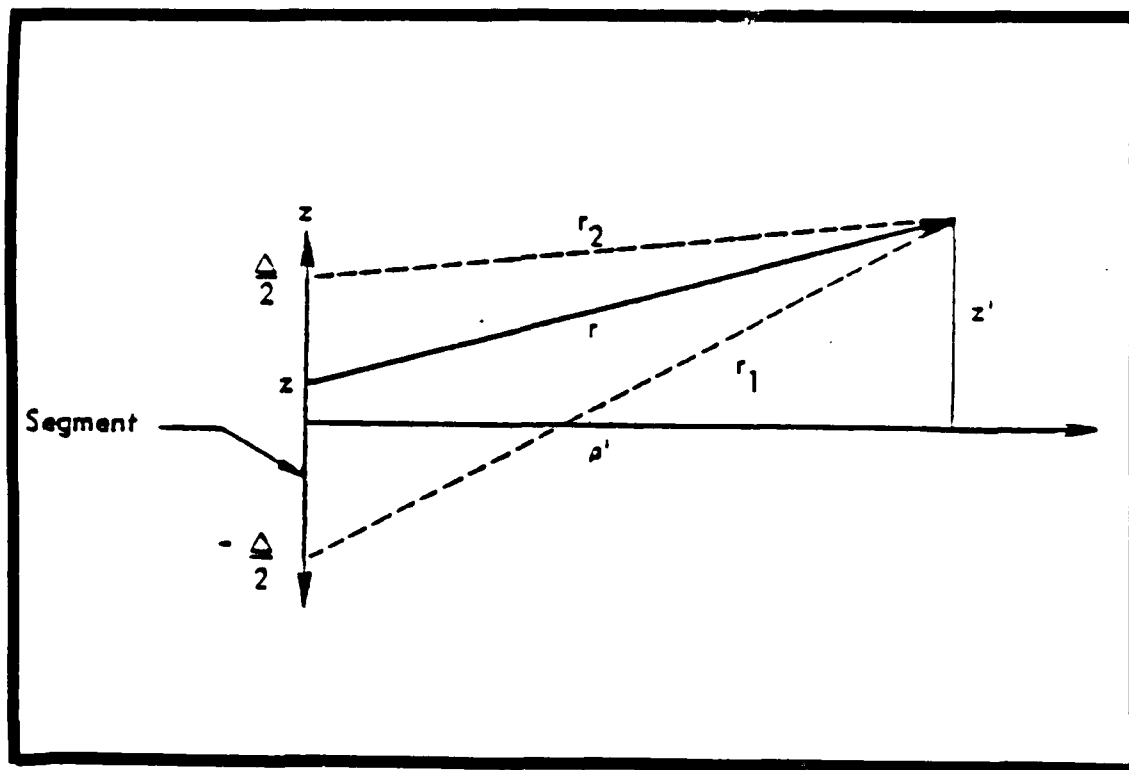


Figure A-1

Geometry of Wire Segment of Length l (7:55)

$$E_p(p', z') = \frac{-jI_0 n k p'}{2} \left[\left(j + \frac{1}{kr_2} \right) \frac{\exp(-jkr_2)}{(kr_2)^2} - \left(j + \frac{1}{kr_1} \right) \frac{\exp(-jkr_1)}{(kr_1)^2} \right]$$

For the electric field determined from the constant current, there is an integral of $\exp(-jkr)/r$ that must be integrated numerically. The electric fields above are given in cylindrical coordinates. It is easy to transform these into rectangular coordinates displayed in this document. These are given by the equations (3:28)

$$E_x = E_p \cos \phi,$$

$$E_y = E_p \sin \phi$$

$$E_z = E_z$$

A.6. GEMACS Program Used for Evaluation (8)

In order to use GEMACS it is necessary to determine the type of data desired, and write an interaction program to utilize the GEMACS routines. The commands used by GEMACS are presented in the GEMACS users manual (8). The commands used in this thesis operation were very straight forward and will be described. There are two sections to a GEMACS implementation routine; the command section and the geometry section. The command section is the operational portion of the routine, while the geometry section gives the parameters for the geometry of the structure being analyzed. A general command section is given below:

```
NFIL=17
FRQ=
GMDT=WIRE
SRC=VSRC(WIRE) V=1000.,0. SEGS=1
SRC=VSRC(WIRE) V=1000.,0. SEGS=
ZLDS=WIMP GMDT=WIRE ZIMP=215 SEGS=545
ZGEN GMDT=WIRE ZMAT=ZIJ ZLDS=WIMP COND= EPSR=
SOLVE ZIJ*I=SRC
FLD=EFLD(1) Z2=12 DZ=4 Y2=-50 DY=-5 X2=20 DX=5 Z1=4 X1=0 Y1=0
```

WRITE FLD LU=3 FILE=FLD

A summary of the commands used is shown below:

NFIL - tells the system to open 17 data files for storage.

FRQ - generates the frequency for which the calculations will be performed.

GMDT - tells the system name of the geometry. SRC - determines the method of excitation on the geometry.

VSRC - voltage source created from a spark gap located on the segment chosen. The V command determines the real and imaginary components of the voltage

ESRC - Electric Field excitation. Used to excite a geometry with an incident electric field. Direction and magnitude of field determined in ESRC command.

ZLDS - Determines the loading requirements on the structure.

ZGEN - Sets up the interaction matrix. Ground plane data and loads are also determined in ZGEN.

SOLVE - Solves the interaction matrix defined above for the currents on the wires. Alternative method of solving for currents is through the banded matrix iteration (BMI) technique

FLD - Calculates the electric fields at defined points from the current data calculated above.

WRITE - Writes the field data to a device defined by LU=3.

The geometry section sets up the geometry of the structure to be solved.

This was very straight forward for the HSI, since it is a wire structure itself.

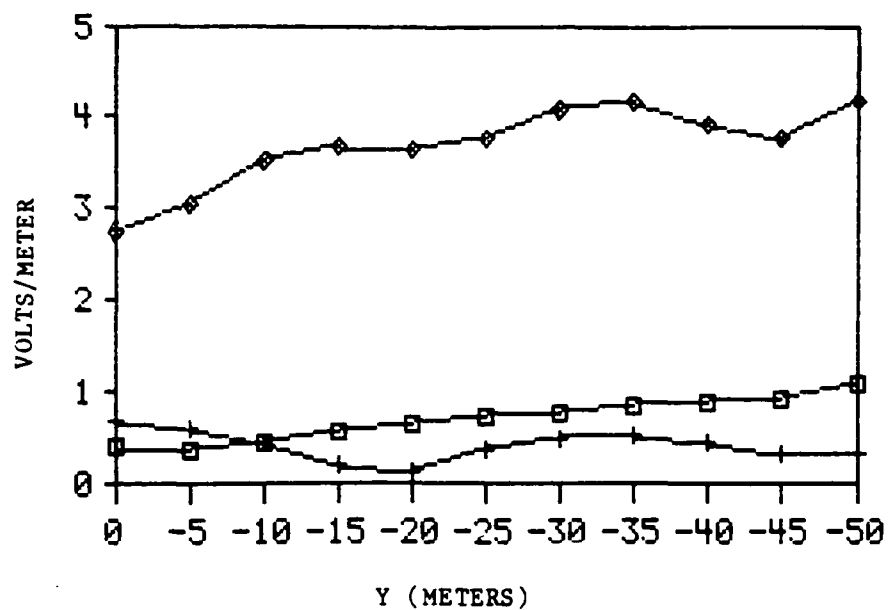
A.7. Summary

The GEMACS program is very flexible and can be used to solve for wire currents and electric fields. For geometries that require a large number of segments the program takes a long amount of time. The data generated for the 30 MHz calculations took up to 5 hours apiece, while the runs attempted for 50 MHz took up to 28 hours. GEMACS can also perform GTD calculations. However, attempts to use this part of the

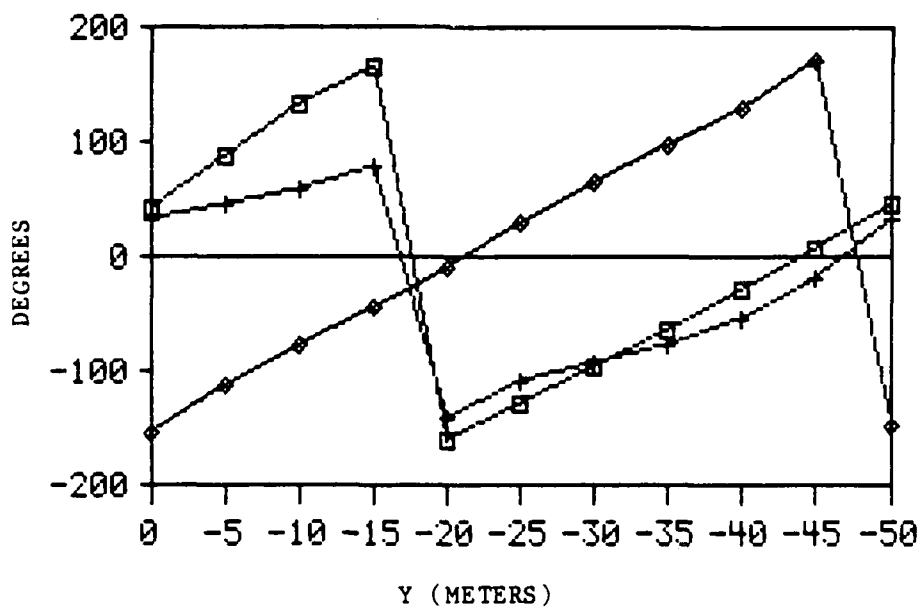
code to predict the electric fields beneath the test object failed.

Appendix B

Appendix B contains additional graphs that specify the fields of the Hardness Surveillance Illuminator (HSI). The graphs that appear in this Appendix are given for the frequencies of 6, 8, 10.71, 12 and 30 MHz. Graphs are provided for both common and differential mode. For each frequency and mode, graphs are provided showing the field distribution at $X = 15$ meters at a height of $Z = 4$ meters and $Z = 8$ meters to illustrate the longitudinal distribution, $Y = -20$ meters and $Z = 4$ meters to illustrate the horizontal distribution, and $Y = -20$ meters and $X = 0$ meters to illustrate the vertical distribution.



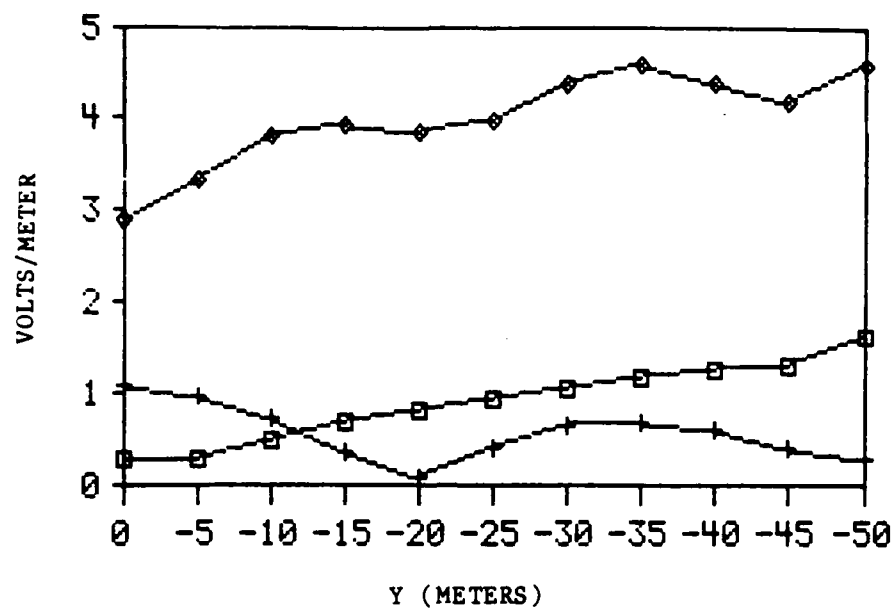
A. MAGNITUDE



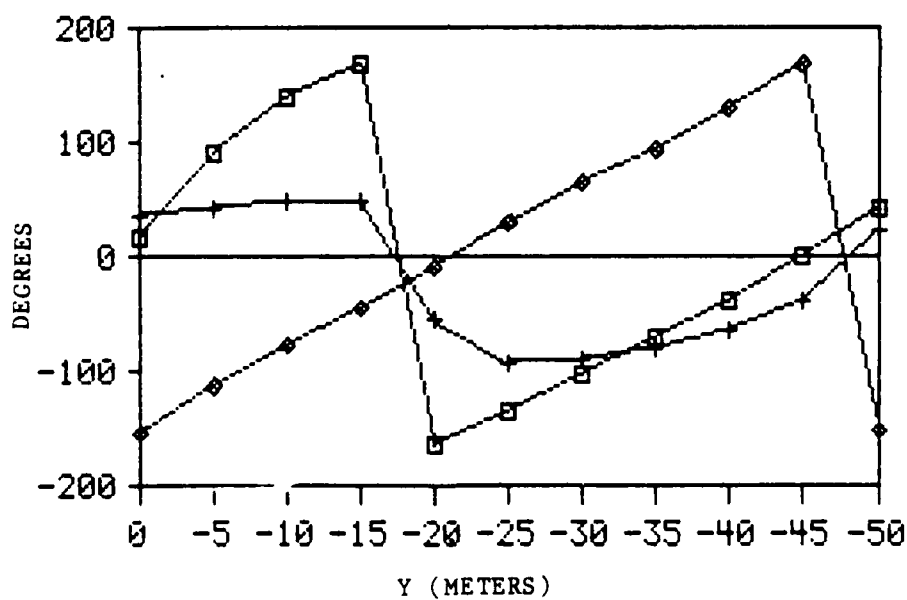
B. PHASE

□ Ex + Ey ◇ Ez

Figure B-1. Common Mode Electric Field Magnitude and Phase For 6 MHz in Longitudinal Direction at X = 15 m, Z = 4 m.



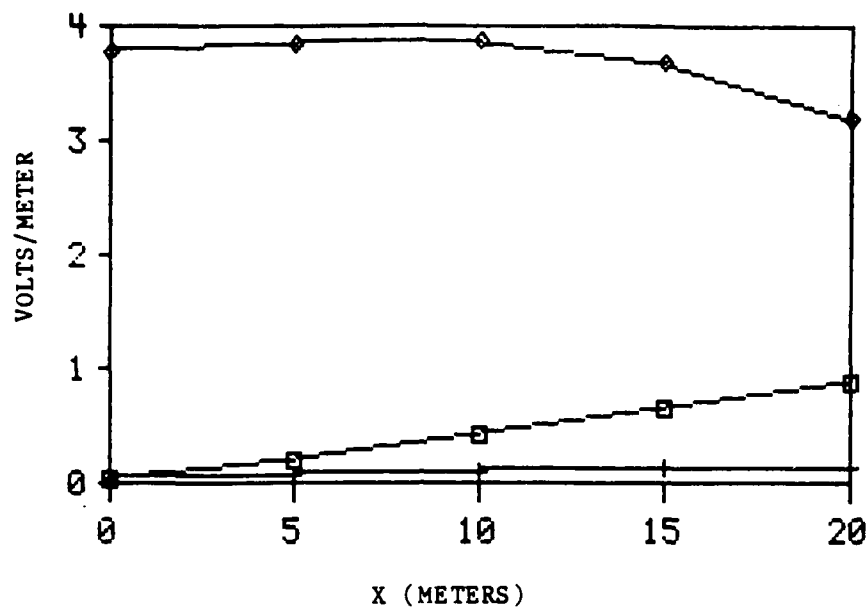
A. MAGNITUDE



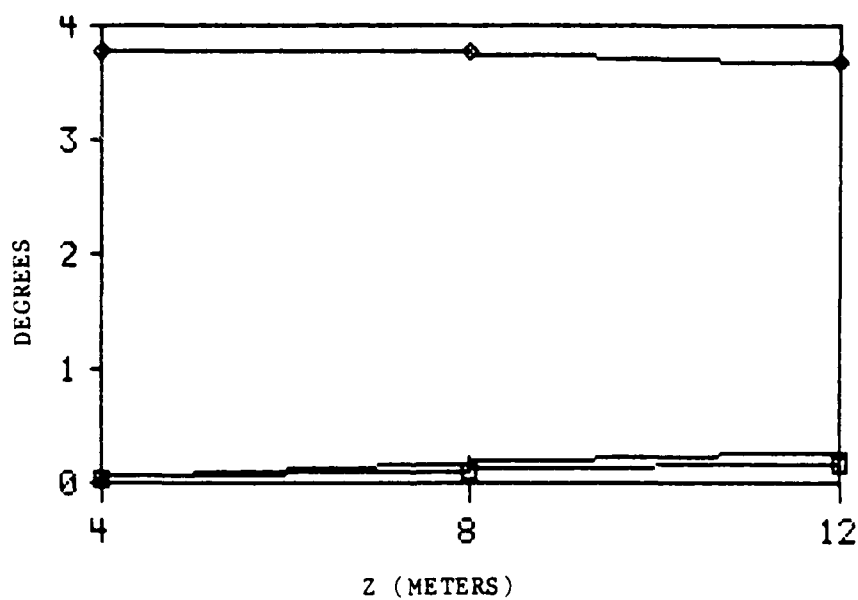
B. PHASE

□ Ex + Ey ◇ Ez

Figure B-2. Common Mode Electric Field Magnitude and Phase For 6 MHz in Longitudinal Direction at X = 15 m, Z = 8 m.



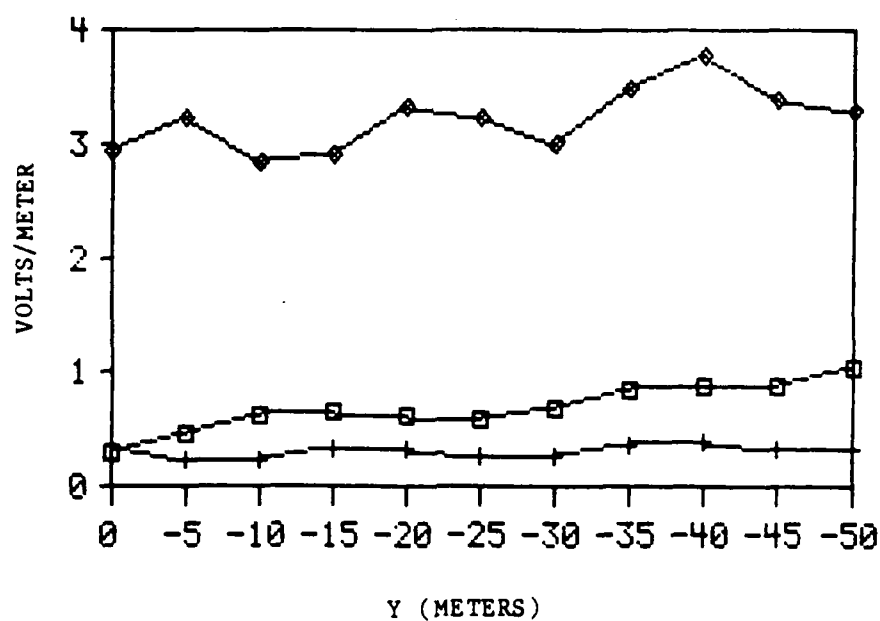
A. Horizontal (Z=4 m, Y=-20 m)



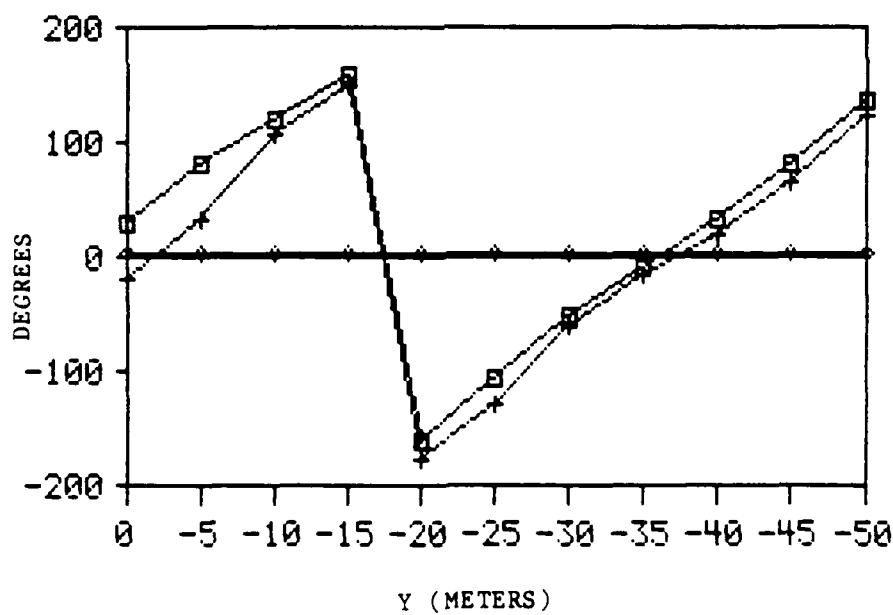
B. Vertical (X=0 m, Y=-20 m)

□ Ex + Ey ◇ Ez

Figure B-3. Common Mode Electric Field Magnitude For 6 MHz in Vertical and Horizontal Direction.



A. MAGNITUDE



B. PHASE

□ Ex + Ey ◇ Ez

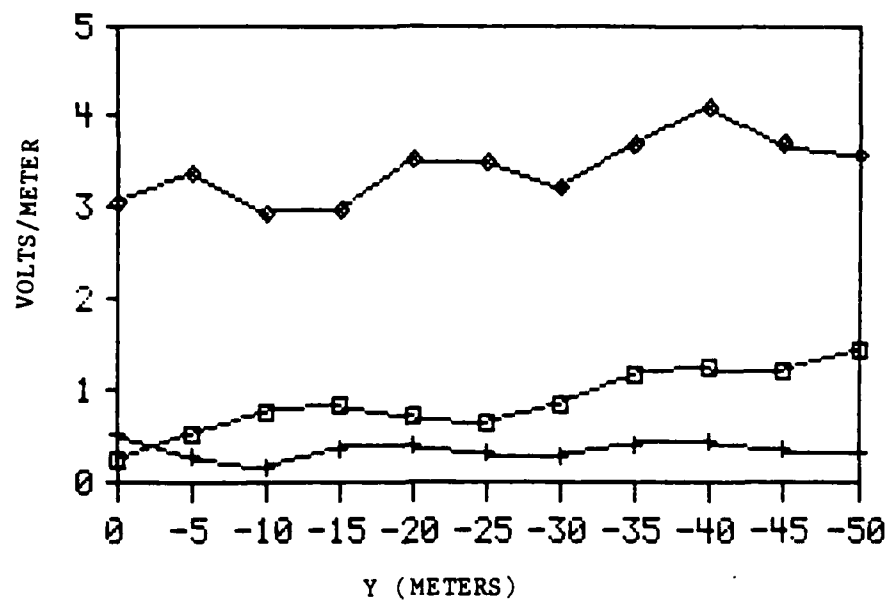
Figure B-4. Common Mode Electric Field Magnitude and Phase
For 8 MHz in Longitudinal Direction at X = 15 m, Z = 4 m.

$$E_z(p', z') = \frac{jI_0 n}{2} \left[\frac{\exp(-jkr_2)}{kr_2} \begin{Bmatrix} \cos kl/2 \\ -\sin kl/2 \end{Bmatrix} - \frac{\exp(-jkr_1)}{kr_2} \begin{Bmatrix} \cos kl/2 \\ \sin kl/2 \end{Bmatrix} \right. \\ \left. - \left(j + \frac{1}{kr_2} \right) \frac{\exp(-jkr_2)}{(kr_2)^2} (kz' - kl/2) \begin{Bmatrix} \sin kl/2 \\ \cos kl/2 \end{Bmatrix} \right. \\ \left. + \left(j + \frac{1}{kr_1} \right) \frac{\exp(-jkr_1)}{(kr_1)^2} (kz' + kl/2) \begin{Bmatrix} -\sin kl/2 \\ \cos kl/2 \end{Bmatrix} \right]$$

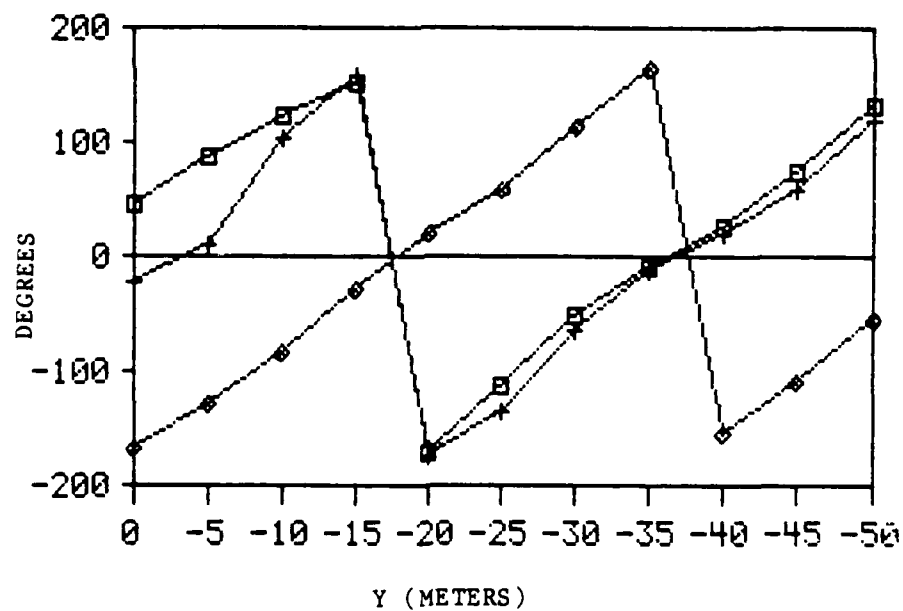
$$E_p(p', z') = \frac{-jI_0 n}{2kp'} \left[(kz' - kl/2) \frac{\exp(-jkr_2)}{kr_2} \begin{Bmatrix} \cos kl/2 \\ -\sin kl/2 \end{Bmatrix} \right. \\ \left. - (kz' + kl/2) \frac{\exp(-jkr_1)}{kr_1} \begin{Bmatrix} \cos kl/2 \\ \sin kl/2 \end{Bmatrix} + \frac{\exp(-jkr_2)}{kr_2} \begin{Bmatrix} \sin kl/2 \\ \cos kl/2 \end{Bmatrix} \right. \\ \left. - (kz' - kl/2)^2 \left(j + \frac{1}{kr_2} \right) \frac{\exp(-jkr_2)}{(kr_2)^2} \begin{Bmatrix} \sin kl/2 \\ \cos kl/2 \end{Bmatrix} \right. \\ \left. + (kz' + kl/2)^2 \left(j + \frac{1}{kr_1} \right) \frac{\exp(-jkr_1)}{(kr_1)^2} \begin{Bmatrix} -\sin kl/2 \\ \cos kl/2 \end{Bmatrix} \right. \\ \left. - \frac{\exp(-jkr_1)}{kr_1} \begin{Bmatrix} -\sin kl/2 \\ \cos kl/2 \end{Bmatrix} \right]$$

For a constant current density, the field components are (7:57)

$$E_z(p', z') = \frac{-jI_0 n}{2} \left[\int_{-L/2}^{L/2} \frac{\exp(-jkr)}{r} dz + \left(j + \frac{1}{kr_2} \right) (kz' - kl/2) \frac{\exp(-jkr_2)}{(kr_2)^2} \right. \\ \left. - \left(j + \frac{1}{kr_1} \right) (kz' + kl/2) \frac{\exp(-jkr_1)}{(kr_2)} \right]$$



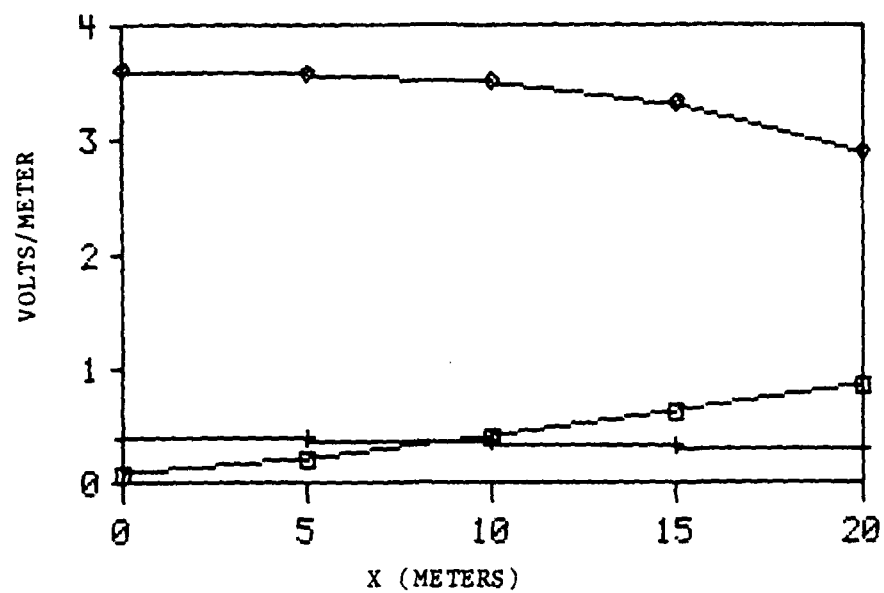
A. MAGNITUDE



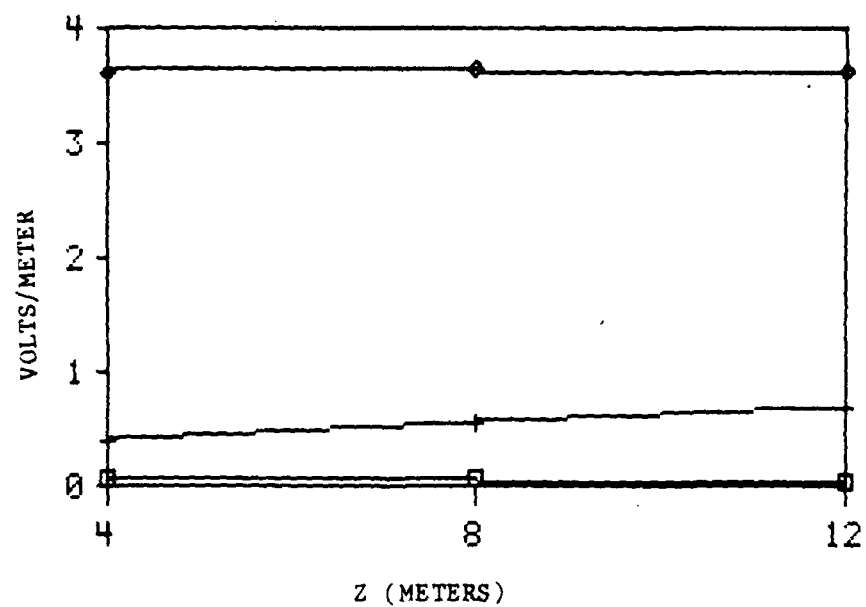
B. PHASE

□ Ex + Ey ◇ Ez

Figure B-5. Common Mode Electric Field Magnitude and Phase For 8 MHz in Longitudinal Direction at X = 15 m, Z = 8 m.



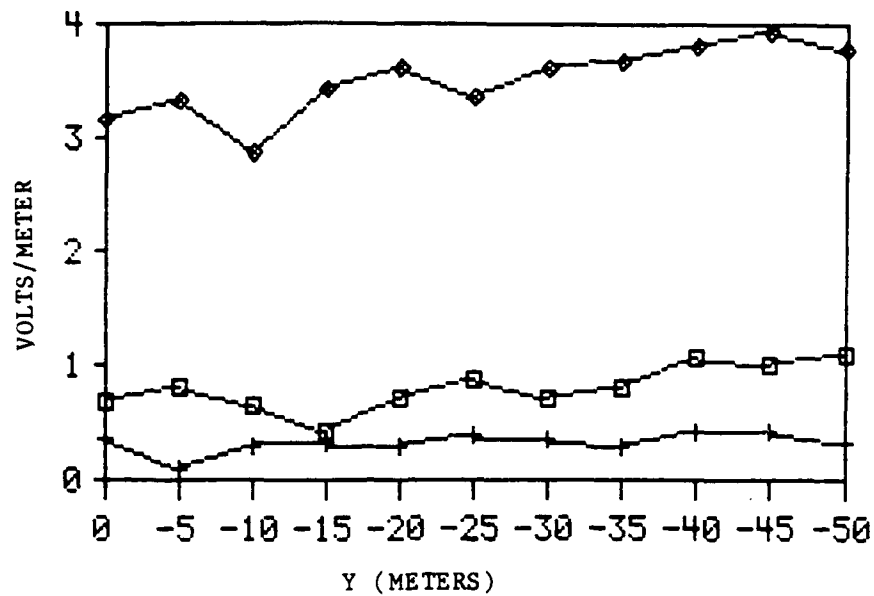
A. Horizontal (Z=4 m, Y=-20 m)



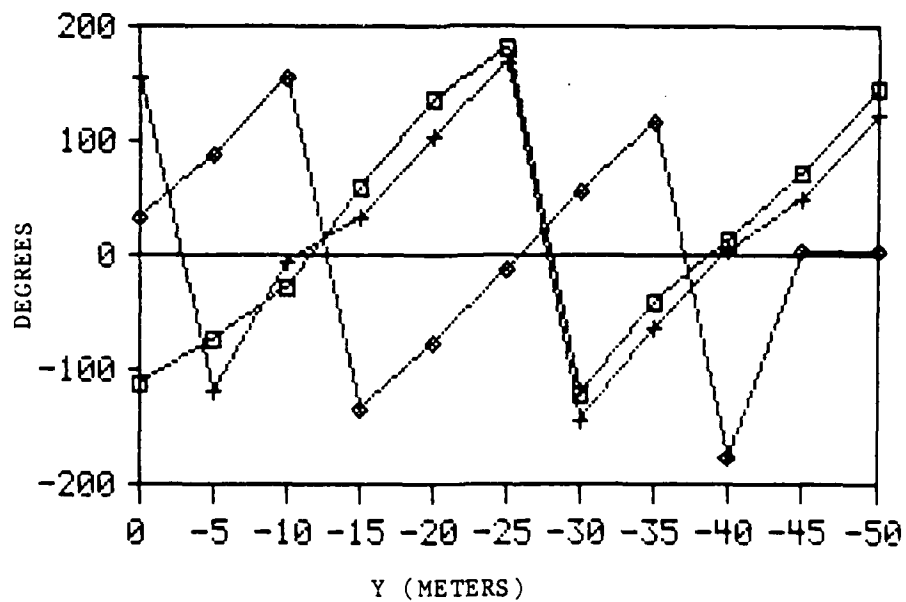
B. Vertical (X=0 m, Y=-20 m)

□ Ex + Ey ◇ Ez

Figure B-6. Common Mode Electric Field Magnitude For 8 MHz in Vertical and Horizontal Direction.



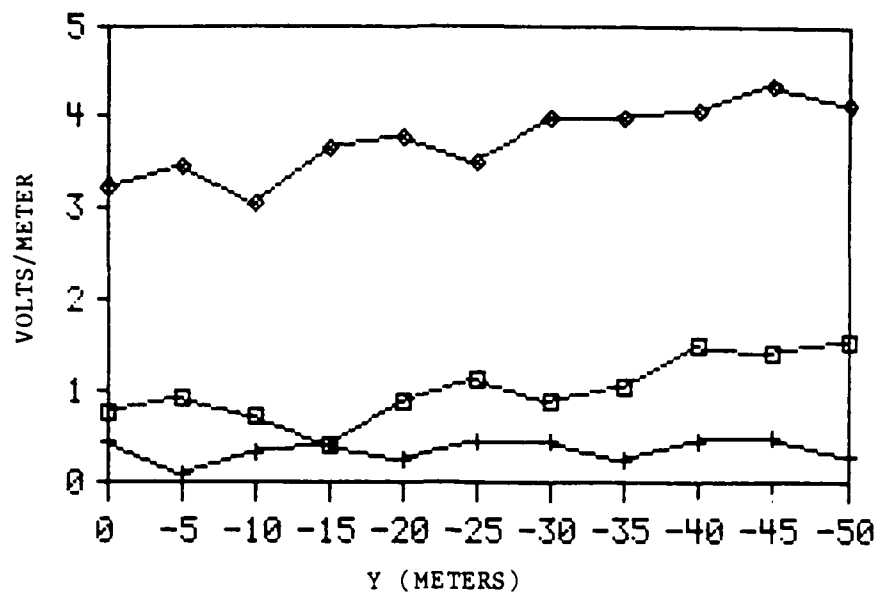
A. MAGNITUDE



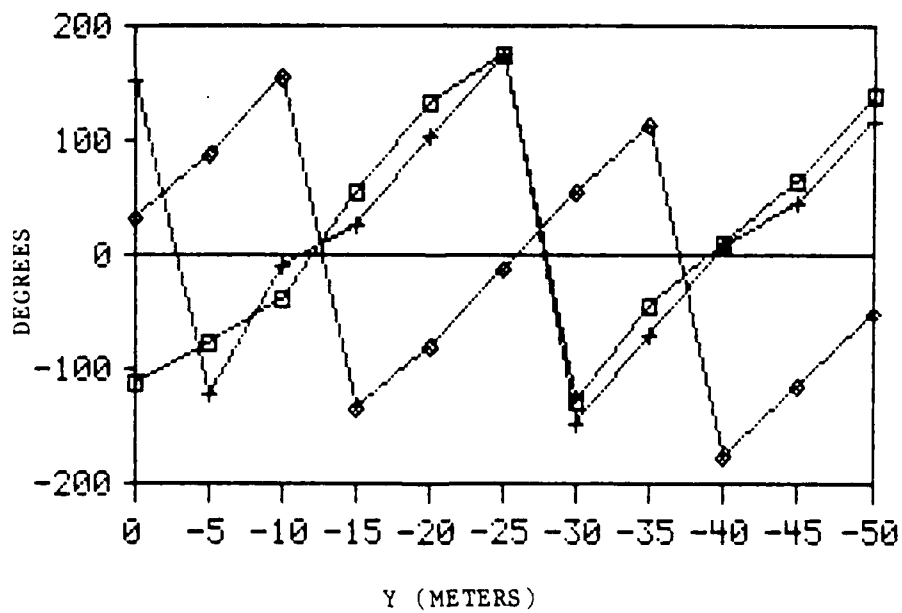
B. PHASE

□ Ex + Ey ○ Ez

Figure B-7. Common Mode Electric Field Magnitude and Phase
For 10.71 MHz in Longitudinal Direction at X = 15 m, Z = 4 m.



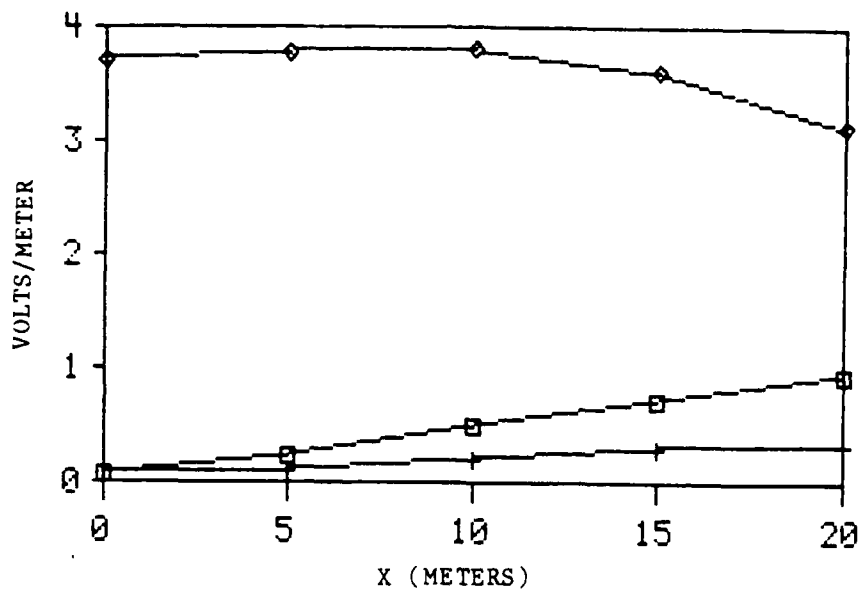
A. MAGNITUDE



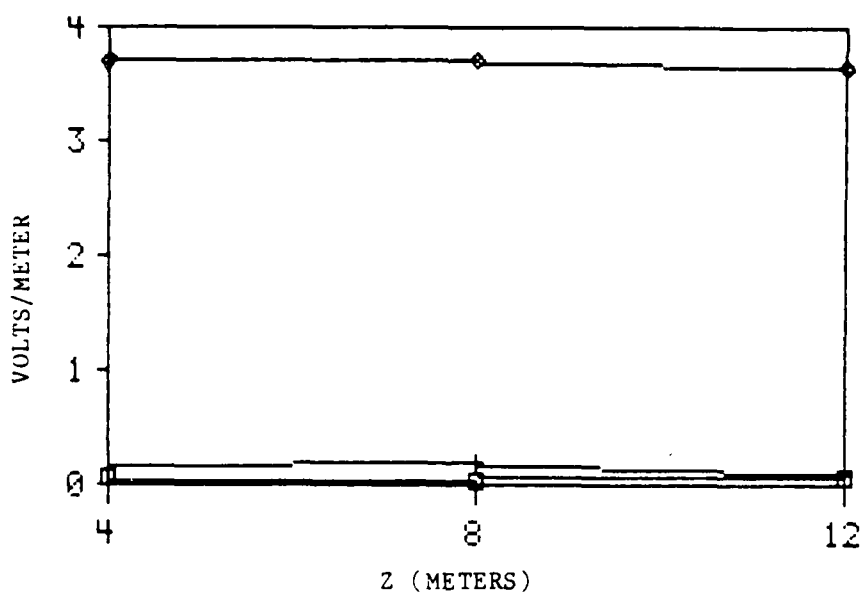
B. PHASE

□ Ex + Ey ◇ Ez

Figure B-8. Common Mode Electric Field Magnitude and Phase
For 10.71 MHz in Longitudinal Direction at X = 15 m, Z = 8 m.



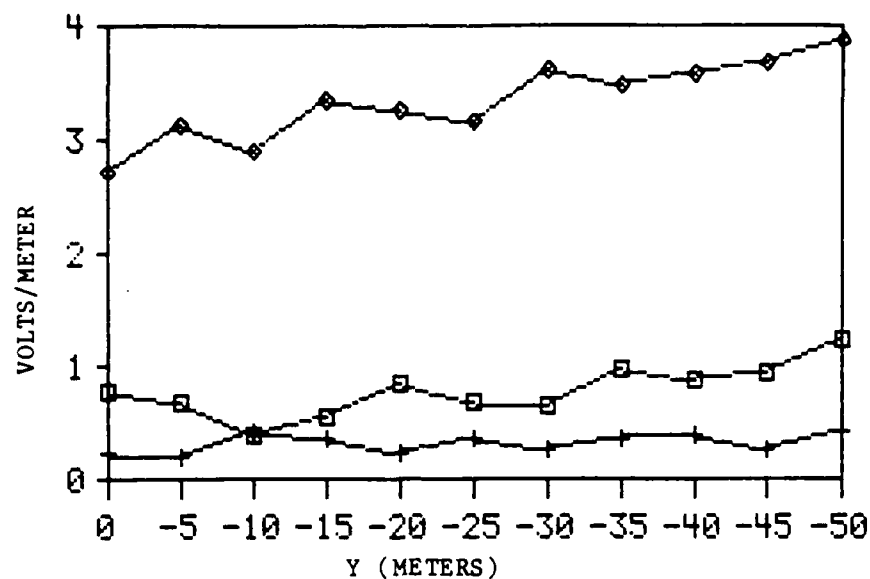
A. Horizontal (Z=4 m, Y=-20 m)



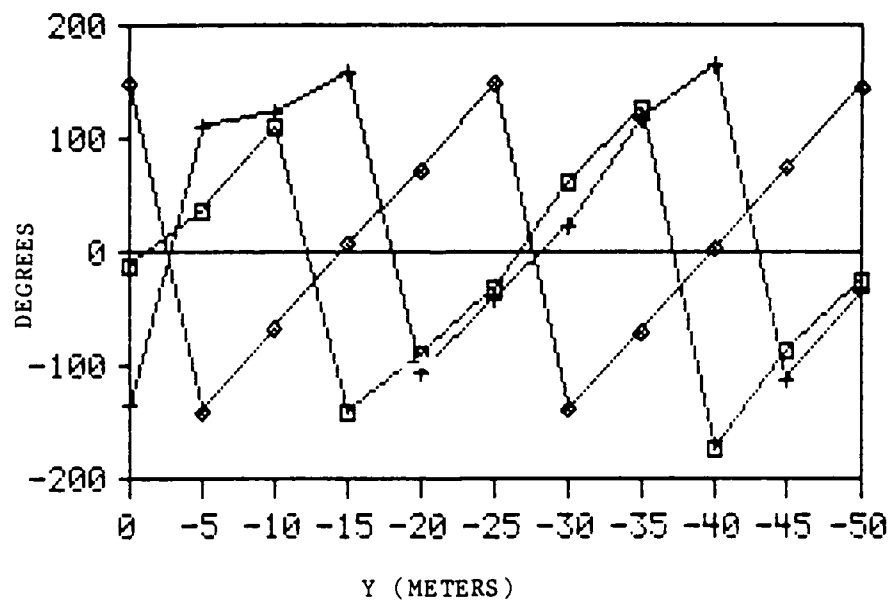
B. Vertical (X=0 m, Y=-20 m)

□ Ex + Ey ◇ Ez

Figure B-9. Common Mode Electric Field Magnitude For 10.71 MHz in Vertical and Horizontal Direction.



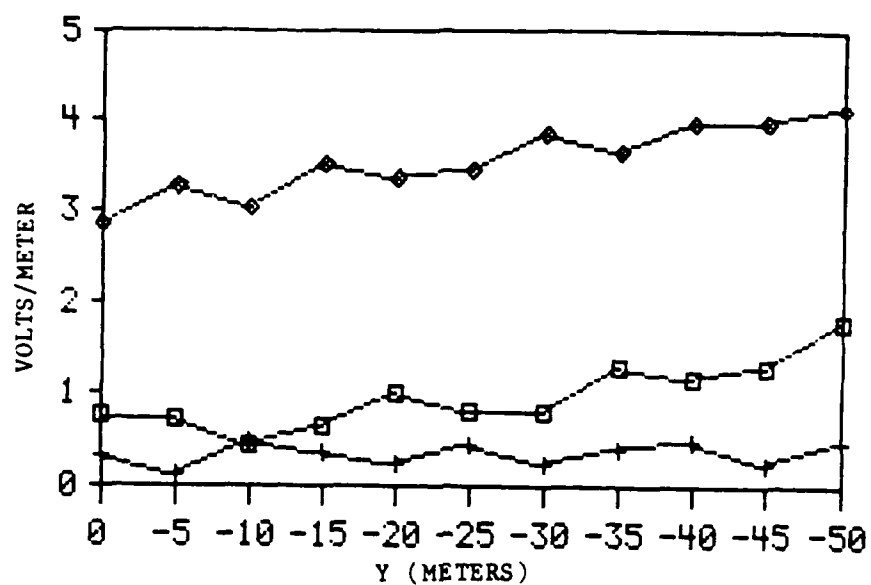
A. MAGNITUDE



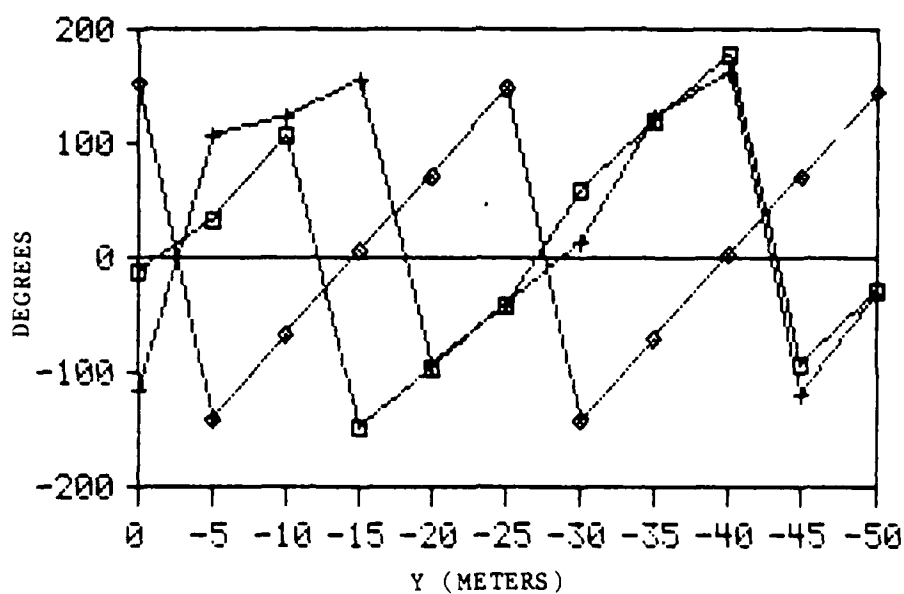
B. PHASE

□ Ex + Ey ○ Ez

Figure B-10. Common Mode Electric Field Magnitude and Phase For 12 MHz in Longitudinal Direction at X = 15 m, Z = 4 m.



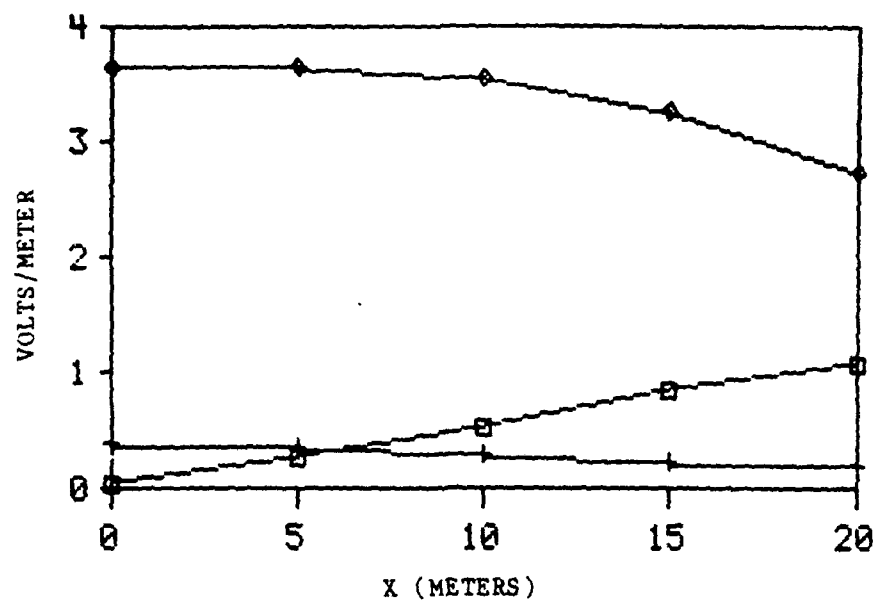
A. MAGNITUDE



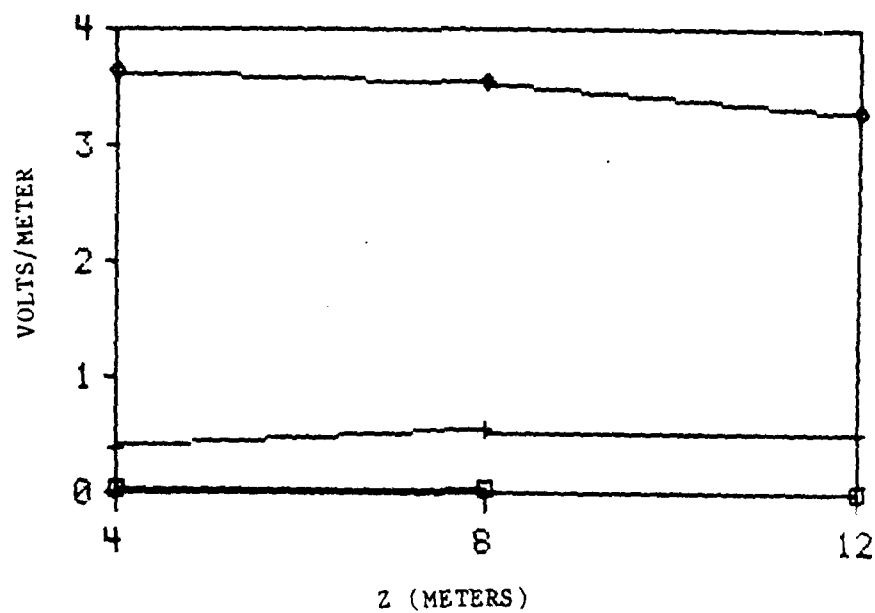
B. PHASE

□ Ex + Ey ◇ Ez

Figure B-11. Common Mode Electric Field Magnitude and Phase
For 12 MHz in Longitudinal Direction at X = 15 m, Z = 8 m.



A. Horizontal (Z=4 m, Y=-20 m)



B. Vertical (X=0 m, Y=-20 m)

□ Ex + Ey ◇ Ez

Figure B-12. Common Mode Electric Field Magnitude For 12 MHz in Vertical and Horizontal Direction.

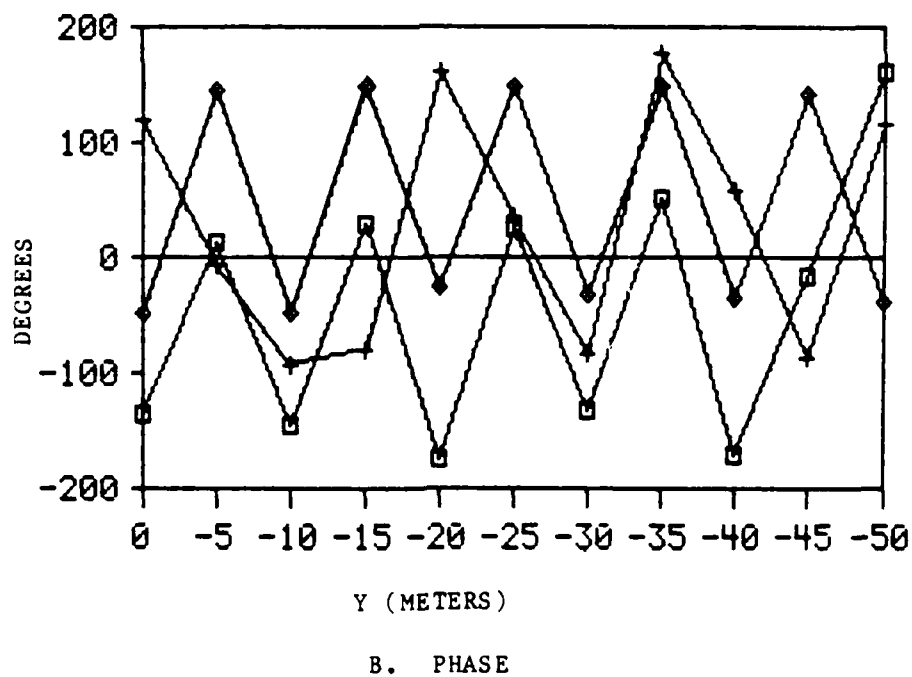
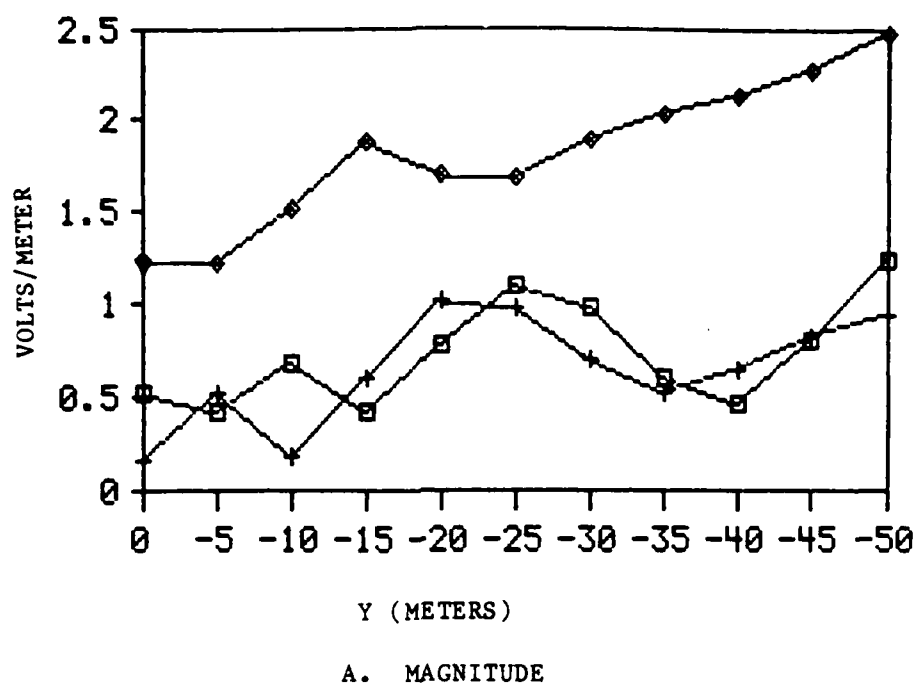
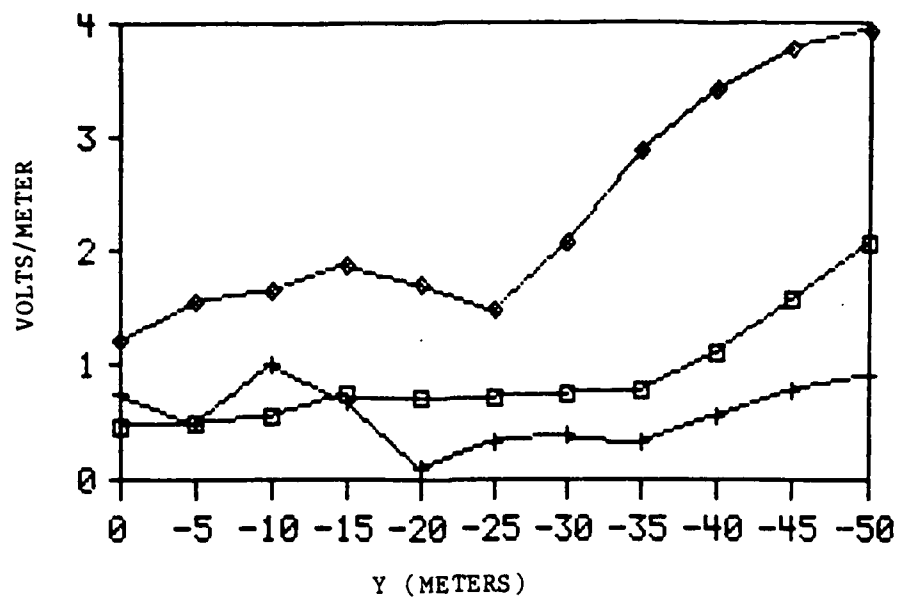
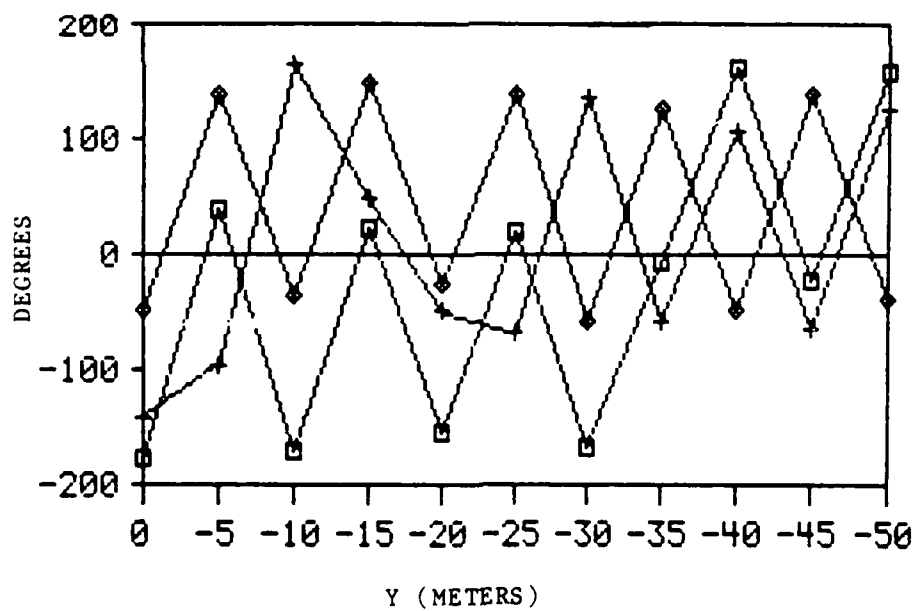


Figure B-13. Common Mode Electric Field Magnitude and Phase For 30 MHz in Longitudinal Direction at X = 15 m, Z = 4 m.



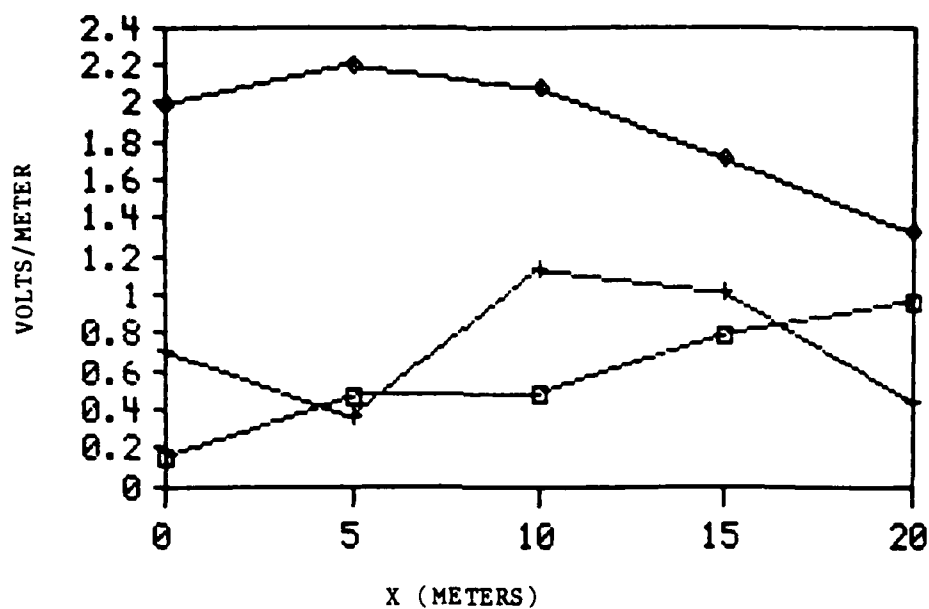
A. MAGNITUDE



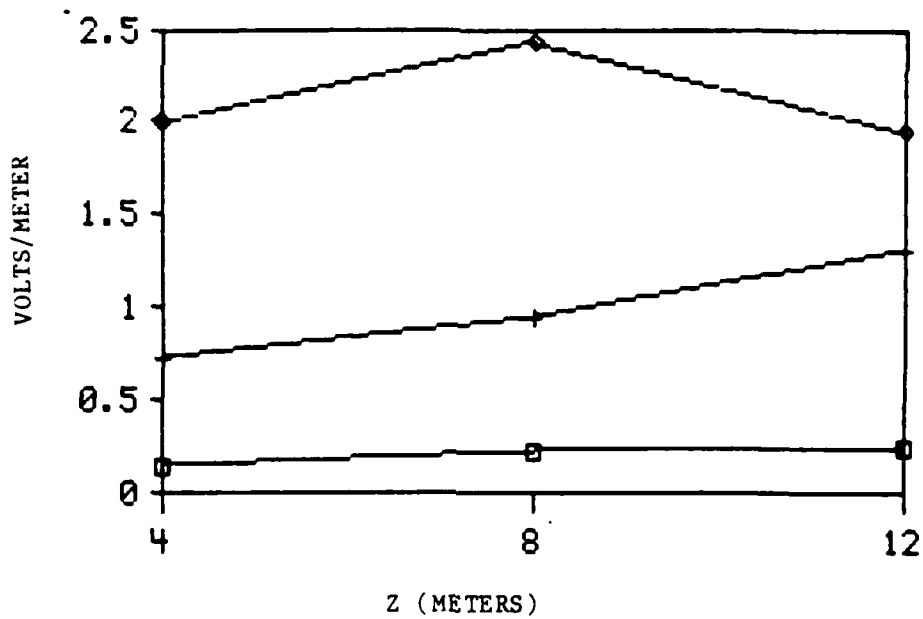
B. PHASE

□ Ex + Ey ◇ Ez

Figure B-14. Common Mode Electric Field Magnitude and Phase For 30 MHz in Longitudinal Direction at X = 15 m, Z = 8 m.



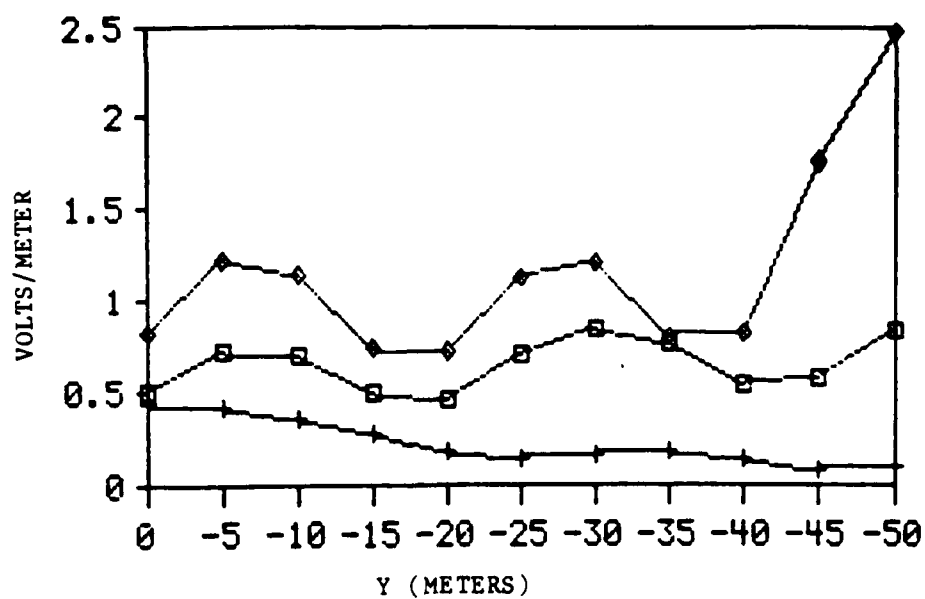
A. Horizontal ($Z=4$ m, $Y=-20$ m)



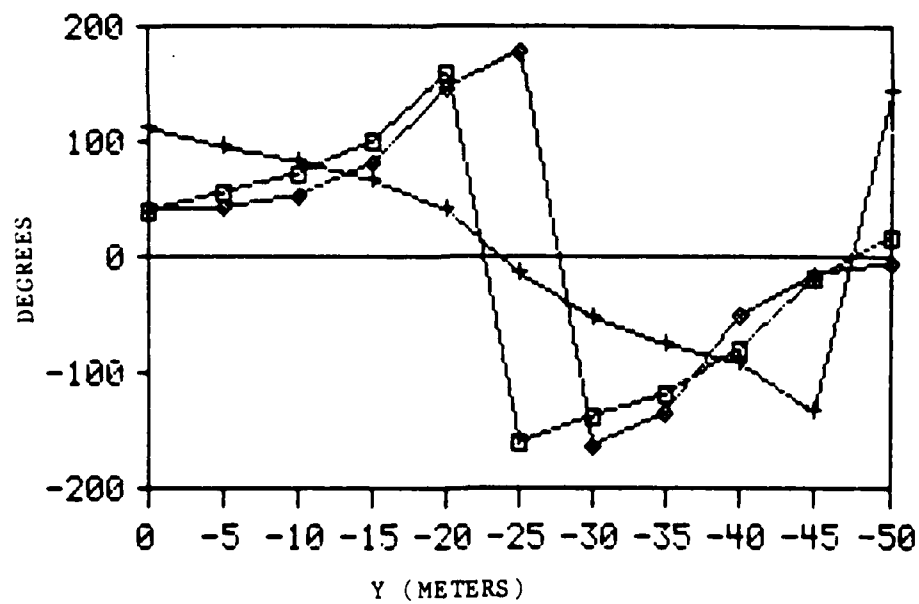
B. Vertical ($X=0$ m, $Y=-20$ m)

□ E_x + E_y ◇ E_z

Figure B-15. Common Mode Electric Field Magnitude For 30 MHz in Vertical and Horizontal Direction.



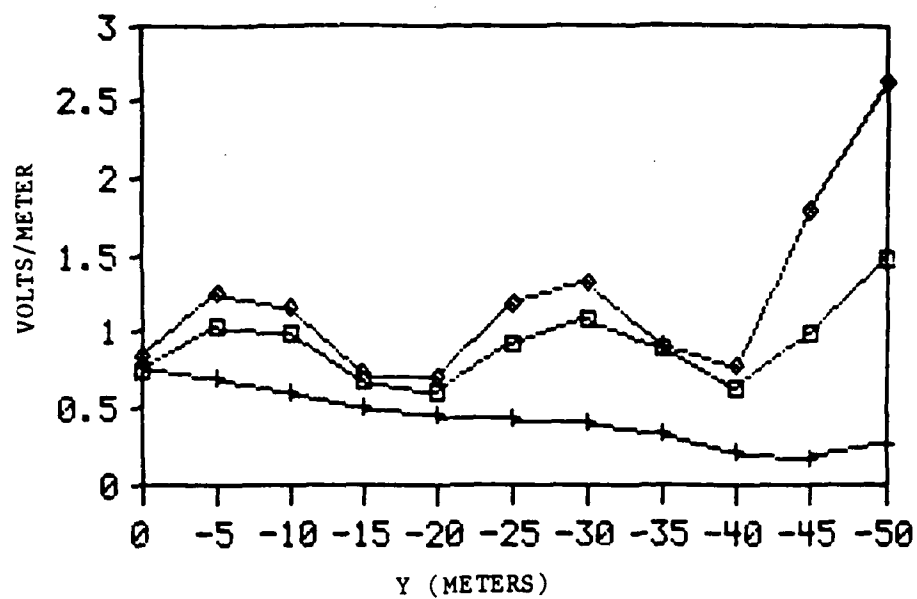
A. MAGNITUDE



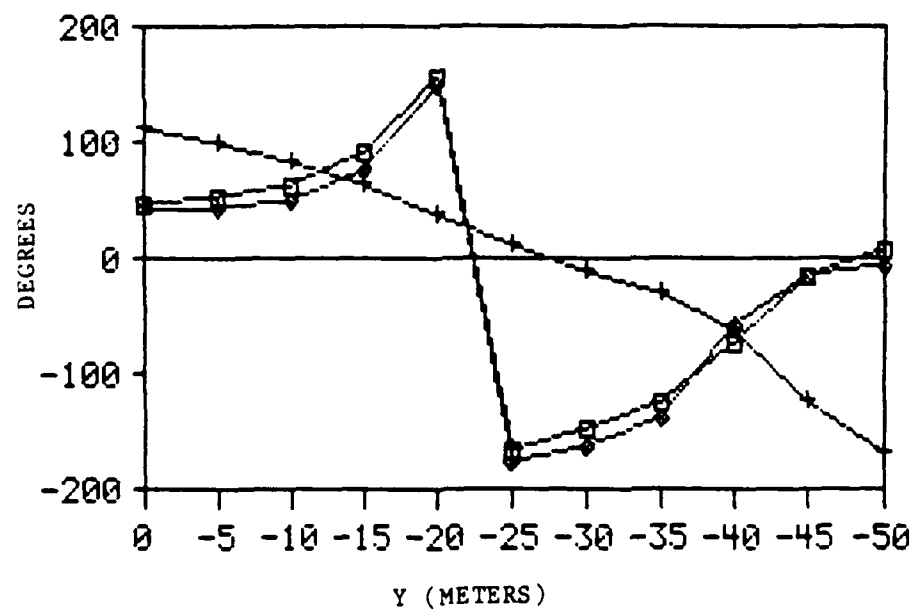
B. PHASE

□ E_x + E_y ◇ E_z

Figure B-16. Differential Mode Electric Field Magnitude and Phase For 6 MHz in Longitudinal Direction at X = 15 m, Z = 4 m.



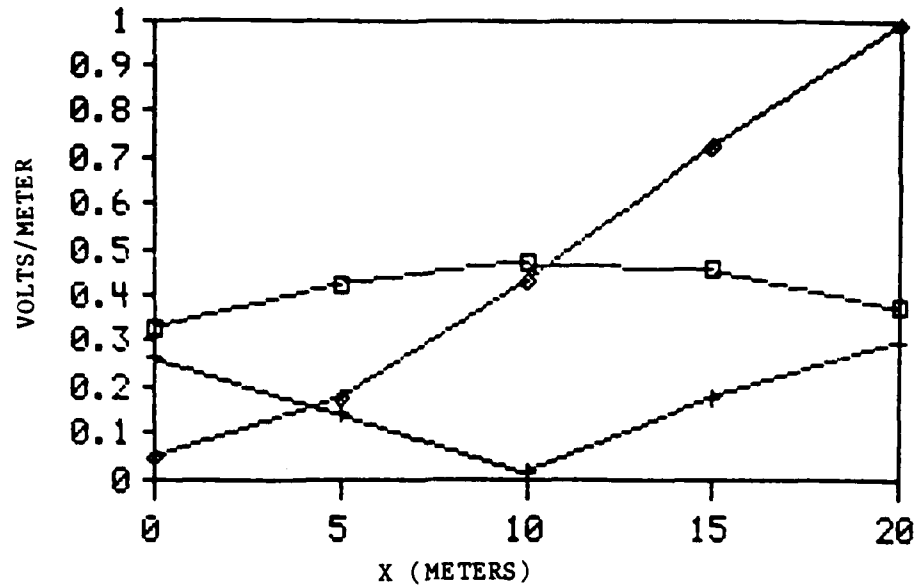
A. MAGNITUDE



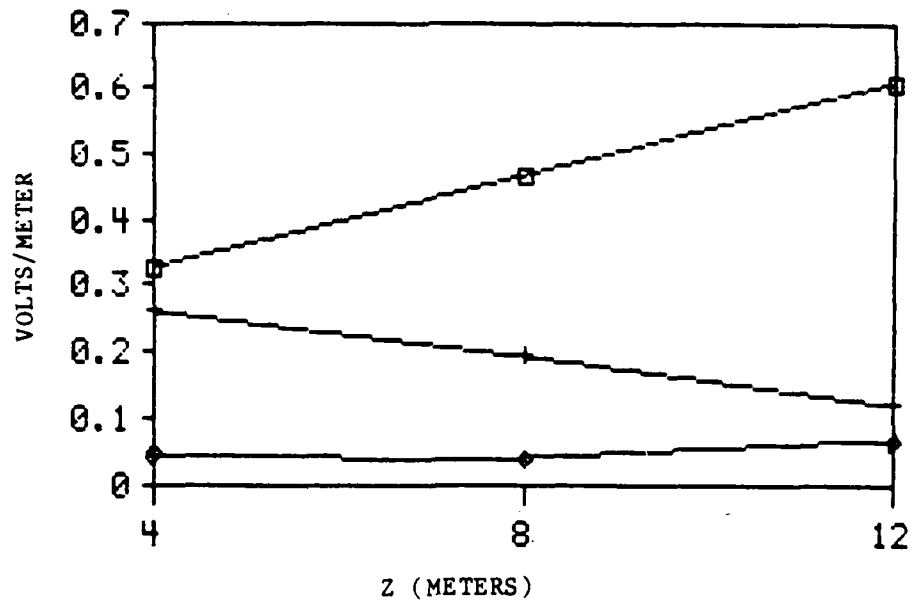
B. PHASE

□ Ex + Ey ◇ Ez

Figure B-17. Differential Mode Electric Field Magnitude and Phase For 6 MHz in Longitudinal Direction at $X = 15$ m, $Z = 8$ m.



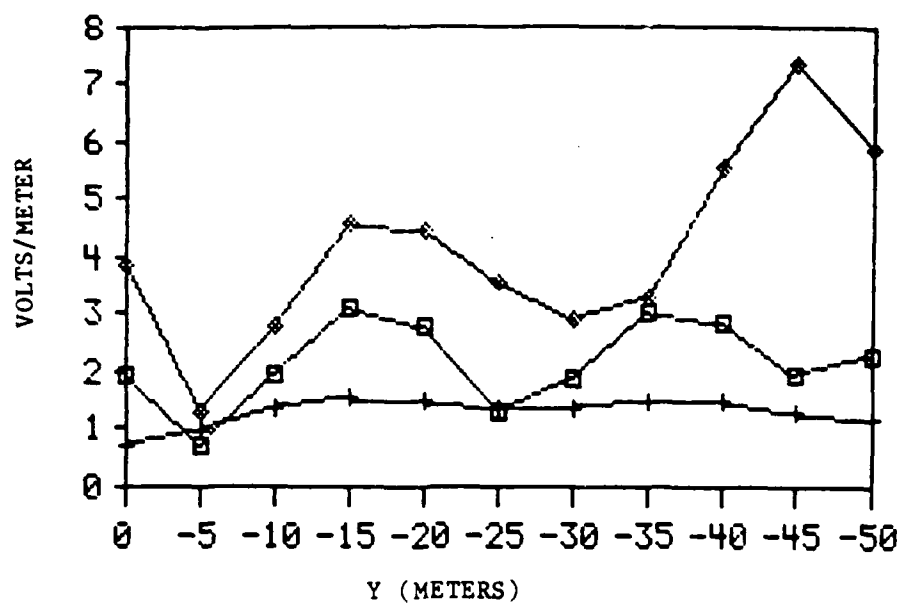
A. Horizontal (Z=4 m, Y=-20 m)



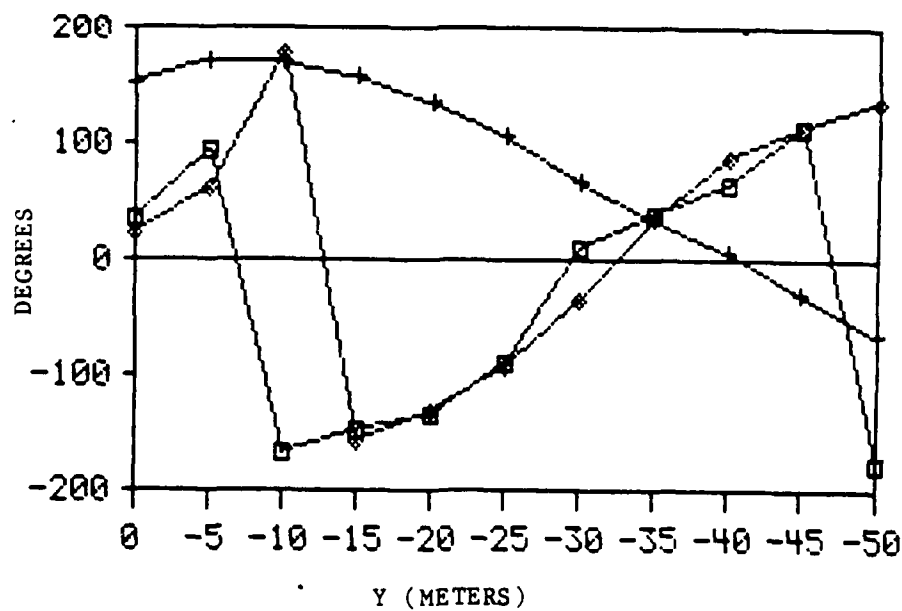
B. Vertical (X=0 m, Y=-20 m)

□ Ex + Ey ◇ Ez

Figure B-18. Differential Mode Electric Field Magnitude For 6 MHz in Vertical and Horizontal Direction.



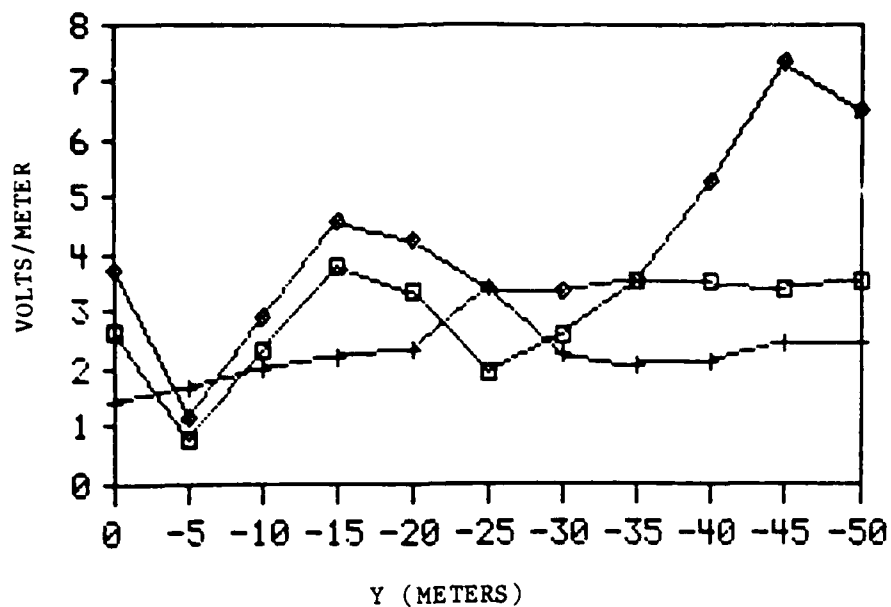
A. MAGNITUDE



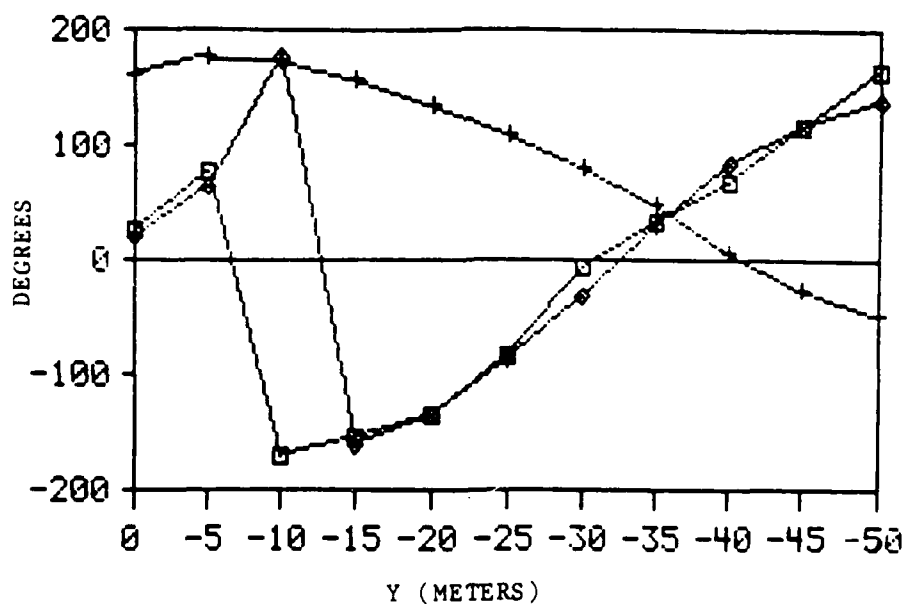
B. PHASE

□ E_x + E_y ◇ E_z

Figure B-19. Differential Mode Electric Field Magnitude and Phase For 8 MHz in Longitudinal Direction at X = 15 m, Z = 4 m.



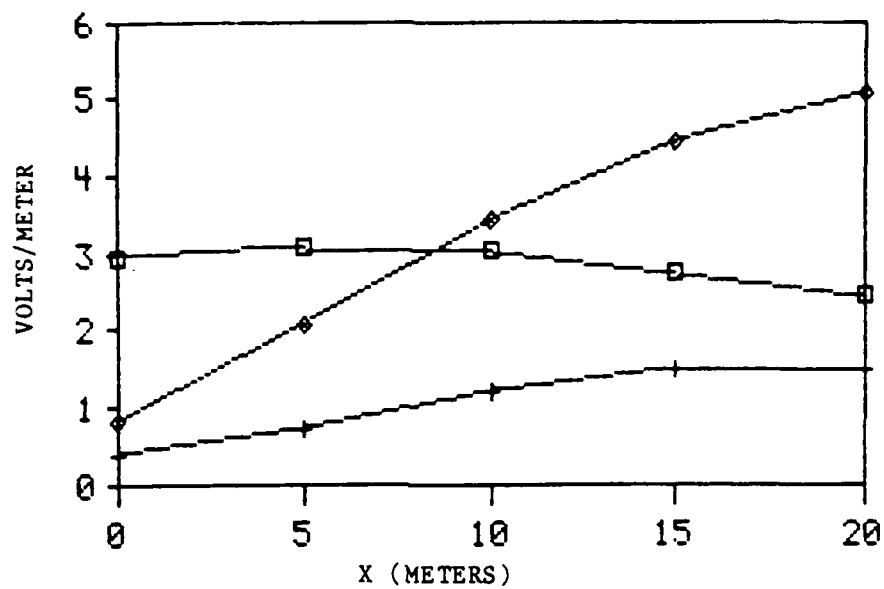
A. MAGNITUDE



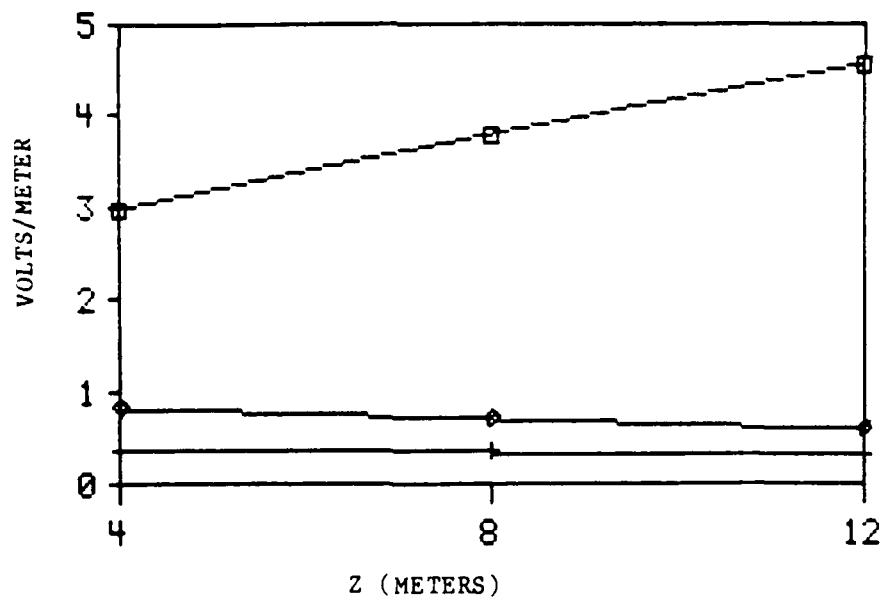
B. PHASE

□ Ex + Ey ◇ Ez

Figure B-20. Differential Mode Electric Field Magnitude and Phase For 8 MHz in Longitudinal Direction at $X = 15$ m, $Z = 8$ m.



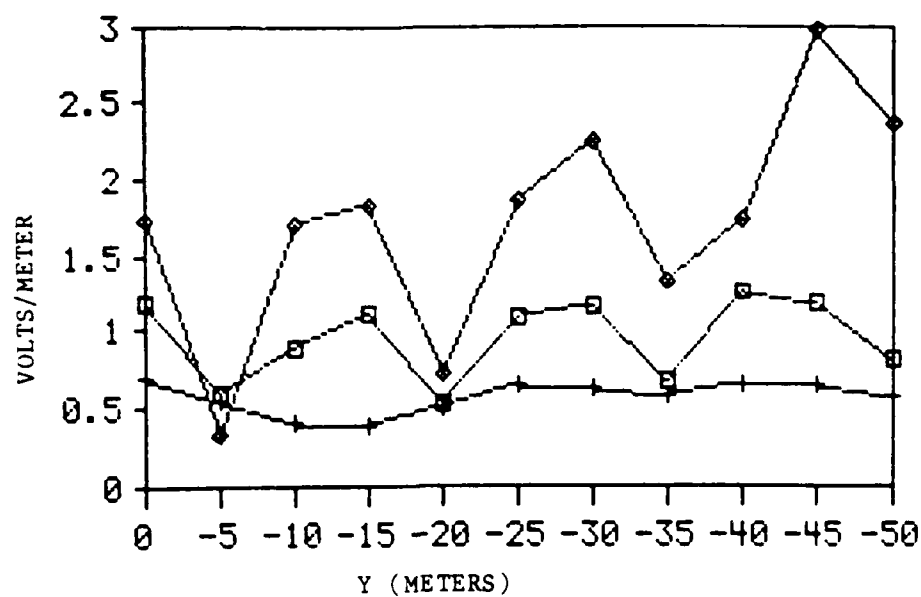
A. Horizontal (Z=4 m, Y=-20 m)



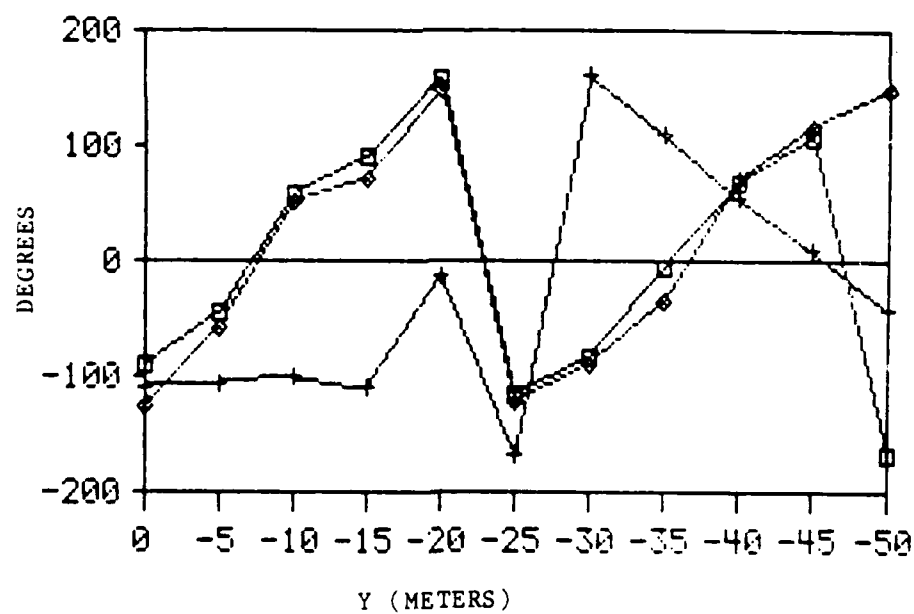
B. Vertical (X=0 m, Y=-20 m)

□ Ex + Ey ◇ Ez

Figure B-21. Differential Mode Electric Field Magnitude For 8 MHz in Vertical and Horizontal Direction.



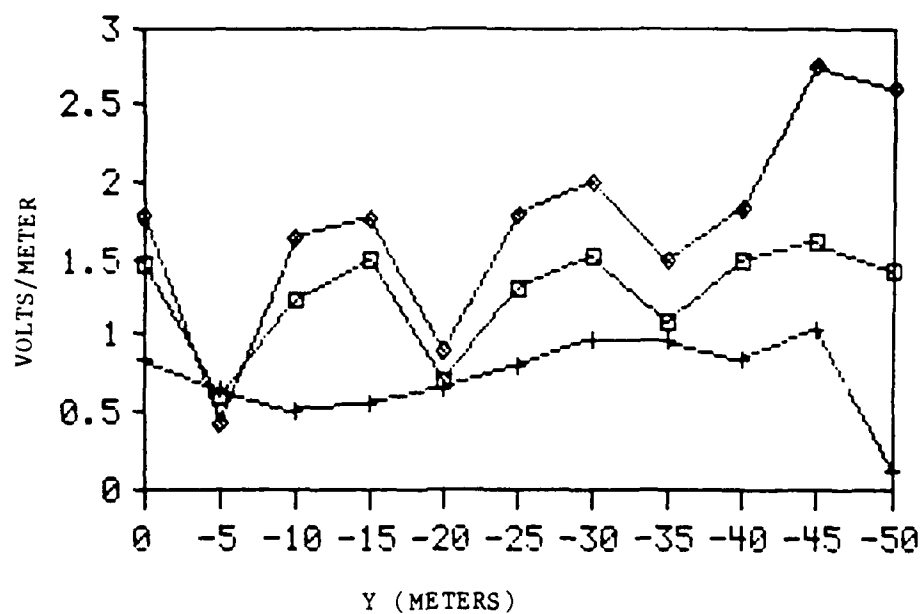
A. MAGNITUDE



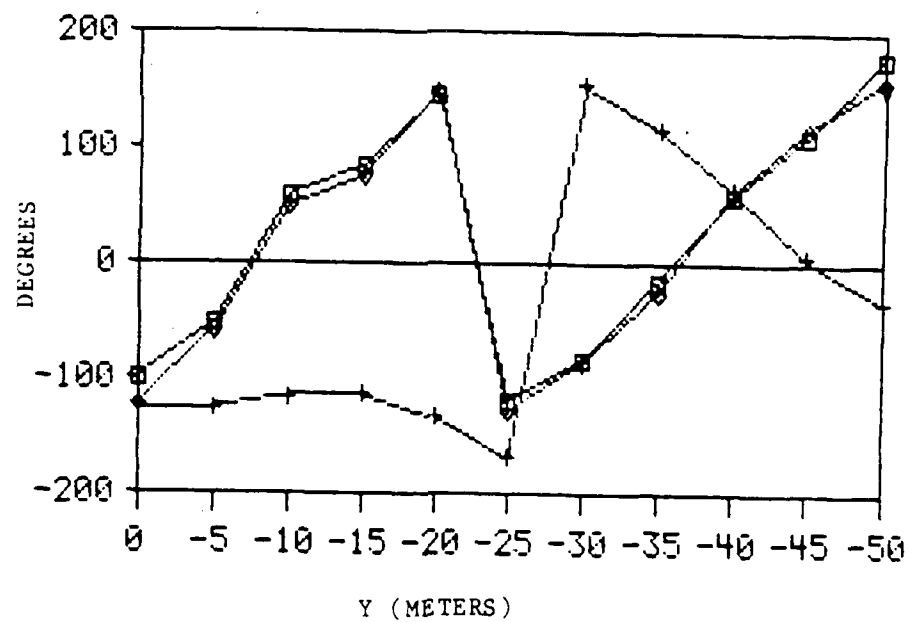
B. PHASE

□ Ex + Ey ◇ Ez

Figure B-22. Differential Mode Electric Field Magnitude and Phase For 10.71 MHz in Longitudinal Direction at $X = 15$ m, $Z = 4$ m.



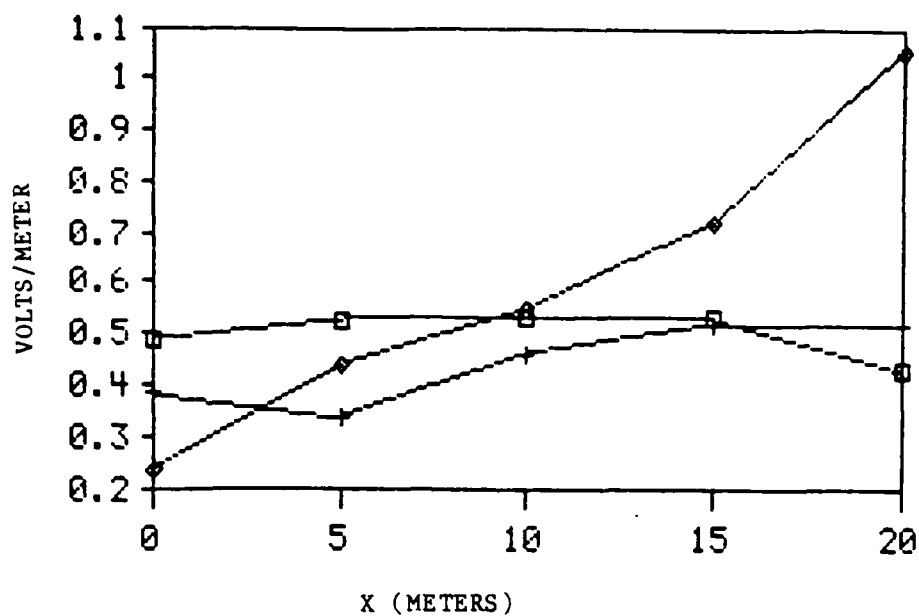
A. MAGNITUDE



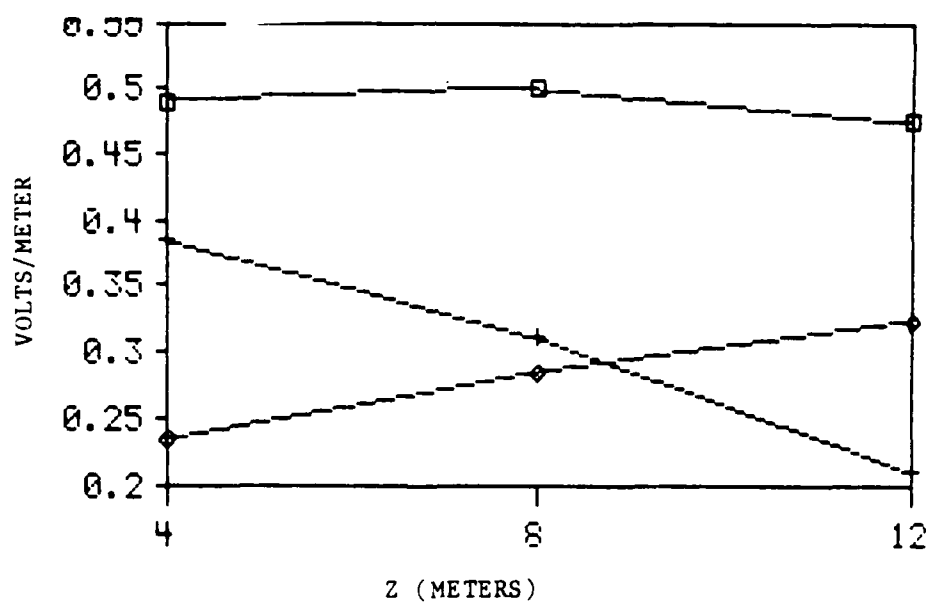
B. PHASE

□ E_x + E_y ◇ E_z

Figure B-23. Differential Mode Electric Field Magnitude and Phase For 10.71 MHz in Longitudinal Direction at $X = 15$ m, $Z = 8$ m.



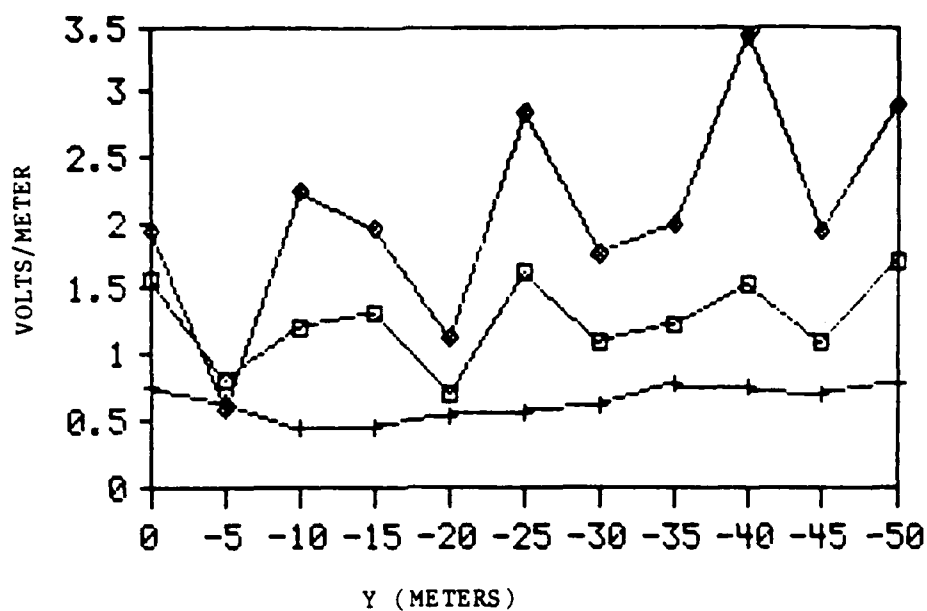
A. Horizontal (Z=4 m, Y=-20 m)



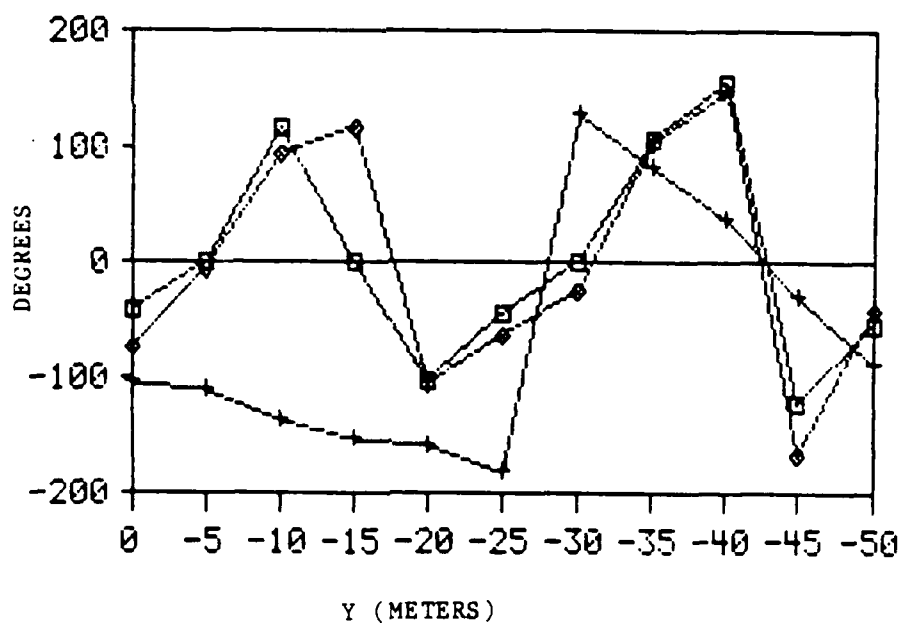
B. Vertical (X=0 m, Y=-20 m)

□ Ex + Ey ◇ Ez

Figure B-24. Differential Mode Electric Field Magnitude
For 10.71 MHz in Vertical and Horizontal Direction.



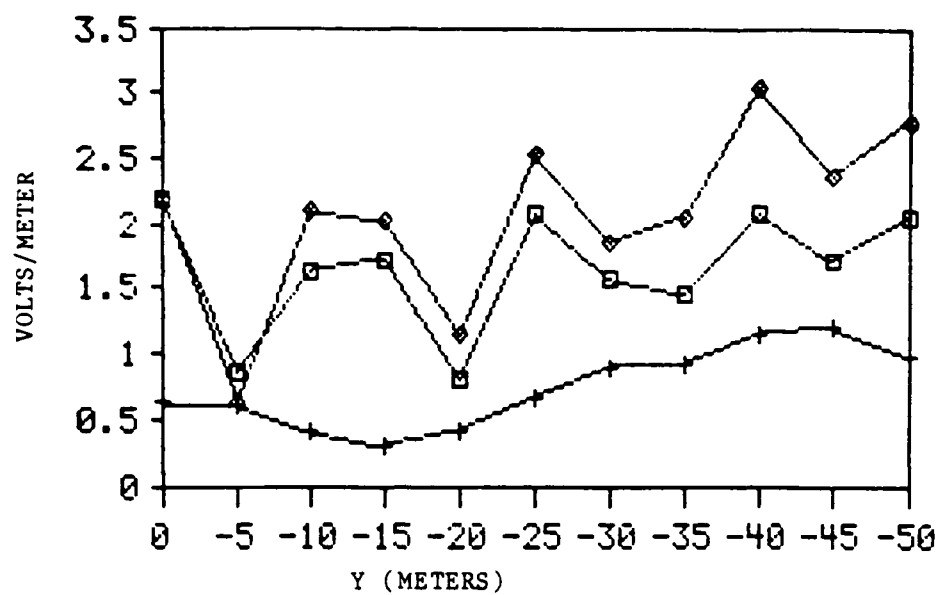
A. MAGNITUDE



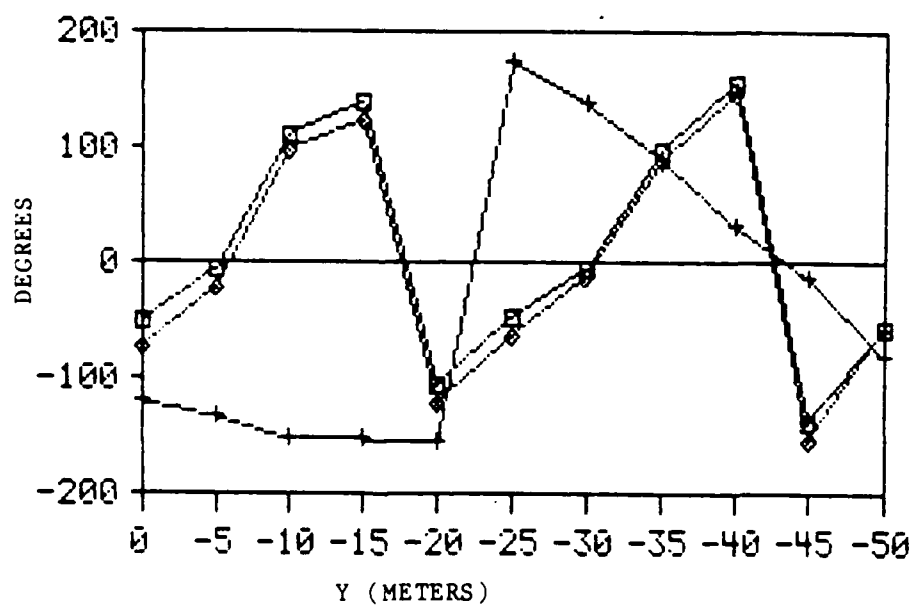
B. PHASE

□ E_x + E_y ○ E_z

Figure B-25. Differential Mode Electric Field Magnitude and Phase For 12 MHz in Longitudinal Direction at $X = 15$ m, $Z = 4$ m.



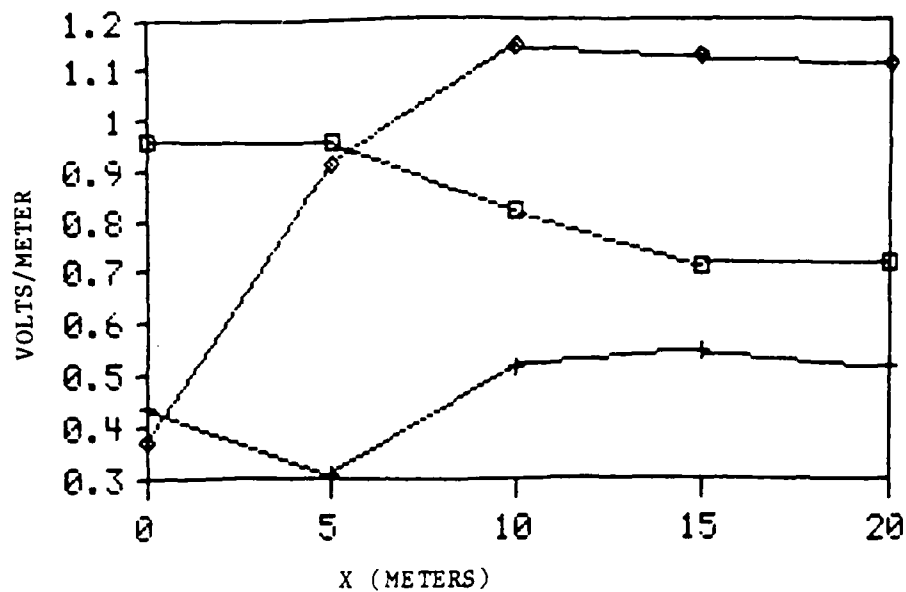
A. MAGNITUDE



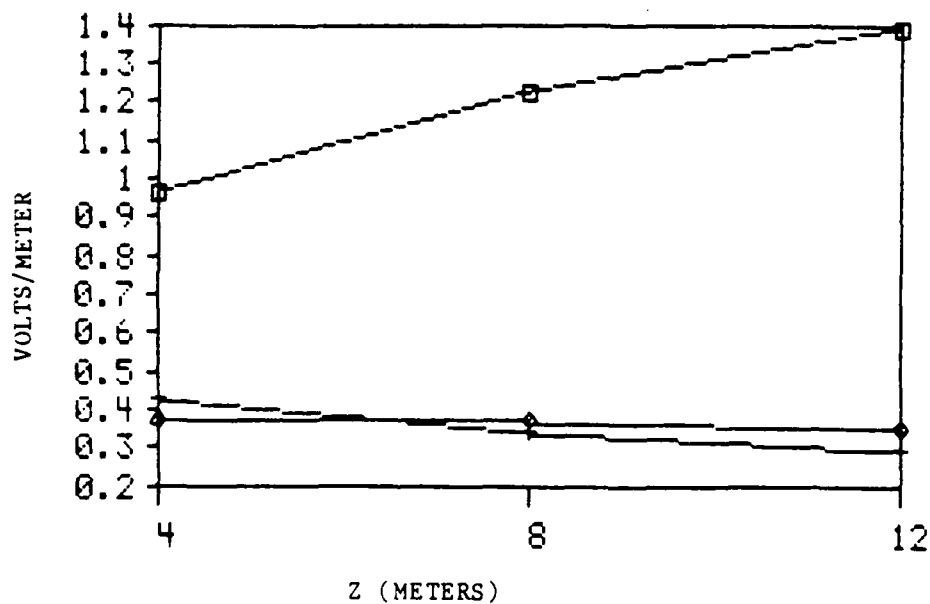
B. PHASE

□ Ex + Ey ◇ Ez

Figure B-26. Differential Mode Electric Field Magnitude and Phase For 12 MHz in Longitudinal Direction at $X = 15$ m, $Z = 8$ m.



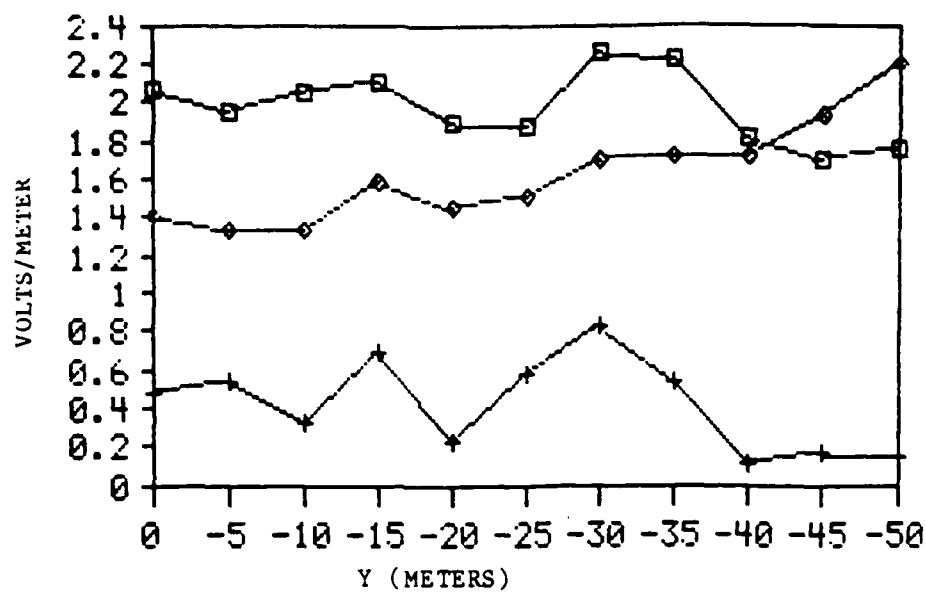
A. Horizontal (Z=4 m, Y=-20 m)



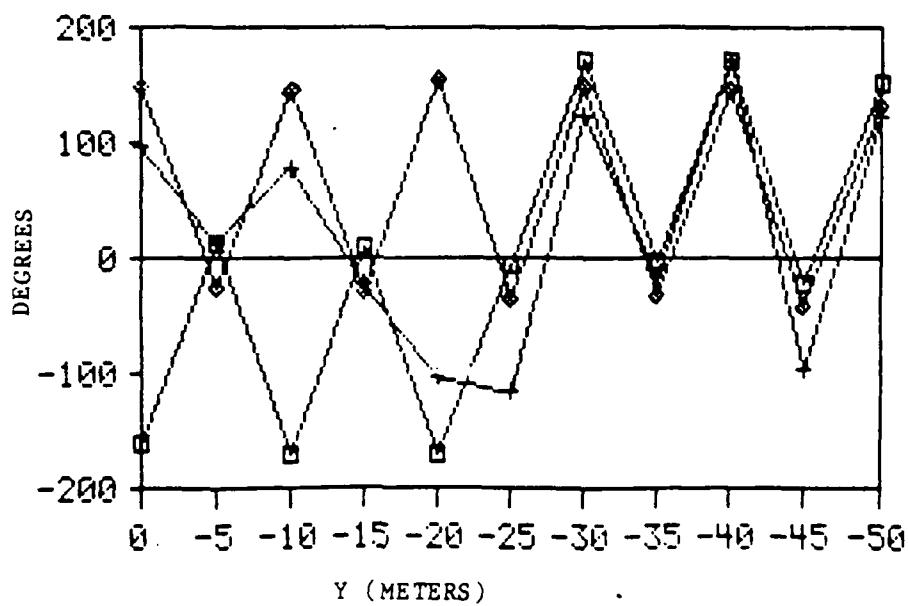
B. Vertical (X=0 m, Y=-20 m)

□ Ex + Ey ◇ Ez

Figure B-27. Differential Mode Electric Field Magnitude For 12 MHz in Vertical and Horizontal Direction.



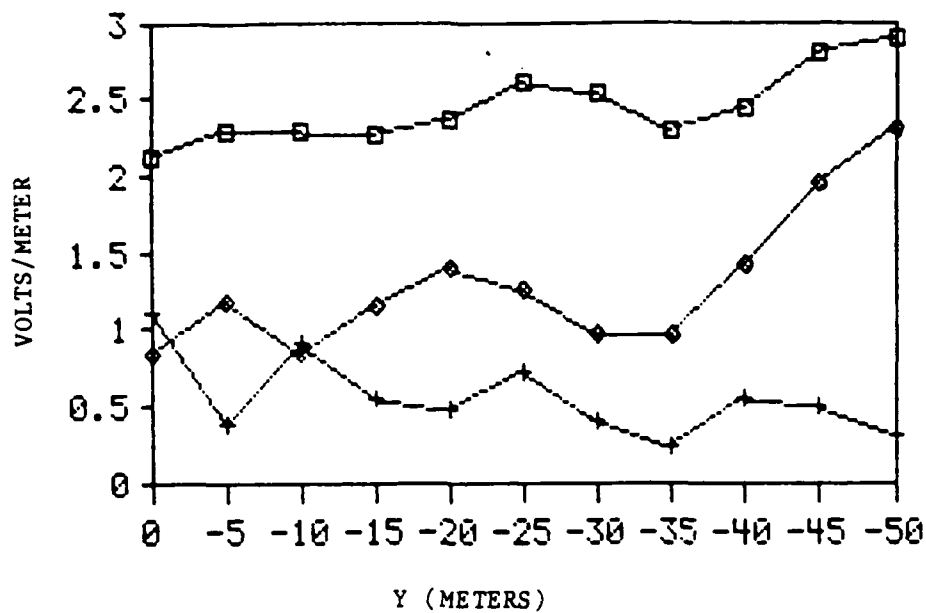
A. MAGNITUDE



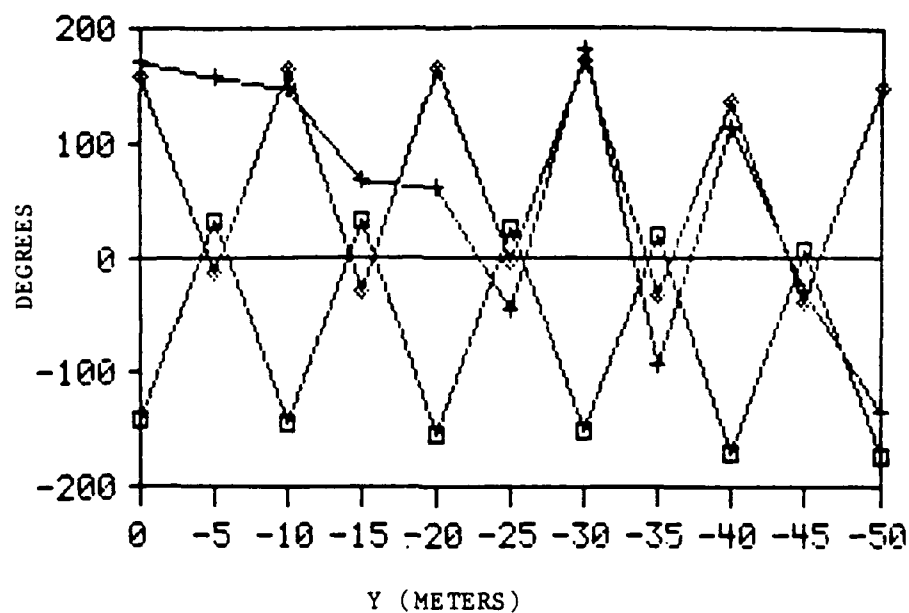
B. PHASE

□ Ex + Ey ◇ Ez

Figure B-28. Differential Mode Electric Field Magnitude and Phase For 30 MHz in Longitudinal Direction at $X = 15$ m, $Z = 4$ m.



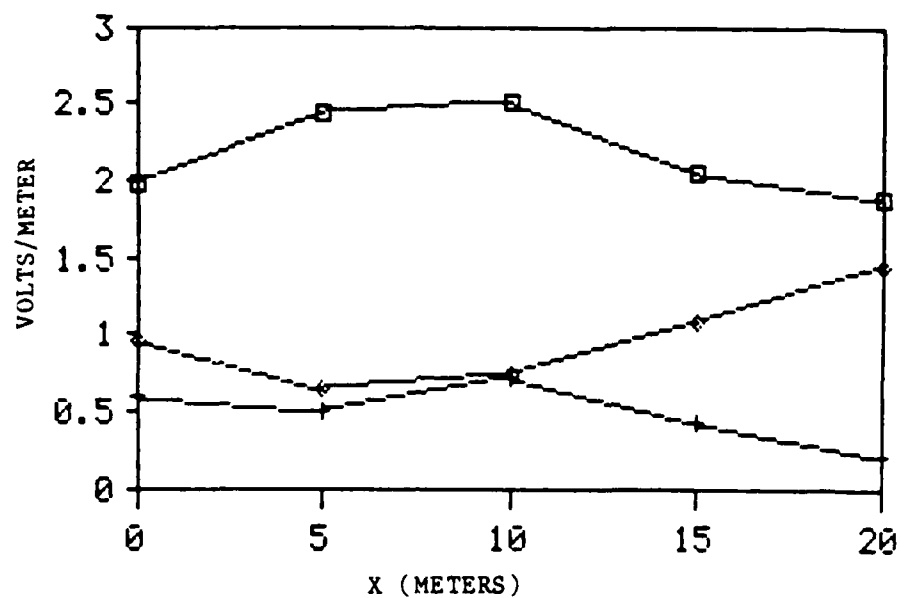
A. MAGNITUDE



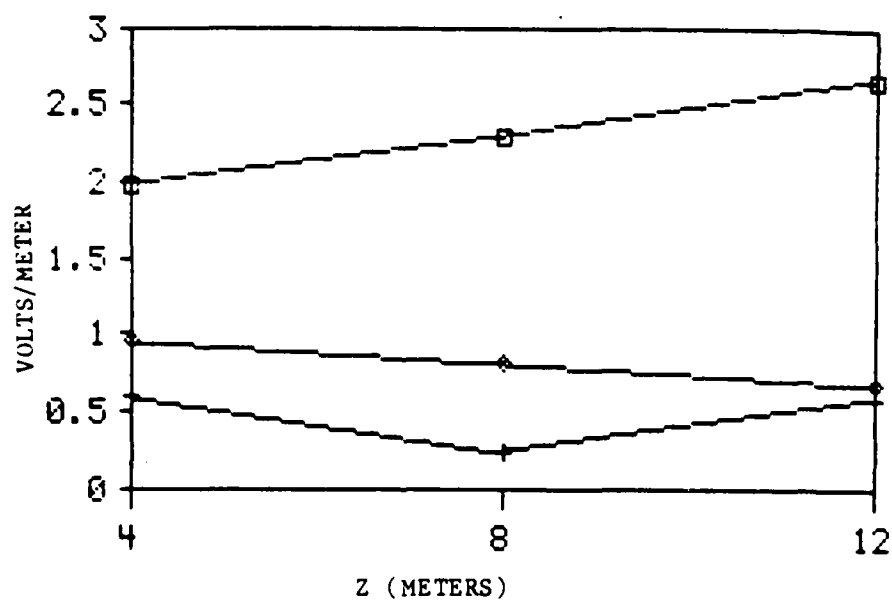
B. PHASE

□ E_x + E_y ◊ E_z

Figure B-29. Differential Mode Electric Field Magnitude and Phase For 30 MHz in Longitudinal Direction at $X = 15$ m, $Z = 8$ m.



A. Horizontal (Z=4 m, Y=-20 m)



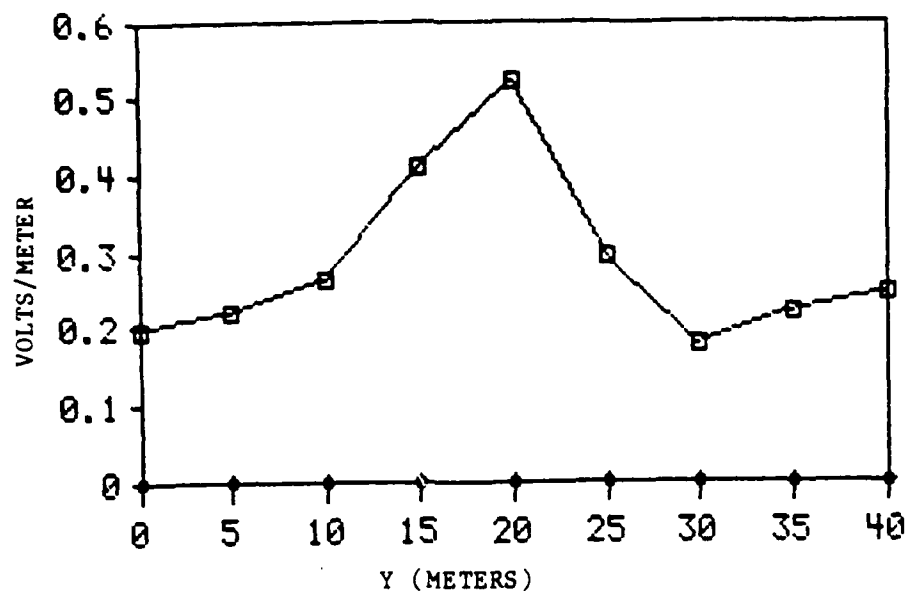
B. Vertical (X=0 m, Y=-20 m)

□ Ex + Ey ◇ Ez

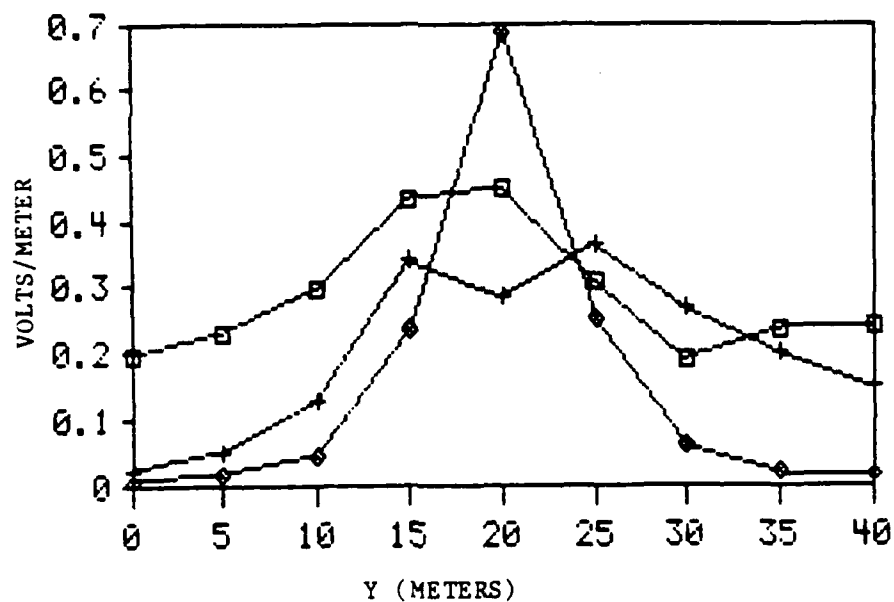
Figure B-30. Differential Mode Electric Field Magnitude
For 30 MHz in Vertical and Horizontal Direction.

Appendix C

Appendix C contains additional graphs of the the fields beneath the test object and the ground plane. Additional plots give the electric field values for different quantities of x at 6 MHz and 12 Mhz. The graphs are provided for both a concrete ground plane and no ground plane. For each frequency and ground plane configuration, graphs are provided that illustrate the electric field at $Z = 4$ meters and $X = 0$ meters, $X = 5$ meters, $X = 10$ meters, $X = 15$ meters, and $X = 20$ meters.



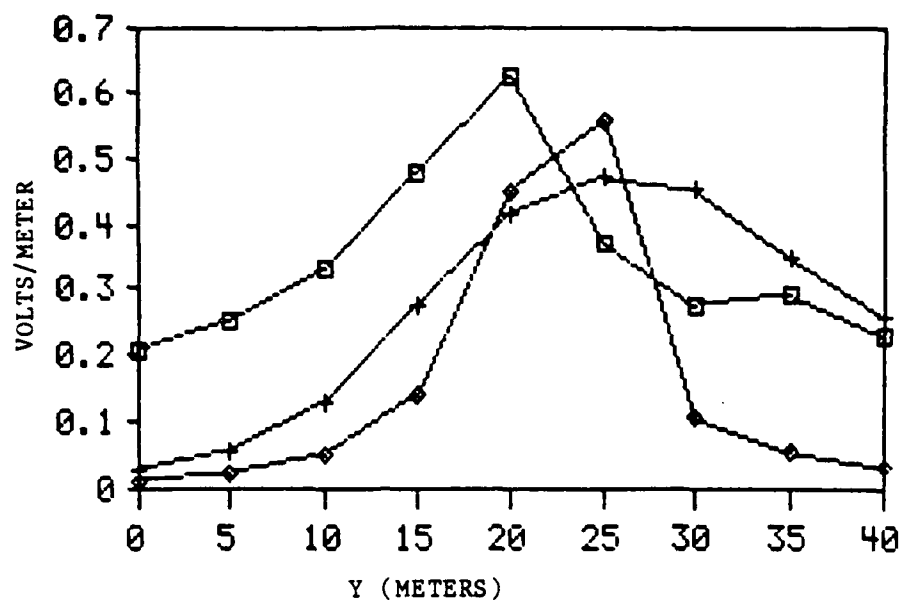
A. Longitudinal Direction at X = 0 M.



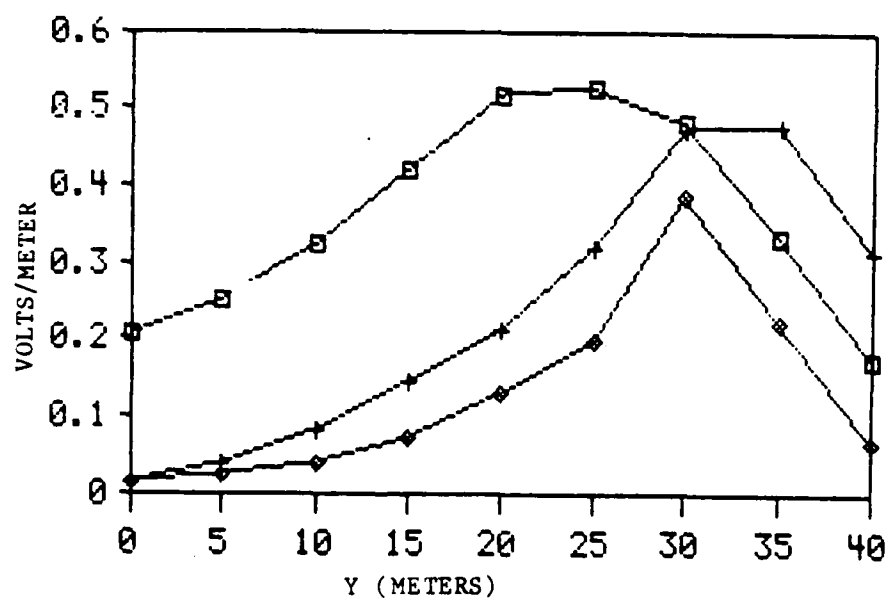
B. Longitudinal Direction at X = 5 M.

□ Ex + Ey ◇ Ez

Figure C-1. Electric Field Magnitude at 3 Meters Below Test Object.
Horizontal Incident Field at 6 MHz with no Ground Plane.



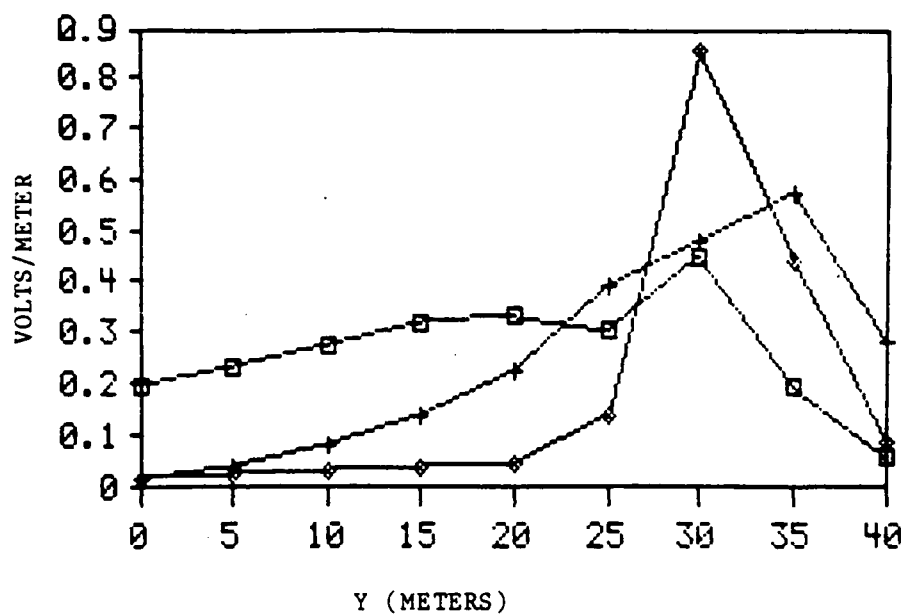
A. Longitudinal Direction at X = 10 M.



B. Longitudinal Direction at X = 15 M.

□ Ex + Ey ◇ Ez

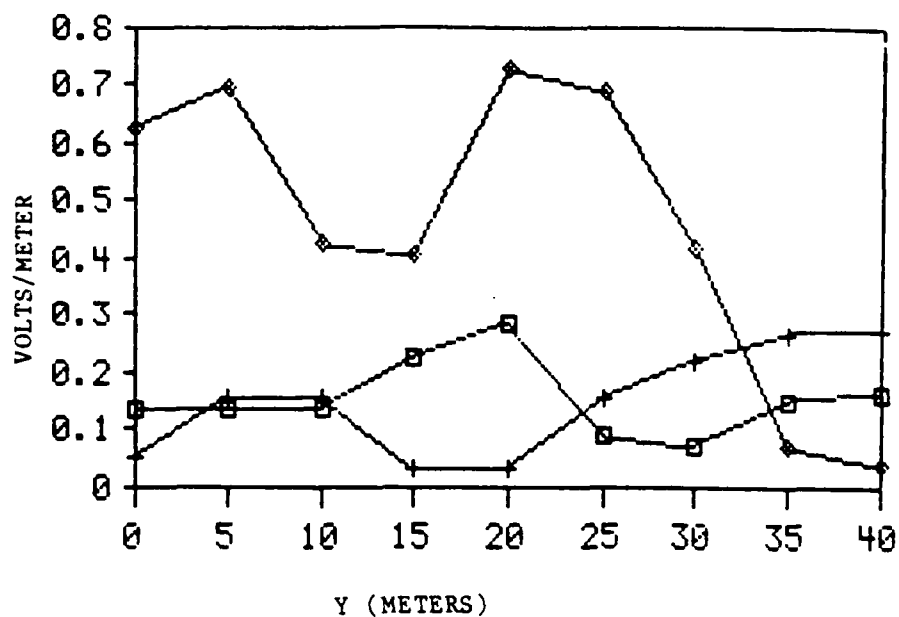
Figure C-2. Electric Field Magnitude at 3 Meters Below Test Object.
Horizontal Incident Field at 6 MHz with no Ground Plane.



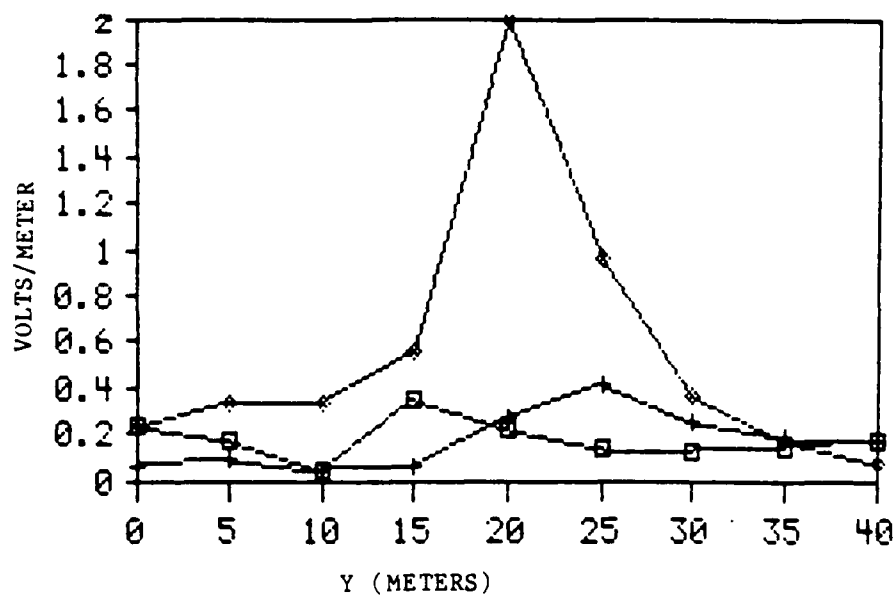
B. Longitudinal Direction at X = 20 M.

□ Ex + Ey ◇ Ez

Figure C-3. Electric Field Magnitude at 3 Meters Below Test Object.
Horizontal Incident Field at 6 MHz with no Ground Plane.



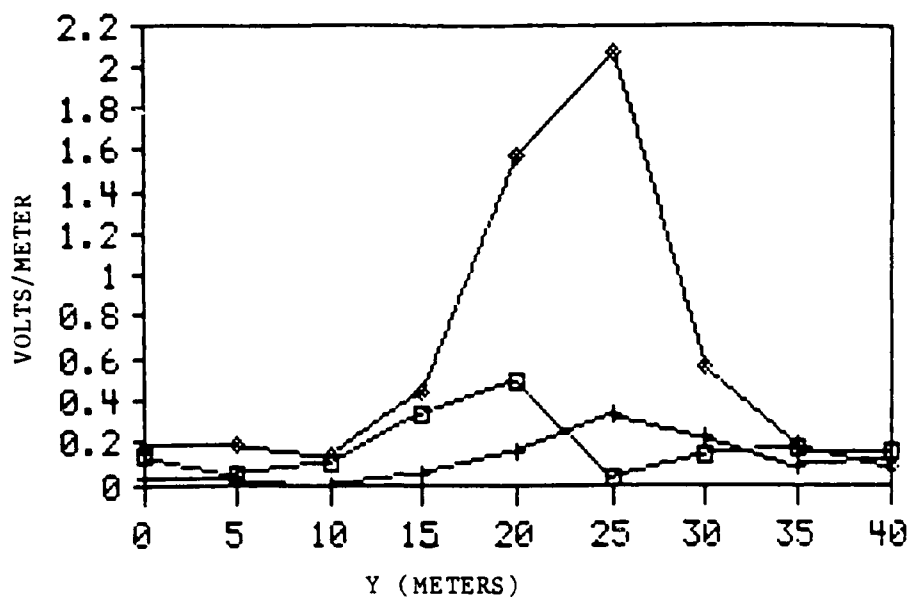
A. Longitudinal Direction at $X = 0$ M.



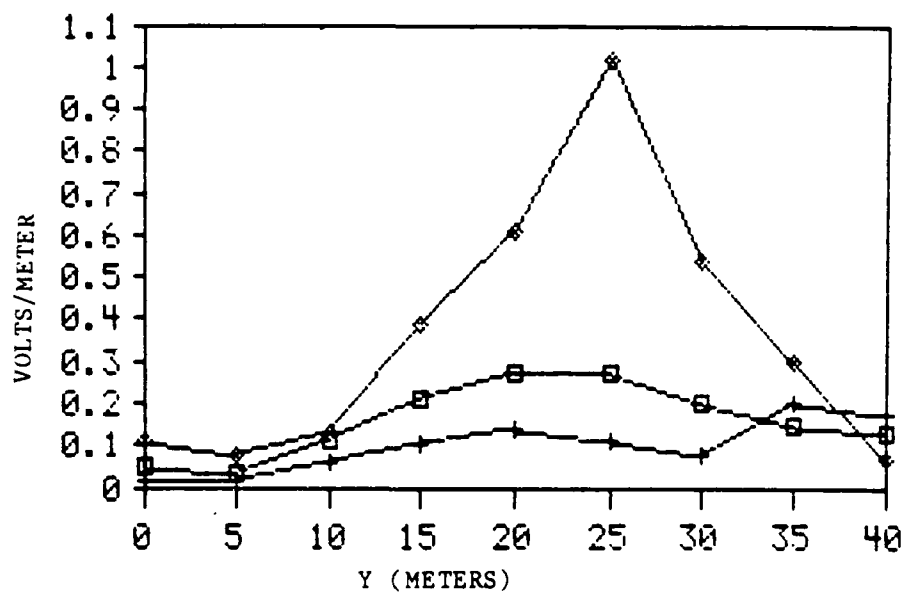
B. Longitudinal Direction at $X = 5$ M.

□ Ex + Ey ◇ Ez

Figure C-4. Electric Field Magnitude at 3 Meters Below Test Object.
Horizontal Incident Field at 6 MHz with Concrete Ground Plane.



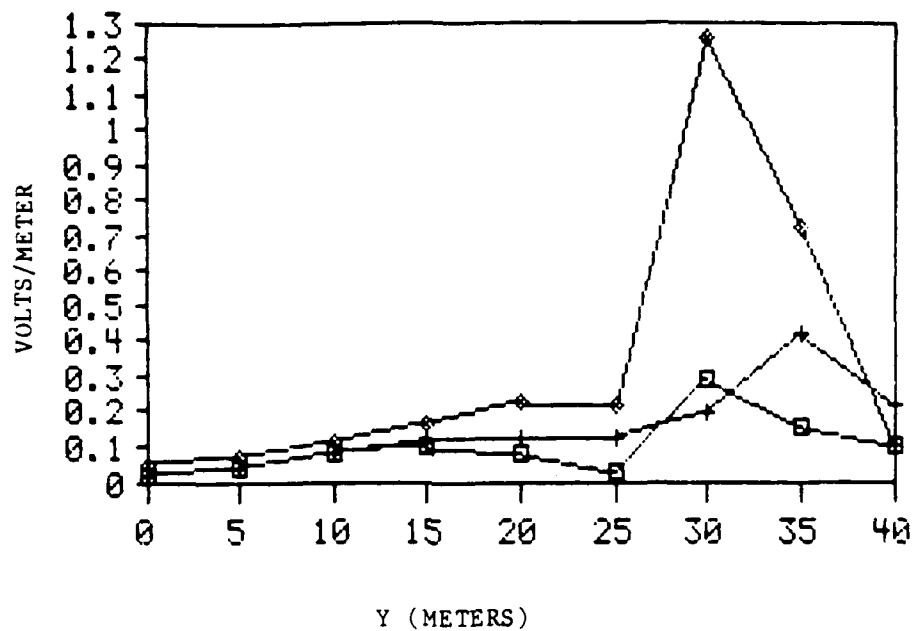
A. Longitudinal Direction at X = 10 M.



B. Longitudinal Direction at X = 15 M.

□ Ex + Ey ◇ Ez

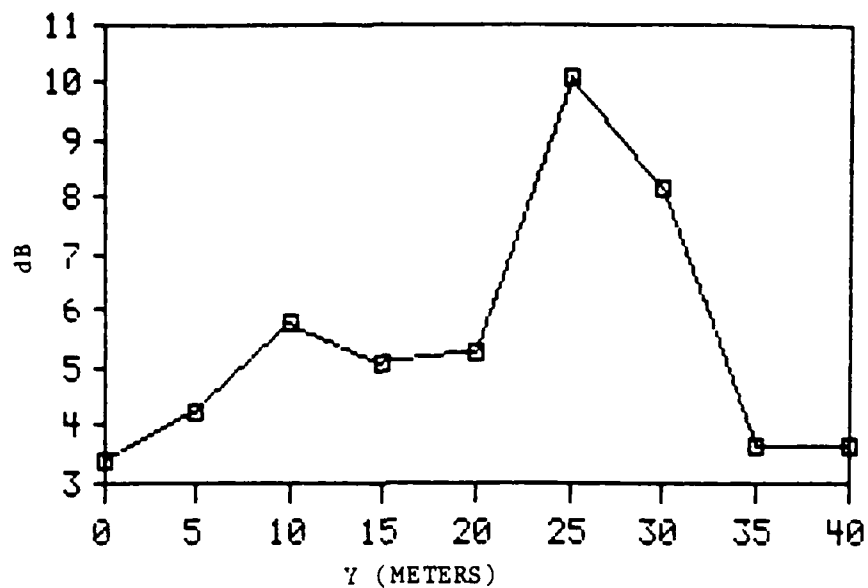
Figure C-5. Electric Field Magnitude at 3 Meters Below Test Object.
Horizontal Incident Field at 6 MHz with Concrete Ground Plane.



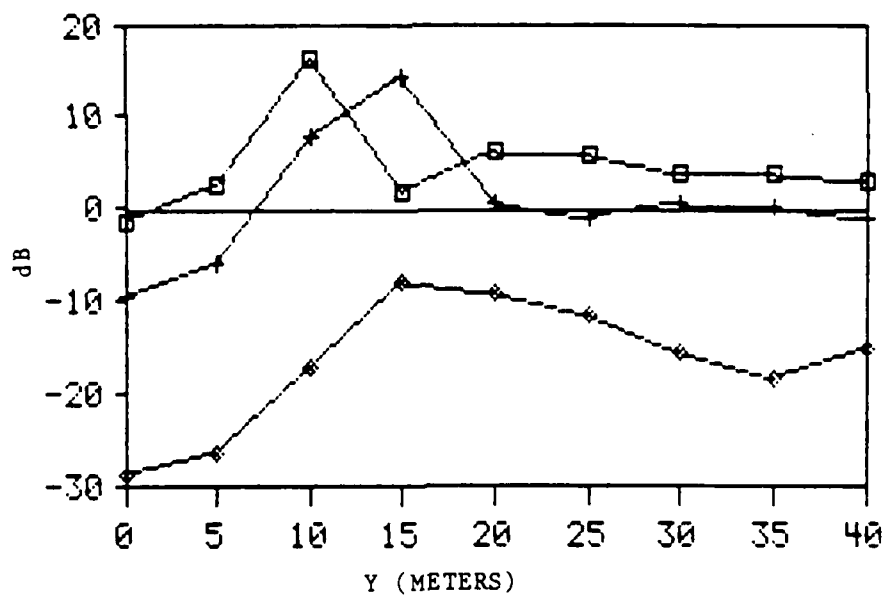
B. Longitudinal Direction at $X = 20$ M.

□ E_x + E_y ◇ E_z

Figure C-6. Electric Field Magnitude at 3 Meters Below Test Object.
Horizontal Incident Field at 6 MHz with Concrete Ground Plane.



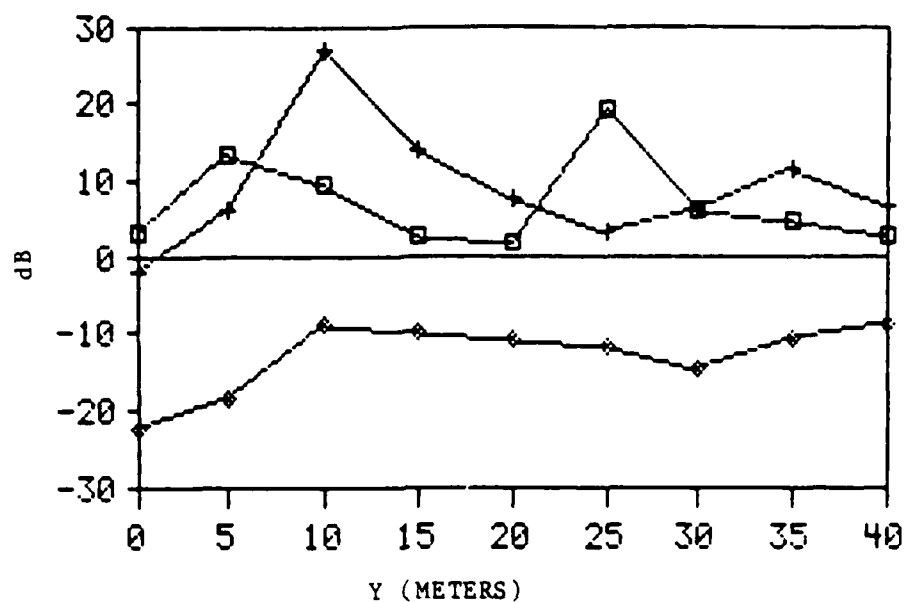
A. Longitudinal Direction at X = 0 M.



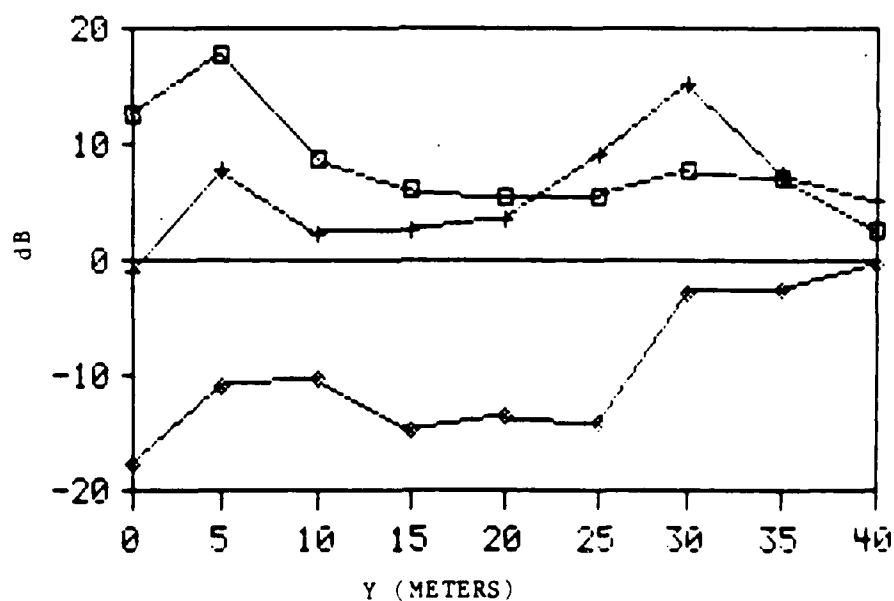
B. Longitudinal Direction at X = 5 M.

□ Ex + Ey ◇ Ez

Figure C-7. Power Ratio Graphs at 3 Meters Below Test Object For Horizontal Polarization at 6 MHz.



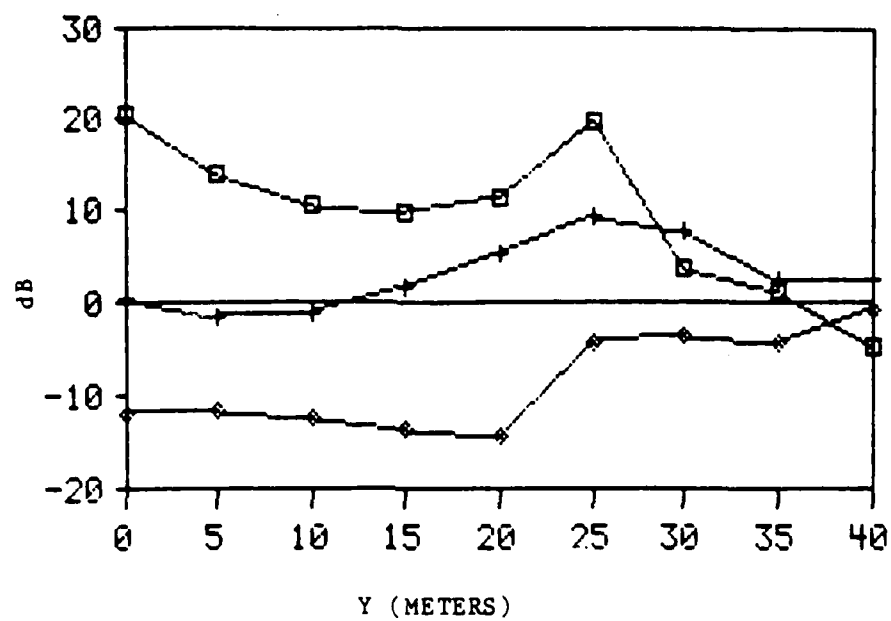
A. Longitudinal Direction at X = 10 M.



B. Longitudinal Direction at X = 15 M.

□ Ex + Ey ○ Ez

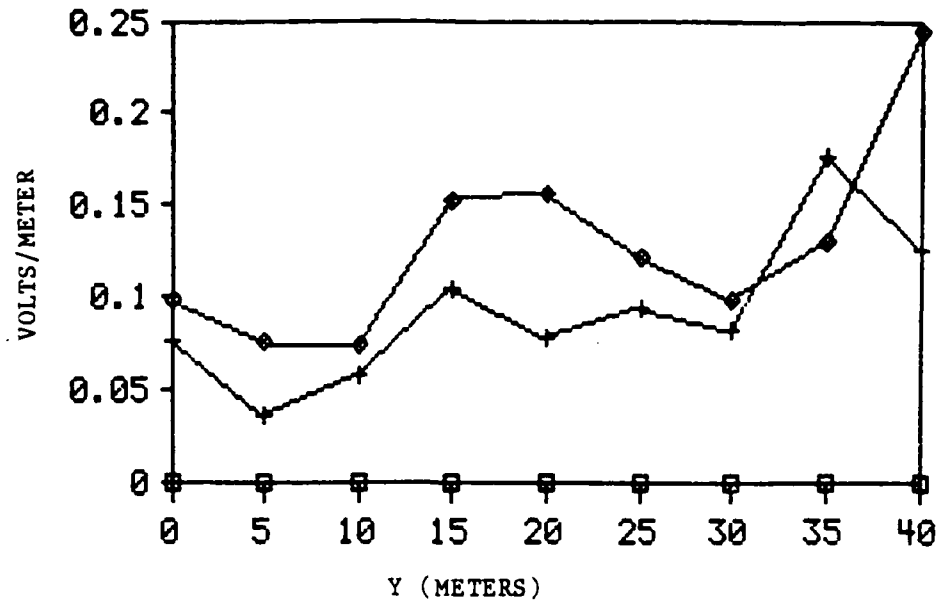
Figure C-8. Power Ratio Graphs at 3 Meters Below Test Object For Horizontal Polarization at 6 MHz.



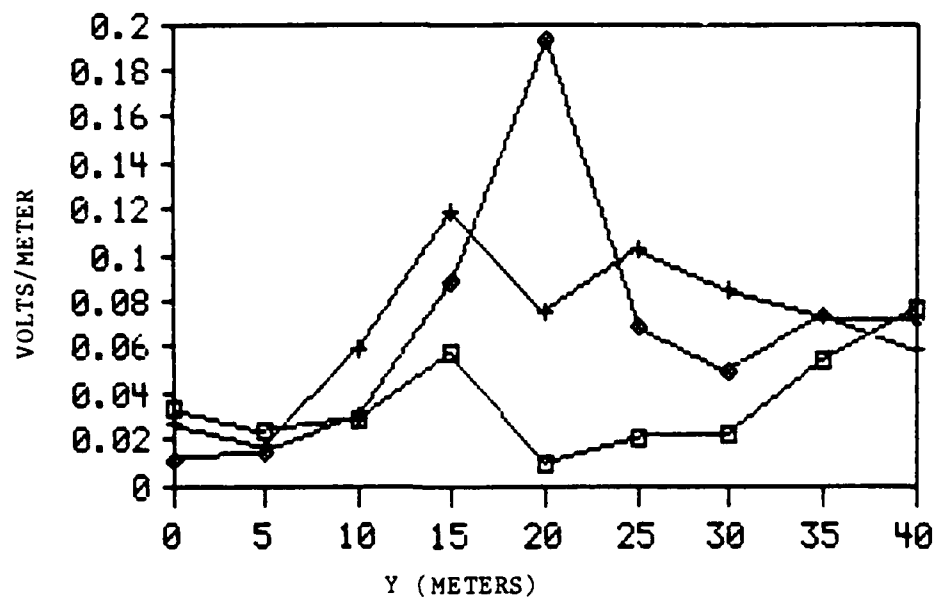
B. Longitudinal Direction at X = 20 M.

□ Ex + Ey ◇ Ez

Figure C-9. Power Ratio Graphs at 3 Meters Below Test Object For Horizontal Polarization at 6 MHz.



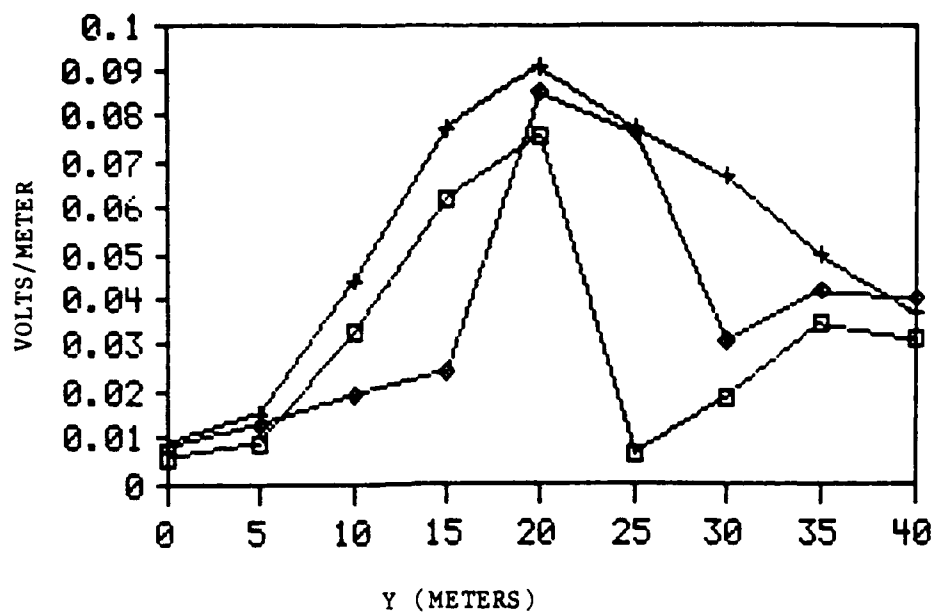
A. Longitudinal Direction at X = 0 M.



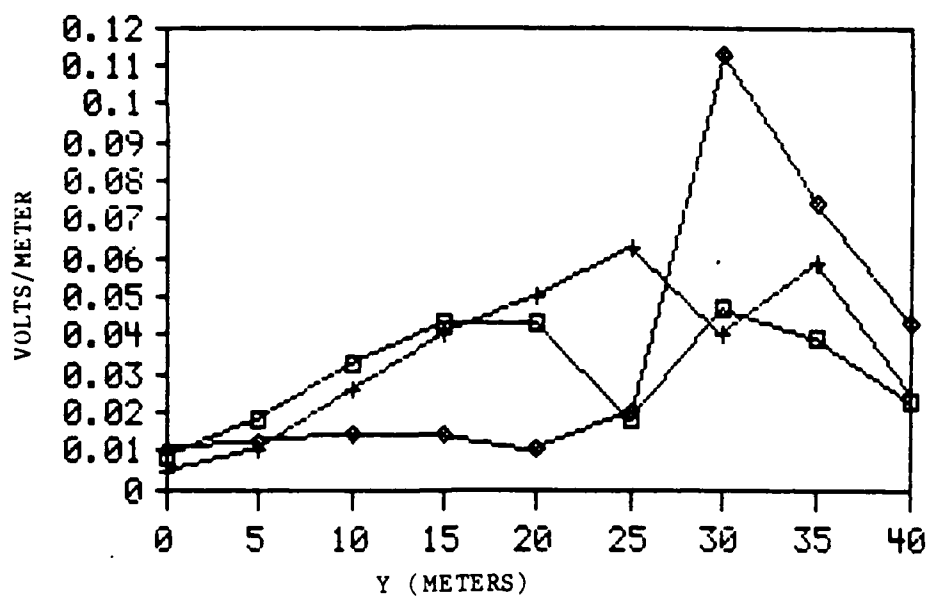
B. Longitudinal Direction at X = 5 M.

□ Ex + Ey ◇ Ez

Figure C-10. Electric Field Magnitude at 3 Meters Below Test Object.
Vertical Incident Field at 6 MHz with no Ground Plane.



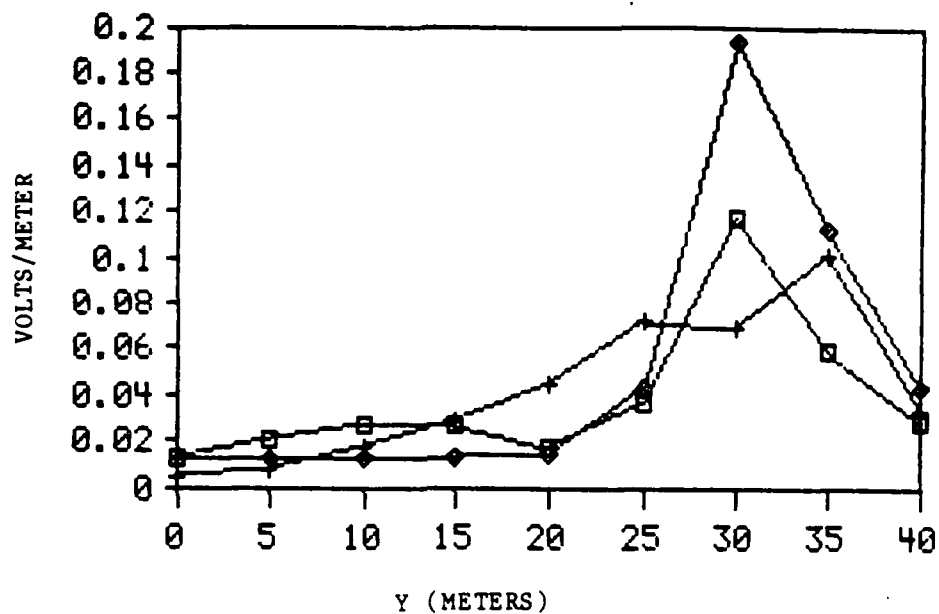
A. Longitudinal Direction at X = 10 M.



B. Longitudinal Direction at X = 15 M.

□ Ex + Ey ◊ Ez

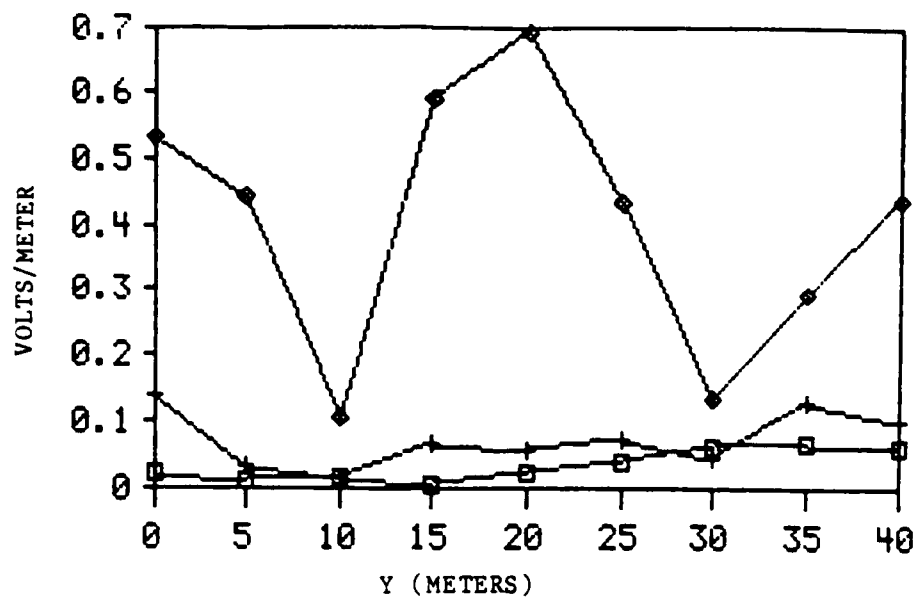
Figure C-11. Electric Field Magnitude at 3 Meters Below Test Object. Vertical Incident Field at 6 MHz with no Ground Plane.



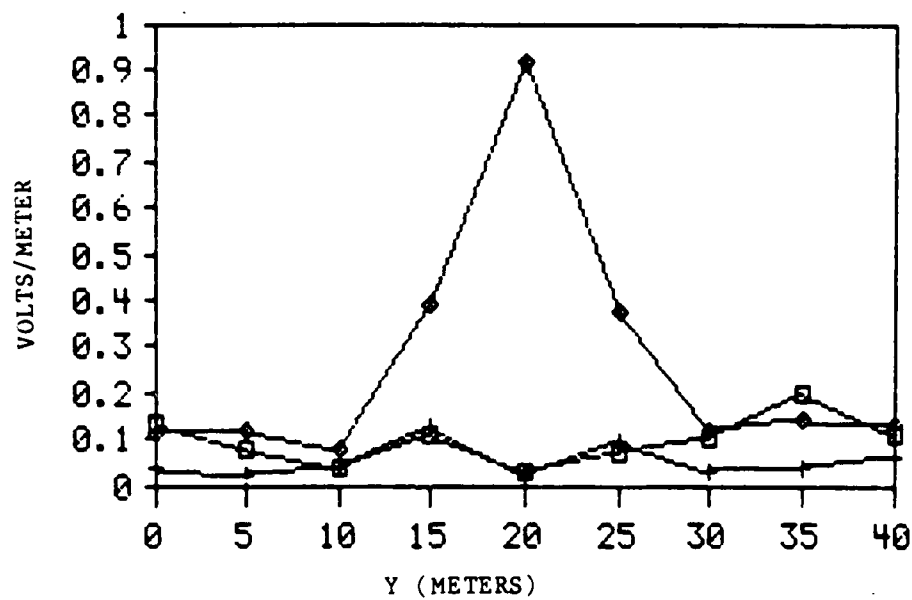
B. Longitudinal Direction at $X = 20$ M.

□ Ex + Ey ◇ Ez

Figure C-12. Electric Field Magnitude at 3 Meters Below Test Object.
Vertical Incident Field at 6 MHz with no Ground Plane.



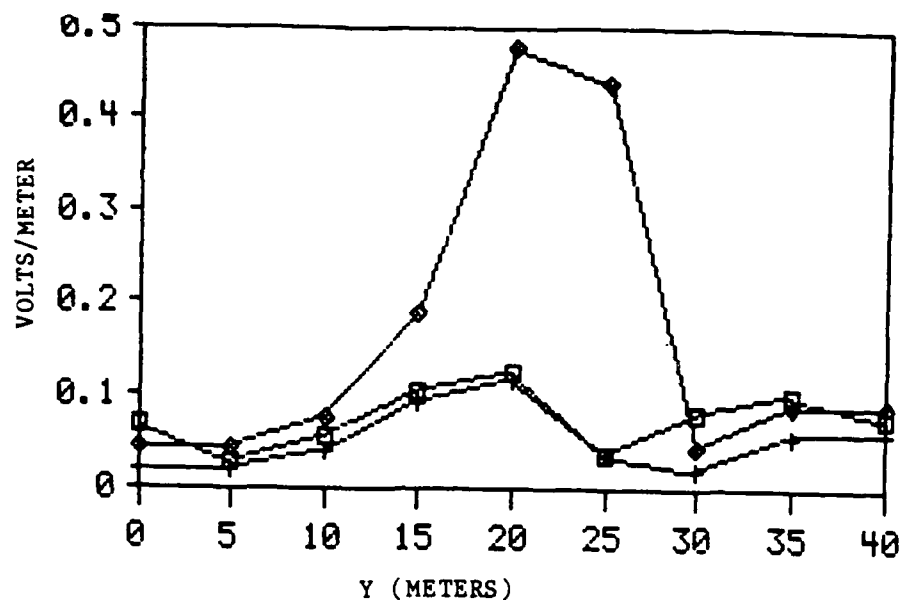
A. Longitudinal Direction at X = 0 M.



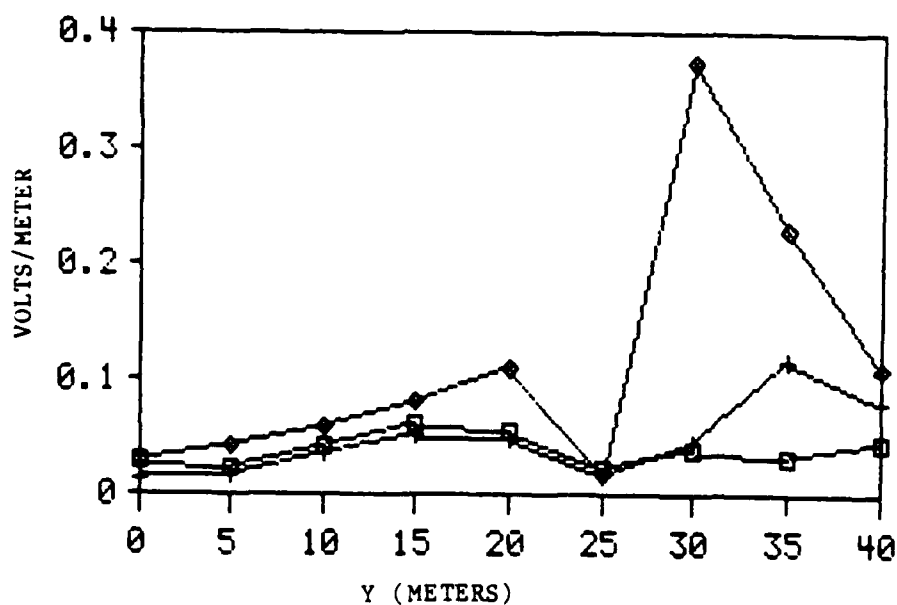
B. Longitudinal Direction at X = 5 M.

□ Ex + Ey ◇ Ez

Figure C-13. Electric Field Magnitude at 3 Meters Below Test Object.
Vertical Incident Field at 6 MHz with Concrete Ground Plane.



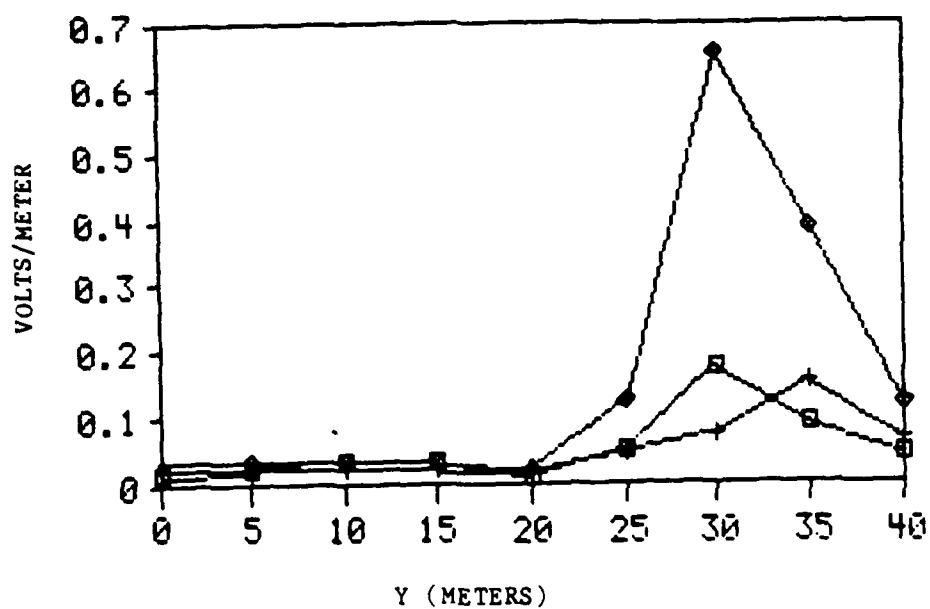
A. Longitudinal Direction at X = 10 M.



B. Longitudinal Direction at X = 15 M.

□ Ex + Ey ◇ Ez

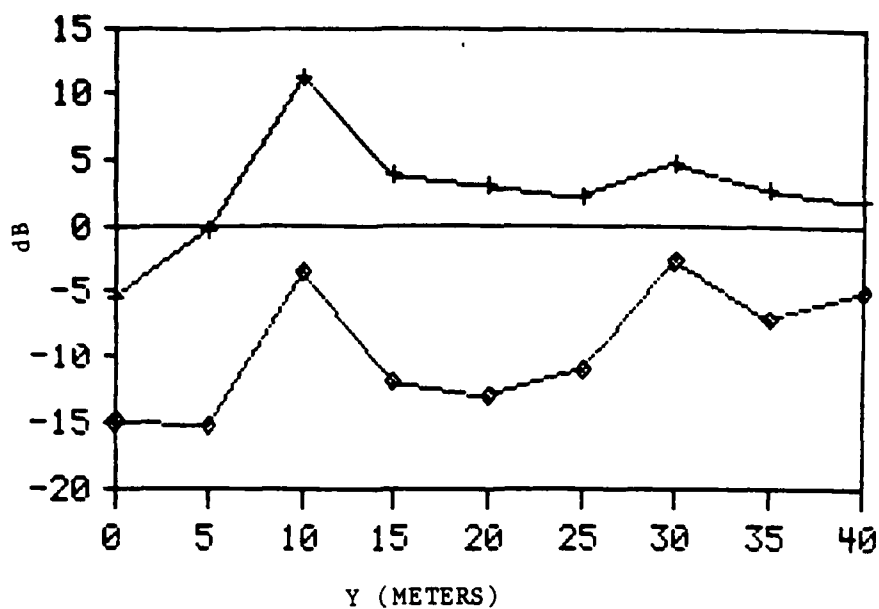
Figure C-14. Electric Field Magnitude at 3 Meters Below Test Object.
Vertical Incident Field at 6 MHz with Concrete Ground Plane.



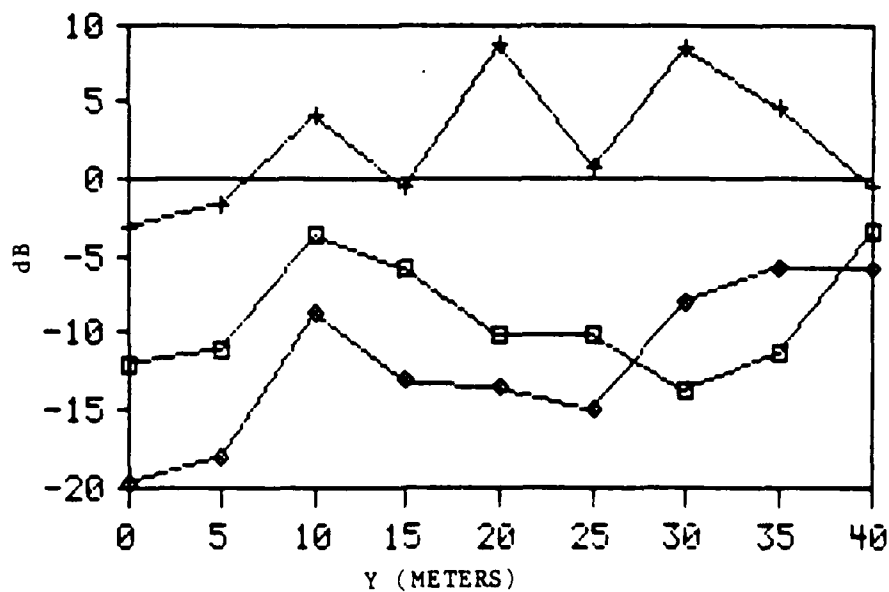
B. Longitudinal Direction at $X = 20$ M.

□ Ex + Ey ◇ Ez

Figure C-15. Electric Field Magnitude at 3 Meters Below Test Object.
Vertical Incident Field at 6 MHz with Concrete Ground Plane.



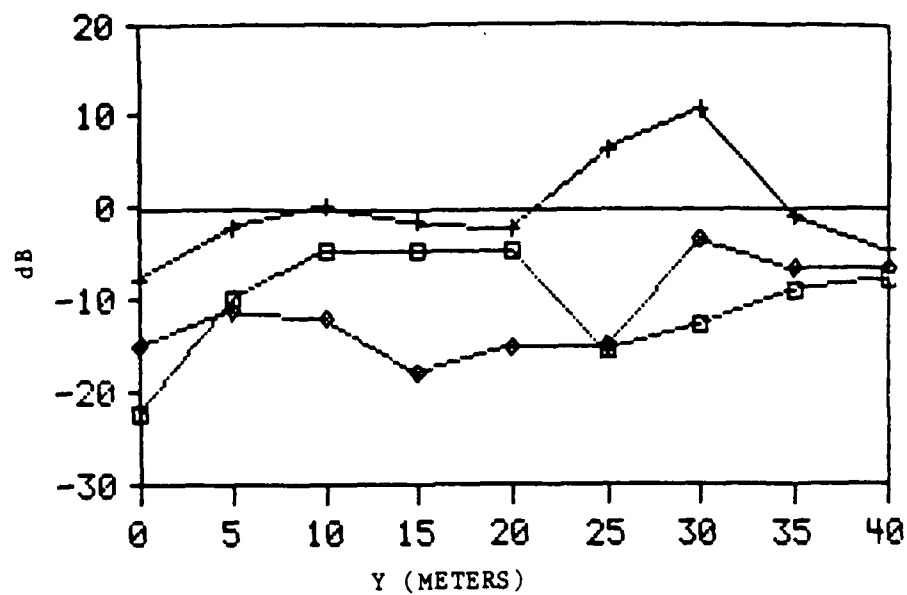
A. Longitudinal Direction at X = 0 M.



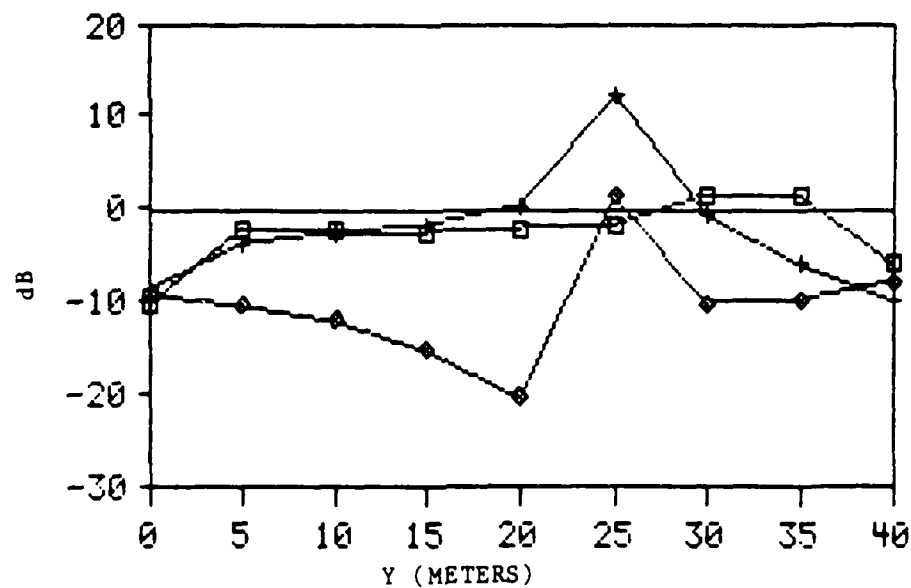
B. Longitudinal Direction at X = 5 M.

□ Ex + Ey ◇ Ez

Figure C-16. Power Ratio Graphs at 3 Meters Below Test Object For Vertical Polarization at 6 MHz.



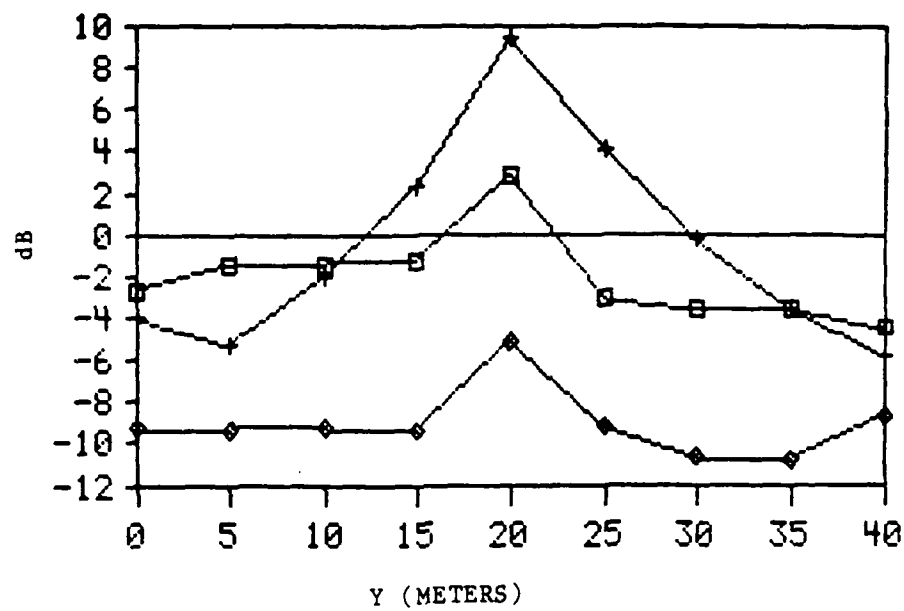
A. Longitudinal Direction at X = 10 M.



B. Longitudinal Direction at X = 15 M.

□ Ex + Ey ◇ Ez

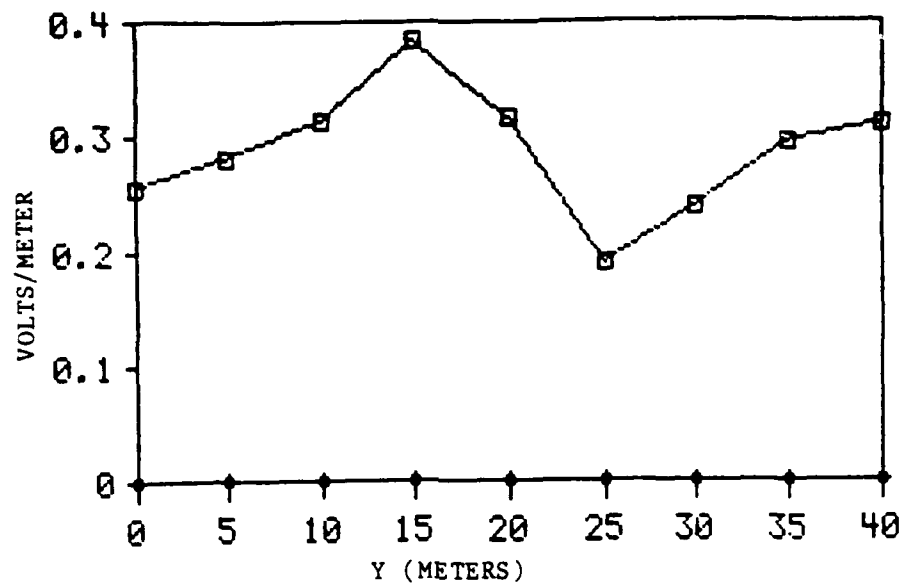
Figure C-17. Power Ratio Graphs at 3 Meters Below Test Object For Vertical Polarization at 6 MHz.



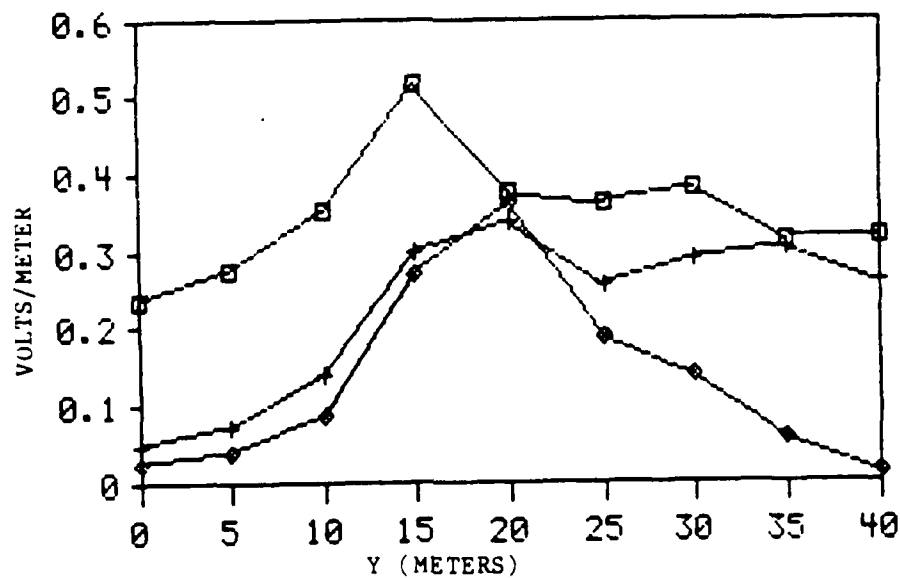
B. Longitudinal Direction at X = 20 M.

□ Ex + Ey ◇ Ez

Figure C-18. Power Ratio Graphs at 3 Meters Below Test Object For Vertical Polarization at 6 MHz.



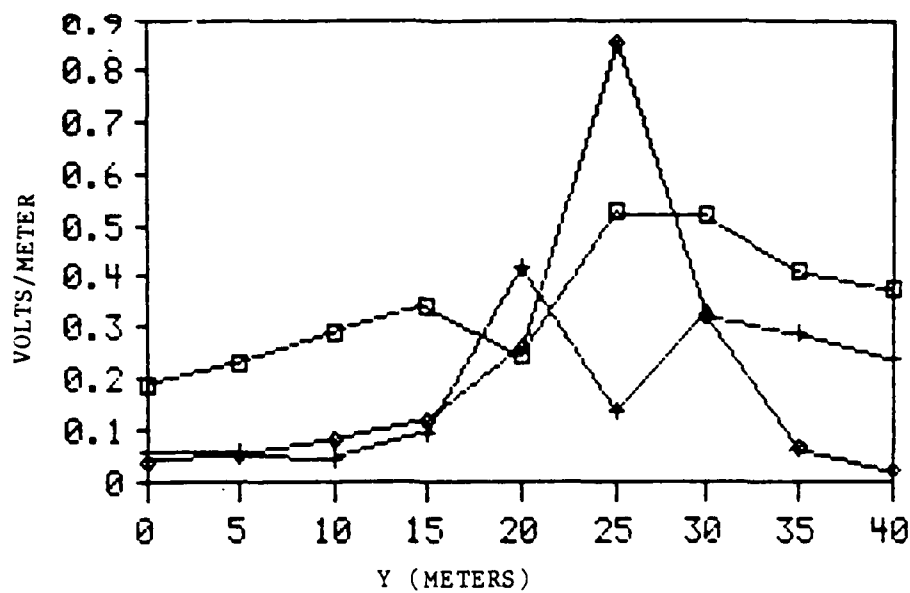
A. Longitudinal Direction at X = 0 M.



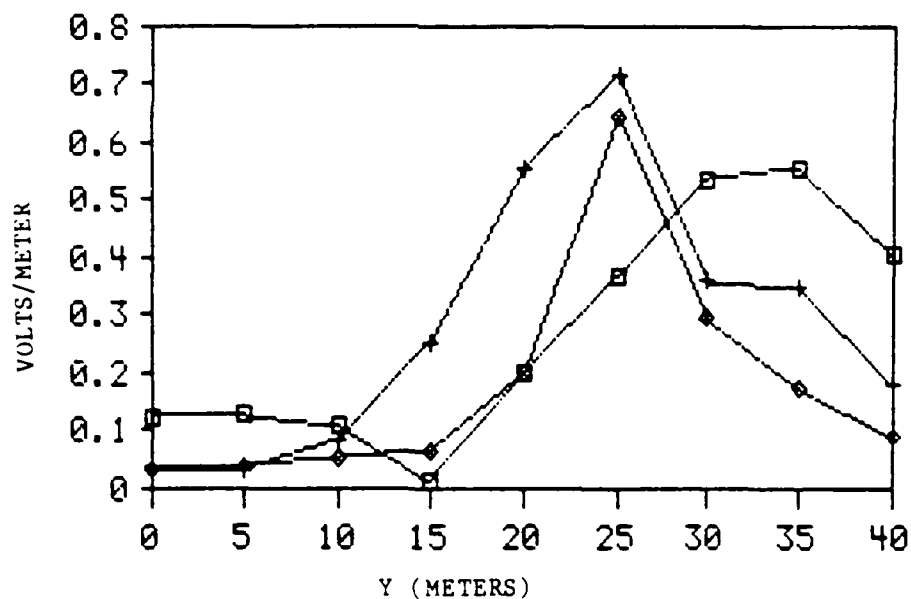
B. Longitudinal Direction at X = 5 M.

□ Ex + Ey ◇ Ez

Figure C-19. Electric Field Magnitude at 3 Meters Below Test Object.
Horizontal Incident Field at 12 MHz with no Ground Plane.



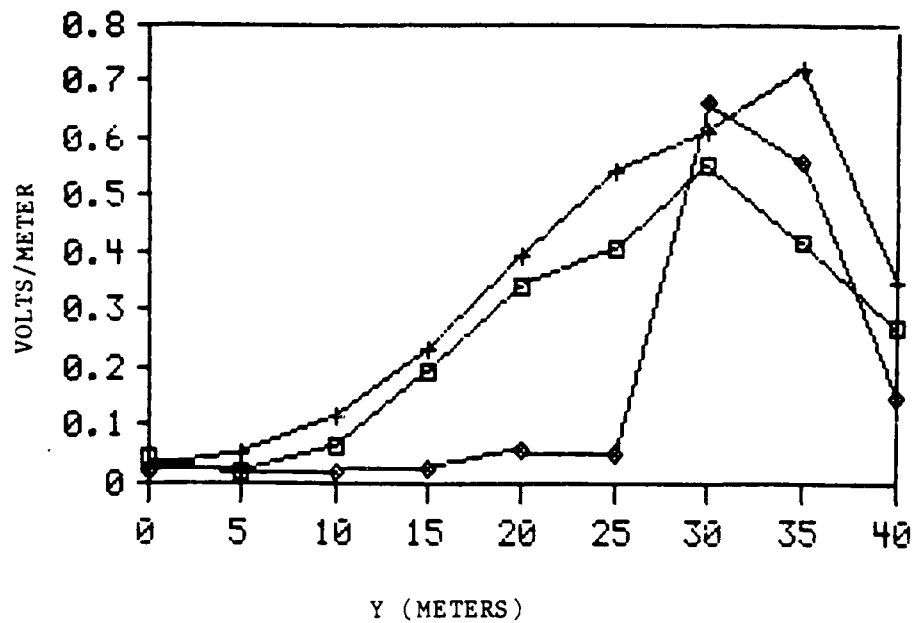
A. Longitudinal Direction at X = 10 M.



B. Longitudinal Direction at X = 15 M.

□ Ex + Ey ◇ Ez

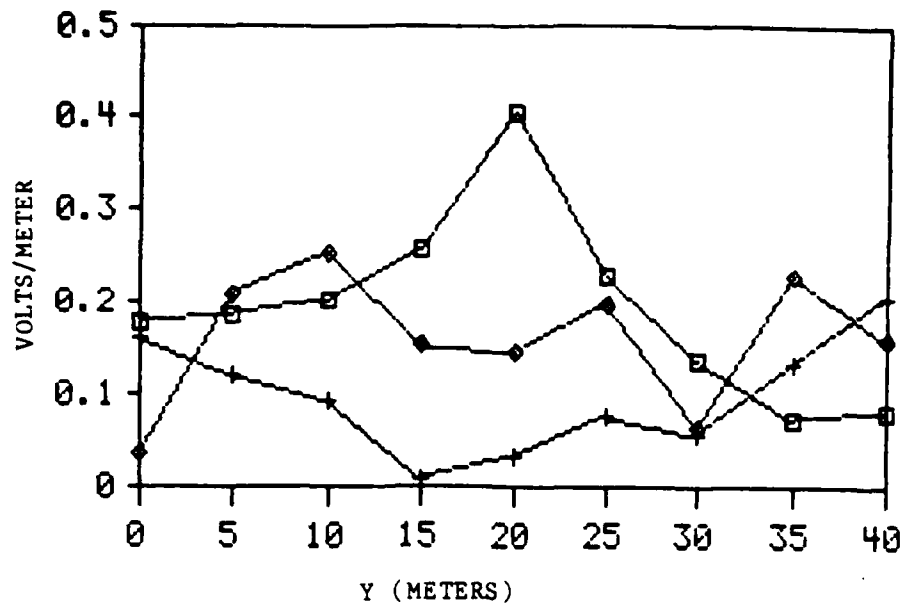
Figure C-20. Electric Field Magnitude at 3 Meters Below Test Object.
Horizontal Incident Field at 12 MHz with no Ground Plane.



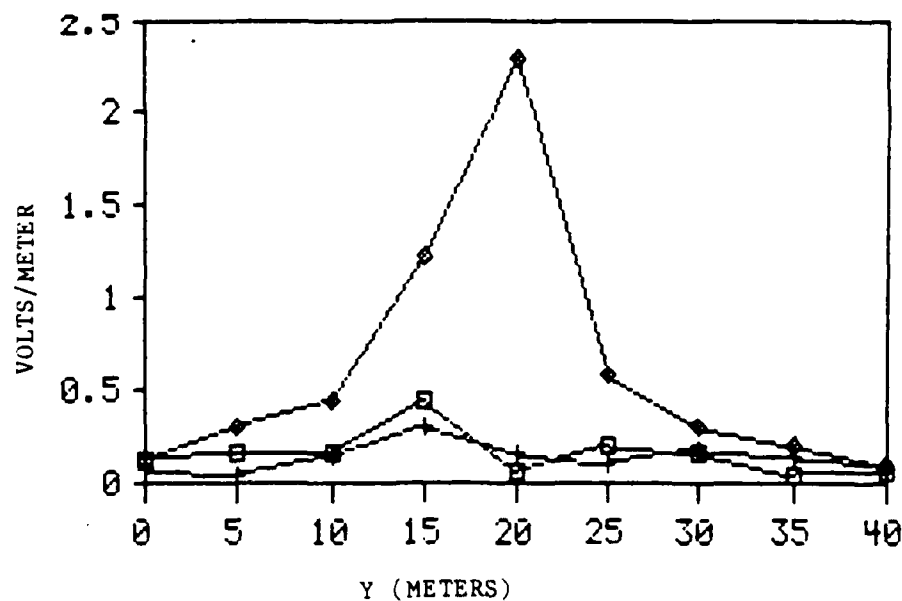
B. Longitudinal Direction at $X = 20$ M.

□ E_x + E_y ◇ E_z

Figure C-21. Electric Field Magnitude at 3 Meters Below Test Object.
Horizontal Incident Field at 12 MHz with no Ground Plane.



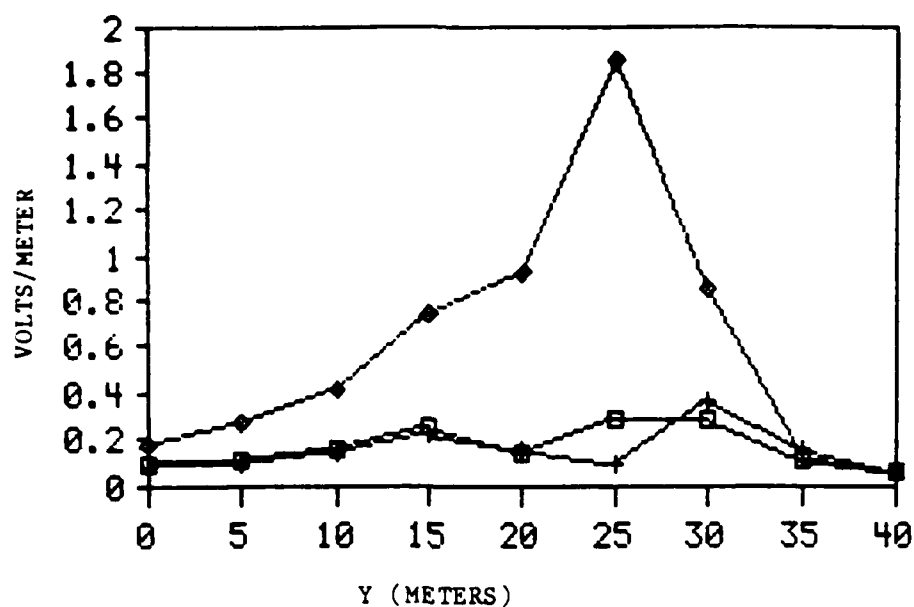
A. Longitudinal Direction at X = 0 M.



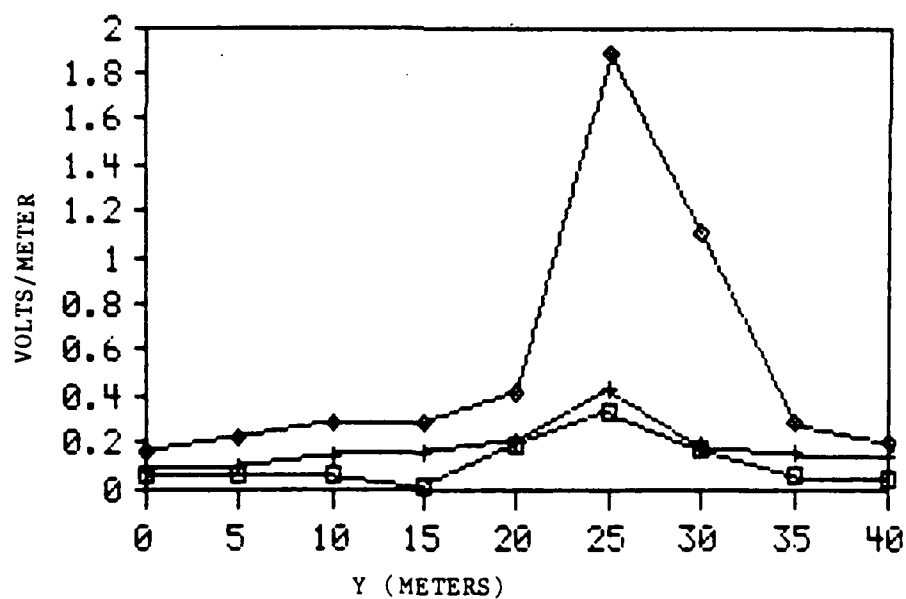
B. Longitudinal Direction at X = 5 M.

□ Ex + Ey ◇ Ez

Figure C-22. Electric Field Magnitude at 3 Meters Below Test Object.
Horizontal Incident Field at 12 MHz with Concrete Ground Plane.



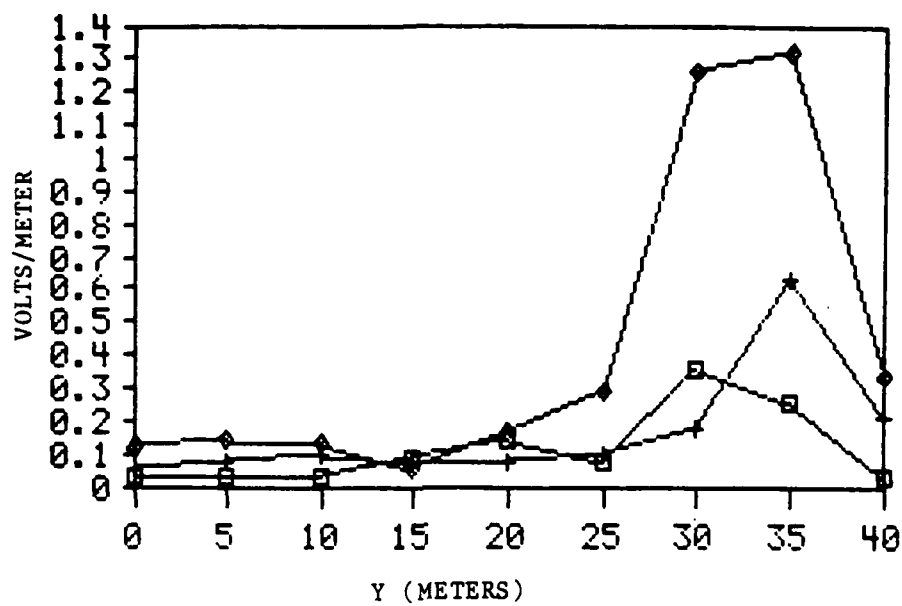
A. Longitudinal Direction at X = 10 M.



B. Longitudinal Direction at X = 15 M.

□ Ex + Ey ◇ Ez

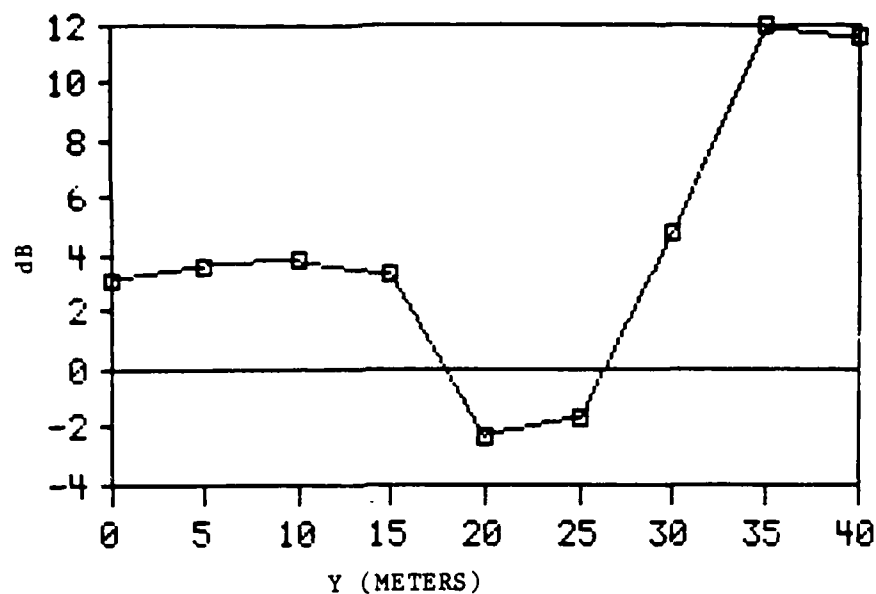
Figure C-23. Electric Field Magnitude at 3 Meters Below Test Object.
Horizontal Incident Field at 12 MHz with Concrete Ground Plane.



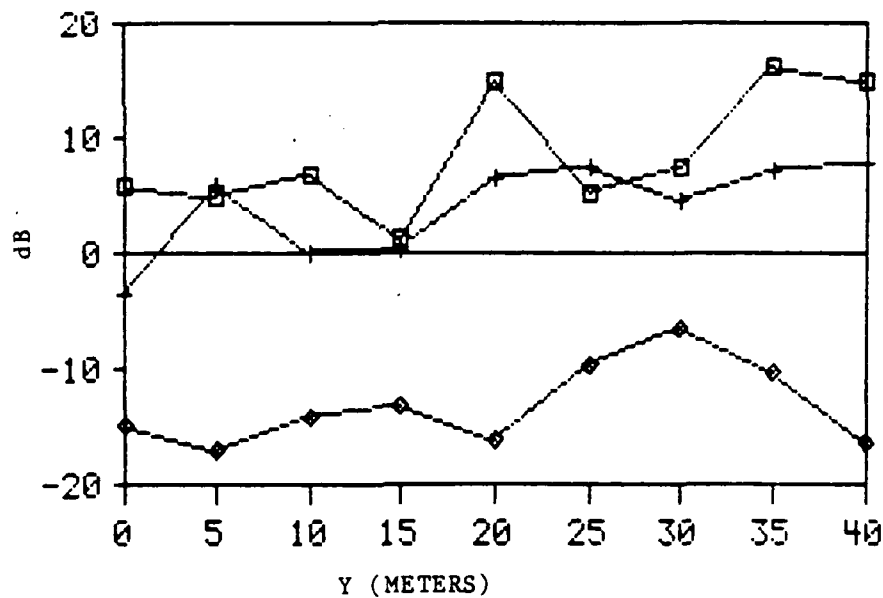
B. Longitudinal Direction at X = 20 M.

□ Ex + Ey ◇ Ez

Figure C-24. Electric Field Magnitude at 3 Meters Below Test Object.
Horizontal Incident Field at 12 MHz with Concrete Ground Plane.



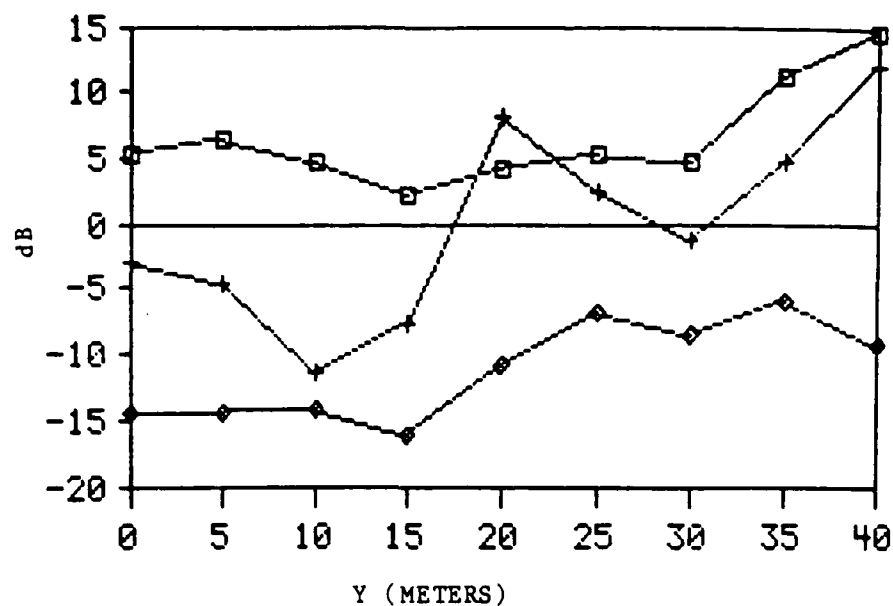
A. Longitudinal Direction at X = 0 M.



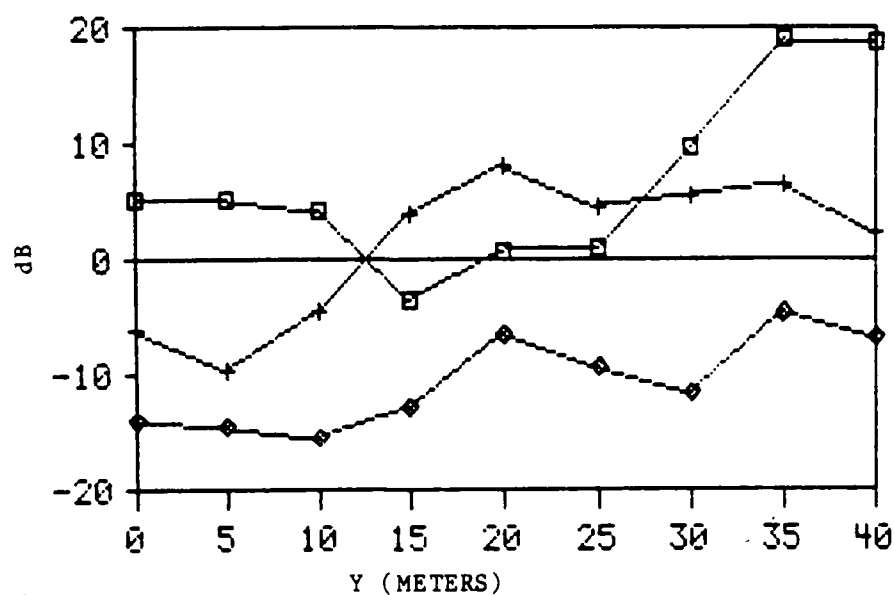
B. Longitudinal Direction at X = 5 M.

□ Ex + Ey ◇ Ez

Figure C-25. Power Ratio Graphs at 3 Meters Below Test Object For Horizontal Polarization at 12 MHz.



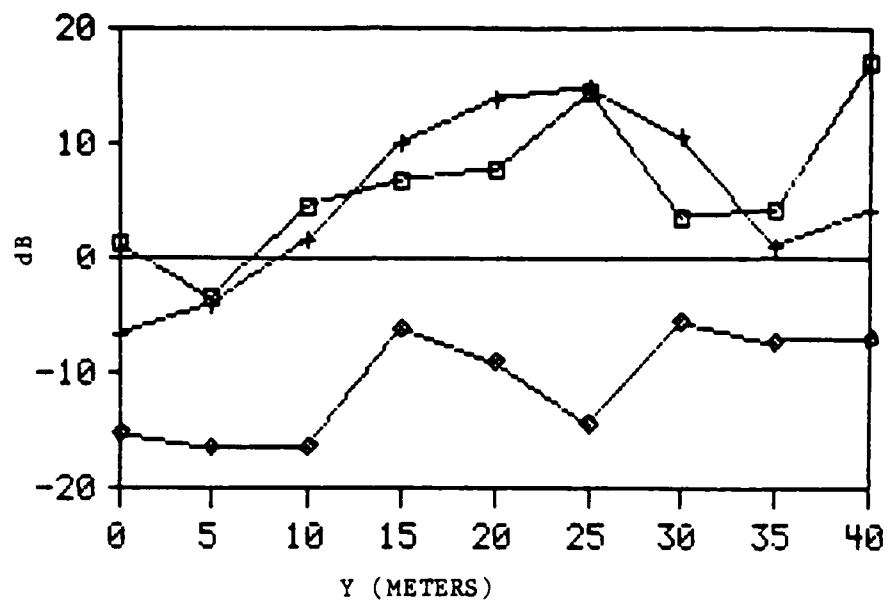
A. Longitudinal Direction at X = 10 M.



B. Longitudinal Direction at X = 15 M.

□ Ex + Ey ◇ Ez

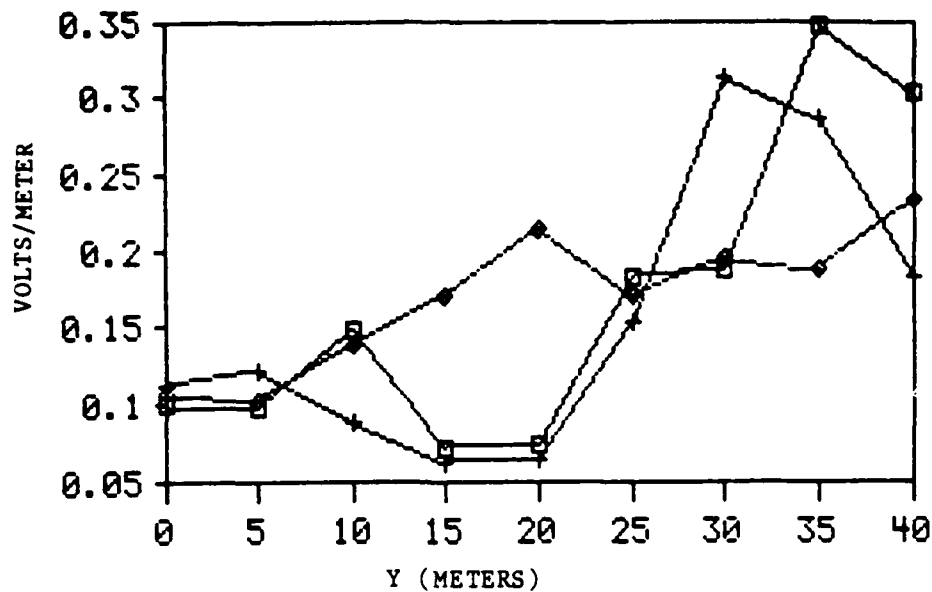
Figure C-26. Power Ratio Graphs at 3 Meters Below Test Object For Horizontal Polarization at 12 MHz.



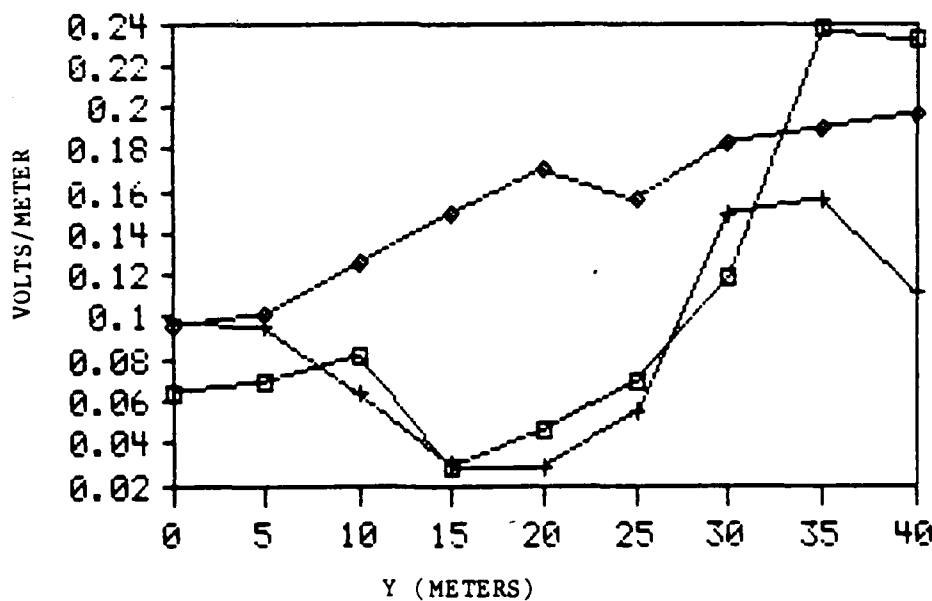
B. Longitudinal Direction at $X = 20$ M.

□ E_x + E_y ○ E_z

Figure C-27. Power Ratio Graphs at 3 Meters Below Test Object For Horizontal Polarization at 12 MHz.



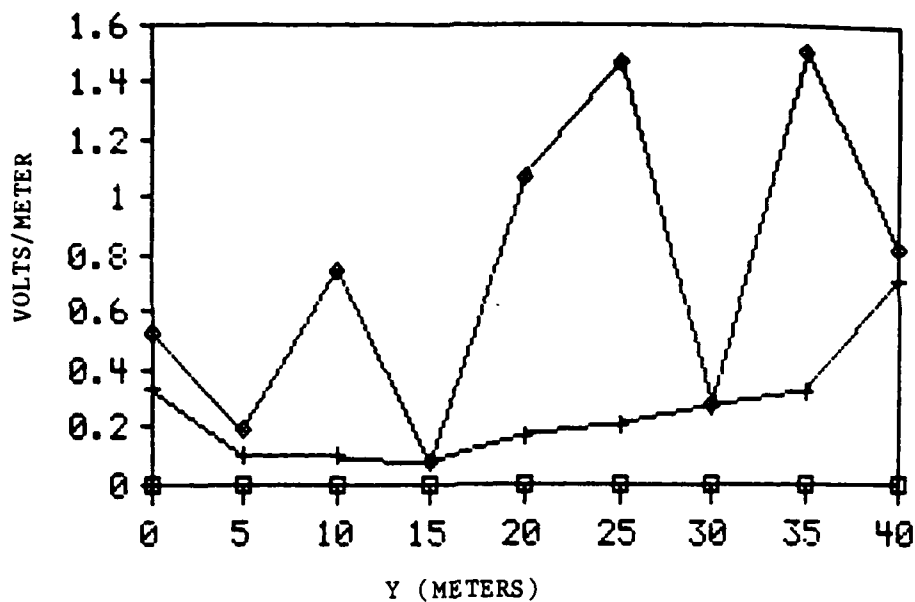
A. Longitudinal Direction at X = 0 M.



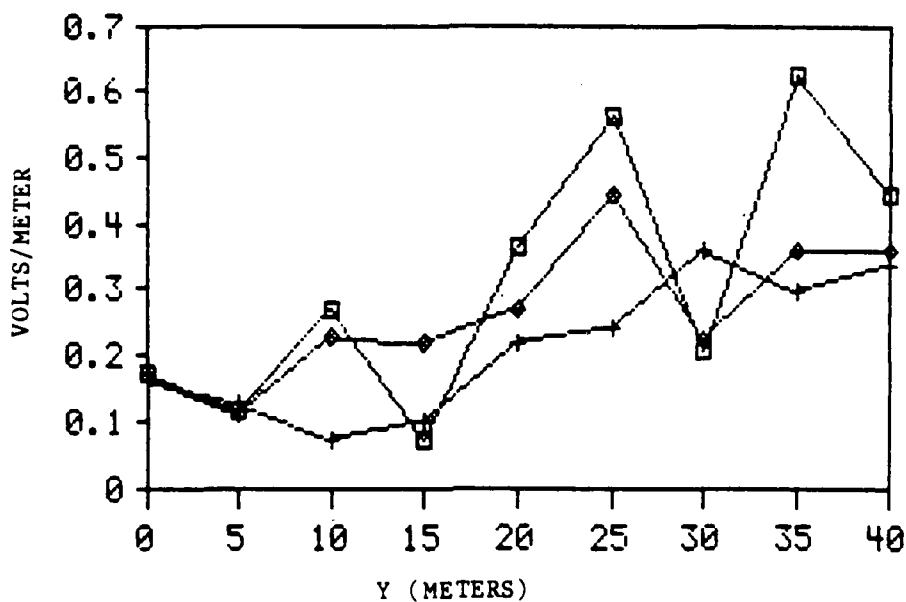
B. Longitudinal Direction at X = 5 M.

□ Ex + Ey ◇ Ez

Figure C-28. Electric Field Magnitude at 3 Meters Below Test Object.
Vertical Incident Field at 12 MHz with no Ground Plane.



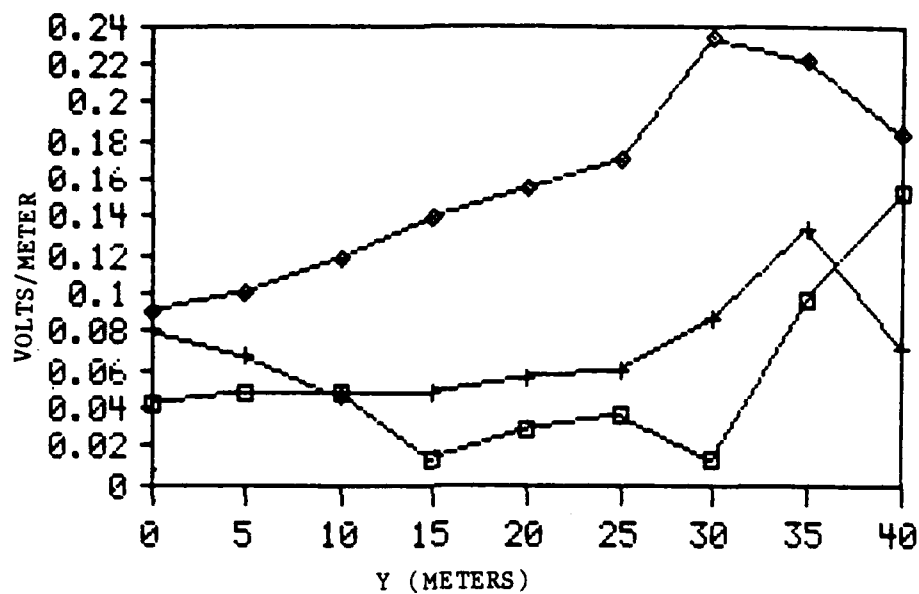
A. Longitudinal Direction at X = 10 M.



B. Longitudinal Direction at X = 15 M.

□ Ex + Ey ◊ Ez

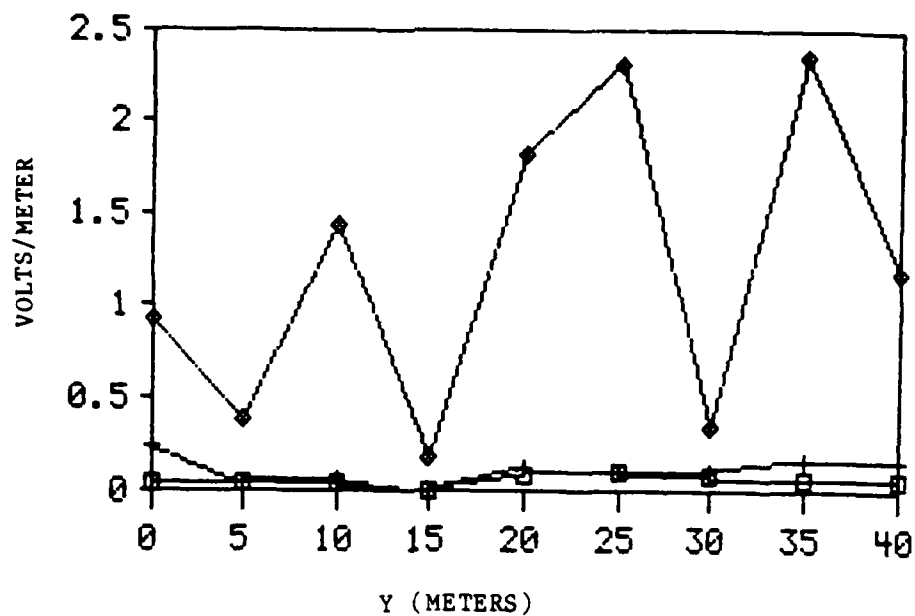
Figure C-29. Electric Field Magnitude at 3 Meters Below Test Object.
Vertical Incident Field at 12 MHz with no Ground Plane.



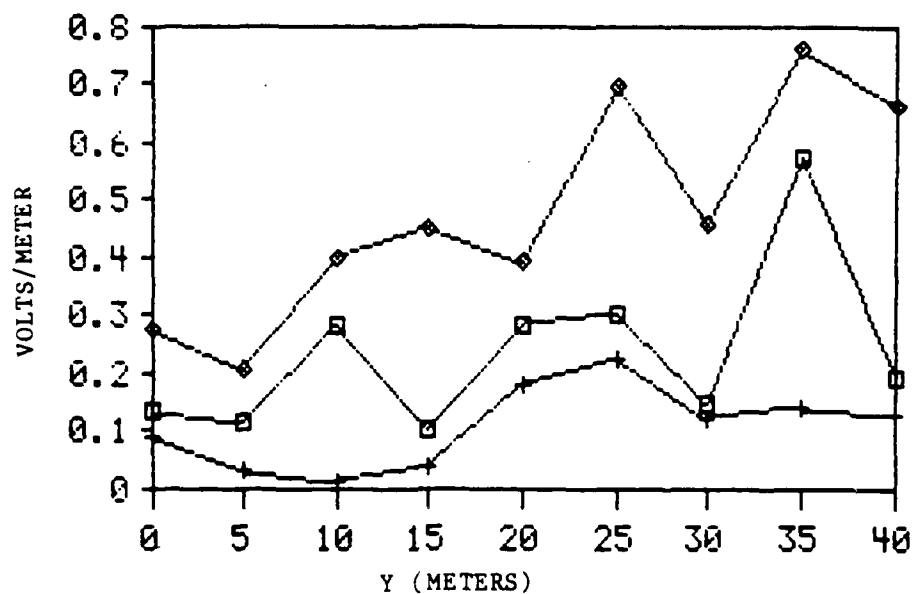
B. Longitudinal Direction at $X = 20$ M.

□ E_x + E_y ◇ E_z

Figure C-30. Electric Field Magnitude at 3 Meters Below Test Object.
Vertical Incident Field at 12 MHz with no Ground Plane.



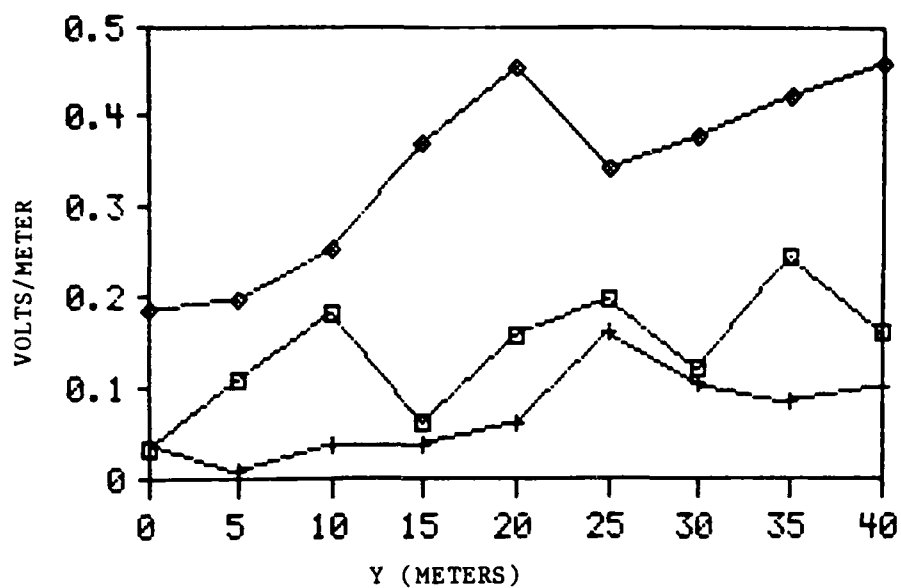
A. Longitudinal Direction at X = 0 M.



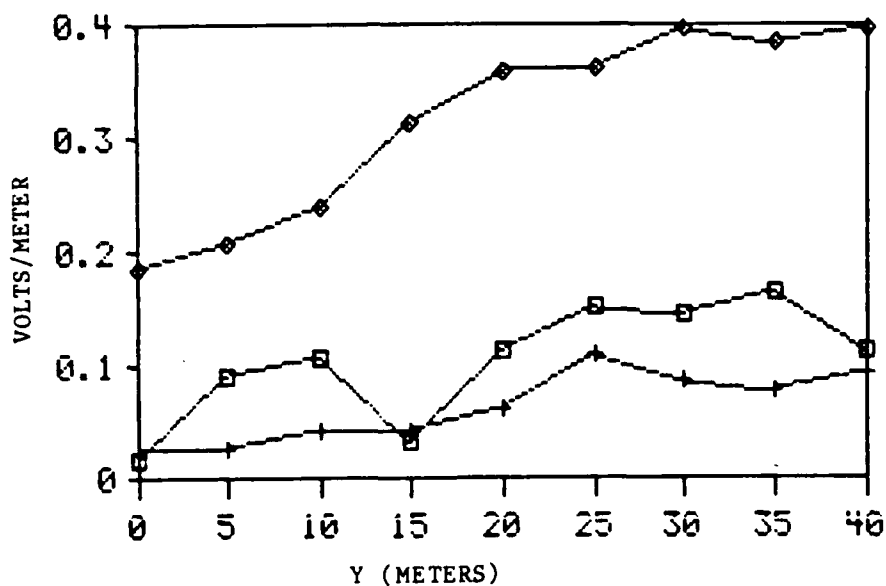
B. Longitudinal Direction at X = 5 M.

□ Ex + Ey ◇ Ez

Figure C-31. Electric Field Magnitude at 3 Meters Below Test Object.
Vertical Incident Field at 12 MHz with Concrete Ground Plane.



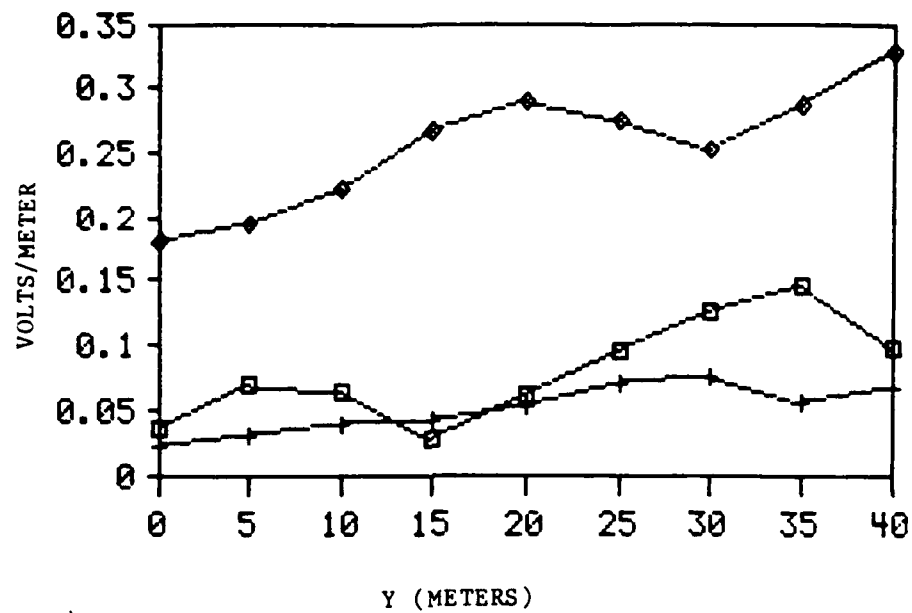
A. Longitudinal Direction at X = 10 M.



B. Longitudinal Direction at X = 15 M.

□ Ex + Ey ◇ Ez

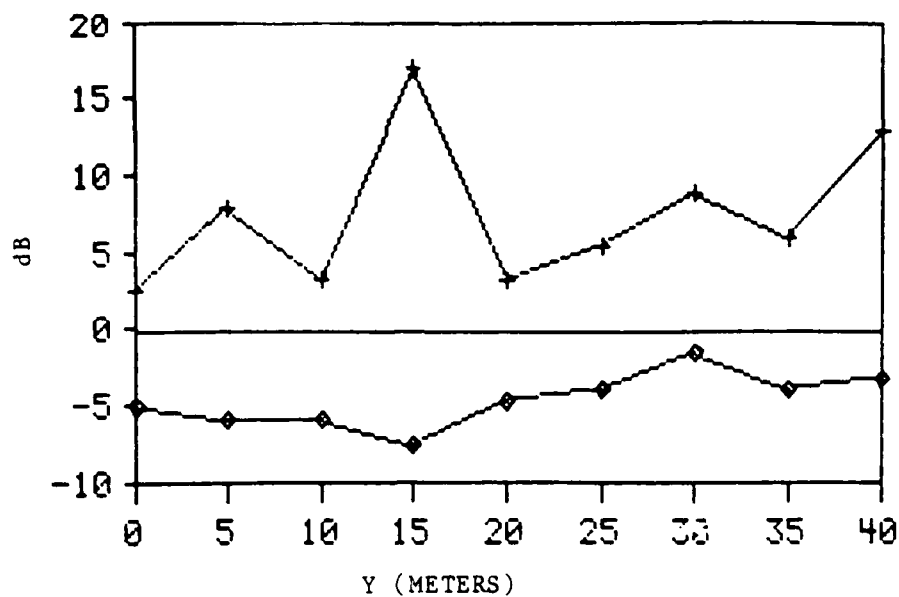
Figure C-32. Electric Field Magnitude at 3 Meters Below Test Object.
Vertical Incident Field at 12 MHz with Concrete Ground Plane.



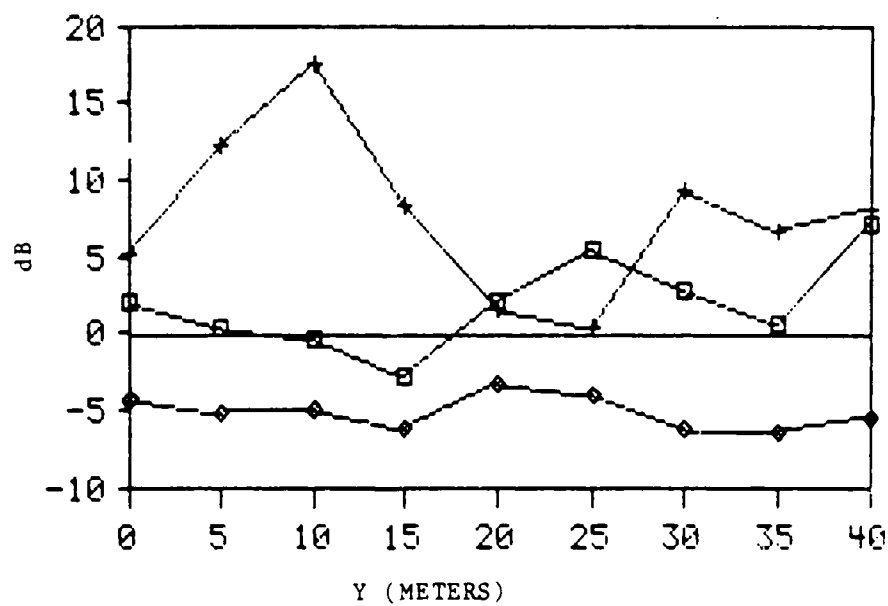
B. Longitudinal Direction at X = 20 M.

□ Ex + Ey ◇ Ez

Figure C-33. Electric Field Magnitude at 3 Meters Below Test Object.
Vertical Incident Field at 12 MHz with Concrete Ground Plane.



A. Longitudinal Direction at X = 0 M.



B. Longitudinal Direction at X = 5 M.

□ Ex + Ey ◇ Ez

Figure C-34. Power Ratio Graphs at 3 Meters Below Test ...
Vertical Polarization at 12 MHz.

AD-A182 668

DETERMINATION AND REDUCTION OF UNWANTED ELECTROMAGNETIC 3/3

WAVE REFLECTIONS I (U) AIR FORCE INST OF TECH

WRIGHT-PATTERSON AFB OH SCHOOL OF ENGI

K A BRUNER

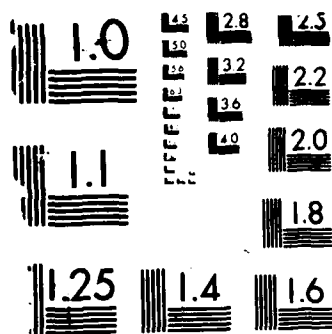
UNCLASSIFIED

MAR 87 AFIT/GE/ENG/87M-8

F/G 28/3

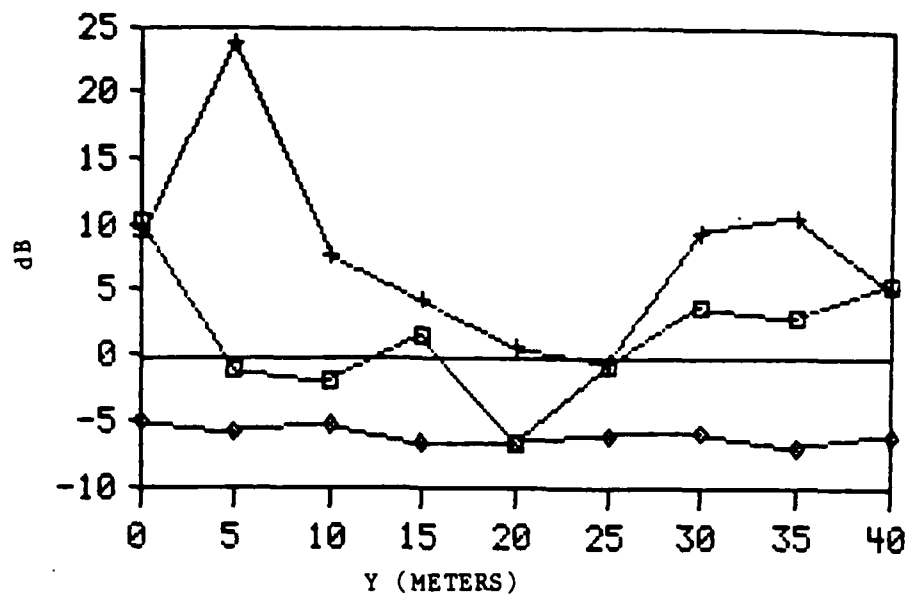
NL

████████████████████ FNL
8 87
DTIC

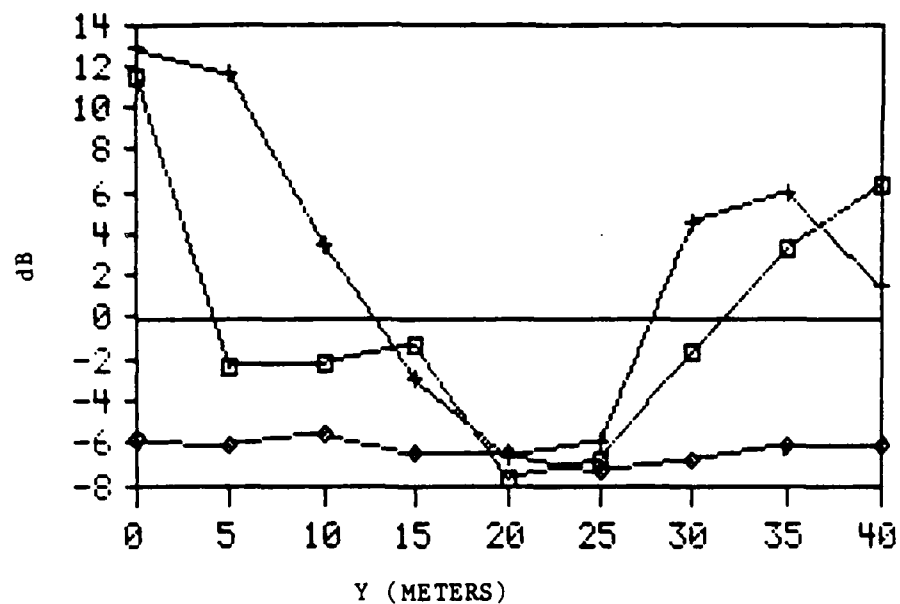


MICROCOPY RESOLUTION TEST CHART

ANSI/ISO 2818-1:1990 (M) 10X



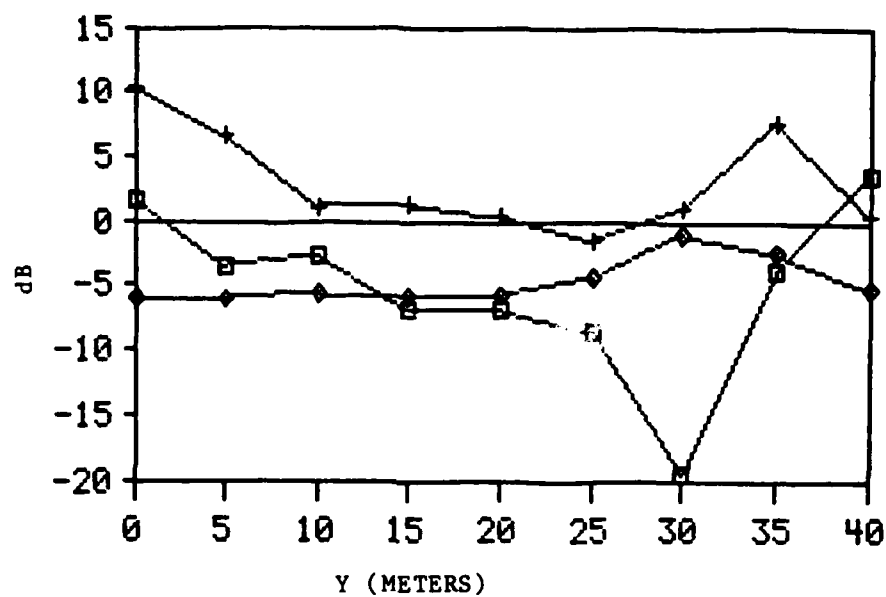
A. Longitudinal Direction at X = 10 M.



B. Longitudinal Direction at X = 15 M.

□ Ex + Ey ◇ Ez

Figure C-35. Power Ratio Graphs at 3 Meters Below Test Object For Vertical Polarization at 12 MHz.



B. Longitudinal Direction at X = 20 M.

□ Ex + Ey ◇ Ez

Figure C-36. Power Ratio Graphs at 3 Meters Below Test Object For Vertical Polarization at 12 MHz.

Bibliography

1. Balanis, Constantine A. Antenna Theory: Analysis and Design. New York: Harper and Row Publishers, 1982.
2. Baum, Carl E. The Conical Transmission Line as a Wave Launcher and Terminator for a Cylindrical Transmission Line. EMP Sensor and Simulation Notes, Note XXXI. Air Force Weapons Laboratory, Kirtland AFB, NM, 16 January 1967.
3. Cheng, David K. Field and Wave Electromagnetics. Reading, Ma: Addison Wesley Publishing Company, 1983.
4. Coffey, Edgar L. Telephonic Communications. Advanced Electronics, Albuquerque, NM, 29 Sept 1986.
5. Collin, Robert E. Field Theory of Guided Waves. New York: McGraw-Hill Book Company, 1960.
6. Hayt, William H. Engineering Electromagnetics. New York: McGraw-Hill Book Company, 1981.
7. Kadlec, Diana L. and others. General Electromagnetic Model for the Analysis of Complex Systems (GEMACS): Engineering Manual (Version 3). Contract F30602-81-C-0084. BDM Corporation, Albuquerque, NM, July 1983.
8. ----. General Electromagnetic Model for the Analysis of Complex Systems (GEMACS): Users Manual (Version 3). Contract F30602-81-C-0084. BDM Corporation, Albuquerque, NM, July 1983.
9. Kehrer, W.S. and others. Conceptual Design of Illuminators for Hardness Surveillance Testing: Revised Draft. Contract DC-IR-4088.430-1B. Dikewood, Santa Monica, CA, 2 June 1982.
10. King, Ronold W.P. and others. "Standing Waves and Notches in an EMP Simulator and Their Reduction," IEEE Transactions on Electromagnetic Compatibility, EMC-23, No. 2: 80-87 (May 1982).
11. King, Ronold W.P. and Dennis J. Blejer. "The Electromagnetic Field in an EMP Simulator at High Frequency," IEEE Transactions on Electromagnetic Compatibility, EMC-21, No. 3: 263-269 (August 1979).
12. Kraus, J. Electromagnetics (Third Edition). New York: McGraw-Hill Book Company, 1984.
13. Lee, K.S.H. (ed). EMP Interaction: Principles, Techniques and Reference Data (A Complete Concatenation of Technology From the EMP Interaction Notes). EMP Interaction 2-1, Contract F29601-76-C-0149 Dikewood, Santa Monica, CA, December 1980.

Bibliography (cont)

14. Microwave Products. Short Form Catalog. Emerson and Cuming Inc, Canton MA, undated.
15. Prather, William D. and Michael G. Harrison. A Comparison of the EC-135 External Coupling Predictions with Scale Model and Full Scale Measurements. Air Force Weapons Laboratory, Kirtland AFB, NM, March 1977.
16. Shen, Hao-Ming and Ronold W.P. King. "Experimental Investigation of the Rhombic EMP Simulator: Comparison with Theory and Parallel Plate Simulator," IEEE Transactions on Electromagnetic Compatibility, EMC-24, No3: 349-355 (August 1982).
17. -----. "The Rhombic EMP Simulator," IEEE Transactions on Electromagnetic Compatibility, EMC-24, No2: 255-265 (May 1982).
18. Smith, 1Lt Terry. Personal Correspondance, Working Paper on Relative Permittivity and Conductivity of Concrete. Air Force Weapons Laboratory, Kirtland AFB, NM, March 1986.
19. -----. Personal Correspondance, Working Paper on Impedance characteristics of the HSI. Air Force Weapons Laboratory, Kirtland AFB, NM, 15 May 1986.
20. Von Hippel, Arthur R. Dielectrics and Waves. New York: John Wiley and Sons, Inc, 1954.
21. Zuffada, C. and N. Engheta. Analysis of a Hardness Surveillance Illuminator: Draft. Contract DC-IR-4088.420-1. Dikewood, Santa Monica, CA, 21 March 1986.

Vita

Captain Kenneth A. Bruner was born in Austin, Texas on 23 March 1959. Since his father was in the Air Force, he had an opportunity to travel throughout the United States when he was young. He graduated from McGavock High School in 1977, and attended Volunteer State Community College in Gallatin, Tennessee for two years, graduating with an Associates degree in Science in 1979. He continued his education by attending Vanderbilt University on an Air Force ROTC scholarship. He graduated from Vanderbilt University in 1981 with a Bachelor of Engineering in Electrical Engineering. Upon graduation, he accepted a commission in the United States Air Force and served his first tour of duty as an Electronic Warfare System Engineer at the Tactical Air Warfare Center, Eglin AFB, Florida until entering the School of Engineering, Air Force Institute of Technology, in May 1985.

REPORT DOCUMENTATION PAGE

Form Approved
OMB No 0704-0188

1a. REPORT SECURITY CLASSIFICATION UNCLASSIFIED			1b. RESTRICTIVE MARKINGS		
2a. SECURITY CLASSIFICATION AUTHORITY			3. DISTRIBUTION/AVAILABILITY OF REPORT Approved for Public Release Distribution Unlimited		
2b. DECLASSIFICATION/DOWNGRADING SCHEDULE					
4. PERFORMING ORGANIZATION REPORT NUMBER(S) AFIT/GE/ENG/87M-8			5. MONITORING ORGANIZATION REPORT NUMBER(S)		
6a. NAME OF PERFORMING ORGANIZATION School of Engineering		6b. OFFICE SYMBOL (If applicable) AFIT/ENG		7a. NAME OF MONITORING ORGANIZATION	
6c. ADDRESS (City, State, and ZIP Code) Air Force Institute of Technology Wright-Patterson AFB, Ohio 45433			7b. ADDRESS (City, State, and ZIP Code)		
8a. NAME OF FUNDING/SPONSORING ORGANIZATION		8b. OFFICE SYMBOL (If applicable)		9. PROCUREMENT INSTRUMENT IDENTIFICATION NUMBER	
8c. ADDRESS (City, State, and ZIP Code)			10. SOURCE OF FUNDING NUMBERS		
			PROGRAM ELEMENT NO	PROJECT NO	TASK NO
			WORK UNIT ACCESSION NO		
11. TITLE (Include Security Classification) Determination and Reduction of Unwanted Electromagnetic Wave Reflections in an EMP Simulator (U)					
12. PERSONAL AUTHOR(S) Kenneth A. Bruner, Capt, USAF					
13a. TYPE OF REPORT MS Thesis		13b. TIME COVERED FROM _____ TO _____		14. DATE OF REPORT (Year, Month, Day) 1987 March	
15. PAGE COUNT 196					
16. SUPPLEMENTARY NOTATION					
17. COSATI CODES			18. SUBJECT TERMS (Continue on reverse if necessary and identify by block number)		
FIELD	GROUP	SUB-GROUP	Electromagnetic Pulse Simulator Electromagnetic Wave Reflections Electromagnetic Absorption		
20	15				
19. ABSTRACT (Continue on reverse if necessary and identify by block number) See Reverse for Abstract					
20. DISTRIBUTION/AVAILABILITY OF ABSTRACT <input checked="" type="checkbox"/> UNCLASSIFIED/UNLIMITED <input type="checkbox"/> SAME AS RPT. <input type="checkbox"/> DTIC USERS			21. ABSTRACT SECURITY CLASSIFICATION UNCLASSIFIED		
22a. NAME OF RESPONSIBLE INDIVIDUAL Capt Randy Jost			22b. TELEPHONE (Include Area Code) (513) 255-5533		22c. OFFICE SYMBOL AFIT/ENG

Approved for public release: IAW AFR 190-14
Lynn E. Wolaver 5 May 87
Dean for Research and Professional Development
Air Force Institute of Technology (AFIT)
Wright-Patterson AFB OH 45433

Abstract

This investigation determined the electromagnetic (EM) wave characteristics of an electromagnetic pulse (EMP) simulator from 6 MHz to 30 MHz, and determined a method of reducing unwanted wave reflections within the simulator. The electromagnetic fields produced by the EMP simulator were determined by using a method of moments routine for both a perfectly conducting ground plane and a concrete ground plane. Comparisons of the method of moments results with theoretical results were accomplished.

The electromagnetic wave absorber ECCOSORB NZ-31 was evaluated for use within the EMP simulator. The absorber was analyzed using two-port network theory. Data for the absorption characteristics of the material when used with various surface are provided.

An analysis of the scattering characteristics of a wire model used within the EMP simulator was accomplished using a method of moments approach. Determination of the electromagnetic wave reflections on the wire was assessed.

A determination of the optimal placement of the absorber material within the EMP simulator is made. A combination of techniques to further reduce wave reflections is suggested.

END

8-87

DTIC